Aerosol-cloud interactions studied with a chemistry-climate model

Dissertation
zur Erlangung des akademischen Grades
"Doctor rerum naturalium (Dr. rer. nat.)"

JOHANNES GUTENBERG
UNIVERSITÄT MAINZ

am Fachbereich Physik, Mathematik und Informatik der
Johannes Gutenberg-Universität Mainz

Dong Yeong Chang
geboren in Seoul

Mainz, September 2014

Abstract

This study aims at a comprehensive understanding of the effects of aerosol-cloud interactions and their effects on cloud properties and climate using the chemistry-climate model EMAC. In this study, CCN activation is regarded as the dominant driver in aerosol-cloud feedback loops in warm clouds. The CCN activation is calculated prognostically using two different cloud droplet nucleation parameterizations, the STN and HYB CDN schemes. Both CDN schemes account for size and chemistry effects on the droplet formation based on the same aerosol properties. The calculation of the solute effect (hygroscopicity) is the main difference between the CDN schemes. The κ-method is for the first time incorporated into Abdul-Razzak and Ghan activation scheme (ARG) to calculate hygroscopicity and critical supersaturation of aerosols (HYB), and the performance of the modified scheme is compared with the osmotic coefficient model (STN), which is the standard in the ARG scheme. Reference simulations (REF) with the prescribed cloud droplet number concentration have also been carried out in order to understand the effects of aerosol-cloud feedbacks. In addition, since the calculated cloud coverage is an important determinant of cloud radiative effects and is influencing the nucleation process two cloud cover parameterizations (i.e., a relative humidity threshold; RH-CLC and a statistical cloud cover scheme; ST-CLC) have been examined together with the CDN schemes, and their effects on the simulated cloud properties and relevant climate parameters have been investigated.

The distinct cloud droplet spectra show strong sensitivity to aerosol composition effects on cloud droplet formation in all particle sizes, especially for the Aitken mode. As Aitken particles are the major component of the total aerosol number concentration and CCN, and are most sensitive to aerosol chemical composition effect (solute effect) on droplet formation, the activation of Aitken particles strongly contribute to total cloud droplet formation and thereby providing different cloud droplet spectra. These different spectra influence cloud structure, cloud properties, and climate, and show regionally varying sensitivity to meteorological and geographical condition as well as the spatiotemporal aerosol properties (i.e., particle size, number, and composition). The changes responding to different CDN schemes are more pronounced at lower altitudes

than higher altitudes. Among regions, the subarctic regions show the strongest changes, as the lower surface temperature amplifies the effects of the activated aerosols; in contrast, the Sahara desert, where is an extremely dry area, is less influenced by changes in CCN number concentration. The aerosol-cloud coupling effects have been examined by comparing the prognostic CDN simulations (STN, HYB) with the reference simulation (REF). Most pronounced effects are found in the cloud droplet number concentration, cloud water distribution, and cloud radiative effect. The aerosol-cloud coupling generally increases cloud droplet number concentration; this decreases the efficiency of the formation of weak stratiform precipitation, and increases the cloud water loading. These large-scale changes lead to larger cloud cover and longer cloud lifetime, and contribute to high optical thickness and strong cloud cooling effects. This cools the Earth's surface, increases atmospheric stability, and reduces convective activity. These changes corresponding to aerosol-cloud feedbacks are also differently simulated depending on the cloud cover scheme. The ST-CLC scheme is more sensitive to aerosol-cloud coupling, since this scheme uses a tighter linkage of local dynamics and cloud water distributions in cloud formation process than the RH-CLC scheme. For the calculated total cloud cover, the RH-CLC scheme simulates relatively similar pattern to observations than the ST-CLC scheme does, but the overall properties (e.g., total cloud cover, cloud water content) in the RH simulations are overestimated, particularly over ocean. This is mainly originated from the difference in simulated skewness in each scheme: the RH simulations calculate negatively skewed distributions of cloud cover and relevant cloud water, which is similar to that of the observations, while the ST simulations yield positively skewed distributions resulting in lower mean values than the RH-CLC scheme does. The underestimation of total cloud cover over ocean, particularly over the intertropical convergence zone (ITCZ) relates to systematic deficiency of the prognostic calculation of skewness in the current set-ups of the ST-CLC scheme.

Overall, the current EMAC model set-ups perform better over continents for all combinations of the cloud droplet nucleation and cloud cover schemes. To consider aerosol-cloud feedbacks, the HYB scheme is a better method for predicting cloud and climate parameters for both cloud cover schemes than the STN scheme. The RH-CLC scheme offers a better simulation of total cloud cover and the relevant parameters with the HYB scheme and single-moment microphysics (REF) than the ST-CLC does, but is not very sensitive to aerosol-cloud interactions.

Zusammenfassung Thema dieser Arbeit ist eine Modellstudie mit dem Chemie-Klimamodell EMAC zum vertieften Verständnis der Aerosol-Wolken-Wechselwirkung und deren Einfluss auf Wolkeneigenschaften und Klima. Diese Studie geht von der Annahme aus, dass die Aktivierung von Kondensationskernen (engl. Cloud Condensation Nuclei, CCN) der dominante Antrieb der Aerosol-Wolken-Rückkopplung in warmen Wolken ist. Die CCN-Aktivierung wird prognostisch berechnet, mittels zweier unterschiedlicher Parametrisierungen (STN und HYB) für die Nukleation von Wolkentropfen (engl. Cloud Droplet Nucleation, CDN). Beide CDN Schemata berücksichtigen sowohl Größen- als auch Chemieeffekte bei der Aerosolaktivierung und der Bildung von Wolkentropfen, wobei sie sich hauptsächlich in der Berechnung der Löslichkeit (Hygroskopizität) unterscheiden. Die κ-Methode ist hier zum ersten Mal in das Abdul-Razzak und Ghan Aktivierungsverfahren (ARG) integriert worden, um Hygroskopizität und kritische Übersättigung zu berechnen (HYB). Dieser modifizierte Algorithmus wird im Vergleich zu Modellsimulationen mit dem Standard-ARG-Verfahren (STN) betrachtet, das ein auf osmotischen Koeffizienten basiertes Modell zur Berechnung der kritischen Übersättigung nutzt. Ausserdem sind beide Verfahren mit dem selben interaktiven Aerosolmodell gekoppelt. Weiterhin wurden zum besseren Verständnis der Aerosol-Wolken-Rückkopplung Referenzsimulationen (REF) mit vorgegebenen Wolkentropfenkonzentrationen durchgeführt. Da die Wolkenbedeckung ein bestimmender Faktor des Strahlungseffekts von Wolken ist und auch die Aktivierung von Aerosolen beeinflusst, wurden zwei Parametrisierungen der Wolkenbedeckung (RH-CLC, grenzwertbasiert für relative Feuchte; ST-CLC, statistisch-basiert) jeweils mit den beiden CDN-Verfahren und der Referenz-Wolkentropfenkonzentration kombiniert. Die resultierenden sechs Modellsimulationen wurden bezüglich der Wolkeneigenschaften und relevanter Klimaparameter untersucht.

Die Wolkentropfenspektren zeigen eine hohe Sensitivität bzgl. des Einflusses der Aersosolzusammensetzung in allen Moden auf die Wolkentropfenbildung. Dies gilt besonders für den Aitken Mode, der den Hauptanteil der Aerosolanzahl bildet und in den Simulationen auch den dominierenden Beitrag zu den CCN. Wegen der geringeren Partikelgröße spielt hier bei der Berechnung der kritischen Übersättigung die Aerosolzusammensetzung (Löslichkeits-Effekt) eine besonders große Rolle und auch die Sensitivität bzgl. des gewälten Verfahrens (STN, HYB) ist hoch. Diese Unterschiede in den Tropfenspektren beeinflussen Strukturen und Eigenschaften von Wolken und somit das Klima und sie zeigen sich regional unterschiedlich sensitiv auf meteorologische und geographische Bedingungen, sowie die räumlich-zeitliche Verteilung der Aerosol-Eigenschaften (Größe, Anzahl und Aufbau). Die Änderungen, die sich auf die unterschiedlichen CDN-Schemata zurückführen lassen, sind in niedrigen Schichten am deut-

lichsten. Generell zeigen die subarktischen Regionen die stärksten Änderungen, da die niedrigen Temperaturen den Effekt der Aerosolaktivierung begünstigen; wohingegen die Sahara, als extrem trockene Region, kaum auf Änderungen der Konzentration von CCN reagiert. Die Aerosol-Wolken-Kopplung wurde untersucht durch den Vergleich der Simulationen mit prognostischer Berechnung der CDN (STN, HYB) mit der Referenzsimulation (REF). Die deutlichsten Effekte zeigen sich für die Wolkentropfenkonzentration, die Wolkenwasserverteilung und für den Strahlungseffekt von Wolken. Die Aerosol-Wolken-Kopplung erhöht generell die Wolkentropfenkonzentration, was wiederum die Bildung von schwachem stratiformen Niederschlag senkt und das Wolkenwasser erhöht. Diese skaligen Änderungen führen zu erhöhter Wolkenbedeckung und Lebensdauer von Wolken. Damit verbunden ist eine erhöhte optische Dicke von Wolken und ein starker Kühlungseffekt. Die kühlere Erdoberfläche erhöht die statische Stabilität der Atmosphäre und reduziert die Konvektion. Die Ausprägung dieser generellen Änderungen durch die Aerosol-Wolken-Kopplung hängt aber auch vom verwendeten Schema zur Berechnung des Bedeckungsgrads ab. Das ST-CLC Verfahren reagiert sensitiver auf die Aerosol-Wolken-Kopplung als RH-CLC, da es lokale Dynamik und die Verteilung von Wolkenwasser bei der Simulation der Wolkenbildung enger koppelt. Für die totale Wolkenbedeckung simuliert RH-CLC eine bessere Übereinstimmung mit Beobachtungen als ST-CLC, aber generell (z.B. Bedeckung, Wolkenwasser) überschätzen die RH-Simulationen, besonders über den Ozeanen. Diese Unterschiede haben ihre Ursache in der berechneten Schiefe des Bedeckungsgrades: die RH-Simulationen berechnen eine Verteilung mit negativer Schiefe, ähnlich den Beobachtungnen, während die positive Schiefe in den ST-Simulationen zu niedrigeren Bedeckungsgraden im Vergleich zu RH-CLC führt. Die Unterschätzung des totalen Bedeckungsgrads über den Ozeanen, besonders in der Intertropischen-Konvergenz-Zone (ITCZ), verursacht den systematischen Fehler in der prognostischen Berechnung der Schiefe durch das verwendete ST-CLC Schema.

Generell, zeigt das EMAC-Modell für alle hier untersuchten Konfigurationen bessere Resultate über den Kontinenten. Zur Simulation der Aersosol-Wolkenwechselwirkung, ist die Berechnung der kritischen Übersättigung mit dem HYB-Verfahren die bessere Methode als das STN-Schema, da es mit beiden Berechnungsverfahren zur Wolkenbedeckung die besten Resultate liefert. Das RH-CLC Verfahren bietet eine bessere Simulation des Wolkenbedeckungsgades und anderer relevanter Parameter, sowohl mit HYB als auch mit REF, als ST-CLC, aber es ist generell nicht sehr sensitiv auf Aerosol-Wolken-Kopplung.

Contents

Chapter 1

Introduction

1.1 Motivation and objectives

1.1.1 Atmospheric aerosols

Atmospheric aerosols are the combination of aerosol particles and the surrounding gaseous molecules. Fig. 1.1 summarizes the mechanisms of aerosol generation (source) and sink according to aerosol size distribution (Whitby and Cantrell, 1976). The fine particles (diameter $< 1\ \mu m$) consist of the Aitken and accumulation modes. These particles are generally newly formed from gas-to-particle conversion (i.e., secondary particles), growing by particle condensation and coagulation, and are removed from the atmosphere by precipitation. The coarse particles (diameter $> 1\ \mu m$) are mechanically generated by windbreaks, tires, and volcanic eruption, and are generally dissipated by sedimentation. The coarse particles are largely composed of primary particles that are directly released into the atmosphere (e.g., dust and sea salt), and their sizes are larger than secondary particles. The overall source and removal processes affect the size, chemical composition, and concentration of atmospheric aerosols.

Aerosol particle distribution varies with the particle number, surface, and volume (See Fig. 1.1; Seinfeld and Pandis, 2006). The Aitken particle has the largest number concentration but the smallest surface area and volume distribution, due to the fact that this particle has the smallest size, whereas the coarse particles in the largest size range dominate the volume, but the smallest number concentration. The distribution of aerosol particles (size and component) also varies depending on origin (natural vs. anthropogenic), region (e.g., continental vs. marine, urban vs. rural, polar, and desert regions), season (i.e., dry, transition, and wet periods) and vertical scales. Many studies have focused on the dominant, and thereby most important, aerosols components – dust, sea spray aerosols (sea salt), sulfate, black carbon, and particulate organic mat-

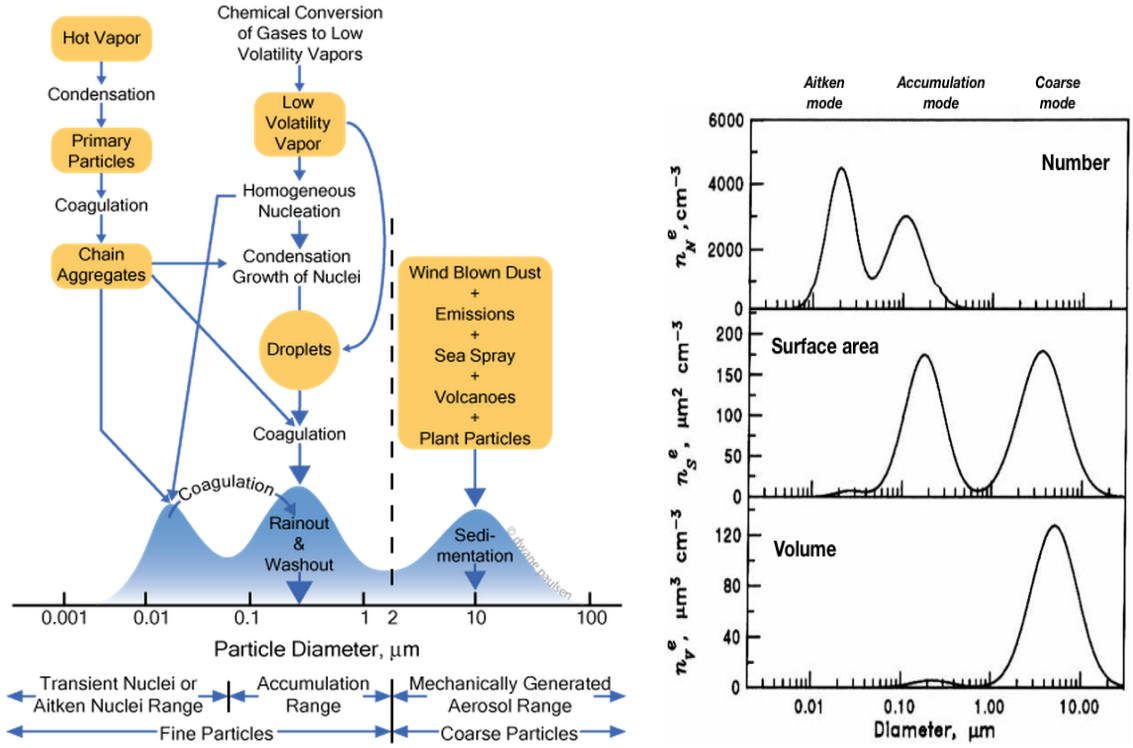

Figure 1.1: Physicochemical processes of atmospheric aerosol responding to aerosol particle size distribution. Based on Whitby and Cantrell (1976), figure from : http://www.dwanepaulsen.net/blog/category/aerosols/. Lognormal size distribution of aerosol number, surface area, and volume from Seinfeld and Pandis (1998).

ter – in order to understand global aerosols and their important role in the climate. For instance, the Aerosol interComparison-project (AeroCom) provides comprehensive aerosol comparisons between observations (e.g., satellite data and ground-based measurement) and model simulations (http://aerocom.met.no/aerocomhome.html).

Major aerosol species are:

- **Atmospheric mineral dust** comes from natural processes (e.g., arid weather, volcanic eruptions) and human activities (e.g., deforestation, desertification by agriculture) and is the most prominent aerosol type due to its huge overall mass (Kaufman et al., 2002, 2005). This dust directly and indirectly influences the radiative fluxes and impacts the climate system, since dust particles can as cloud condensation nuclei (CCN) and ice nuclei (IN) in the cloud formation, can affect cloud properties, and cloud radiation budgets, like other aerosols. The understanding of dust particles is lower than that of other known particles due to the difficulties of defining the element of mineral dust particles and the size distribu-

tion of these particles, since their size and composition varies greatly with regard to their source (origin) and their feedback with physicochemical processes (i.e., dry and wet sedimentation).

- **Sea salt or sea spray aerosol** is the largest contributor to aerosol mass besides dust aerosols (Andreae, 1995; Penner et al., 2001;Andreae et al., 2007a), and is composed of a substantial amount of organic matter including both soluble and insoluble constituents in addition to $NaCl$ and sulfate (Novakov et al., 1997; Middlebrook et al., 1998; Cavalli et al., 2004; O'Dowd et al., 2004; Kaku et al., 2006).

- **Sulfate** in the atmosphere is mostly formed by the oxidation of gaseous SO_2 and then is formed as particles through the nucleation and condensation processes. These particles are also generated from primary sources (e.g., sea salt aerosol), but this is a minor source (Andreae and Rosenfeld, 2008).

- **Black carbon** is generated from the incomplete combustion of biomass, biofuel and fossil fuel made up of predominantly carbonaceous materials, i.e., organic carbon and elemental carbon (soot); various inorganic materials are also minor components (Andreae et al., 1996). Black carbon may contribute semi-directly to the warming effect on Earth (i.e., semi-direct effect); this will be explained in Section 1.1.4.

- **Organic compounds** are directly emitted as primary organic aerosols or from secondary organic aerosol particles in the atmosphere (Kanakidou et al., 2005). They are further classified by water solubility: water soluble organic compound can be a secondary formed from the atmospheric oxidation products of volatile organic compounds, or through gas-to-particle conversion, aging and in-cloud processing (Kondo et al., 2006; Pio et al., 2007). These particles influence clouds and the climate by causing changes in hygroscopic behavior (i.e., chemical composition effects) and radiative properties (Jacobson et al., 2000).

1.1.2 Aerosols and climate

Aerosol particles are very important to the human life due to their profound effects on air quality and climate. Fig. 1.2 clearly demonstrates the mutual interactions between human activity and atmospheric aerosols and the aerosols' effects on the dynamics, chemistry and radiation of the climate (Gottwald et al., 2006). Aerosols can scatter and absorb radiation by themselves and directly impact climate (i.e., direct effects).

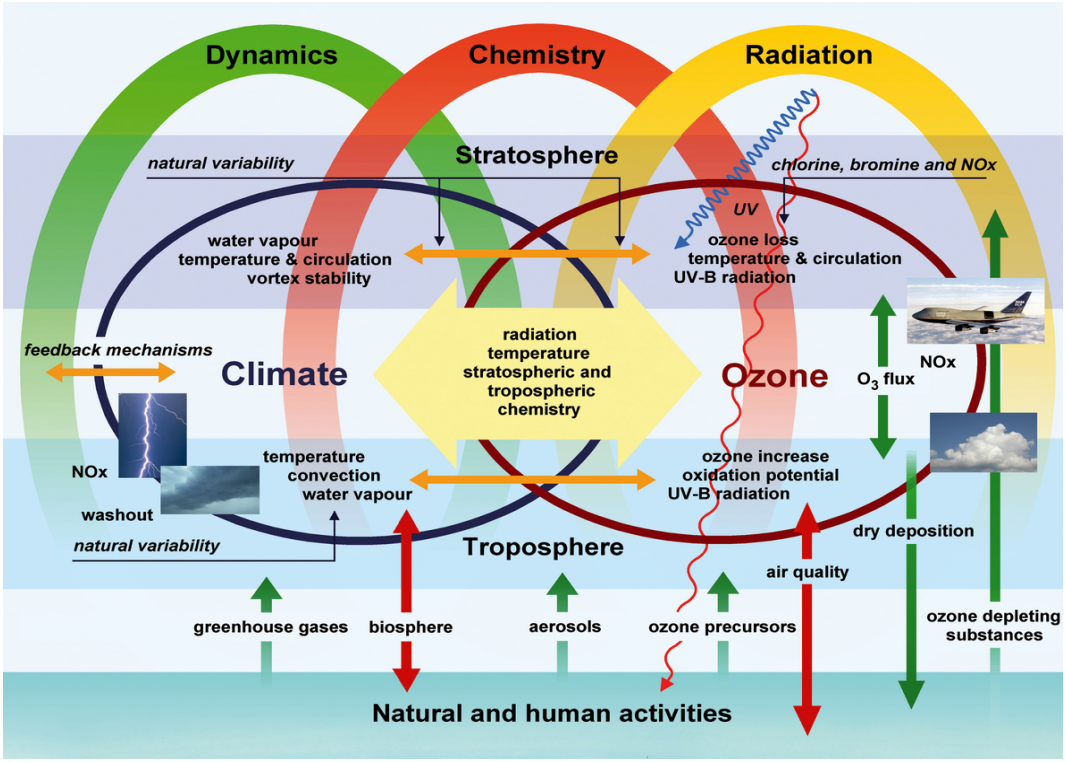

Figure 1.2: Interactions among human activity, atmospheric composition, chemical and physical processes and climate (graphics: DLR-IMF, after WMO-IGACO 2004) referred from Gottwald et al. (2006).

They also can indirectly impact the Earth's radiation budget by acting as cloud condensation nuclei (CCN) and ice nuclei (IN). Elevated CCN and IN modify cloud properties and change cloud optical properties and cloud coverage, and thereby modulating cloud radiative effects on climate and precipitation (i.e., indirect effects). The aerosol indirect effects are generally considered to be mostly cooling effects, which moderate the greenhouse warming effect that greenhouse gases (GHGs; e.g., CO_2, CH_4, N_2O, $CFCs$, O_3, and the water vapor in the atmosphere) absorb and emit radiation, and thereby affecting the temperature of Earth. Precipitation processes are also changed by aerosols, and are generally accompanied by the redistribution of latent heat releases and the modification of the tropospheric lapse rate (Rosenfeld, 2006). The overall mechanisms of aerosols affect the distribution of clouds and precipitation, and consequently the atmospheric circulation.

1.1.3 Clouds and climate

Clouds play a major role in the climate by controlling the Earth's radiation budget and the hydrological cycle (IAPSAG, 2007; IPCC, 2007, 2013). They generate both

cooling and warming effects on Earth, therefore modulating the Earth's temperature. Clouds can reflect the incoming solar radiation (shortwave: SW) from the sun to the Earth; this is known as the cloud albedo effect (SW cloud radiative effect: SCRE) and also trap the outgoing infrared energy (long wave radiation: LW) from the Earth's surface to space; this is known as the cloud greenhouse effect (LW cloud radiative effect: LCRE). The efficiency of reflected incoming shortwave radiation (a negative feedback) and re-emitted outgoing longwave radiation (a positive feedback) are highly correlated with cloud height and optical thickness. The optical properties are determined by cloud droplet/ice crystal size and number distribution, and cloud water properties, and hence are involved in aerosol and cloud feedback. The combined effects of SCRE and LCRE determine whether cloud radiation feedback warms or cools the climate, the net cloud radiative effect (NCRE). However, the net effects vary spatiotemporally.

The energy and water balance in the climate system is highly correlated with distinct feedbacks depending on cloud types. Cloud type can be characterized by the height, shape (size), and color (induced by their particle properties) of clouds. Clouds can be roughly divided into low (below 2.5 km), middle (2.5 to 6 km), and high (above 6 km) levels by height (MetOffice http://www.metoffice.gov.uk/learning/clouds; see Fig.1.3). The vertical distribution of cloud types can different somewhat depending on the method of classification. The International Satellite Cloud Climatology Project (ISCCP) classifies clouds by their top pressure and optical thickness: high-level clouds are cirrus, cirrostratus and deep convection, and occur above 440 mb. Middle-level clouds are altocumulus, altostratus and nimbostratus, and are located between 440 mb and 680 mb. Low-level clouds are formed near the surface from 1000 mb to 680 mb, and include cloud types such as cumulus, stratus, and stratocumulus (see Section B.4).

Fig. 1.3 summarizes the general features of cloud radiative effects by cloud type: the thin high-level clouds (i.e., cirrus clouds) are mostly penetrated by the incoming solar radiation (SW), but are able to effectively trap the emitted terrestrial radiation (LW) from the Earth's surface due to the absorption properties of water for radiation in the infrared range. The net effect of high thin cirrus clouds is a warming effect on the Earth system. In contrast, low-level clouds (i.e., stratocumulus clouds) are thicker and warmer than high-level clouds, so their cloud albedo effect (SCRE) is generally larger than the greenhouse warming effect (LCRE); this cloud type therefore, overall, cools the Earth's surface. Regarding cloud shape, the deep convective clouds (i.e., cumulonimbus clouds) vertically extended from the surface to the upper troposphere (often higher than 10 km) and are optically very thick and therefore have large reflectances of both SW and LW. The net effect of the cloud albedo and greenhouse

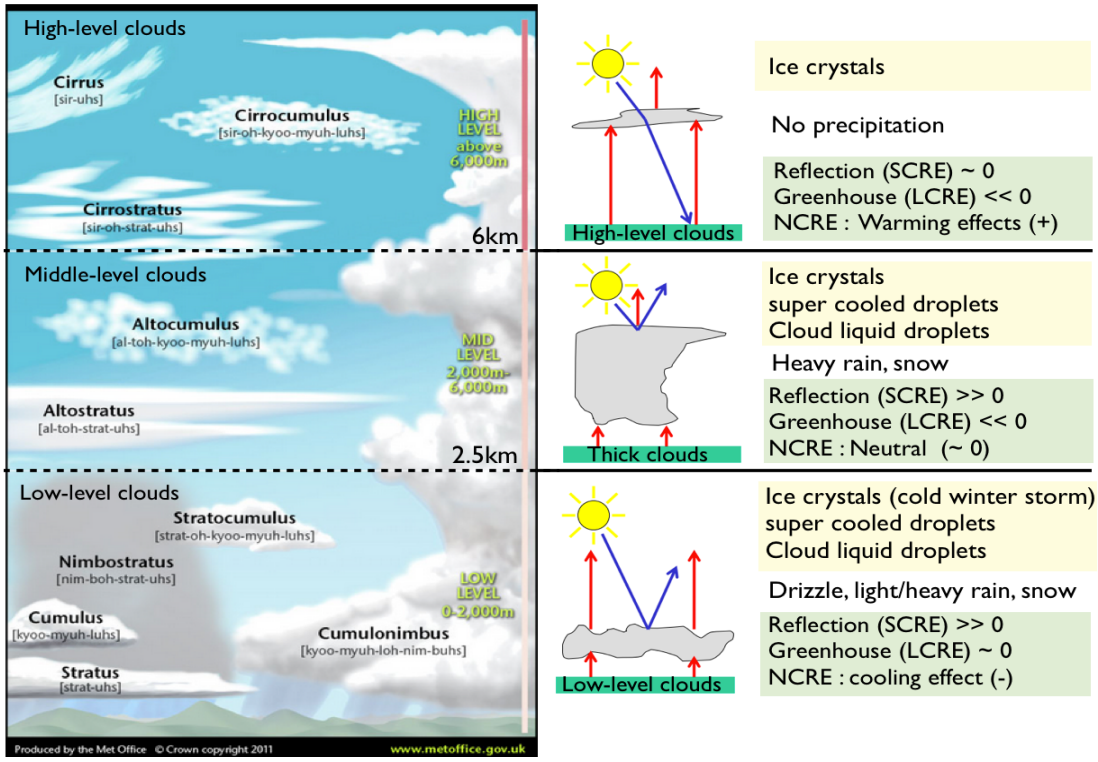

Figure 1.3: Overview of the cloud types and the roles played by cloud composition, precipitation, and radiative effects on the Earth climate system. This form combines the vertical distribution of cloud types, referred from MetOffice [http://www.metoffice.gov.uk/learning/clouds] with the schematic description of the SW and LW cloud effects on the Earth, adopted from a presentation made by Joel Norris (see more in [http://meteora.ucsd.edu/ jnorris/presentations/Caltechweb.pdf]).

effects is almost a balance, and therefore has a neutral effect on the Earth's climate (http://Earthobservatory.nasa.gov/Features/Clouds/clouds5.php).

Clouds also play a very important role in precipitation, a key part of the hydrological cycle between the Earth and atmosphere. Precipitation forms differently in clouds depending on the clouds' properties (cloud water, droplets), temperature (altitude), and vertical dynamics (i.e., vertical updraft) in the atmosphere. At high altitudes, clouds are composed of ice crystals in cold temperature, and mostly do not precipitate. The middle-level clouds are composed of liquid water droplets and ice crystals, depending on the atmospheric conditions. The low-level clouds usually consist of liquid cloud droplets, but can also contain ice crystals, as well as supercooled droplets. The different vertical development of clouds under different atmospheric conditions and in different regions therefore produces various types of precipitation (i.e., drizzle, light/heavy rain, showers, or snow; NOAA http://www.crh.noaa.gov/lmk/?n=cloudclassification).

These various types of clouds and precipitation can be modified by the aerosol-cloud interactions.

1.1.4 Aerosol-cloud interactions

Aerosol activity as CCN is a key factor to understanding aerosol-cloud interactions. As mentioned above, aerosols can act as cloud condensation nuclei (CCN) and ice nuclei (IN), thereby modifying cloud properties, structure, and dynamics. Changes in cloud droplet size and number distribution, and water content directly affect radiation due to changes in cloud albedo and cloud cover, and indirectly influence the efficiency of precipitation formation. Precipitation is closely associated with cloud lifetime, representing a sink term in the budget equation for cloud water. The overall processes are summarized in Fig. 1.4 (IPCC 4th report, 2007), and will be discussed in detail below.

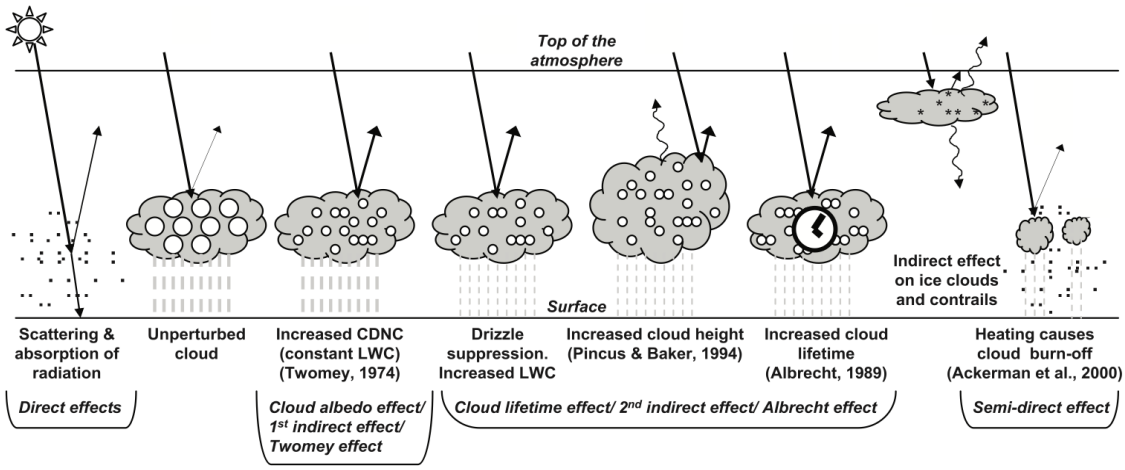

Figure 1.4: Aerosol effects on climate. This figure taken from the IPCC 4th report (2007).

When clouds are unperturbed by aerosols, clouds generally consist of small number of larger cloud droplets, and are able to form rain rapidly. This leads to decreases in cloud water and cloud coverage, and clouds subsequently dissipate. This series of changes in clouds results in less reflectance of SW. With a high CCN number concentration, clouds form with more numerous and smaller cloud droplets. When cloud liquid water (LWC) is constant, this leads to increases in cloud optical properties, causing them to reflect more solar radiation (i.e., cloud albedo effect, first aerosol indirect effect (AIE) or Twomey effect; Twomey, 1974). An increase in cloud droplet number

Table 1.1: Summary of aerosol indirect effects and the sign of their net radiative flux changes (F_{TOA}) at the top of the atmosphere and summary of precipitation (Precip.) with expected magnitudes. Referred from the IPCC 4th assessment report (2007).

Effect (Cloud tyeps)	Process	Sign of Δ F_{TOA} (Magnitude)	Sign of Δ Precip (Magnitude)
Cloud albedo effect (All clouds)	Increased smaller cloud droplet particles enhance the cloud albedo with a constant cloud water or ice content	Negative (Medium)	n.a. (n.a)
Cloud lifetime effect (All clouds)	Decreases in the precipitation efficiency by smaller cloud particles prolong cloud lifetime	Negative (Medium)	Negative (Small)
Semi-direct effect (All clouds)	Aerosols absorb solar radiation and heat clouds and evaporate cloud particles	Positive or negative (Small)	Negative (Large)
Glaciation indirect effect (Mixed-phase clouds)	An elevation of ice nuclei increases the efficiency of precipitation formation	Positive (Medium)	Positive (Medium)
Thermodynamic effect (Mixed-phase clouds)	Reduced freezing processes in cloud by enhanced smaller cloud droplets lead to super-cooled clouds, which extends cloud vertically, and colder temperatures	Positive or negative (Medium)	Positive or negative (Medium)

concentration is also redistributed as a narrow spectrum of cloud droplets, which decreases the efficiency of collisions between cloud droplets. This makes it harder for cloud droplets to coalesce into raindrops, thereby decreasing the efficiency of precipitation formation (i.e., the mechanism of rain formation of warm clouds). This can suppress precipitation spatiotemporally and can lead to higher LWC, and therefore can prolong cloud lifetime (i.e., cloud life time effect, Albrecht effect; Albrecht, 1989; Small et al., 2009). More moisture then remains in the atmosphere, which allows clouds to develop vertically (Koren et al., 2005; Devasthale et al., 2005; Stevens and Feingold, 2009). These clouds allow more cloud droplets to reach the freezing level, and increase the number of ice nuclei, which could invigorate precipitation at a later time. Absorbing aerosols such as soot into clouds may evaporate cloud particles and reduce cloud lifetime by increasing the absorption of solar radiation (semi-direct effect, Ackerman et al., 2000). The overall processes redistribute atmospheric heat sources spatiotemporally with changes in precipitation accompanied by the release of the latent heat (Rosenfeld, 2006). The impacts of aerosols and clouds interactions on climate, (i.e., changes in the top of the atmosphere (TOA) radiation, and in precipitation) are summarized in Table 1.1 (IPCC 4th report, 2007).

1.2 State of knowledge

1.2.1 Theory of cloud formation

Ascending air parcels can become saturated and form clouds through condensation. Formed clouds grow or fade based on cloud microphysics. The phase changes of cloud water entails the following processes:

- vapor $\Longleftrightarrow$ liquid (condensation, evaporation)
- liquid $\Longleftrightarrow$ solid (freezing, melting)
- vapor $\Longleftrightarrow$ solid (deposition, sublimation)

These processes are based on the thermodynamics of water, and are controlled by atmospheric conditions. Particularly with regard to aerosol activation in warm clouds, the processes of condensation and evaporation are important to understanding droplet formation. Köhler (1936) established the relationship between equilibrium size and saturation ratio for a droplet:

$$\frac{e_s(r)}{e_s(\infty)} = a_w exp K_e = a_w exp(\frac{2\tau\rho_L}{RTr}) \tag{1.1}$$

where $e_s(r)$ is the saturation vapor pressure over the surface of a spherical droplet radius r with surface tension τ and density ρ_L at temperature T. R is the gas constant for water vapor and $e_s(\infty)$ is the saturation vapor pressure over bulk water. a_w is water activity, K_e is the Kelvin factor which is determined by droplet radius (r) and the surface tension (τ). For smaller particles, higher water vapor pressure is required to achieve equilibrium, as smaller particles have stronger surface tension than larger particles.

A simplified form of this equation was provided by Rogers and Yau (1989), Pruppacher and Klett (1997) and Seinfeld and Pandis (1998):

$$S = \frac{e_s(r)}{e_s(\infty)} \approx 1 + \frac{A}{r} - \frac{B}{r^3} \tag{1.2}$$

The Kelvin term (or curvature effect) and the Raoult term (or solute effect) are denoted by A and B in Eq.1.2, respectively. The Köhler equation elucidates a function of both particle size and chemistry effects as shown in Fig. 1.5. The Köhler curve illustrates droplet activation through the competition between the curvature effect and the solute effect (McFiggans et al., 2006). The solute effects are determined by the number and dissociation of the solution particles, and therefore depend on the chemical composition of the aerosol particles. With this simplified equation, the critical radius (r_c) and

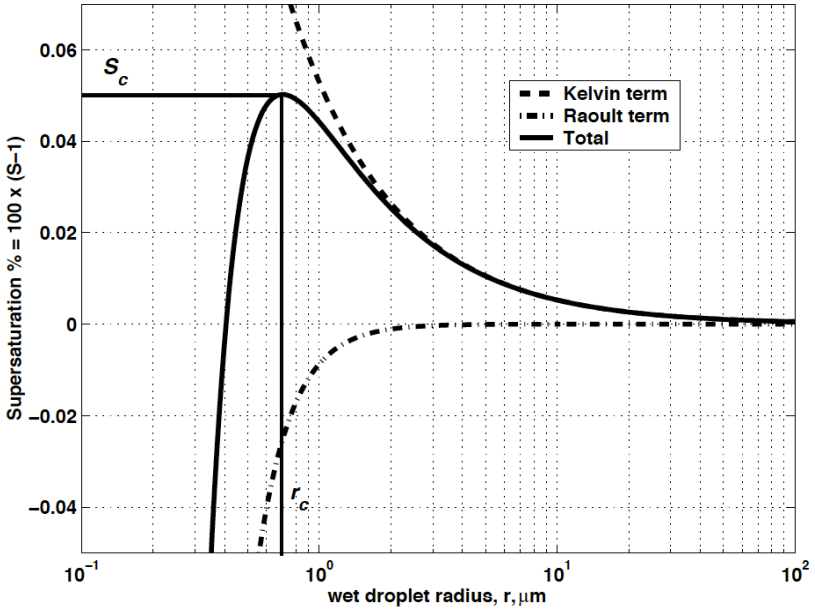

Figure 1.5: The Köhler curve illustrates the competition effects of particle size and chemistry, which represent the Kelvin term and the Raoult term, respectively. This figure taken from McFiggans et al. (2006).

critical supersaturation (S_c) values are estimated to calculate the formation of cloud droplets and the hygroscopic growth of particles. More detailed formulae can be found in the Appendix and Chapter 2.

1.2.2 Cloud parameterizations in climate models

To simulate clouds using general circulation models (GCMs), cloud microphysics need to be parameterized, since clouds and the processes within clouds cannot be explicitly resolved in a GCM grid box as a sub-scale phenomenon. This is one of challenges of representing clouds properties in GCMs (the scales of cloud processes in climate systems and model simulations are discussed in detail in the 5th of the IPCC report, 2013; see Fig.1.6).

Most climate model simulations use horizontal spatial resolutions of 100 to 300 km and vertical spatial resolutions ranging from 100 m (near the surface) up to few thousand meters. The spatial resolution depends on the purpose of the studies; for example, for the T42L19 resolution in the EMAC climate-chemistry model, a grid box size is about 250 km at the equator. Macro- and microphysical interactions between aerosols, cloud and climate are also parameterized in GCMs, which intend to describe

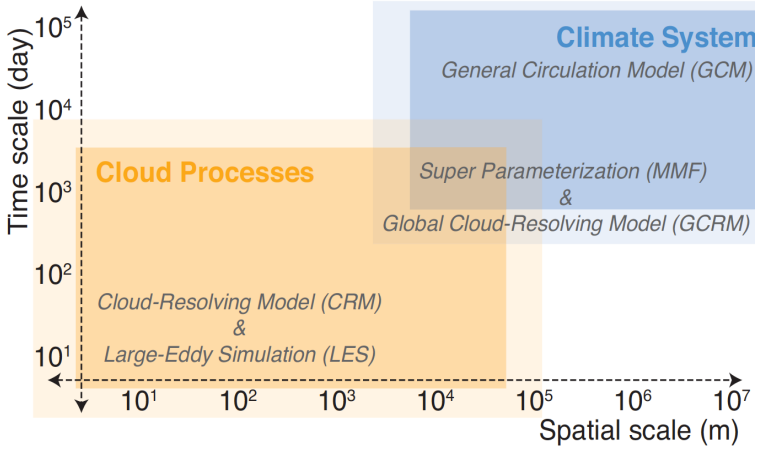

Figure 1.6: Spatiotemporal scales of cloud processes and climate systems and the corresponding models. Reported by the IPCC 5th report (2013).

the basic characteristics of atmospheric clouds and their influences on climate. These parameterizations also depend on aerosols' physical and chemical characteristics and dynamic properties, together with the coupling of cloud microphysics schemes. To represent aerosol effects on simulated clouds in climate models, an advanced cloud droplet nucleation scheme is required to account for the interaction between aerosols and cloud as well as to provide a good description of cloud properties and atmospheric aerosols.

1.2.3 Modeling study of aerosol-cloud interactions

The Intergovernmental Panel on Climate Change (IPCC) reports show a comprehensive understanding of the status of climate changes comprising many assessments based on the collaborated work of thousands of scientists. In the 4th IPCC report (2007), aerosol radiative forcing on the climate between 1750 and 2005 had been estimated as representing the direct and indirect effects of aerosols on the climate (see Fig. 1.7). The aerosol indirect effects, which result from aerosol-cloud interactions represent the cloud albedo effect. The cloud albedo effect has been understood as having a cooling effect on the climate, i.e., -0.7 (-0.3 to -1.8) Wm^{-2}. This is the largest contributor to the total uncertainty of the estimated anthropogenic radiative forcing on climate, i.e., 1.6 (0.6 to 2.4) Wm^{-2}, (Forster et al., 2007; Kiehl, 2007; Haywood and Schulz, 2007). The uncertainty range of the cloud albedo effect has been increased, and as of the most recent 5th IPCC report (2013), it remains the largest uncertainty contributor, i.e., -0.9 (-0.1 to -1.9) Wm^{-2}. To decrease these uncertainties and give a better understanding of aerosol-cloud interactions in the climate (i.e., changes in cloud properties, cloud

microphysics, and interactions with climate parameters), it is necessary to model and predict the resulting climate change in GCMs. Peters et al. (2012) has also emphasized the importance of understanding aerosol microphysical interactions and the size distributions of emissions as compared to the amount of the emissions to decrease the uncertainty of the estimated aerosol indirect effects (AIEs) using GCMs.

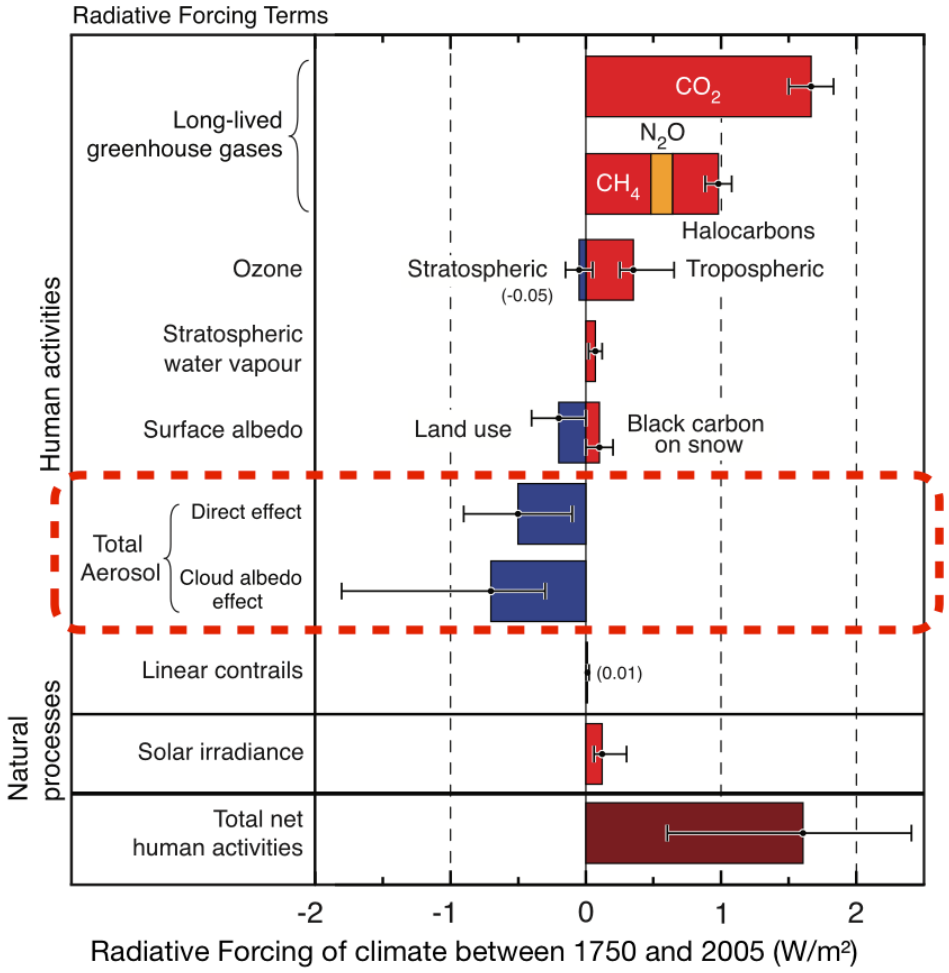

Figure 1.7: Radiative forcing on climate between 1750 and 2005. Reported by the IPCC 4th report (2007).

Climate models have been attempted to represent aerosol effects on clouds and climate through a parameterization of clouds and radiation properties (e.g., Jones et al., 1994; Lohmann, 1995; Lohmann and Lesins, 2002; Anderson et al., 2003; Rosenfeld, 2006). Scientists have studied aerosol effects (e.g., the cloud albedo effect, Twomey (1977); the cloud lifetime effect, Albrecht (1989); and the semi-direct effect, Ackerman et al., (2000)) using general circulation models (GCMs) and found substantial differ-

ences between different GCMs, with large uncertainty ranges (e.g., Ackerman et al., 2000; Penner et al., 2003; Lohmann and Fetter, 2005; Schulz et al., 2006; Forster et al., 2007). These differences and uncertainties are mostly caused by feedback between parameterized processes of cloud macro- and microphysical processes and the systematic misrepresentation of simulated clouds in global models (Stevens and Feingold, 2009). A substantial part of the effects of aerosol-cloud interactions on clouds are generally assumed to be cloud droplet nucleation processes in cloud microphysics; model results could therefore differ greatly depending on how aerosolloud interactions are parameterized.

The early GCMs used simple parameterizations based on empirical relationships between aerosol number or mass and cloud droplet number distribution. These studies were restricted to regional or case study observations, leading to differences and discrepancies in the estimates of AIEs (e.g., Jones et al., 1994; Lohmann and Lesins, 2003; Anderson et al., 2003). These parameterizations of cloud droplet formation use single solute particles such as sulfate to represent atmospheric aerosols (Jones et al., 1994; Boucher and Lohmann, 1995; Gultepe and Isaac, 1996; Jones and Slingo, 1996; Feichter et al., 1997; Lohmann and Feichter, 1997; Menon et al., 2002; Lance et al., 2004). These approaches may overestimate aerosol cooling effects by not considering the effects of aerosol size distribution and chemical composition on aerosol hygroscopic growth and activation. In the mechanism of forming cloud droplets, the ability of aerosol particles to take up water is an important factor to measure the CCN activation, and is governed by the size of particles and their soluble hygroscopic chemical components (McFiggans et al., 2006). Detailed information regarding atmospheric aerosol composition and chemical reactions (i.e., the size-resolved chemical compounds and mixing state of atmospheric aerosols) is therefore necessary to predict a realistic cloud droplet number and size distribution, as well as to predict the available ambient aerosol population in the cloud droplet nucleation process (Andreae and Rosenfeld, 2008; McFiggans et al., 2006).

More realistic cloud droplet nucleation processes have been developed using physics-based parameters such as the aerosol size and number distribution, composition, and vertical velocity. The Köhler equation is widely used for describing aerosol-cloud interactions in both experimental and theoretical studies. This equation addresses the curvature and solute effects of aerosol particles in the water activity and hygroscopic growth of aerosols (Seinfeld and Pandis, 1998; Pruppacher and Klett, 2000; McFiggans et al., 2006). Using Kölher theory, various implementations have been applied for various models, from single column models (parcel model) to global models. These

parameterizations account for the aerosol size distribution and solute effects, and allow many studies to explicitly or analytically calculate the cloud droplet number concentration (Hänel, 1987; Ghan et al., 1993, 1995, 1997; Abdul-Razzak et al., 1998; Feingold and Heymsfield, 1992; Chuang and Penner, 1995; Lohmann et al., 1999; Cohard et al., 2000; Abdul-Razzak and Ghan, 2000, 2002, 2004; Nenes and Seinfeld, 2003; Fountoukis and Nenes, 2005; Ming et al., 2006; Khvorostyanov and Curry, 2009; Shipway and Abel, 2010; Wang and Penner, 2009). Previous studies have shown discrepancies between model results, in part due to differences in the interpreted aerosol chemistry (parameterization of hygroscopicity). Nevertheless, the aerosol chemical composition is considered to be a minor impact on large-scale cloud formation compared to other properties (e.g., the number and size distribution of particles, transport processes, and the atmospheric ambient conditions; Pöschl et al., 2009).

In estimating of nucleated cloud droplet number, the calculated critical supersaturation or critical dry particle diameters are key factors to determine the total activated aerosol number concentration. Activation of aerosol particles occurs when the particles within an aerosol distribution are larger than the calculated critical dry particle size. These parameters can vary about 20% due to the parameterization of the hygroscopic properties in various Köhler models, even for simple and well-defined particles (Pöschl et al., 2009). This difference could yield more substantial changes in the total cloud droplet size spectrum by changes in activated aerosol number concentration. On top of that, the estimated solute effect of aerosols could be substantially different depending on the quantifying approaches used (e.g., activity parameterization, osmotic coefficient, van't Hoff factor models, effective hygroscopicity parameter and analytical approximations; Rose et al., 2008). Particularly for low water vapor supersaturations, low aerosol number concentrations and organic components, the description of physicochemical aerosol properties is important for cloud formation (McFiggans et al., 2006; Rose et al., 2008, 2010; Kreidenweis et al., 2009). Note that the aerosol size effect is dominant in the droplet nucleation process compared to aerosol chemical composition effect (Feingold, 2003; Dusek et al., 2006; Andreae and Rosenfeld, 2008). Nonetheless, to fully describe aerosol-cloud interactions, more detailed representations of aerosol composition and hygroscopicity are required to parameterize cloud formation.

The κ–method was introduced by Petters and Kreidenweis (2007) to describe the aerosol composition effect on hygroscopic growth. This method describes the aerosol composition effect on hygroscopic growth using the effective hygroscopicity parameter. This can conveniently represent the effect of aerosol chemical composition and hygroscopicity on cloud formation in numerical models due to the flexible extension

of aerosol chemical components, without needing to explicitly calculate the density, molecular mass, and dissociation number of each individual species, as is the case for the van't Hoff factor or osmotic coefficient models (Petters and Kreidenweis et al., 2007; Pöschl et al., 2009; Pringle et al., 2010b). Gunthe et al. (2009) and Rose et al. (2010) have evaluated the calculated κ with measurement-based variables and confirm that the κ–method can calculate realistic values. For this reason, the κ–method has been applied to many recent studies.

For field studies and laboratory experiments the κ–method has been widely applied to represent the the aerosol chemical composition or the CCN activity of aerosols on the cloud droplet nucleation processes (Petters and Kreidenweis, 2007; Snider and Petters, 2008; Wang et al., 2008; Gunthe et al., 2009; Bougiatioti et al., 2009; Rose et al., 2008, 2010, 2011; Niedermeier et al., 2008; Mikhailov et al., 2009; Wex et al., 2009; Dusek et al., 2010; Henning et al., 2010; Shinozuka et al., 2010; Snider et al., 2010; Moore et al., 2012). For numerical models the κ–method has been applied to calculate of the CCN activity of specific aerosol compounds, or certain sizes of aerosols under controlled conditions (Kim et al., 2008; Spracklen et al., 2008; Ruehl et al., 2009; Reutter et al., 2009; Kazil et al., 2010; Su et al., 2010; Pringle et al., 2010b). The utility of κ in calculating cloud formation has been also suggested by its numerical effectiveness and robustness in calculating solute effects (Pöschl et al., 2009; Pringle et al., 2010b).

In spite of the advantages of using κ, the κ–method has not been extensively used for cloud formation in GCMs; rather, the application of κ has been limited to specific aerosol species and controlled conditions. In the present study, I therefore apply the κ-method (Petters and Kreidenweis, 2007) to calculate Raoult effects in the Köhler model for all size modes of aerosols, to predict cloud droplet formation in the atmospheric chemistry-climate EMAC model.

1.3 Purpose of the dissertation

The experiments are designed to improve the understanding of aerosol–cloud interactions and their effects on cloud properties and climate parameters. In this study, CCN activation is understood as the dominant driver in aerosol–cloud feedback loops in warm clouds. The CCN activation is calculated prognostically using two different cloud droplet nucleation parameterizations, the STN and HYB CDN schemes. Both CDN schemes are based on the Köhler theory to estimate the size of the activated particles (r_c) that rely on the critical supersaturation (S_c) of aerosols. Size and chemical composition effects account for droplet formation in the Köhler curve; these effects are described using the Kelvin and Raoult terms (also known as the solute effect), respectively. The computed critical supersaturation in each CDN scheme is integrated into

the hygroscopic growth in the Abdul-Razzak and Ghan activation scheme (ARG).

The nucleated droplets directly influence cloud structure by interacting with cloud properties and relevant climate parameters through multiple processes, mutually affecting climate (See Fig. 2.1). I will first quantify and investigate the multitudes of the aerosol and cloud interaction effects on clouds and climate using an analysis of the sensitivity simulations. These simulations are based on a combination of cloud droplet nucleation parameterization and cloud cover schemes, and have the following goals:
1) to generally understand aerosol–cloud interactions and their significance on the simulated cloud and climate system.
2) to identify the aerosol chemical composition effects on warm clouds formation (to do this, I conduct a sensitivity analysis of the treatment of aerosol hygroscopicity and critical saturation in cloud droplet nucleation parameterization).
3) to examine the effect of the cloud cover schemes on the simulated cloud properties and climate relevant parameters via the inter-comparison of all simulations integrated with RH-CLC and ST-CLC.

1.4 Outline of the dissertation

General knowledge about aerosols, clouds, and climate, as well as their interactions and mutual effects, are addressed in **Chapter 1**. **Chapter 2** describes the model and relevant sub-models, with a focus on cloud droplet nucleation parameterizations and cloud cover schemes. **Chapter 3** explains the experimental designs and how they serve the purpose of the study. In **Chapter 4**, the performance of cloud droplet nucleation parameterizations and cloud cover schemes is evaluated using observations. In **Chapter 5** the simulated results (e.g., total cloud cover, cloud radiative effects at the top of the atmosphere, and precipitation) are analyzed to see how they respond to CCN activation mechanisms. The relevant effects of the cloud droplet nucleation schemes are discussed in **Chapter 6**, to understand aerosol feedback effects on clouds. The impacts of the cloud cover scheme on overall cloud properties are discussed in **Chapter 7**. Finally, **Chapter 8** offers concluding remarks.

Note that the present thesis is largely composed of the recent publication "Aerosol–cloud interactions studied with the chemistry–climate model EMAC, D. Y. Chang, H. Tost, B. Steil, and J. Lelieveld, *Atmos. Chem. Phys. Discuss.*, 14, 21975-22043, doi:10.5194/acpd-14-21975-2014, 2014".

Chapter 2

Model description

2.1 EMAC (ECHAM5/MESSy) Atmospheric Chemistry-Climate model

This study uses the ECHAM5-MESSy Atmospheric Chemistry-Climate model (EMAC) to simulate aerosol and cloud properties and relevant climate parameters. EMAC is a numerical chemistry-climate model based on the general circulation model ECHAM5 (Roeckner et al., 2006, version 5.3.01), combined with the Modular Earth Sub-model System (MESSy version 1.10; Jöckel et al., 2005, 2006). A full description of the EMAC model, its evaluation, and the relevant studies can be found in Jöckel et al. (2005, 2006, 2010), Pozzer et al. (2010, 2012), Pringle et al. (2010a), de Meij et al. (2012), see also http://www.messy-interface.org.

The current EMAC model applies sub-models to simulate dynamics, thermodynamics and chemistry of atmosphere as summarized in Table2.1. Fig. 2.1 illustrates the model structure for simulating clouds and climate-relevant parameters, which are the integrated effects of the aerosol-cloud interactions on the climate system. The EMAC model is able to simulate the various ranges of resolutions from T21 to T159 horizontally and from L19 to L90 vertically. This study uses the T42L19 resolution corresponding to a gaussian grid ≈ 2.8 °by 2.8 °in latitude and longitude and 19 vertical hybrid pressure levels up to 10 hPa (30 km).

The next section gives specific descriptions of how clouds form in the EMAC model, using relevant sub-models. Further information of other sub-models are found in Appendix B.

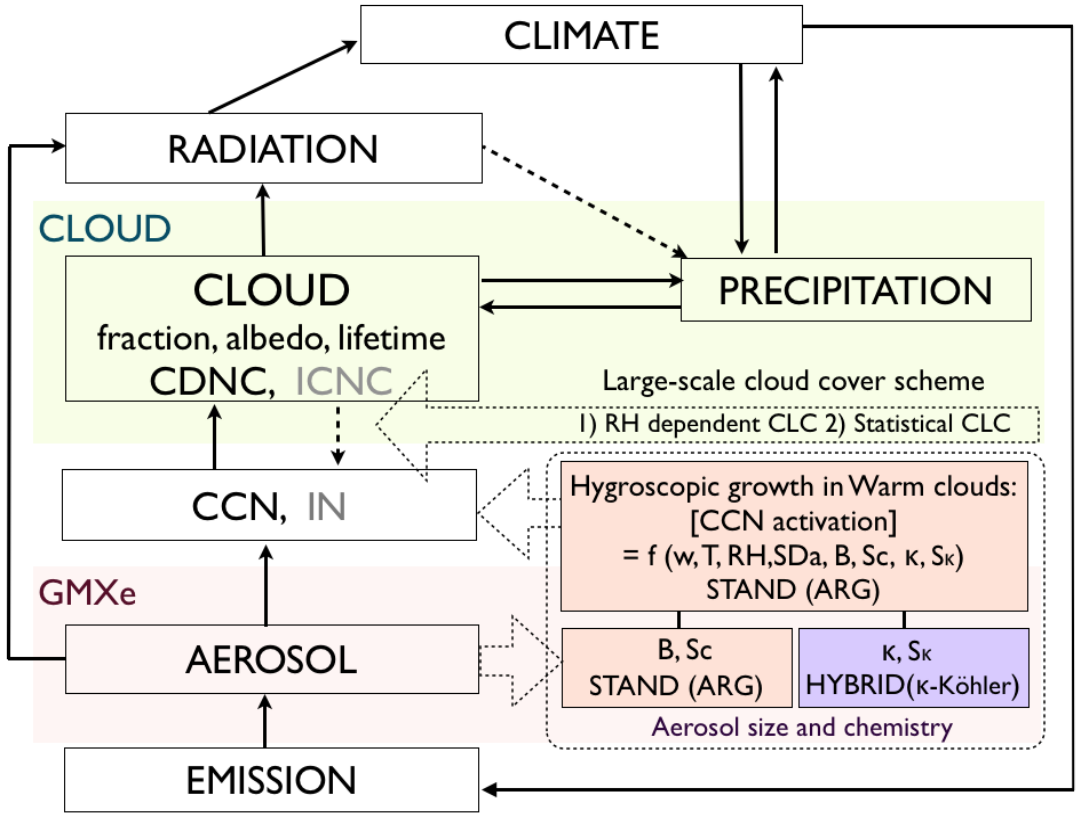

Figure 2.1: Overview of the EMAC model structure for simulating climate parameter including the aerosol-cloud interaction: ω (vertical updraft), T (temperature), RH (relative humidity), SD_a (a size distribution of ambient aerosol), B (hygroscopicity), S_c and S_κ (Critical supersaturation), κ (the effective hygroscopicity parameter)

2.2 Atmospheric aerosol [GMXe]

The aerosol sub-model GMXe provides ambient aerosol size and number, as well as the chemical composition including the hygroscopicity effective parameter κ and supersaturation of aerosol in the cloud forming process. In this sub-model, aerosols are treated with the lognormal size distributions with seven interacting multimodes, i.e., four hydrophilic modes (nucleation, Aitken, accumulation and coarse mode) and three hydrophobic modes (Aitken, accumulation and coarse mode):

$$n(\ln r) = \sum_{i=1}^{7} \frac{N_i}{\sqrt{2\pi}\ln\sigma_i} \exp\left(-\frac{(\ln r_i - \ln \bar{r}_i)^2}{2\ln^2\sigma_i}\right) \tag{2.1}$$

where N_i is the number concentration, σ_i is the geometric standard deviation, and $\bar{r}_i$ is the number mean radius for each aerosol mode (i). The aerosol size and number

Table 2.1: Summary of the EMAC submodels used in this study.

Submodel name	Purpose	Reference
AEROPT	Aerosol optical properties	Lauer et al. (2007)
CLOUD	Clouds and Precipitation	Jöckel et al. (2006)
CONVECT	Convection	Tost et al.(2010)
CVTRANS	Convective tracer transport	Tost et al. (2000b)
DRYDEP	Dry deposition of gases and aerosol	Kerkweg et al. (2006a)
GMXe	Aerosol dynamics and thermodynamics	Pringle et al. (2010)
HETCHEM	Heterogenous chemistry (reaction rates)	Jöckel et al. (2006)
JVAL	Rate of photolysis	Jckel et al. (2006)
LNOX	Product of NO_x by lightning	Tost et al. (2007b)
MECCA1	Chemical atmospheric reactions	Sander et al. (2005)
OFFLEM	Offline emissions	Kerkweg et al. (2006b)
ONLEM	Online emissions	Kerkweg et al. (2006b)
RAD4ALL	Radiation for all wavelengths	Jöckel et al. (2006)
SATSIMS	Classification of cloud types by ISCCP simulator	Gerald et al. (2010)
SCAV	Wet deposition of gases and aerosols	Tost et al. (2006a, 2007a)
SEDI	Aerosol sedimentation	Kerkweg et al. (2006a)
TNUDGE	Tracer nudging	Kerkweg et al. (2006b)
TROPOP	Calculation of the tropopause and boundary layer	Jöckel et al. (2006)

concentration are prognostically calculated with the prescribed aerosol number, mass, and the fixed σ_i of each aerosol mode (σ=2.0 for coarse mode, σ=1.59 for the other modes) and the relevant variables summarized in Table B.1.

The chemical composition of soluble (hydrophilic) and insoluble (hydrophobic) modes is chemically distinct, and within each mode aerosol compounds are internally well mixed, but the modes themselves are treated as an external mixture. The GMXe submodel treats bulk species (e.g., black carbon (BC), particulate organic matter (POM), mineral dust (DU) and sea spray (SS)), and explicit aerosol ions and molecules (e.g., SO_4^{2-}, H_2SO_4, HSO_4^-, NO_3^-, NH_4^+, Na^+, Cl^-, H_2O). The setup of aerosol distribution used in this study is comparable to the simulated aerosol distribution in Pringle et al. (2010a).

The hygroscopicity effective parameter κ and water uptake (a_w) of aerosol in each size mode are calculated based on the κ-Köhler theory in Petters and Kreidenweis (2007). These calculated values are used for the calculation of the aerosol activation in the cloud forming processes (i.e., cloud droplet nucleation scheme). Pringle et al. (2010b) has presented the global distribution of the simulated κ in the EMAC model, and evaluated the calculated κ with the observations. Note that in that study the simulated κ only represents the chemical composition of the aerosol and that the simulation results did not include any feedback with clouds.

2.3 Cloud droplet nucleation

2.3.1 Standard CDN parameterization [STN]

A cloud droplet nucleation parameterization for a single solute aerosol mode was developed by Abdul-Razzak et al., (1998) and was extended for multiple aerosols in Abdul-Razzak and Ghan (2000); this extended version will hereafter be called standard STN. This extended version was implemented by Holger Tost in a preliminary version of EMAC (1.10) and coupled with aerosol submodel GMXe.

The STN describes the droplet formation (the nucleation process) using the dependence of saturation ratio on the size of a solution droplet. The STN can account for the curvature effect (Kelvin effect, A) and the solute effect (also known as Raoult effect, B) in the Köhler equilibrium curve. The curvature effect is described with the surface tension (τ) of aerosol particle, which depends on particle size, while the solute effect is represented using the chemical component of aerosols, as summarized in Table 2.2. The hygroscopic growth parameterizes instant and subsequent growth of particles by condensation during the adiabatic lifting by vertical updraft. Ascending air parcels become saturated and reach maximum saturation rates (maximum supersaturation: S_{max}); the particles grows by consuming the supersaturation (i.e., water vapor) until the saturated aerosol exceeds critical supersaturation (S_c). This relationship can be described as the change of S depending on time, with a source and a sink term for S; a rising air parcel with the vertical updraft (V) produces the saturation through adiabatic cooling (i.e., source term) and the condensation of particle uses this saturated water vapor (liquid water mass mixing ratio: w) in the air parcel (i.e., sink term). This process can be formulated with the following equation, defined by Leaitch et al. (1986);

$$\frac{dS}{dt} = \alpha V - \gamma \frac{dw}{dt} \tag{2.2}$$

where α and γ are size-invariant coefficients influenced by temperature (T) and the water vapor pressure (e_s). The condensation rate (dw/dt) of the activated droplets is calculated using the sum of the hygroscopic growth of particles during the changes of S_c, and can be expressed with:

$$\frac{dw}{dt} = 4\pi\rho_w \sum_{i=1}^{7} \int_0^S r_i^2 \frac{dr_i}{dt} \frac{dn_i(S_c)}{dr_{d,i}} dS_c \tag{2.3}$$

where r_i is the radius of the forming droplet in aerosol mode (i) and $n_i(S_c)dS_c$ is the number concentration of activated particles for the dry radius in aerosol mode (i) during the changes of S_c over time (i.e., between S_c and $S_c + dS_c$).

The relationship between the saturation ratio and droplet radius derives the smallest activated particle radius with S_c using the analytic solutions, and calculates the fraction of activated aerosol (AF_i) in each mode. Using the AF_i and number of available aerosol particles ($N_{a,i}$) for each mode, the STN determines total number of activated aerosol particels (N) by integrating the activated aerosols (N_i) in each aerosol mode (i),

$$AF_i = \frac{1}{2}[1 - erf(u_i)] \tag{2.4}$$

$$N_i = N_{a,i} \times AF_i, N = \sum_{i=1}^{I} N_i \tag{2.5}$$

where u_i is defined with the geometric standard deviation σ_i, the mode median radius, and the cut-off radius of the aerosol in each mode (i). Further specific formulae and relevant parameters are provided in Appendix C.2.1.

The calculated N_i is incorporated into the cloud microphysics as the nucleated droplets representing the aerosol-cloud interactions. The performance of the STN parameterization has presented and discussed for the single aerosol mode in Abdul-Razzak et al. (1998) and for the multi-modal aerosol distributions in Abdul-Razzak and Ghan (2000, 2002).

2.3.2 Hybrid CDN parameterization [HYB]

The hybrid CDN parameterization (hereafter, called HYB) uses the critical supersaturation ($S_{C\kappa}$) in the κ-Köhler theory based on Petters and Kreidenweis (2007), Kreidenweis et al. (2009), Gunthe et al. (2009), Pöschl et al. (2009), and Rose et al.(2010). As summarized in Table2.2, in the calculation of the Kelvin effect, the surface tension is assumed to be that of pure water (0.072 J/m^2), with a fixed temperature T=298.15 K. These assumptions are made since the κ-Köhler theory presumed that the effective hygroscopicity parameter would represent the solute effects on both water activity and surface tension. The diagnosed aerosol hygroscopicity parameter for each aerosol mode (κ_i) is calculated using the volume–weighted mean of the solute hygroscopicity (κ_j). The water activity a_w is estimated with the volume–weighted mean of the solute particles. These diagnosed parameters of solute particles (i.e., κ_i and a_w) determine the solute effect (the Raoult term) in the calculation of critical supersaturation ($S_{C\kappa}$; see Table2.2). This computed $S_{C\kappa}$ is applied into droplet formation and hygroscopic growth in the ARG scheme (Abdul-Razzak et al., 1998), i.e., HYB. The HYB scheme estimates aerosol activity and determines the activated aerosols within cloud microphysics as a component of the cloud droplets in warm clouds.

In summary, the HYB scheme is applied to the Sc algorithm based on κ-method

Table 2.2: Summary of main differences between the STN and HYB cloud droplet nucleation parameterizations.

Parameter	STN (ARG)	HYB (ARG-κ)
Critical saturation	$s_{c,i}$= $S_{C,i}$ + 1	$s_{c_\kappa,i} = a_w exp\frac{A}{D_i} = exp\left(\sqrt{\frac{4A^3}{27\kappa_i D_i^3}}\right)$
Critical supersaturation	$S_{C,i} = \frac{2}{\sqrt{\bar{B}_i}}\left(\frac{A}{3r_{c,i}}\right)^{\frac{3}{2}}$	$S_{C_\kappa,i} = s_{c_\kappa,i}$ -1
Kelvin effect	$A \equiv \frac{2\tau M_w}{\rho_w RT}$	$A \equiv \frac{4\sigma_{sol} M_w}{\rho_w RT}$ ($\approx 0.66 \times 10^{-6} Km \times T^{-1}$)
Solute effect	$\bar{B}_i \equiv \frac{M_w \sum_{j=1}^{J} \nu_{i,j}\mu_{i,j}\phi_{i,j}\epsilon_{i,j}/M_{a_{i,j}}}{\rho_w \sum_{i=1}^{J} \nu_{i,j}/\rho_{a_{i,j}}}$	$a_w = \frac{1}{1+\kappa_i\left(\frac{V_s}{V_w}\right)}$, $\kappa_i = \sum_{j=1}^{J} \hat{\epsilon}_{i,j}\kappa_j$

S_C is the critical supersaturation ($s_c \cong S_C + 1$) in STN and is comparable to S_{C_κ} (= s_{c_κ} -1) in HYB.

r_c is the dry radius of the smallest activated aerosol and is used for estimating the fraction of aerosol activation.

M_w is the molecular weight of water vapor, ρ_w is the density of water, τ is the surface tension for water ($\tau = (76.10 - 0.155[T - T_{melt}])10^{-3}$) (Pruppacher and Klett, 1978), $R = 8.315 JK^{-1}$ is the ideal gas constant, and T is temperature (K).

A in HYB uses a surface tension of the pure water ($\sigma_{sol} = 0.072\ J/m^2$) and a fixed temperature T= 298.15 K denoted by T_κ

$\nu_{i,j}$ is the mass mixing ratio, $\mu_{i,j}$ is the number of ions after the salt dissociates into water, $\phi_{i,j}$ is the Osmotic coefficient, $\epsilon_{i,j}$ is the mass fraction of soluble material, and $M_{a_{i,j}}$ is the molecular weight, $\rho_{a_{i,j}}$ is the density of the aerosol of component j and mode i (i=1,7).

D_i is the dry aerosol diameter, r_i is the dry aerosol radius, a_w is the water activity, κ_i is the hygroscopicity of aerosol mode (i), the volume of the dry particle (V_s) and the volume of water (V_w).

$\hat{\epsilon}_{i,j}$ is the volume fraction of chemical component j in mode i, and κ_j is an independent hygroscopicity parameter of aerosol species (j).

in the ARG scheme; the calculation of S_C based on an osmotic coefficient model is replaced by the $S_{C\kappa}$ based on the κ-method (see Table2.2 and Fig.2.1 for a summary). The relevant parameters are also illustrated in Table2.2.

The individual κ values for aerosol particles (κ_j) are mainly from the hygroscopic parameters (e.g., Petters and Kreidenweis, 2007 and Pringle et al., 2010b); see Appendix C.3). The calculated κ is comparable to derived values from measurement that estimate CCN activity (Rose et al., 2010 and Gunthe et al., 2009). As mentioned before, the computed κ in the EMAC model has been extensively validated by Pringle et al. (2010b).

Applying κ allows for a more efficient accounting for overall physicochemical aerosol properties in the calculation of CCN activation, and gives researchers more flexibility

to extend (speciate) aerosol chemical components without needing to conduct explicit calculations (as is the case in, for example, the osmotic method as applied in STN). Consequently, it is more consistent to consider the aerosol chemical composition and its hygroscopicity effect on warm clouds (Pöschl et al., 2009).

2.4 Cloud microphysics [CLOUD]

In the EMAC model convective and large-scale clouds are separately treated, and are individually calculated in the sub-models CONVECT and CLOUD, respectively. The CLOUD sub-model prognostically calculates large-scale cloud properties (i.e., cloud water and ice content, cloud cover, cloud droplet number) and vertically integrated specific humidity and precipitation using the prognostic equations for the water phase and bulk cloud microphysics. Fig.2.2 summarizes the large-scale cloud microphysics for simulating cloud properties. Convection determines the detrainment of convective water flux, which is a source term of the large-scale cloud water budget. Convection and convective transports are treated in submodel CONVECT and CVTRANS (see Appendix B).

The estimation of CCN and IN is a prior step to forming large-scale clouds, and is based on the provided values (e.g., B_i, κ_i, $S_{C,i}$, $S_{C\kappa,i}$), which originate from the aerosol size and number distribution, as well as from the chemical composition. These overall aerosol properties are determined by the aerosol submodel (GMXe), described in Section 2.3. This estimated CCN represents the activation of the freshly nucleated cloud droplets and is integrated into the cloud droplet number concentration budget for large-scale clouds (CDNC). The estimated CCN is modified via the bulk cloud microphysics (i.e., the process of condensation and deposition, evaporation and sublimation, and freezing and melting). The distribution of cloud water and ice content (ql and qi) is closely linking to the CDNC and ICNC, and is therefore perturbed by CCN activation via precipitation effects. The cloud hydrology (i.e., ql and qi) interfaces with the meteorological condition (i.e., temperature (T), relative humidity (RH), specific humidity (qs), and etc.) and influences precipitation and cloud cover. Cloud hydrology also has effects on the atmospheric dynamics, which in turn create feedback for the cloud microphysical properties.

The large-scale cloud microphysics calculations are based on Lohmann et al. (2007); the calculation of cloud properties applies a two-moment cloud microphysics for cloud water mass and droplet distributions and uses prognostic equations (Lohmann and

Roeckner, 1996; Lohmann et al., 2007). The calculation of ice crystal number concentrations (ICNC) in large-scale clouds is based on Kärcher and Lohmann (2002), and interacts with the nucleated cloud droplets are calculated using the CDN parameterizations (HYB and STN).

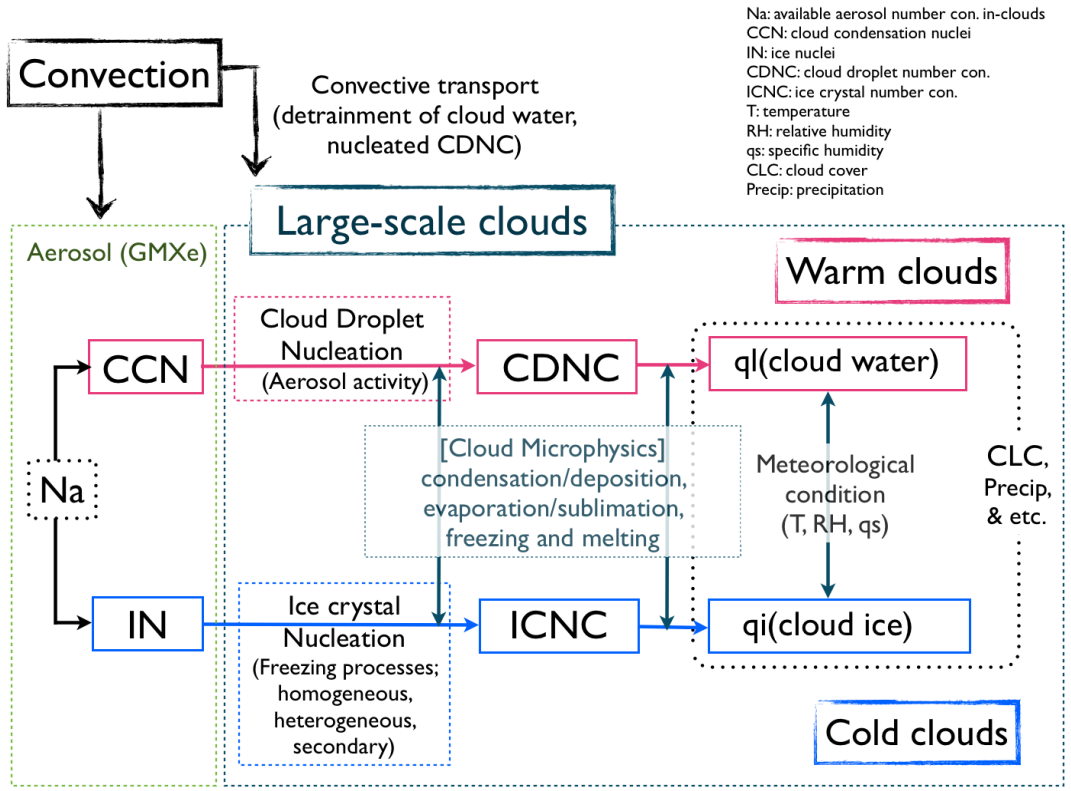

Figure 2.2: Overview of the large-scale cloud microphysics for simulating cloud droplet and ice crystal number concentrations, cloud water and ice contents, and cloud cover.

In the bulk cloud microphysics, changes in the total number of cloud droplets are treated in the individual microphysical processes, and are described as follow:

$$\frac{dN_d}{dt} = \left[\frac{N_d}{dt}\right]_{transport} + R_{nuc} + R_{melt} - R_{auto} - R_{self} - R_{acc} - R_{frz} - R_{evap} \quad (2.6)$$

$$\frac{dN_i}{dt} = \left[\frac{N_i}{dt}\right]_{transport} + R_{nuci} + R_{frz} + R_{secp} - R_{agg} - R_{selfi} - R_{acci} - R_{melt} - R_{sub} \quad (2.7)$$

the first terms on the right-hand sides ($[\frac{N_d}{dt}]_{transport}$ and $[\frac{N_i}{dt}]_{transport}$) denote the rate of changes in cloud droplet and ice-crystal numbers by all transport processes, including advection, convection, and diffusion. The R-terms denote the rate of changes in cloud droplet number by nucleation (R_{nuc}), melting (R_{melt}), autoconversion (rain

droplets; R_{auto}), self-collection (R_{self}), accretion (falling rain or snow; R_{acc}), heterogeneous freezing (contact and immersion; R_{frz}) and evaporation (R_{evap}). The $\frac{dN_i}{dt}$ is determined by the rate of changes in ice-crystal numbers via homogenous nucleation (which takes place below -35°C; R_{nuci}) and heterogenous nucleation (which takes place between -35°C and 0°C; R_{frz}), the secondary production (R_{secp}), aggregation (snow; R_{agg}), self-collection (R_{selfi}), accretion (falling snow; R_{acci}) and by sublimation (R_{sub}).

The homogenous freezing of supercooled aerosols by adiabatic ascent is based on Kächer and Lohmann (2002). Heterogenous freezing has two processes: contact freezing for hydrophobic DU and BC, and immersion freezing for hydrophilic DU and BC; both of these processes influcence CDNC and ICNC.

The R_{auto}–the autoconversion rate parameterized by Kharioudinov and Kogan (2000)–changes total cloud droplet number concentration and mass through decreases in the cloud water and ice contents by forming both precipitation and R_{agg}. The R_{auto} is a relevant parameter of the secondary AIE in terms of a cloud lifetime effect (Tompkins, 2002; Lohmann et al., 2007; Pincus et al., 2008; Reichler and Kim, 2008). The self-collection terms (R_{self} and R_{selfi}) can also change cloud particle size distribution, but not the total mass of clouds. More details of cloud microphysics and properties can be found in Lohmann and Roeckner (1996), Lohmann et al. (1999), Lohmann (2002, 2007), and Hoose et al. (2007).

The EMAC model can also, alternatively, calculate cloud properties based on single moment cloud microphysics, using four different cloud droplet parameters in the CLOUD submodel. These parameterizations roughly approximate cloud droplet formation using empirical relationships, and based on aerosol quantities (e.g., mass or number; Lohmann and Roeckner, 1996; Rotstayn, 1997; Jones et al., 2001; Menon et al., 2002). These parameterizations are summarized in Appendix C.1.

2.5 Large-scale cloud cover

Cloud cover, especially fractional cloudiness, is not resolved in GCMs since it is a subgrid scale phenomenon; it therefore needs to be parameterized. EMAC has two cloud cover schemes to diagnose cloud cover as a fractional cloudiness in each grid box; a relative humidity threshold scheme (RH-CLC) and a statistical cloud cover scheme (ST-CLC).

2.5.1 RH dependent cloud cover scheme [RH-CLC]

This scheme is based on Sundqvist et al. (1989) and was discussed in Lohmann and Roeckner (1996). The scheme allows sub-scale clouds to be formed when the mean of RH in the grid box ($\bar{RH}$) is lower than 1 (it is not saturated). This scheme determines the fraction of cloudiness in a grid box using the critical RH (RH_{crit}) when clouds fill in the entire gird box. The cloud cover (C) is diagnosed using the variable of humidity of the grid box, by applying this formula:

$$C = 1 - \frac{\sqrt{1 - RH}}{\sqrt{1 - RH_{crit}}} \tag{2.8}$$

where the RH_{crit} is a tunable value depending on the size of grid. Model resolutions can therefore influence the estimated cloud cover.

The RH-CLC scheme could generate excessive fog near the surface, or could be insensitive to changes in local cloud properties (i.e., aerosol indirect effects) due to insufficient linkage among local dynamics (Tompkins, 2005).

2.5.2 Statistical cloud cover scheme [ST-CLC]

This scheme uses a probability density function (PDF) to assign the variables relevant to cloud formation, and diagnoses subgrid-scale cloud fractions (Tompkins, 2002). This scheme specifies the variability of humidity for each grid box with $G(q_t)$, which is the PDF of total water q_t (i.e., the sum of water vapor, cloud liquid water and cloud ice; q_t = q_v+q_l+q_i), and the saturation mixing ratio q_s without temperature effects. Cloud formation is allowed when the total cloud water exceeds the saturation mixing ratio (q_s). The cloudy part in a grid is estimated with a mathematical integration of PDF for each grid box. This scheme can produce various cloud distributions with the same amount of total water in the grid box. It may sensitively represent the aerosol indirect effect (AIE) attributable to perturbed cloud cover distribution. The cloud cover (C) can be determined as follows:

$$C = \int_{q_s}^{\infty} G(q_t) dq_t \tag{2.9}$$

where

$$G(t) = \frac{1}{B(p,q)} \frac{(t-a)^{p-1}(b-t)^{q-1}}{(b-a)^{p+q-1}} (a \leq t \leq b) \tag{2.10}$$

where the variables p and q are determined by the shape of the Beta distribution use to diagnose cloud cover; in the current model setup, a bell-shaped regime is applied ($p > 1, q > 1$).

Chapter 3

Experimental designs

The purpose of the present study is to investigate the effects of aerosol-cloud interactions on clouds and climate, i.e., the sensitivity of CCN activation to aerosol chemical composition, using the different Sc algorithms; the significance of aerosol-cloud interactions; the impact of cloud cover scheme on simulated cloud properties, climate parameters, and the effects of aerosol-cloud interactions.

All simulations in this thesis are performed with meteorologically identical boundary conditions using the climatological sea surface temperature (SST) and sea-ice cover (SIC) in free-running simulations. The emission fields represent the year 2000 and cycle for simulating periods to avoid differences in the aerosol emission field. When calculating the radiation budget, constant volume mixing ratios of climatological values are applied for greenhouse gases in all simulations. Cloud radiative effects are thereby induced by aerosol and cloud feedbacks on the Earth radiation.

The nucleated cloud droplets are prognostically calculated with different cloud droplet nucleation schemes (i.e., STN and HYB; see Section 2.3). The basic framework for simulating clouds is based on Lohmann et al. (2007). The simulated clouds influence all cloud-relevant properties, and the temporal-spatial distribution of clouds is an important controller of the earth radiation budget. For this reason, the cloud cover schemes (i.e., RH-CLC and ST-CLC) are tested in sensitive simulations. The model resolution applied in all simulations is T42L19, which corresponds to a quadratic Gaussian grid of approximately 2.8°by 2.8°in latitude and longitude, and 19 vertical hybrid pressure levels up to $10hPa$ ($30km$).

First, the reference simulations (i.e., RH-REF, ST-REF, or the REF-simulations) have been carried out for 5 years after a 1-year for spin-up time for each cloud cover schemes, RH-CLC and ST-CLC. The simulated clouds do not include the nucleated cloud droplets from aerosols (the CCN activation process), and therefore do not in-

Table 3.1: Summary of sensitivity simulations.

Simulation	CDN scheme	CLC scheme	Simulation	CDN scheme	CLC scheme
RH-REF	Not considered	RH-CLC	ST-REF	Not considered	ST-CLC
RH-STN	STN	RH-CLC	ST-STN	STN	ST-CLC
RH-HYB	HYB	RH-CLC	ST-HYB	HYB	ST-CLC

clude the aerosol-cloud feedback loop (i.e., the aerosol indirect effects). Second, the prognostic CDN schemes (i.e., STN and HYB) have been applied in simulations spanning 10 years after a 1-year for spin-up time for both RH-CLC and ST-CLC. These simulations–RH-STN, RH-HYB, ST-STN, and ST-HYB–account for the aerosol-cloud interactions using prognostic cloud droplet nucleation parameterizations (see Section 2.3).

A short overview of the experimental set-up is given in Table 3.1. All simulations have been performed with same conditions; the only exception is the CCN activation parameters which use the prognostic CDN schemes (i.e., STN and HYB) and cloud cover scheme (i.e., RH-CLC and ST-CLC). In these sensitive simulations, the effects of aerosol-cloud feedbacks on clouds and climate are investigated using the following comparisons:

- Comparisons between the REF simulations and the prognostic CDN simulations (i.e., the STN and HYB simulations) show the effects of aerosol-cloud feedbacks on cloud and climate
  : RH-REF vs. RH-STN, ST-REF vs. ST-STN
  : RH-REF vs. RH-HYB, ST-REF vs. ST-HYB

- Differences between the STN and the HYB simulations demonstrate the sensitivity of the S_c algorithm, including differences in the solute effect
  : RH-STN vs. RH-HYB, ST-STN vs. ST-HYB

- Variations between the RH and the ST simulations show the dependency of the CLC scheme on clouds, including their trend of simulating cloud covers and their effects on climate
  : RH-REF vs. ST-REF, RH-STN vs. ST-STN, RH-HYB vs. ST-HYB

The following observational data are used to evaluate simulated clouds and climate parameters in EMAC: cloud properties (e.g., total cloud cover fraction, cloud water and ice water contents) in Moderate Resolution Imaging Spectroradiometer (MODIS), International Satellite Cloud Climatology Project (ISCCP), Clouds and the Earth's Radiant Energy System (CERES), and A-Train (Aqua, Aura, CloudSat and CALIPSO

satellites); cloud radiative forcing at the top of atmosphere (e.g., SCRE, LCRE and NCRE) in CERES EBAF; aerosol optical properties in MODIS data; and the global precipitation climatologies in the Global Precipitation Climate Project (GPCP).

Chapter 4

Evaluation with observations

All observation data in this thesis are regridded to the model's horizontal resolution (T42) to allow consistent inter-model comparisons. This regridding calculation could change the original observation data, potentially losing some data by downgrading their resolution. A simple regridding test has therefore been done comparing the downgrading and upgrading calculations for the total cloud cover: the derived TCC from MODIS is reproduced from $1^\circ \times 1^\circ$ (360×180 grid points) to the model grid size $2.815^\circ \times 2.815^\circ$ (124×64 grid points) and the simulated TCC is rescaled with the opposite direction. The down-graded TCC shows less than 0.04% error in the arithmetic mean, whereas the upscaled TCC shows about 10% error in the arithmetic mean; the area weighted mean distances between the original and regridded TCCs are much smaller in both cases. The overall errors from the regridding calculations are negligible. Therefore, the model simulations are compared with the regridded observations using the downgrading calculation (i.e., from high to low resolution).

4.1 Annual global mean

Global means of cloud properties, radiation and water budgets are summarized in Table 4.1 for the simulations and observational data. These values are area-weighted mean since a gridbox covers different surface areas depending on the latitude.

The vertically integrated cloud droplet number concentration (N_d) calculated in the simulations are compared with the observed N_d using ISCCP in Han et al., (1998). The observed N_d amounts to $4.0 \times 10^{10}/m^2$ between 50°N and 50°S during the four months of January, April, July, and October in 1987. The N_d is strongly sensitive to the CDN scheme, since the nucleated cloud droplets are a major component of the total cloud droplet number concentration (CDNC). In Table 4.1 the HYB simulations (i.e.,

Table 4.1: Annual global mean cloud properties and the top of the atmosphere (TOA) energy budget for 10-year multiyear mean.

CDN scheme	No AIE inclusion		STN (ARG)		HYB (ARG-κ)		Evaluation
Simulation	RH-REF	ST-REF	RH-STN	ST-STN	RH-HYB	ST-HYB	Observed ranges
N_d ($10^{10}/m^2$)	2.18	1.72	9.41	9.73	4.30	3.43	4^a
N_i ($10^{10}/m^2$)	0.40	0.38	0.41	0.40	0.40	0.39	-
LWP (g/m^2)	44.3	24.9	93.2	75.4	61.2	38.1	37.8^{b1} 30-50^{b2}
IWP (g/m^2)	29.0	20.9	29.9	23.2	29.4	22.2	26.7^{c1},24-70^{c2}
WVM (kg/m^2)	26.2	26.0	25.7	25.2	26.1	26.0	24.7 ^{d1}, 23^{d2}
TCC (%)	68.3	55.6	69.3	62.2	68.6	57.4	66.7^{e1}, 65.4^{e2}
P_{total} (mm/day)	3.01	2.97	2.96	2.95	3.00	2.97	2.68^f
P_{strat} (mm/day)	1.14	1.22	1.11	1.15	1.13	1.21	-
P_{conv} (mm/day)	1.87	1.75	1.86	1.80	1.87	1.76	-
SCRE (W/m^2)	-56.6	-33.6	-67.9	-52.1	-60.3	-38.9	-47.2^g (-43.2– -51.2)
LCRE (W/m^2)	28.5	24.3	28.7	25.5	28.6	24.7	26.3^g (23.8–28.8)
NCRE (W/m^2)	-28.1	-9.3	-39.2	-26.6	-31.7	-14.1	-21.0^g (-14.4– -27.4)
AOD	0.20	0.19	0.23	0.22	0.21	0.19	0.16^{h1}, 0.15-0.19^{h2}

[a] Vertically integrated cloud droplet (N_d) is drived by ISCCP [Han et al., 1994,1998].

[b] Liquid water path (LWP) is from [1]CERES Terra SYN1 deg–lite Ed2.6 data for years 2001 to 2010 [Wielicki et al., 1996] and analysis of [2]A-Train satellite observations from CloudSat (August 2006 to July 2010) and MODIS (October 2002 to September 2008) observation [Jiang et al.,2012].

[c] Ice water path (IWP) is from ISCCP data[1] [Storelvmo et al., 2007] and analysis of [2]CloudSat and MODIS observation [Jiang et al.,2012].

[d] Water vapor mass (WVM) are from [1]CERES Terra SYN1 deg–lite Ed2.6 data for years 2001 to 2010 [Wielicki et al., 1996] and A-Train satellite observations from AIRS (October 2002 to September 2010) + MLS (September 2004 to August 2011) observation [Jiang et al.,2012].

[e] Total cloud cover (TCC) is obtained [1] from Terra and Aqua MODIS data from the year 2001 to 2010 and [2]ISCCP data from years 2001 to 2008.

[f] Total precipitation (P_{total}) is estimated by the Global Precipitation Climatology Project (GPCP) long term monthly mean from years 1981 to 2010 [Adler et al., 2003].

[g] The shortwave (SCRE), longwave (LCRE) and net cloud radiative effect (NCRE) at the top of the atmosphere (TOA) are estimated from the Clouds and the Earth's Radiant system experiments, Energy Balanced and Filled data (CERES EBAF) for 2001 to 2010 [Loeb et al., 2009].

[h] Aerosol optical depth (AOD) is obtained from [1]CERES SYN1deg Month Terra Aqua MODIS Ed3A Subset from the year 2001 to 2010 and from [2]different observations [Kinne, 2006].

RH-HYB and ST-HYB) predict N_d reasonably close to the observation, while the STN simulations substantially overestimate, by more than a factor of 2 for the N_d of the HYB simulations. The vertically integrated ice crystal number concentration (N_i) does not show sensible differences among all simulations. Unfortunately, the observation data is not available for the annual global mean of N_i. The calculated CDNC also influences ICNC via the cloud droplet freezing rate. In general, the freezing rate is closely related to temperature and available cloud droplet number concentration, and under the same atmospheric condition, high CDNC is likely to contribute to more ICNC. However, high CDNC does not substantially change the annual global mean of N_i as the frozen cloud droplet rate is relatively very small compared to total cloud droplet concentration. For this reason the frozen cloud droplet rate is only a minor factor, and may have only local sensitive effects.

The global mean of liquid water path (LWP) as estimated from recent observations of A-Train (6 years for MODIS Aqua; October 2002 to September 2008; and 5 years for CloudSat; August 2006 to July 2010) ranges from 30 to 50 g/m^2. This range is considered the best estimate, as the values are derived from CloudSat Total and noPrep in Jiang et al. (2012). Another LWP value deduced from CERES Terra SYN1deg between March 2000 and February 2010 is approximately 38 g/m^2. The LWPs simulated in RH-REF and ST-HYB fall into these two observed ranges. Overall, all simulations are in the range of the uncertainty level provided in Jiang et al. (2012).

The reference runs (REF) estimate relatively small values of LWP compared to the simulations that use prognostic CDN parameterizations (STN, HYB). The LWP in the ST-REF simulation amounts to only 60 % of ones in the ST-HYB simulations, representing an 18 % underestimation relative to the lower boundary of the observations. By including aerosol-cloud feedback, the nucleated cloud droplets enhance total CDNC (N_d) in the HYB and STN simulations, reducing the efficiency of precipitation spatiotemporally. The suppressed precipitation allows more cloud water to be sustained, thereby increasing LWP. Besides the reduced precipitation decreases the wet deposition (scavenging rate) of aerosols, prolonging cloud lifetime and increasing cloud cover (Lohmann and Feichter, 1997; Lohmann et al., 2007). The HYB and STN simulations therefore predict higher LWP with higher CDNC and larger cloud cover than do the REF-simulations. It is apparent in the STN simulation that LWP amounts to 93.2 g/m^2 (for RH-STN) and 75.4 g/m^2 (for ST-STN) with similarly strong increases in CDNC (N_d). The RH simulations predict higher LWP than do the ST simulations. This higher predicted LWP seems to be attributable to higher cloud water loading from larger cloud cover, particularly over oceans.

The global mean of ice water path (IWP) estimated by ISCCP, CloudSat and MODIS observation ranges from 24 to 70 g/m^2 (Jiang et al., 2012). The IWP calculated in all simulations is within the range of the best estimates taken from the observations. The global mean of the IWP does not show strong differences between the CDN schemes similar to the calculated N_i. The IWP estimated in the RH simulations is generally higher than those in the ST simulations, indicating an influence of cloud cover scheme on IWP. This influence likely results from the vertical distribution of clouds and cloud water, which varies by CLC scheme. These effects of the CLC scheme on IWP slightly vary by CDN scheme–about 30 % for REF, about 20 % for STN, and about 25 % for HYB–since the simulated CDNC also affects IWP by suppressing precipitation, vertical development of clouds, and prolongation of cloud lifetime.

The global annual means of total water vapor mass (WVM) are estimated as 24.7 and 23 kg/m^2 from CERES Terra from MODIS Terra for 10 years (Wielicki et al., 1996), and A-Train satellite observation (from AIRS (October 2002 to September 2010) and MLS (September 2004 to August 2011)) (Jiang et al., 2012), respectively. The WVM estimated in all simulations is overestimated by 10 % as compared to the observations (this was previously shown by Tost et al. (2006) in a comparison of GOME WVM). Notable differences are not found in the simulations because the values are mostly governed by the climatological values.

The derived global means of total cloud cover (TCC) are 65.4 % and 66.7 % by ISCCP (from 2001 to 2008), and by Terra and Aqua MODIS (from 2000 to 2010), respectively. In the simulations a general trend in TCC is indicated by the dependence of the CLC scheme; the RH simulations overestimate TCC by 4 % as compared to the observations, while the ST-simulations underestimate TCC by 9 %. The sensitivity of aerosol activation (i.e., aerosol-cloud feedbacks) to the simulated clouds also shows the dependency of the CLC scheme; the RH-CLC combinations are minimally influenced by the nucleated cloud droplets from aerosols, while the ST-CLC combinations are more sensitive to variations in how TCC interacts with changes in cloud properties (e.g., cloud droplet number (N_d), cloud water, and cloud ice). These variations reflect a high sensitivity of the ST-CLC scheme to local cloud properties in the cloud distribution as discussed in Chapter 2 and also in previous studies (Lohmann et al., 2007; Hoose et al., 2008).

A global mean of total precipitation (P_{total}) is estimated to be 2.68 mm/day from the Global Precipitation Climatology Project (GPCP). This estimation is based on a long-term monthly mean from 1981 to 2010 (Adler et al., 2003). All simulations slightly overestimate P_{total} by about 10 % as compared to the observations. Similar to the total

water mass (WVM), a strong sensitivity to the nucleated cloud droplets from aerosols is not found in the global mean of total precipitation. This can be explained by the fact that precipitation is largely influenced by changes in the ocean, whereas the current model is not fully coupled with air–ocean feedback, instead using the prescribed SST and SIC.

The clouds predicted in the STN and HYB simulations have relatively high cloud droplet number concentration than the concentrations in the REF-simulations; this higher concentration is induced by CCNs from aerosol-cloud interactions. These enhanced cloud droplet numbers increase their optical properties and albedo (i.e., cloud albedo effect), and could enlarge cloud cover or prolong cloud lifetime (i.e., cloud life time effect), consequently changing the climate with different magnitudes. These overall changes closely relate to the cloud radiative effects. The cloud radiative effect (CRE) is defined as the deviation of the radiation fluxes of shortwave and longwave radiation (SW, LW) for all sky, including cloudy and cloud-free regions (i.e., all sky, clear sky). The all sky fluxes include aerosol–cloud interactions, while the clear sky fluxes are independent of the mixing ratios of all hydrometers.

The CRE of SW and LW (respectively, SCRE and LCRE) at the top of the atmosphere (TOA) are calculated for individual SW and LW radiative fluxes. The net cloud radiative effect (NCRE) is a combination of SCRE and LCRE. The simulations have been evaluated against the CREs estimated by Clouds and the Earth Radiant system experiments, Energy Balanced and Filled data (CERES EBAF) from 2001 to 2010 (Loeb et al., 2009). Regarding the regional uncertainties of the SW and LW fluxes, they range from -43.2 to -51.2 W/m^2 for the SW, and from 23.8 to 28.8 W/m^2 for the LW (CERES EBAF Edition2.6r Data Quality Summary).

The SCREs predicted in the simulations show high sensitivity to aerosol-cloud feedbacks similar to LWP and N_d. This high sensitivity is because these values (e.g., CDNC, ICNC, cloud water content, and ice content) are associated with cloud optical properties. The largest cloud albedo effects (SCRE) are simulated in the STN simulations (i.e., RH-STN, ST-STN) since strongly enhanced CDNC and LWP increase cloud optical thickness. The cloud radiative effects are also influenced by the cloud cover scheme: the RH simulations predict stronger SCRE and LCRE with larger cloud amounts (cloud cover and cloud water path) as compared to the estimated CREs in the ST simulations. In the RH simulations, the calculated cloud albedo effects (SCRE) are overestimated the SCREs by 44 % in RH-STN, by 28 % in RH-HYB, and by 20 % in RH-REF as compared to the observations. In the ST simulations, the estimated SCRE differs by -28.8 % in ST-REF, -17.5 % in ST-HYB, and 10 % in ST-STN as compared to the observations. This underestimation in the ST simulations results in largely underdevel-

oped marine clouds in the ST simulations (particularly in the tropics and subtropics); in the ST-STN simulation, the abundant CCN number concentration compensates for this systematic underestimation of clouds.

For the LCRE, the variations in the estimated LCRE are smaller than the variations in the SCRE, particularly in the RH simulations. The RH simulations calculate the LCRE to be about 10 % stronger than do the ST simulations. The LCRE in all simulations falls within the observed range. Comparing the net effects, the simulated NCREs in ST-HYB and ST-STN are reasonably close to the observations, but with different directions of bias: ST-HYB underestimates, and ST-STN overestimates SCRE.

The aerosol optical depth (AOD) calculated in all EMAC simulations is overestimated by up to 25 % as compared to the global mean of AOD obtained from combination data provided by Terra and Aqua in MODIS for the 10 years (from 2001 to 2010). This overestimation might be decreased by updating data on the aerosol emission field. According to de Meij et al. (2012), agreement can also be improved by running higher resolution simulations. However, despite this overestimation, all EMAC simulations (except RH-STN) fall within the observed uncertainty range in Stier et al. (2005) .

4.2 Annual zonal mean

Annual zonal means of cloud properties, water budgets, and cloud radiative effects are presented in Figs. 4.1, 4.2 and 4.3 for the simulations and observational data.

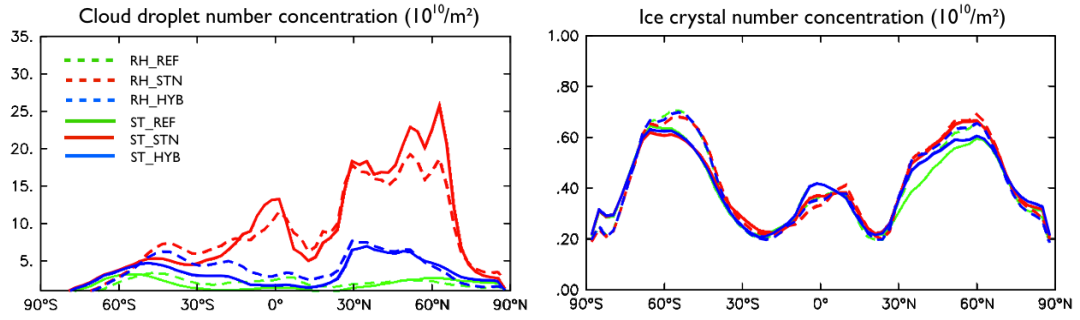

Figure 4.1: Annual zonal means of vertically integrated cloud droplet number concentration (N_d) and ice crystal number concentration (N_i). STN simulations are red and HYB simulations are blue. Couplings with RH-CLC are dashed lines and couplings with ST-CLC are solid lines.

In the zonal mean distributions of vertically integrated cloud droplets (N_d), both prognostic CDN (STN and HYB) simulations show higher CDNC than the REF simulations do. This can be expected from the model set-ups, as REF simulations do not

account for nucleated cloud droplets from aerosol particles. Fig. 4.1 shows the strong dependency of the droplet nucleation parameterizations on simulated total cloud droplet number concentration, as was already shown by the global mean values in Table 4.1. In general, the STN-simulations predict larger number of cloud droplets than the HYB simulations for both CLC schemes. The strongest effect appears in the Northern Hemisphere (NH), which has higher aerosol emissions. CCN activation is highly correlated with aerosol concentration, as indicated in the global distribution of cloud droplet number concentration for both the RH and ST simulations (see Figs. F.11 and F.12) for areas such as the eastern US, Europe, China, central Africa, and tropical Brazil. This regional sensitivity to CCN activation will be discussed more extensively in Chapter 5.

The zonal means of the vertically integrated ice crystal numbers (N_i) do not sensitively respond to the aerosol–cloud coupling, but do show a weak variation depending on CLC coupling. The calculated N_i in the RH simulations is slightly higher at middle latitudes and lower at the tropics, as compared to the ST simulations; these two differences are both due to simulated cloud cover. This pattern can also be found in the zonal distribution of ice water path (IWP) in Fig.4.2.

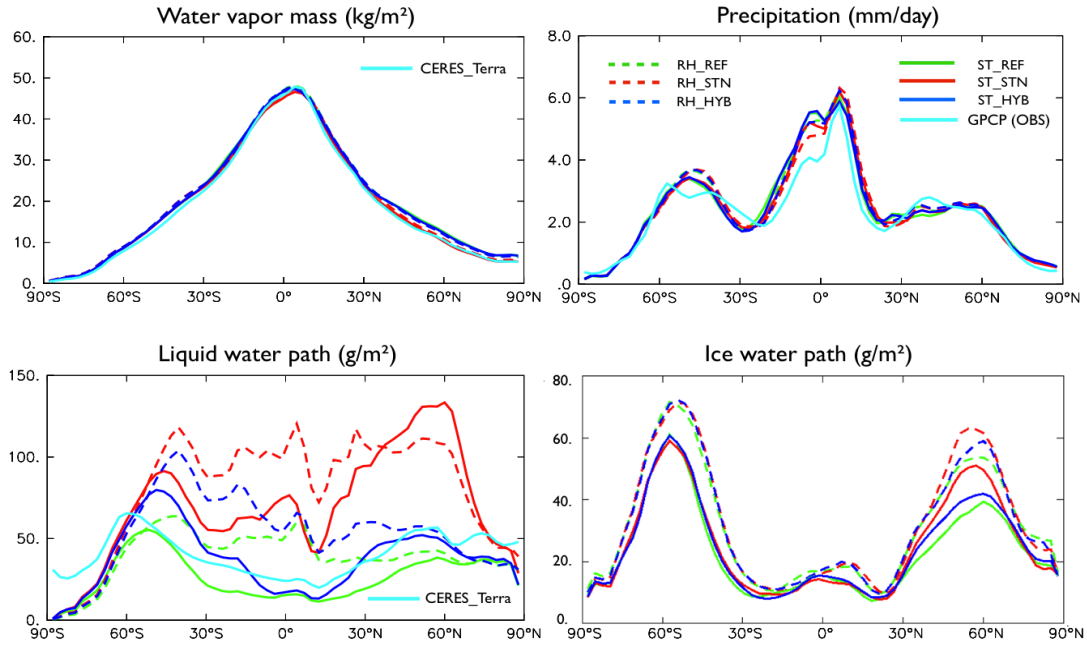

Figure 4.2: Zonal mean distributions of water vapor mass (WVM), total precipitation (P_{tot}), liquid water path (LWP), and ice water path (IWP). The simulations are represented in the same way as in Fig.4.1. The light blue lines represent observations.

Fig. 4.2 shows the annual zonal mean of hydrologic cycle for all simulations and observations. The calculated WVM in all simulations seems more dependent on cli-

matology than the aerosol–cloud coupling. The simulated P_{tot} in the extratropics is similar to the precipitation observed from GPCP. In contrast, in the tropics (at 10° in the Southern Hemisphere; SH) all simulations slightly overestimate total precipitation (with varying amplitude) as compared to the observations. This is in part due to the systematic overestimation of precipitation over the South Pacific convergence zone (SPCZ), which extends from the western Pacific warm pool. The current model does not realistically considered the inter-seasonal variations such as the monsoon trough, nor is it fully coupled with an ocean model. Furthermore, this overestimation may be attributable to a vertically coarse resolution. According to Hagemann et al. (2006), a higher vertical resolution can lead to systematic increases in both total and large-scale precipitation, as well as to decreases in convective precipitation. This effect of vertical resolution causes convective precipitation in L19 simulations to be overestimated, but is realistic in the L31 simulations. The dependency of vertical resolution on precipitation can also be related to atmospheric dynamics and thermodynamics. As discussed in Roeckner et al. (2006), a higher vertical resolution (L31) together with higher horizontal resolution (higher than T63) can improve the simulation results substantially; however, the horizontal resolution T42 performs better with the vertical resolution L19. In general, the simulated zonal mean distributions of P_{tot} are not strongly influenced by the experiment set-up, except for in the tropics of the SH. This lack of influence could be explained by the constraint of changes in precipitation by the fixed SST and SIC, since precipitation is largely controlled by the amount of the evaporation over ocean.

The zonal mean distribution of liquid water path (LWP) shows substantial variations among the experiment set-ups, as expected from the global mean of LWP (see Table 4.1; Fig. 4.2). The simulated LWP strongly responds to both the aerosol–cloud interactions and the coupling of cloud cover schemes, since cloud water content is closely associated with changes in CDNC, the hydrologic cycle (e.g., precipitation and evaporation), and cloud cover distribution. The relationship between LWP and CDNC are demonstrated in Figs. 4.2 and 4.1 that a large amount of LWP corresponds to a high CDNC. In the STN simulations, strong variations in CDNC enhance differences between the simulated LWP and the observation, particularly in the NH, due to too high CDNC originated from the strong CCN activation over land. In the SH, variation of the LWP is more sensitively associated with cloud properties (i.e., total cloud cover and cloud water) over ocean. This is because the SH is relatively cleaner regions than the NH, making the simulated CDNC is less different between the simulations (see Fig. 4.1). The large variations in LWP correspond to total cloud cover distributions (see Fig. 4.3), meaning that the RH simulations yield higher LWP values due to the larger marine cloud cover fraction than do the ST simulations. Overall, higher values of LWP

are generally accompanied by high CDNC (e.g., strong CCN activation from STN), particularly over land in the NH, and/or by larger amounts of clouds (e.g., from the RH-CLC simulations), which are more pronounced in the oceans, especially those in the SH.

All simulations except ST-REF overestimate LWP. ST-REF and ST-HYB could only reproduce the similar meridional pattern of the observed LWP, which has been shown to have its minimum at low latitudes and its maxima in middle latitudes. Overall, ST-HYB is fit the observations best with respect to the magnitude and patterns of zonal distribution. This zonal distribution of LWP strongly influences the cloud radiative flux, as the LWP is highly correlated with the cloud optical properties, particularly over ocean, as well as the distribution of CDNC over land.

The zonal mean distribution of IWP seems to be more sensitive to the cloud cover scheme than to aerosol-cloud feedbacks. This distribution is similar to the zonal mean distribution of N_i, with distinct patterns for the RH and ST simulations. These patterns are particularly at mid latitudes in the SH, and vary at mid latitudes in the NH with a combination of CDN and CLC scheme (see Fig.4.1). IWP is not as sensitive as LWP and CDNC. These small variances come from different cloud droplet nucleation number concentrations, which influence the heterogeneous freezing processes.

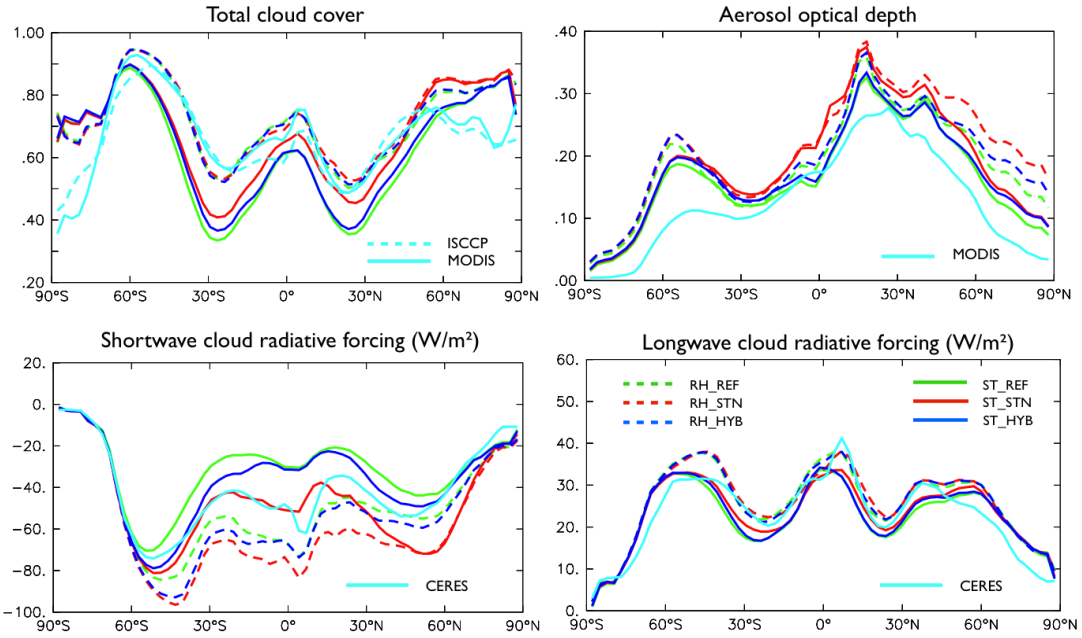

Figure 4.3: Annual zonal means of the total cloud cover (TCC), aerosol optical depth (AOD), shortwave cloud radiative effect (SCRE) and longwave cloud radiative effect (LCRE) at the top of the atmosphere (TOA). The simulations are represented in the same way as in Fig.4.1.

The zonal mean distribution of TCC in Fig 4.3 shows notable differences between the simulated TCC and the observations at high latitudes in both polar regions. These differences may relate to deficiencies in the satellite observational data over bright surfaces such as deserts areas and glacial (snow or ice) regions. The TCC simulated in the RH simulations (i.e., RH-REF, RH-STN, and RH-HYB) is close to the observations derived by MODIS and ISCCP, but, unlike the ST simulations, does not vary between simulations in response to the CDN schemes. In contrast, the predicted TCC in the ST simulations is rather sensitive to the aerosol-cloud coupling. Further analysis of the simulated cloud cover and relevant parameters can be found in Section 4.3.1 and Chapter 7.

The zonal mean distribution of SCRE and of LCRE at TOA in Fig.4.3 shows strong sensitivity to both aerosol-cloud feedbacks and the coupling of cloud cover schemes. Since CDNC and LWP make large contributions to the cloud optical properties (Lohmann et al., 2007; Koch et al., 2011), they directly influence the cloud radiative fluxes, in turn affecting the hydrological cycle and cloud properties. At mid latitudes (i.e., between 60°S and 30°S) ST-STN and ST-HYB are able to reproduce the SCRE, while the RH simulations generally overestimate SCRE. Since the faction of ocean-covered surface in the SH is larger than the fraction of land-covered surface, cloud optical properties are more closely associated with the distribution of LWP than with CDNC, as shown by the zonal mean distributions of LWP and TCC in Fig. 4.2. Koch et al. (2011) also found that cloud optical properties are strongly influenced by changes in LWP, particularly over cleaner areas and ocean. In the tropics, particularly between 0 and 10°N, two notable differences between the RH and ST simulations occur: small dips in the SCREs and a small bump in LCREs. These differences may be associated with ST-CLC's tendency to strongly underestimate clouds over ocean. Between 30°S and 15°N, the SCRE in ST-STN is close to the observed values, but this is an offset that the enhanced cloud optical properties due to high CDNC (from STN) compensates for by underestimating cloud cover (ST-CLC), particularly over ocean. Over other high latitudes in the NH, ST-STN yields a strong bias toward the cooling effect. This bias is due to the enhanced cloud optical thickness created by strong CCN activation over land. The increases in the nucleated cloud droplets number concentration (CDNC) are accompanied by higher cloud water content (LWP) and TCC (see Figs 4.1 and 4.2). In contrast, for ST-HYB at most latitudes in the NH (i.e., from 15°N up to the North Pole), the SCRE is similar to the observed values; ST-HYB also reproduces the LWP distribution. Further analysis is presented in Section 4.3.

4.3 Global distribution

This section presents global comparisons of simulated cloud properties and relevant climate parameters and corresponding observations (OBS) using deviations, relative errors (relative differences), and Taylor diagrams. Additionally, the performance of model set-ups is evaluated with Taylor skill score based on statistical variables (Taylor, 2001). As mentioned earlier in this chapter, the observational data have been regridded to the model's horizontal resolution, T42. The time periods of the observations are not exactly the same as the model outputs, but the temporal trends in cloud and water vapor do not significantly differ over time. The general spatial pattern similarities and tendencies of the relevant variables are therefore sufficient to qualitatively analyze and understand the model results refereed to the spatial distribution of the observations.

4.3.1 Total cloud cover (TCC)

To understand the global distribution of clouds, Fig. 4.4a shows the total cloud cover observed by MODIS. The spatial deviation between two different retrieved TCCs from MODIS and ISCCP is also presented in Fig. 4.4b. The discrepancy between the observed TCCs illustrates the uncertainty of the observations, as shown by positive and negative deviations in Fig. 4.4b. Positive deviations occur over the tropics, subtropics, and ocean; MODIS retrieves larger cloud fractions than does ISCCP. The larger cloud cover over the ocean could be associated with the cloud masking process in MODIS, which leads to overestimated cloud cover over the oceans (Weber et al., 2011). Negative deviations are found largely over arid regions (the Sahara desert, south Africa, Arabian peninsular, and the Gobi desert), some mountain areas, (i.e., Rocky mountain and southern part of Andes mountain), and Australia in addition to both polar regions including Antarctica, Arctic oceans and Greenland; MODIS estimates smaller cloud fractions than does ISCCP. Deserts are likely to be particularly relevant to the underestimation of high thin cirrus clouds in MODIS (Holz et al., 2008). The negative deviations seem more relevant to the deficiency of the satellite retrieval over bright surface (i.e., the regions covered by sand, snow and ice) to distinguish cloud cover (Weber et al., 2011).

The simulated TCCs (Model) are compared with the TCC derived by MODIS, using a deviation (Model – OBS) and relative error (R_{ERR} (%) $= \frac{Model-OBS}{OBS} \times 100$; see Figs. 4.5 and 4.6). When the simulated TCCs are compared with the MODIS data, the largest deviations are found over the desert areas of North and Central Africa, and the arid regions such as Saudi Arabia and Iran (see Figs. 4.5 and 4.6). These positive

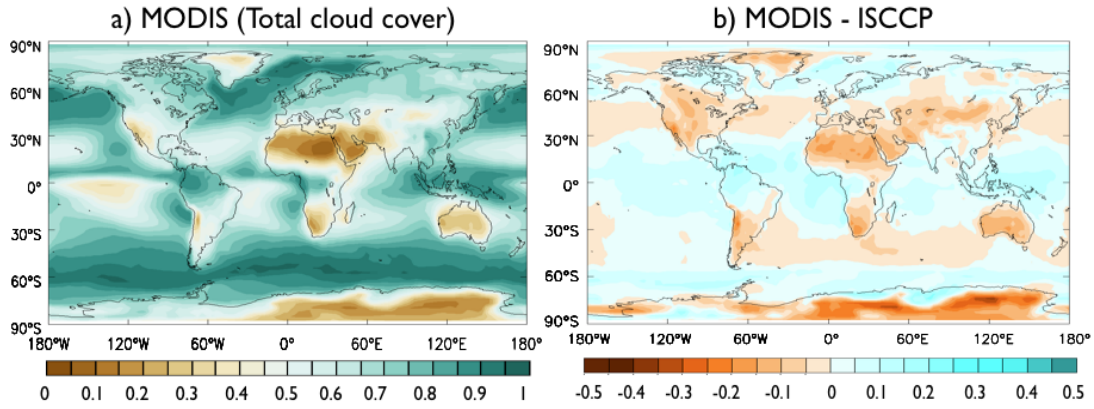

Figure 4.4: Global distribution of total cloud cover (TCC) estimated by MODIS (a), differences between MODIS and ISCCP data (b).

errors are not distinct in the comparison with the ISCCP (see Fig. F.7). This largest deviations could be understood as a systematic underestimation of total cloud cover in MODIS data rather than as a model error. Regarding the uncertainty of the observations, the simulated cloud fractions generally fall within ± 20% relative difference for all regions in the RH simulations. The simulated cloud cover by RH-CLC is slightly overestimated about 10% - 20% over ocean, as shown in Fig. 4.6 a), c), and e); there are also some regional variations in Northern Europe.

While the ST simulations present a strong land–sea contrast in the deviation of the simulated TCCs from the observations (MODIS; see Fig. 4.5 b, d and f), strong negative biases are found over ocean in all ST simulations. These biases are slightly lower than those in the comparison with ISCCP (see Fig. F.7). The underestimation of marine stratocumulus at low latitudes is a common feature of the ST simulations, especially in ST-REF and ST-HYB (see Fig.4.6). For ST-STN, these strong negative biases are offset by high CDNC from strong continental outflow, which can be attributed to larger cloud cover. This underestimation of shallow marine clouds seems to be relevant to the insufficient skewness setting of the ST-CLC scheme as discussed by Weber et al. (2011), and is due in part to the sensitivity of simulated clouds to aerosol-cloud coupling (Lohmann et al., 2007).

Over land, positive biases over Europe, the subarctic, and Siberia in the STN simulations (RH-STN and ST-STN) match the high CDNC distribution, and substantially affect the cloud radiative fluxes (see Fig. 4.5c and d). Negative biases over North America and the Mediterranean Basin in the ST-REF simulation (Fig. 4.5b), are moderated by including the aerosol-cloud feedback; this moderation is evidenced by the diminished errors in ST-STN and ST-HYB (see Fig. 4.6d and f). These overall varia-

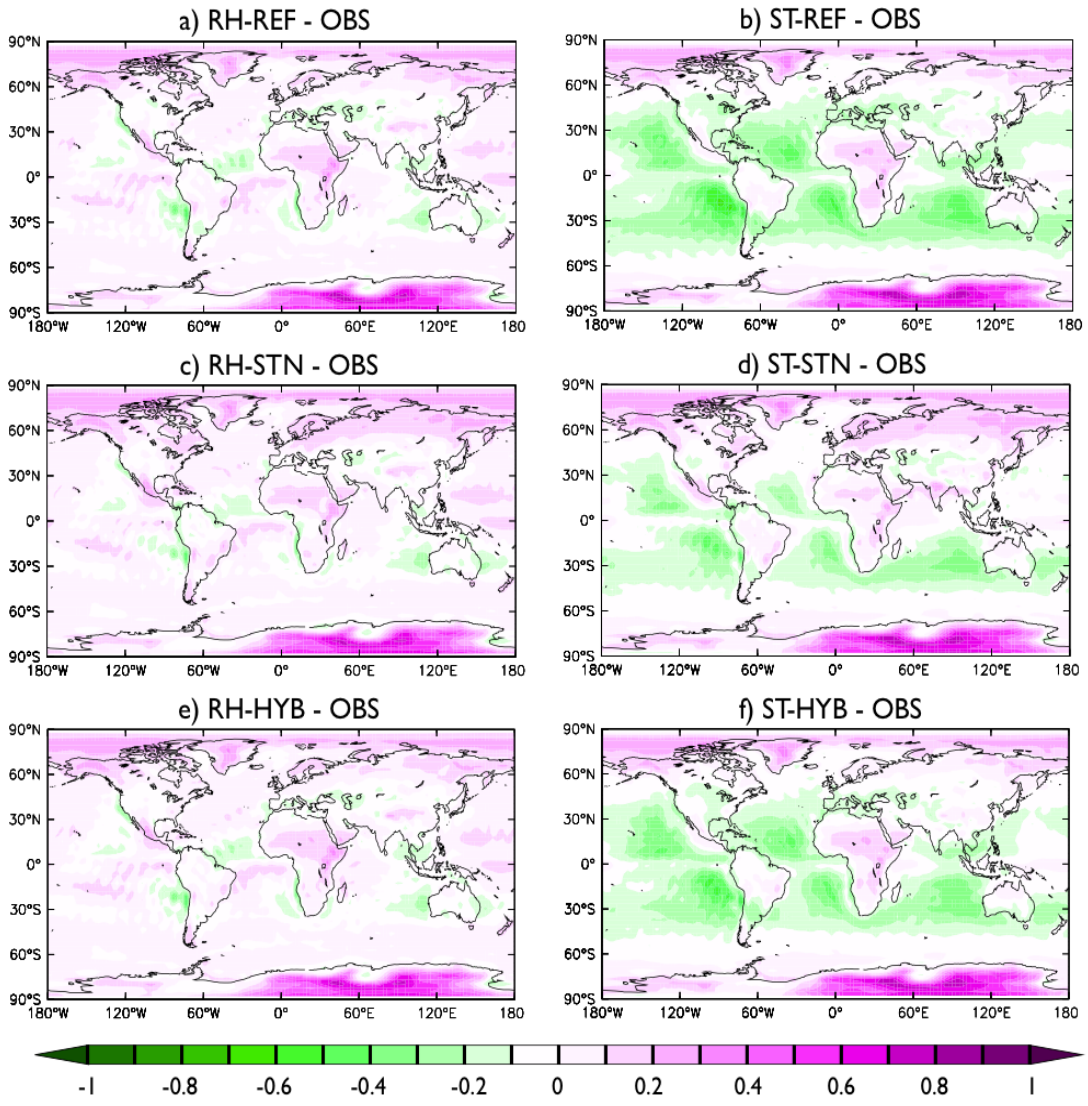

Figure 4.5: Deviations of the simulated TCCs from the observed TCC by MODIS [Model – OBS] for (a) RH-REF, (b) ST-REF, (c) RH-STN, (d) ST-STN, (e) RH-HYB, and (f) ST-HYB.

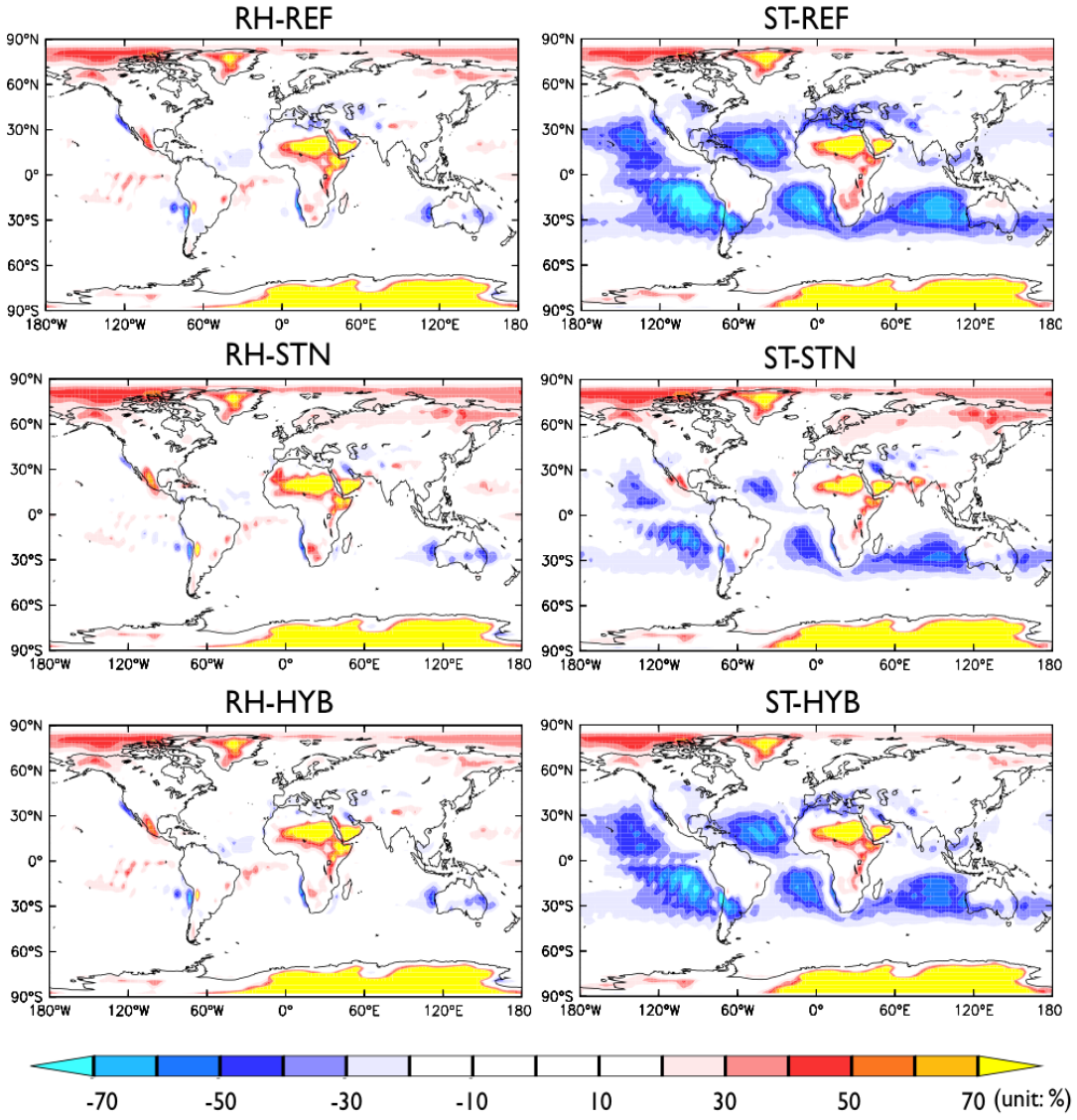

Figure 4.6: Relative differences between the simulated TCCs and the derived TCC from MODIS (OBS) for (a) RH-REF, (b) ST-REF, (c) RH-STN, (d) ST-STN, (e) RH-HYB, and (f) ST-HYB.

tions in the ST simulations are not found in the RH simulations, demonstrating that the clouds simulated with the ST-CLC scheme are more sensitive to changes in the nucleated cloud droplets.

Overall, marine clouds are more related to cloud water content distribution than to the cloud droplet number concentration, while continental clouds seem more sensitive to the enhanced concentration of cloud droplets from the aerosol-cloud interactions. To simulate clouds over continents, the HYB simulations show noticeable improvement compared to the STN simulations, while the simulated marine clouds show that the RH-CLC scheme performs marginally better than does the ST-CLC scheme. These different patterns of TCC are influenced by changes in cloud properties, which in turn strongly impact cloud radiative effects (CREs) at the top of the atmosphere (TOA). These impactions are discussed more in the following section.

4.3.2 Cloud radiative effects

In the present study, the estimated aerosol indirect effects (AIEs), which here refer to the overall aerosol effects, including the Twomey effect and cloud lifetime effect, are quantified as the changes in cloud radiative effects (CREs) at TOA. This is done due to the difficulty of isolating individual aerosol effects in the current model set-ups. For example, to quantify the first indirect effect (Twomey effect), a prescribed constant LWC has to be used in calculations of cloud scheme. However, the present cloud model set-ups are designated to reshape the cloud droplet size and number with the nucleated or the auto-conversed cloud drops; these set-ups are therefore not satisfied with the condition of a constant LWC. The AIEs in this study is therefore defined as the overall aerosol effects on clouds and climate, rather than individual aerosol effects.

The global distributions of the cloud radiative effects closely relate to the CCN number concentration (Figs. F.11 and F.12) and cloud cover distributions (Fig. 4.5), since cloud optical properties are correlated with the number of cloud droplets and cloud coverage, and thereby influencing cloud radiation fluxes. An enhanced CCN substantially impacts low clouds and cloud optical properties. Low clouds primarily reflect the incoming solar radiation, and their optical properties regulate the magnitude of cloud cooling effects (SCRE). A strong SCRE cools the Earth's surface and increases atmospheric stability; it also reduces convective activity (e.g., amplitude and frequency of convection) and the corresponding convective fluxes (entrainment and detrainment). The reduction of convection can then influence large-scale clouds and high clouds, such

as cloud vertical extension (cloud top height), cloud properties, and cloud water distributions. High clouds are more relevant to the cloud warming effect (LCRE). The changes in SCRE and LCRE corresponding to aerosol-cloud interactions are strongly reflected in the net cloud radiative effect (NCRE) in the simulations, and also show variations according to the coupling of the cloud cover schemes. The SCRE shows more sensitive, and stronger changes in response to aerosol-cloud interactions, and its magnitude is generally larger than that of the LCRE.

Fig. 4.7 shows biases in the simulated NCRE as compared to the observations, and presents the trends of these biases in each simulations, as well as how these biases correspond with the comprehensive effects of aerosol-cloud feedback and the coupling of cloud cover schemes. As discussed in the previous sections, in the simulated CREs the aerosol-cloud feedback effects are more pronounced over land and the coupling of cloud cover schemes are more distinct over ocean. Over the lands, the NCRE calculated in ST-REF is strongly biased toward underestimating cloud cooling effects, as shown in Figs. 4.7b and F.8b. This underestimation relies highly on the exclusion of aerosol-cloud interactions. Positive deviations and relative errors appear in areas with polluted air (e.g., Europe and East Asia), which are generally associated with CCN abundance. As discussed above, the REF simulations do not take into account aerosol-cloud feedback; as a result, these simulations predict relatively small amounts of CDNC and LWP, and consequently optically thin clouds. The low values of CDNC and LWP influence cloud optical properties and contribute to a less strong cloud cooling effect than that produced by other simulations. This shows the importance of aerosol-cloud feedback effects on cloud formation and cloud radiative effects, and thereby on the climate. For the STN simulations, the strong CCN efficiency induces a high CDNC, which is indicated by strong negative deviations (see Figs. 4.7c and d). Most of the strong cooling effects appear over the CCN-abundant areas (see Figs. F.11 and F.12). The strong net cooling effect patterns of the NCRE are a result of the strong SCRE. In the HYB simulations these strong negative biases of the NCRE (which occur over India and East Asia in the STN simulations) are notably diminished (see Figs. 4.7e and f) due to moderating effects of CCN efficiency. The positive biases over North America and Europe in the REF simulations are also attenuated by applying the HYB scheme to both the RH-CLC and ST-CLC coupling.

Over ocean, the RH simulations (i.e., RH-REF, RH-STN, and RH-HYB) generally overestimate the cloud cooling effect, as evidenced by negative deviations and relative errors, particularly over ocean (see the left-hand columns in Figs.4.7 and F.8). This negative bias corresponds to the trend of over-predicting cloud cover in the RH sim-

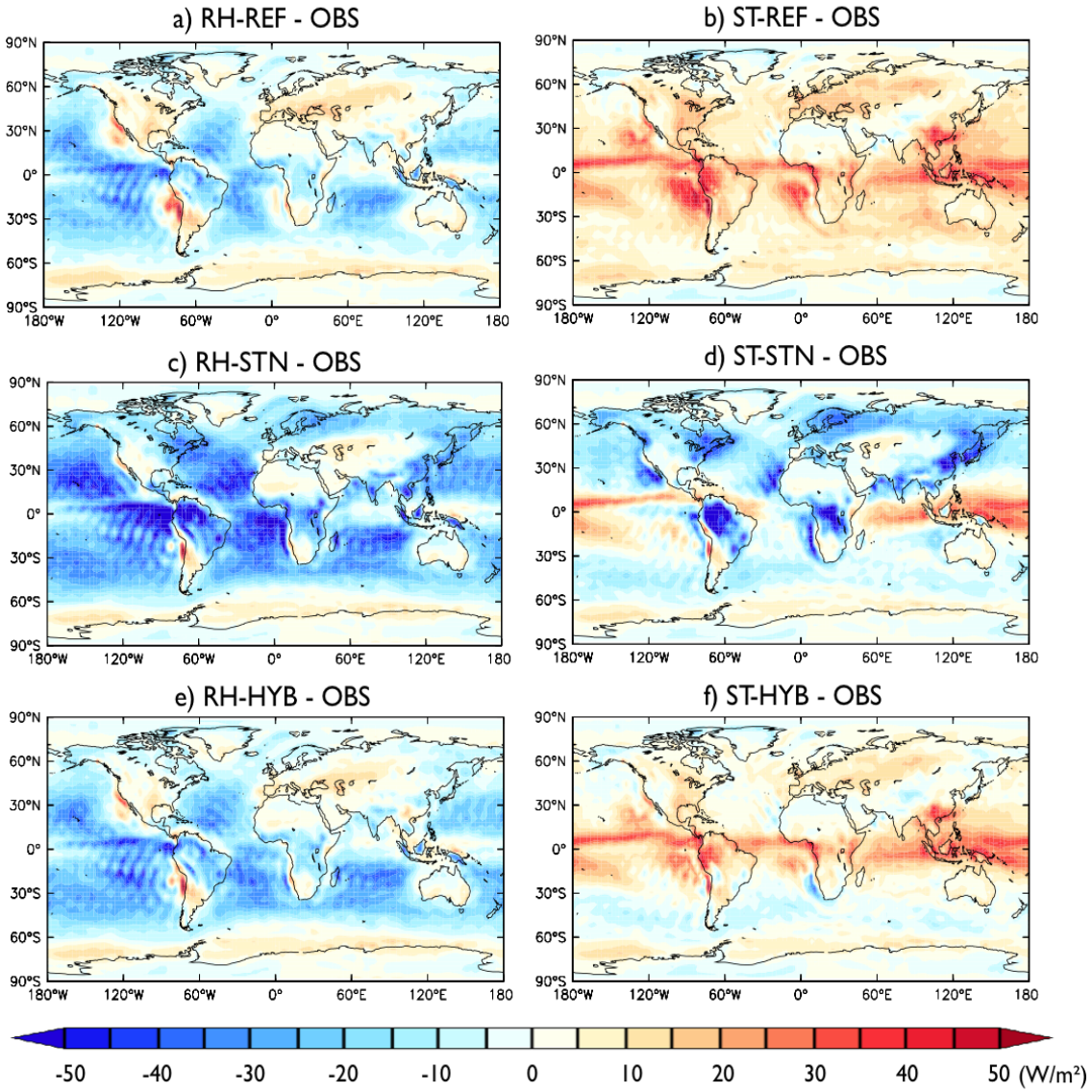

Figure 4.7: Deviations of the annual means of NCRE at the top of the atmosphere (TOA) compared to the observations (CERES EBAF). For simulations a) RH-REF, b) ST-REF, c) RH-STN, d) ST-STN, e) RH-HYB, and f) ST-HYB.

ulations with high LWP values. These negative biases over the ocean are attenuated in the HYB simulations with different magnitudes. The overall estimates of CREs in the HYB simulations agree relatively well with the observations in both CLC schemes (see Table E.3 and Fig. E.1). However, underestimated cloud cooling effects over the ITCZ occur in all the ST simulations, but with different magnitudes (see Figs. F.8e and f, and 4.7e and f). This underestimation seems to be relevant to the deficiency in the current setting of the ST-CLC scheme, similar to the underestimation of clouds over the ocean and the ITCZ, as discussed above (see also Lohmann et al., 2007; and Weber et al., 2011). In the ST-STN simulation these underestimated cooling effects are smaller than for the other ST simulations, ST-REF and ST-HYB. These effects are smaller because relatively high cloud droplet number concentration (from the STN scheme) compensates for the underestimated clouds and low cloud water that originates from the ST-CLC scheme (Fig. 4.7c). Similarly, the global distribution of total cloud cover shows that the underestimation of clouds over the ocean is moderated by strongly enhanced CCN from continental outflows (ST-STN; see Figs. 4.5). In the RH-STN simulation, the larger cloud cooling effects are more pronounced than in the ST-STN, since larger cloud cover and higher liquid water path–both of which relate to the RH-CLC scheme–amplify cloud albedo via high CDNC (see Fig. 4.7d).

Overall, the impact of the CLC scheme on the CREs is clear: the RH simulations calculate strong cooling effects over ocean and are less sensitive to changes in cloud properties, while the ST simulations predict differentiated cooling effects over land in response to changes in CDNC. The ST simulations also make a distinction for effects over the ocean, via changes in LWP, with lower cooling effects over the tropical oceans. The ST-CLC appears to perform marginally better in representing the regional CRE responses to regional changes (Lohmann et al., 2007), but seems does not simulate marine clouds over ITCZ well. The CDN parameterizations STN and HYB play a strong role in estimating both cloud radiative effects and cloud properties. These effects are magnified or attenuated by the CLC schemes except for when CDNC is overly high, as occurs over land in the STN simulation. The estimated CREs in the REF simulations are improved by applying the HYB scheme in either the RH-CLC or ST-CLC scheme. Further evaluation of estimated cloud radiative effects is found in the Appendix.

4.4 General assessments

This section assesses general performances of the aerosol-cloud coupling (CDN scheme) and cloud cover parameterization in the EMAC model using a Taylor diagram (Taylor,

2001). This diagram provides information about how closely the simulated patterns match observations (OBS) using the statistical variables of correlation (R), differences in centered root mean squares (CRMS; E'), and standard deviations (σ; see Appendix D.2). In this thesis, the spatial pattern comparisons are calculated separately for land and ocean.

To plot different fields on the same diagram (Fig. 4.8), the statistical variables are normalized by the standard deviations of corresponding observations (σ_r), i.e., the normalized CRMS difference ($\hat{E}'$) and the ratio of the standard deviation of the model results to the observations ($\hat{\sigma_x}$). Correlation coefficients (R) are not changed by the normalization. Fig. 4.8 shows the global spatial similarities of clouds and the relevant climate parameters predicted in the simulations using observations; these parameters are total cloud cover (TCC), cloud radiative effects (SCRE, LCRE), total precipitation (P_{tot}), and aerosol optical depth (AOD). All comparisons are based on the multi-year mean of the simulated and observed data (Table 4.1), and the observations are regridded to the model resolution (T42, 2.8°).

Fig. 4.8 demonstrates that the current EMAC model set-ups, which combine the CDN and CLC scheme, perform better over continents for all simulations. This superior performance is apparent from comparing two Taylor diagrams (for land and ocean), as well as from comparing the model skill scores for simulated clouds and climate. Over ocean, the simulated clouds and climate parameters have larger variations than those in the observations, and relatively lower pattern correlation with observations than continental simulations. Furthermore, larger CRMS errors (0.55 to 1.0) appear when comparing marine parameters, although most of the continental statistical variables (see Fig. 4.8a) fall within the range of 0.40 and 0.75 for normalized CRMS differences. Based on the calculated skill scores, more than 83% of the simulated continental parameters approach more than "Good" skill performance (here, over 0.8500 skill score); over ocean, the overall skill scores are relatively lower than the ones for the continental parameters. Despite poorer performance over ocean, the simulated TCC and LCRE are relatively skillful, with mostly "Very good" (higher than 0.9000 skill score) and the rest "Fair" (0.8499 to 0.7500) skill scores. A more detailed analysis of model performance is followed by an interoperation of statistical variables (see Fig. 4.8 for summary).

For the total cloud cover (see Table 4.1), Terra and Aqua MODIS data from the year 2000 to 2010 are used to compare simulated total cloud cover (TCC), which is denoted by purple dots. The observation is firstly selected from the available data and averaged with the good values in each grid; these values are then regridded to the

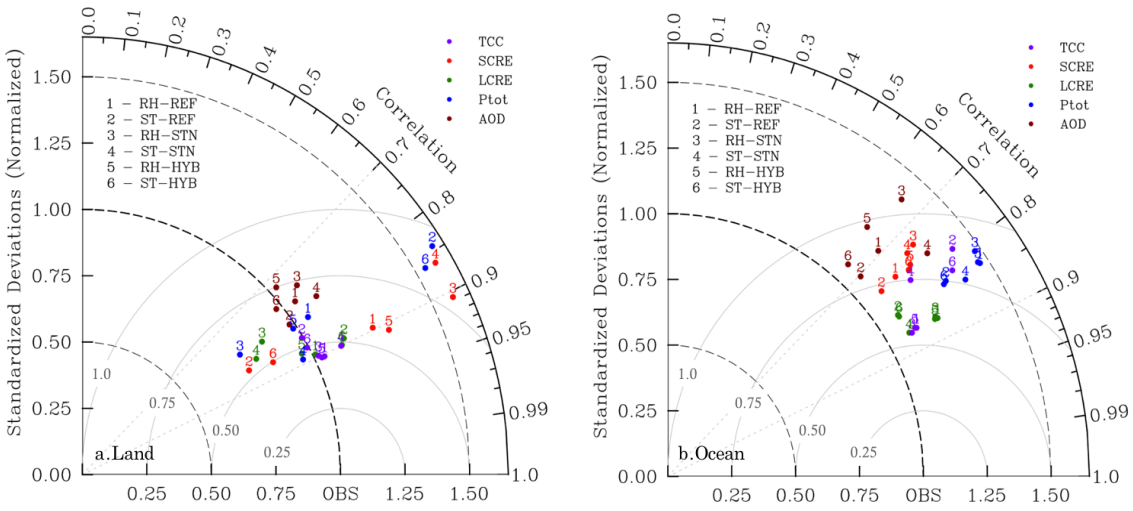

TCC	SCRE	LCRE	Ptot	AOD
5 RH-HYB	6 ST-HYB	1 RH-REF	4 ST-STN	2 ST-REF
1 RH-REF	1 RH-REF	5 RH-HYB	5 RH-HYB	1 RH-REF
3 RH-STN	5 RH-HYB	6 ST-HYB	1 RH-REF	4 ST-STN
4 ST-STN	2 ST-REF	2 ST-REF	3 RH-STN	6 ST-HYB
6 ST-HYB	3 RH-STN	3 RH-STN	6 ST-HYB	3 RH-STN
2 ST-REF	4 ST-STN	4 ST-STN	2 ST-REF	5 RH-HYB

TCC	SCRE	LCRE	Ptot	AOD
3 RH-STN	2 ST-REF	4 ST-STN	6 ST-HYB	2 ST-REF
5 RH-HYB	1 RH-REF	6 ST-HYB	2 ST-REF	6 ST-HYB
1 RH-REF	6 ST-HYB	2 ST-REF	4 ST-STN	1 RH-REF
4 ST-STN	5 RH-HYB	5 RH-HYB	5 RH-HYB	4 ST-STN
6 ST-HYB	4 ST-STN	1 RH-REF	1 RH-REF	5 RH-HYB
2 ST-REF	3 RH-STN	3 RH-STN	3 RH-STN	3 RH-STN

Rating	Excellent	Very good	Good	Fair	Poor
Skill Score	1.0000-0.9500	0.9499-0.9000	0.8999-0.8500	0.8499-0.7500	0.7499-

Figure 4.8: Taylor diagrams for land and ocean. Statistical comparison of observations with estimates of total cloud cover (TCC), cloud radiative effects at TOA (SCRE, LCRE), total precipitation (P_{tot}), and aerosol optical depth (AOD) for all EMAC simulations. The statistical variables are normalized by the standard deviations of corresponding observations (σ_r), i.e., the normalized CRMS difference ($\hat{E}'$; gray arcs) and the ratio of the standard deviation of the model results to the observations ($\hat{\sigma}_x = \frac{\sigma_x}{\sigma_r}$, x and y axes; black dashed arcs). Correlation coefficients (R; gray dashed radii) are not changed by the normalization. Taylor skill scores are calculated and model set-ups are ranked by skill scores (from high to low) for each parameter. The relevant statistical variables are summarized in Table F.2, more detailed information can be found in Section D.2 and D.3 in the Appendix.

model's horizontal resolution (T42, 2.8°). Only data from between 60°S and 60°N is used due to the uncertainty of the observation data over the both poles (see Section 4.3.1). Most of the simulations show high spatial correlations (0.8 to 0.9) with the observations over lands. All the RH simulations have the same high correlations (0.9), the same standard deviation for observations, and low CRMS errors. The sensitivity of TCC to aerosol-cloud coupling, however, is not notable (see Section 4.3.1). The ST simulations have similar spatial variabilities to the observations, but show relatively lower spatial correlations (0.78 to 0.85) and higher CRMS errors than the RH simulations. These pattern dissimilarities in the ST simulations and the large variances in the simulated marine clouds are caused in part by the strong underestimation of marine clouds in the tropics and subtropics (see Figs. 4.5 and 4.6). Within the same cloud cover scheme, the TCC in the REF simulations can be slightly improved by applying the aerosol-cloud interactions, which reduces variances and CRMS errors in the STN and HYB simulations. Based on the skill scores of simulating TCC, the RH-CLC scheme seems more skillful in reproducing total cloud cover than the ST-CLC scheme, particularly over ocean. The low skill scores achieved by the ST-CLC scheme for simulating TCC over ocean seem relevant to the systematic underestimation of total water vapor, due to high frequency of shallow convection, especially in the tropics. In addition, higher stratiform precipitation in the tropics could lead to low cloud water. This higher precipitation also affects aerosol optical depth due to changes in the efficiency of the aerosol removal process, such as a wet scavenging rate. These overall processes influence cloud optical properties, and by extension cloud radiative effects. Further discussion of cloud distribution relying on cloud cover schemes and the effects of different cloud cover schemes is found in Chapter 7.

To assess the CREs calculated in the simulations, the CERES EBAF data from 2001 to 2010 are compared with the calculated SCREs (red dots) and LCREs (dark green dots). The calculated patterns of the LCRE are a relatively tight cluster in the diagram, indicating that the experimental set-up impacts the LCRE less than it does than the SCRE. This different magnitude of impacts confirms the previous assertion that aerosol-cloud coupling influences strongly low cloud properties by enhancing CDNC and thereby has substantial effects on the SCRE, particularly over continents. The predicted LCREs in all simulations generally agree with observations; all of them have relatively high spatial correlations (higher than 0.85) and similarly low CRMS errors (about 0.5). Most of the simulated LCREs also have relatively high skill scores for both land and ocean.

The calculated SCREs over continents also show relatively high pattern correlations (about 0.9) with the observed SCREs. Distinct variations can also be found in the REF

and HYB simulations depending on the ST-CLC and RH-CLC scheme, with slightly higher CRMS errors in the RH simulations. Among the statistical variables for the SCRE, the largest CRMS error and variance as compared to the observations appear in the STN simulations. These discrepancies originate from the overly high SCREs, which are caused by the high CCN efficiency calculated in the STN scheme. Within the same combination of cloud cover scheme, the amplitudes of variation and CRMS error are likely to be associated with aerosol-cloud coupling (CDN scheme). Overall, the HYB simulations perform better than the STN simulations based on all three statistical variables (i.e., the centered root mean square error, spatial correlation, and standard deviation).

Over ocean, the simulated SCREs have relatively low pattern correlations (about 0.75; see Fig. 4.8b) and larger variances than the observed ones. These variances of SCREs as compared to the observations increase with the coupling of the CDN scheme (STN and HYB) for both CLC schemes (RH-CLC and ST-CLC) due to the enhanced SCRE over the coastal regions. The marine LCREs are generally reproduced well, as shown by the small CRMS errors and high pattern correlation coefficients, both of which are similar to those for the continental LCREs.

To evaluate simulated total precipitation (P_{tot}), the Global Precipitation Climatology Project (GPCP) long-term monthly mean, derived from the years 1981 to 2010 (Adler et al., 2003), is compared with the simulated precipitations. The estimated total precipitations show high spatial pattern correlations (about 0.80 - 0.90) with the observations (see blue dots in Fig.4.8). Statistical variables have a wider range over land than over ocean due to the constraint of a prescribed SST and SIC. The large uncertainty in the estimated precipitation over ocean from GPCP (Adel et al., 2001; Hagemann 2002) may also contribute to larger differences in CRMS and variance. This simulated precipitation could be improved by applying higher model resolutions (Hagemann et al., 2006; Roeckner et al., 2006).

To appraise the aerosol optical depth (AOD) in the simulations, the CERES SYN1deg Month Terra Aqua MODIS Ed3A Subset data for the years 2001 to 2010 are also treated in the same way as are the other observations. The estimated AODs show relatively lower spatial correlations (0.70 - 0.80 for land and 0.65 - 0.75 for ocean) than do other variables, in part due to the fixed aerosol emission field. Typically, AOD is highly correlated aerosol emissions. However, in the simulation set-ups the emissions are fixed for the year of 2000, and data from this year are cycled for all model simulations; this set-up is made due to the purpose of the study (see Chapter 3). Additionally,

Table 4.2: Evaluation of EMAC model performance based on skill scores. Skill scores are calculated using standard deviation and correlation coefficient (Taylor, 2001), see Appendix D.3.

Continental							
RH-CLC	TCC	SCRE	LCRE	P_{tot}	AOD	Sum	Average
RH-REF	5	4	4	4	3	20	4.0
RH-STN	4	2	3	2	3	14	2.8
RH-HYB	5	3	4	4	3	19	3.8
ST-CLC	TCC	SCRE	LCRE	P_{tot}	AOD	Sum	Average
ST-REF	4	3	4	1	4	16	3.2
ST-STN	4	2	3	4	3	16	3.2
ST-HYB	4	4	4	2	3	17	3.4
Marine							
RH-CLC	TCC	SCRE	LCRE	P_{tot}	AOD	Sum	Average
RH-REF	4	3	4	2	2	15	3.0
RH-STN	4	2	3	2	1	12	2.4
RH-HYB	4	2	4	2	2	14	2.8
ST-CLC	TCC	SCRE	LCRE	P_{tot}	AOD	Sum	Average
ST-REF	2	3	4	2	2	13	2.6
ST-STN	3	2	4	2	2	13	2.6
ST-HYB	2	2	4	3	2	13	2.6

Rating is based on the calculated skill score (S), see Table F.2 and Fig.4.8

Excellent = 5, Very good = 4, Good = 3, Fair = 2, Poor =1

the uncertainty of the MODIS AOD data could also be related to the lower pattern similarity for simulated AODs and the MODIS AOD. The expected MODIS AOD error ($\Delta\tau_{550nm}$) is $\pm$ (0.03 + $0.05\tau_{550nm}$) over ocean (Kaufmann et al., 1997; Tanré et al., 1997) and $\pm$ (0.05 + $0.15\tau_{550nm}$) over land (Chu et al., 2002; Levy et al., 2010; Yoon et al., 2014). Particularly over ocean, the absolute uncertainty term (0.03) is not negligible for relatively low AOD values. However, these overall lower pattern similarities for simulated AOD also could be improved with higher model resolution (de Meji et al., 2012).

To compare overall model performance, Table 4.2 summarizes the ratings of model skill based on Taylor skill scores (Taylor, 2001; for more detailed information see D.3 in the Appendix). These ratings are based on five categories (i.e., Excellent = 5, Very good = 4, Good =3, Fair = 2, Poor = 1) referred to model skill scores (see Fig. 4.8 and Table F.2). Comparing overall model performance, the RH simulations show higher skill scores than the ST simulations (see Table 4.2). These higher skill scores are mainly due to the high skill scores for simulated total cloud cover. As can be expected from the global distribution of total cloud cover (see Section 4.3.1), the RH simulation show a robust performance to simulate cloud cover. A further analysis of the cloud cover scheme can be found in Chapter 7. For the ST simulations, the simulated TCC is sensitive to aerosol-cloud interactions, but is less effective in simulating clouds over the tropics and subtropics, particularly over ocean; this model weakness contributes to lower overall model skill scores. The precipitation formation in the ST simulations also respond too sensitively to simulated cloud properties such as changes in cloud droplet size spectra and cloud water budget, which leads to lower skill than the robust performances of the RH simulations. This oversensitivity could be explained by the simulated TCC's sensitivity to changes in cloud water and droplets. This sensitivity mutually influences precipitation, since the ST-CLC scheme is tightly connected with the cloud water variations and hydrological cycles, as discussed in Section 4.2 and in Lohmann et al. (2007).

Overall, over the continent, RH-REF is the most skillful set-up (out of the simulations assessed in the present study) to simulate cloud- and climate-relevant properties that are spatially close to the observed patterns. This is not surprising, since the radiative parameters are tuned in the model (Roeckner et al., 2006), and in the current model set-ups the tuned parameters optimize simulating properties in RH-REF as a default set-up. The simulated results show the lowest skill scores for RH-STN. For ST-STN, based on the average value, the simulated properties seem to be similarly skillful to the other ST simulations; however, this is only because a high skill score for total

precipitation compensates for low skill scores in other parameters. Within the HYB scheme, the overall model performance of RH-HYB is comparable to RH-REF, based on skill scores, and ST-HYB shows superior estimation of SCRE and P_{tot} as compared to the ST-REF simulation. Overall, to take into account aerosol-cloud feedback, the HYB scheme is a better choice to predict cloud and climate relevant parameters for both the RH-CLC and ST-CLC schemes. Over the ocean, although it is difficult to conclude which model set-up performs better (due to the constraint of prescribed SST and SIC), the EMAC model generally performs more than "Fair" to "Good" based on the skill scores in Table 4.2.

4.5 Conclusion

In this chapter, the general performance of the CDN and CLC schemes in the EMAC model are presented based on overall comparisons with the observations. As demonstrated in the previous sections, calculated CCN activation in each CDN scheme causes changes in cloud properties, and lead to distinctively different climate statuses in the model results. In the simulations, cloud water and radiative properties are highly correlated with changes in the cloud droplet spectra (cloud droplet size and number distributions) and cloud cover distributions. These overall changes have important impacts on the atmospheric energy budget on both the local and global scale, underlining the wide-ranging effect of cloud microphysics, cloud cover schemes, and cloud droplet nucleation schemes on the simulated climate.

Compared to the observations, the overall simulated cloud properties and relevant climate parameters have shown relatively high pattern similarities based on the annual mean data, particularly over land. According to the statistical variables in the Taylor diagrams and skill scores, the HYB cloud droplet nucleation scheme performs better with both the RH-CLC and ST-CLC cloud cover schemes. The RH-CLC scheme simulates TCC and relevant parameters more effectively, but is not very sensitive to aerosol-cloud interactions. The ST-CLC scheme sensitively reflects aerosol-cloud coupling in the model results. Due to this sensitivity, the aerosol-cloud coupling seems to be necessary to the ST-CLC scheme for simulating reliable model results.

Following this general overview of the simulated cloud properties and cloud radiative effects at TOA for each simulation, further investigation into aerosol-cloud interactions are discussed in detail in the upcoming chapters.

Chapter 5

Aerosol activation (CCN efficiency)

Aerosol activation (i.e., forming CCNs in warm clouds) is calculated in the STN and HYB cloud droplet nucleation schemes, which describe the hygroscopicity and supersaturation of aerosols in the warm cloud formation (summarized in Table 2.2). CCN efficiency can be quantified by the fraction of the activated aerosols (CCN) relative to the total available aerosols in each aerosol size mode (hereafter, the activated aerosol fraction; AF). Similarly, measurements or field studies measure the ratio of CCN to CN (cloud nuclei), which provides intrinsic information regarding the CCN efficiency in droplet nucleation, as it relates to the aerosol size and number spectrum. CCN efficiency in this study is represented by AF_i in each mode and the cloud droplet nucleation rate (R_{nuc}) for all size modes, as an important indicator of the aerosol-cloud interactions. Note that these values are only valid within clouds, as values are filtered with cloud cover.

5.1 Annual global mean

Table 5.1 shows the volume-weighted global mean values of CCN efficiency from the surface to the upper troposphere (about 10km). Large particles show stronger activity than small particles in both the STN and HYB simulations ($AF_{Acc,Cor} > AF_{Atk}$), see the activated aerosol fractions in the accumulation and coarse modes (about 60% for STN, about 40% for HYB) and in the Aitken mode (about 20% for STN, about 12% for HYB). As expected for the Köhler equilibrium curve, larger particles nucleate at lower S_c than smaller particles, since the Kelvin effect decreases with increasing particle size (which is associated with lower surface tension). This reduces the relevance of the solute effect to overcome the aerosol radius. Besides, mostly large particles contain

Table 5.1: Global means of the activated aerosol fractions (AF_i) and CCN (CCN_i) in each mode, cloud droplet nucleation rate (R_{nuc}), and cloud droplet nucleation number (CDN) from the surface to the upper troposphere (10km). These values are selected when cloud cover exceeds 5 % in a grid box.

mode (i)	Aitken	Accumulation	Coarse	Total amount
Global	AF_{Atk}	AF_{Acc}	AF_{Cor}	R_{nuc}
RH-STN	21.3 %	61.0 %	62.4 %	1.2e+04 $m^{-3}s^{-1}$
ST-STN	20.9 %	60.1 %	61.3 %	1.1e+04 $m^{-3}s^{-1}$
RH-HYB	12.2 %	39.0 %	40.3 %	5.5e+03 $m^{-3}s^{-1}$
ST-HYB	11.9 %	40.4 %	41.8 %	5.4e+03 $m^{-3}s^{-1}$
Global	CCN_{Atk}	CCN_{Acc}	CCN_{Cor}	CDN
RH-STN	8.9e+07	3.0e+07	4.9e+05	9.9e+07 m^{-3}
ST-STN	7.8e+07	2.7e+07	4.0e+05	9.0e+07 m^{-3}
RH-HYB	5.8e+07	1.1e+07	2.0e+05	5.0e+07 m^{-3}
ST-HYB	4.9e+07	1.2e+07	1.6e+05	4.5e+07 m^{-3}

enough soluble substances to activate (McFiggans et al., 2006). In general, particle size dominates CCN activation (Feingold, 2003; Dusek et al., 2006; Andreae and Rosenfeld, 2008).

For small particles, aerosol activation is more sensitive to aerosol composition than for larger particles. Since small particles have a strong surface tension of the particle (Kelvin effect), the composition of the particle (Raoult effect or Solute effect) is relatively important to overcome the Kelvin effect as an offset effect. McFiggans et al. (2006) also reported the importance of aerosol composition in droplet activation for small particles (smaller than $20nm$ radius), which are relevant to the Aitken mode in the simulations. In comparing the AF_{Atk} in the STN and HYB simulations, the largest variance is clearly present in the AF_{Atk} relative to other size modes (see Table 5.1).

Different aerosol activations are strongly depending on the CDN schemes (STN and HYB) as discussed above. Appling different approaches of the solute terms in warm cloud formation (i.e., the osmotic model and κ-Köhler method) seem to be important to droplet nucleation. As discussed in Rose et al. (2008), even if aerosol composition is relatively simple and well known, discrepancies in the computed solute effect of aerosols could be substantial; these discrepancies could then influence overall simulated cloud properties by inducing different cloud droplet number concentrations. Pöschl et al. (2009) reported that the model results could be affected by as much as 20 %, depending on the parameterization of the hygroscopicity of aerosols despite the fact that the aerosol chemical composition is assumed to have smaller effects than other variables (e.g., the number and size distribution of particles, transport processes, and the atmospheric ambient conditions) on large-scale cloud formation. Particularly for low water-vapor supersaturations, low aerosol concentrations, and organic components, and

the inclusion of specific description of physicochemical aerosol appear to be significant (McFiggans et al., 2006; Rose et al., 2007, 2010; and Kreidenweis et al., 2009).

When particle numbers are considered, the Aitken mode is substantial for the droplet nucleation. As shown by Table 5.1 ($CCN_{Acc,Cor} << CCN_{Atk}$), the Aitken particles are a major component of the total activated aerosol number concentration (CCN_{total}), even though their CCN efficiencies are lower as compared to those of large particles. Feingold (2003) examined the sensitivities of aerosol properties by using the input variables of size and number concentration for aerosol distribution; and sigma, vertical velocities, and aerosol composition for droplet formation. Feingold's (2003) study reported that the number of particles is the strongest factor affecting droplet activation, both in polluted and clean areas.

To sum, particle size is relatively more sensitive to aerosol activation than to particle composition. Considering the number distribution, Aitken particles constitute the majority of CCN_{total}. Aitken particles are most sensitive to chemical composition (i.e., Solute effect or Raoult effect) in aerosol activation. Aerosol composition effects therefore contribute significantly to warm cloud formation. The overall sensitivities of aerosol activation are strongly dependent on regional location (vertical and horizontal distribution), as aerosol size, number, and composition vary spatiotemporally. This will be discussed more in Section 5.2.

5.2 Vertical profiles of global means

ST-STN and ST-HYB simulate different activated aerosol fractions (AF) by altitude, over both land and ocean (see Fig. 5.1). The activated fractions in the two RH simulations, RH-STN and RH-HYB, are similar to those in the ST simulations (see Appendix). This is because the calculation of the aerosol activated fraction is largely controlled by the CDN schemes, as discussed in the previous chapters. The vertical distributions of the total activated fraction AF are composed of the sum of the activated fractions of the Aitken, accumulation and coarse mode (i.e., $AF_{Atk,Acc,Cor}$). Each AF_i ranges from 0 to 1; when all aerosols are activated in mode (i), the AF_i approaches the maximum value of 1. At each vertical model level, the accumulated AF_i for all three modes ranges from 0 to 3. Since mutual aerosol-cloud interactions are closely related to the atmospheric structure, the simulated tropopause and planetary boundary layer (PBL) are presented in the diagrams.

In Figs. 5.1a and b, the vertical distribution of the total activated fraction creates an L-shape for ST-STN and a C-shape for ST-HYB. For ST-STN, most particles are activated within the PBL, with decreases of 50 % in the $AF_{Acc,Cor}$ and more extreme

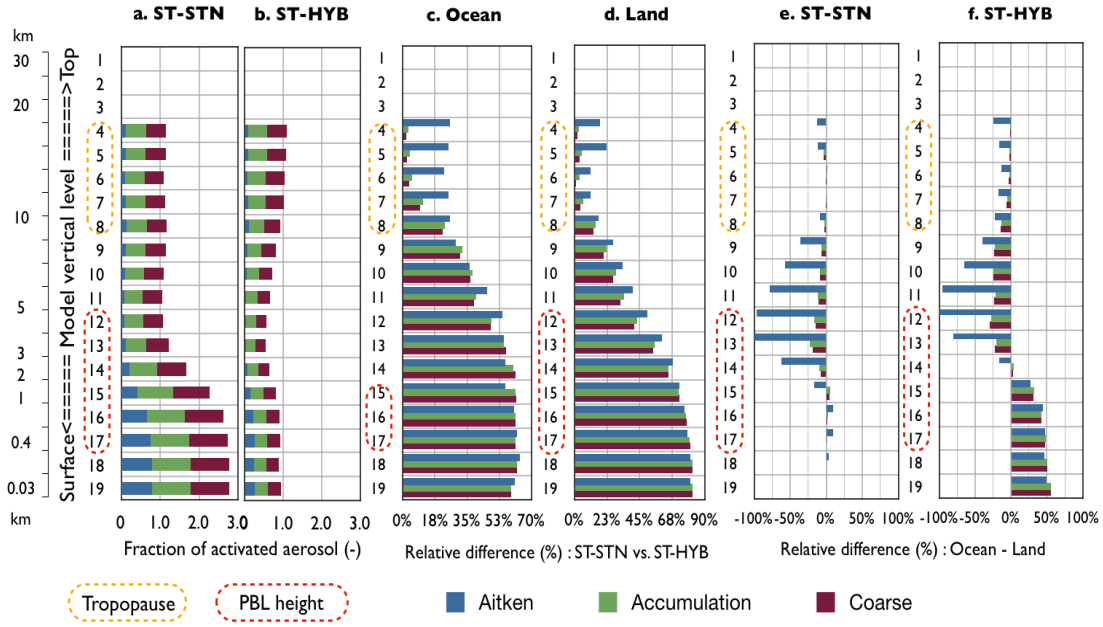

Figure 5.1: Vertical distributions of CCN activation in ST-STN and ST-HYB.

decreases in the AF_{Atk} above the PBL. For ST-HYB the activated fractions are smaller at low altitudes and vertical variance is less strong than for ST-STN. These differences illustrate how aerosol activation is directly influenced by the planetary surface, since ambient aerosols sensitively respond to changes in surface physical quantities, such as velocity and temperature, and thereby changes in saturation vapor pressure of aerosols. The vertical distribution of the activated aerosol fraction is also influenced by the vertically distributed values (i.e., total available aerosol size and number concentrations, and aerosol composition), which can be altered via chemical processing and large-scale meteorology (Morgan et al., 2009).

Figs. 5.1c and d compare the AF_i in ST-STN and ST-HYB separately for ocean and continent. Generally, ST-STN simulates a stronger vertical gradient in the total activated aerosol fraction from the surface to the free troposphere, for both continental and marine cases. This stronger gradient is even more pronounced over land, particularly at low altitudes, with a distinct vertical gradient of 50 – 70 % in the PBL and 25 – 50 % in the free troposphere (up to the tropopause). These differences diminish in the tropopause region, except for the Aitken mode particles, for which a difference of 10 – 25 % remains. Relative differences between ST-STN and ST-HYB over ocean are about 50 % at low altitudes; these difference decline towards the tropopause, with a slightly higher activation of Aitken mode in the tropopause like the continental cases.

The overall differences between ST-STN and ST-HYB initially result from different representations of the chemical composition effect, as well as also from changes in the vertical distribution of hygroscopicity due to chemical processes. This is in line with Pringle et al. (2010b) that the horizontal distribution of κ is strongly related to freshly emitted aerosols, and that the vertical distribution of κ gets higher with altitude due to chemical processes.

Figs. 5.1e and f show contrasting patterns of aerosol activation over land and ocean for each ST-STN and ST-HYB simulation. The relative difference is calculated at each vertical model level ($\frac{[ocean-land]}{ocean} \times 100$ %). The positive and negative signals represent the relative strength of aerosol activation over ocean and land, respectively. The Aitken particles show strong activity (AF_{Atk}) over land and at high altitudes in both of the CDN schemes. For the larger particle size modes (i.e., accumulation and coarse mode), some land-sea gradients ($\approx$ 10 % STN, $\approx$ 25 % HYB) are also indicated at high altitudes; however, these gradients are not distinct as in the Aitken mode.

At low altitudes aerosol chemical composition is closely related to freshly emitted particles. The aerosols in marine regions contain more high hygroscopic particles than does the air in continental regions (Andreae and Rosenfeld, 2008; Pringle et al., 2010b; and Wex et al., 2010). This distinct composition creates different cloud droplet formation behavior in ST-HYB and ST-STN. In ST-STN, the continental activated fraction is not much different from the marine activated fraction (as evidenced by the L-shaped curve for the global scale in Fig. 5.1a, which is similar to the curve for selected continental regions in Fig. 5.6). This small difference might be due to the fact that the STN might be less sensitive to aerosol composition, or that continental aerosol activity is about as high as the marine aerosol activity when calculating aerosol activation (except for the Aitken mode particles). In contrast to this low difference between land and ocean for ST-STN, the activated aerosol fractions (AF) over ocean show about 50 % higher for ST-HYB than the continental mean for all aerosol size modes. The HYB scheme calculates the total activated aerosol fraction for global and marine mean values as a C-shape (Fig. 5.1b). This vertical activity pattern is affected by aerosol compositions, with diverse funnel- and D-shapes for selected continental regions (see Fig. 5.6).

Note that these distinct activated fraction patterns (AF) are based on the relative values, which means that even though the marine and continental activated aerosol fractions (AF) are comparable, total activated aerosols can be very different due to differences between the available aerosol number concentration over land and ocean.

The total activated aerosols also could be influenced by the vertical aerosol size and number distribution; in general, larger particles in accumulation and coarse mode tend to be located at or near the surface and decrease with height; the Aitken particles are relatively more abundant than other particles in all altitudes, as evidenced by the fact that the proportion of Aitken particles in the total aerosol number concentration is more than 60 %, and this fraction increases with altitude for both land and ocean.

In summary, particle size dominates chemical composition in droplet formation (CCN activation); however, near the surface (for low clouds) other variables (e.g., aerosol distribution, composition, and vertical velocity) have substantial effects. Overall, these effects are reflected in spatiotemporal variation in atmospheric conditions (dynamics and chemical reactions; Figs 5.5 and F.10). The number of small particles in the Aitken mode seem to play a substantial role in droplet formation; at the same time, Aitken particles are the most sensitive particle to aerosol composition in aerosol activation. In droplet formation, both size and composition are very important factors in representing overall aerosol-cloud interactions.

5.3 Global distributions

The overall variation in CCN activation between the HYB and STN simulations is a major contributor to the distinct distributions of CCN and CDNC, which affects substantially low clouds. Both simulations show the effect of continental outflows with different magnitudes. Strong outflows contain continental aerosol emissions, and lead to distinctly higher CCN (aerosol activation) over oceans. This effect is more pronounced in the STN simulations than in the HYB simulations due to CCN abundance (see Figs F.11c and d; Figs. F.12c and d; and Fig. 5.4).

The maxima of the total activated aerosol (CCN) number concentration generally matches strong anthropogenic aerosol emission areas, i.e., northern America and east Asia in the northern hemisphere (NH) for all simulations, as shown by the vertically integrated CCN from the surface to 10km (Fig. 5.2). The magnitudes of the maxima are strongly dependent on the CDN scheme. At the tropics the STN simulations show relatively high CCN number concentrations as compared to the HYB simulations. These differences are founded over Central Africa and the Amazon forest in Brazil where organic aerosol compounds are expected as well as biomass burning combustions. Both of these areas are relevant to the regional analysis of CR2 and CR5 (more detailed discussion can be found in Section 5.4). These different CCN number concentrations may be associated with the distinct behavior of Aitken particles in cloud droplet formation (i.e., AF_{Atk}).

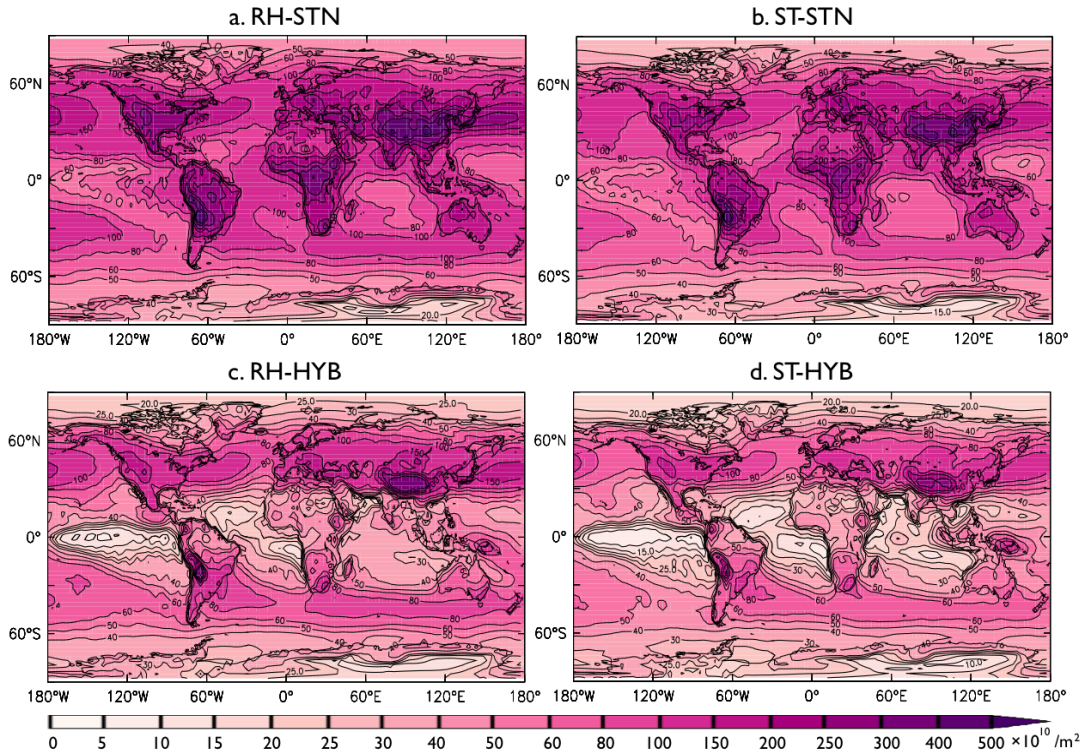

Figure 5.2: Global distributions of the vertically integrated total CCN number concentration (N_{CCN}) from the surface to 10 km for (a) RH-STN, (b) ST-STN, (c) RH-HYB, and (d) ST-HYB.

In general, the STN simulations yield strong CCN efficiency, and thereby high number concentrations of CCN and CDNC (see Figs. 5.2 and 5.3). It has been discussed in the vertical distribution of the AF that the STN simulations simulate more low clouds with higher activated aerosol fractions (see Fig. 5.1). This feature of STN simulations is apparent when one compares the global distributions of vertically integrated CCNs at low altitudes (from the surface to 2 km) to those at high altitudes (from 2 km to the upper troposphere; 10 km) (see Figs. F.11 and F.12). These CCN patterns directly affect cloud properties (e.g., cloud water, cloud optical properties, etc.) and cloud distributions.

Fig. 5.4 shows the differences in simulated clouds for the STN and HYB simulations, by altitude. The simulated clouds are classified into low (1000 - 680 mb cloud top pressure), middle (680 - 440 mb) and high (higher than 440 mb) clouds. This cloud classification is based on the ISCCP simulator (see the Appendix). Low clouds in ST-STN show larger cloud fractions over the continents (i.e., Northeastern America, South America, Central Africa, Europe, and India and China), and coastlines as compared to low clouds in ST-HYB (see Fig. 5.4e). These larger cloud fractions occur because clouds

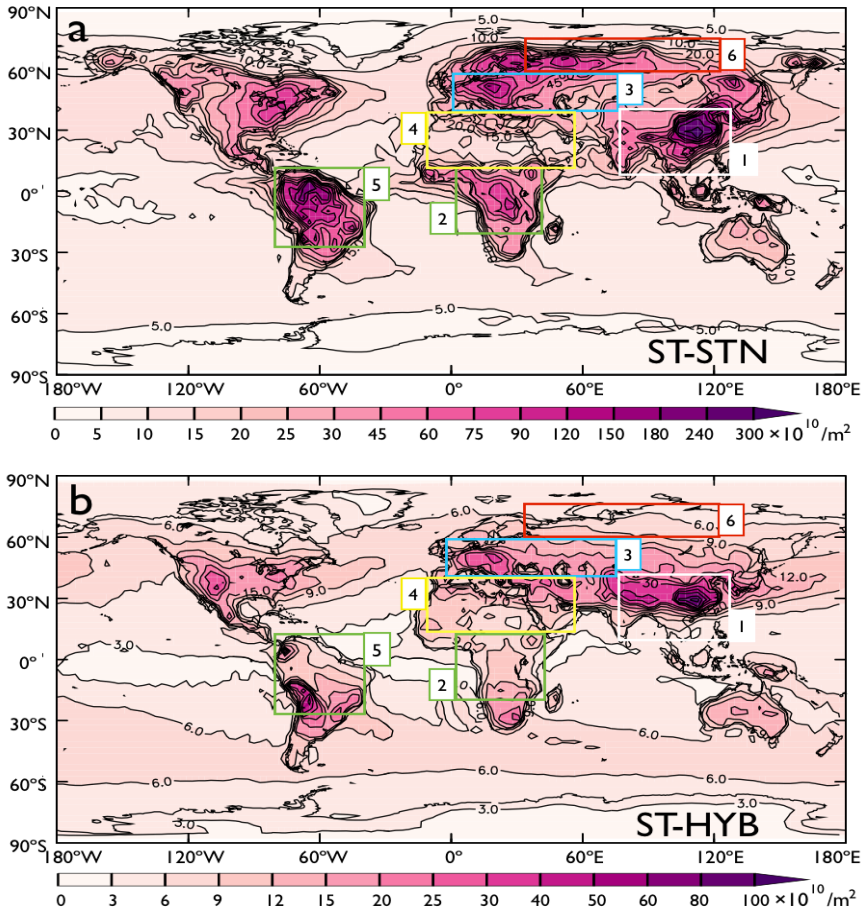

Figure 5.3: Global distributions of the cloud droplet number concentration (CDNC) for (a) ST-STN and (b) ST-HYB, represented by numbered color boxes over the continents. For RH-STN and RH-HYB, see the Appendix.

are rapidly and intensively developed by strong aerosol activations near the surface, and by consuming cloud water with a high CDNC. High CDNC in low clouds with larger amount of cloud water induces strong SCRE, and may reduce convection. This reduced convection results in smaller convective entrainment of water. Overall, all of the processes discussed here distribute relatively small amounts of water for developing high clouds in ST-STN. These effects are reflected in the differences in simulated clouds between ST-STN and ST-HYB (Fig. 5.4); compared to the ST-HYB simulation, smaller fractions of high clouds in ST-STN (in Fig. 5.4a) are likely to correspond to larger fractions of low clouds in ST-STN (in Fig. 5.4b). These distinct patterns are moderated in the RH simulation due to the effects of cloud cover scheme (see the right-hand column in Fig. 5.4). This confirms Tompkins' (2005) previous finding that clouds simulated with RH-CLC are generally less sensitive to local variations.

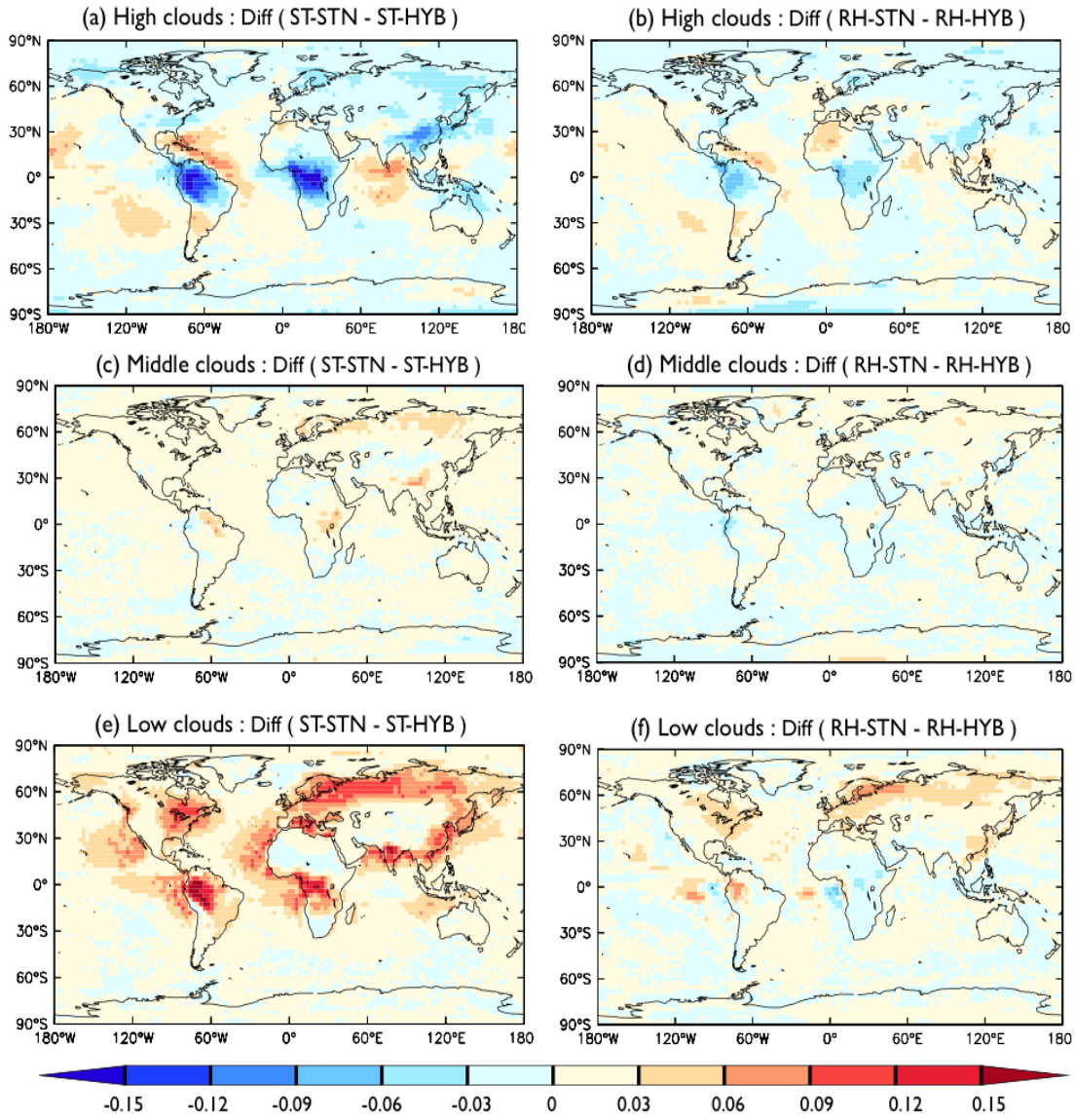

Figure 5.4: Comparison of deviations of estimated cloud covers at low, middle, and high altitudes for a) ST-STN and ST-HYB, b) RH-STN and RH-HYB, c) ST-STN and ST-HYB, d) RH-STN and RH-HYB, e) ST-STN and ST-HYB, and f) RH-STN and RH-HYB.

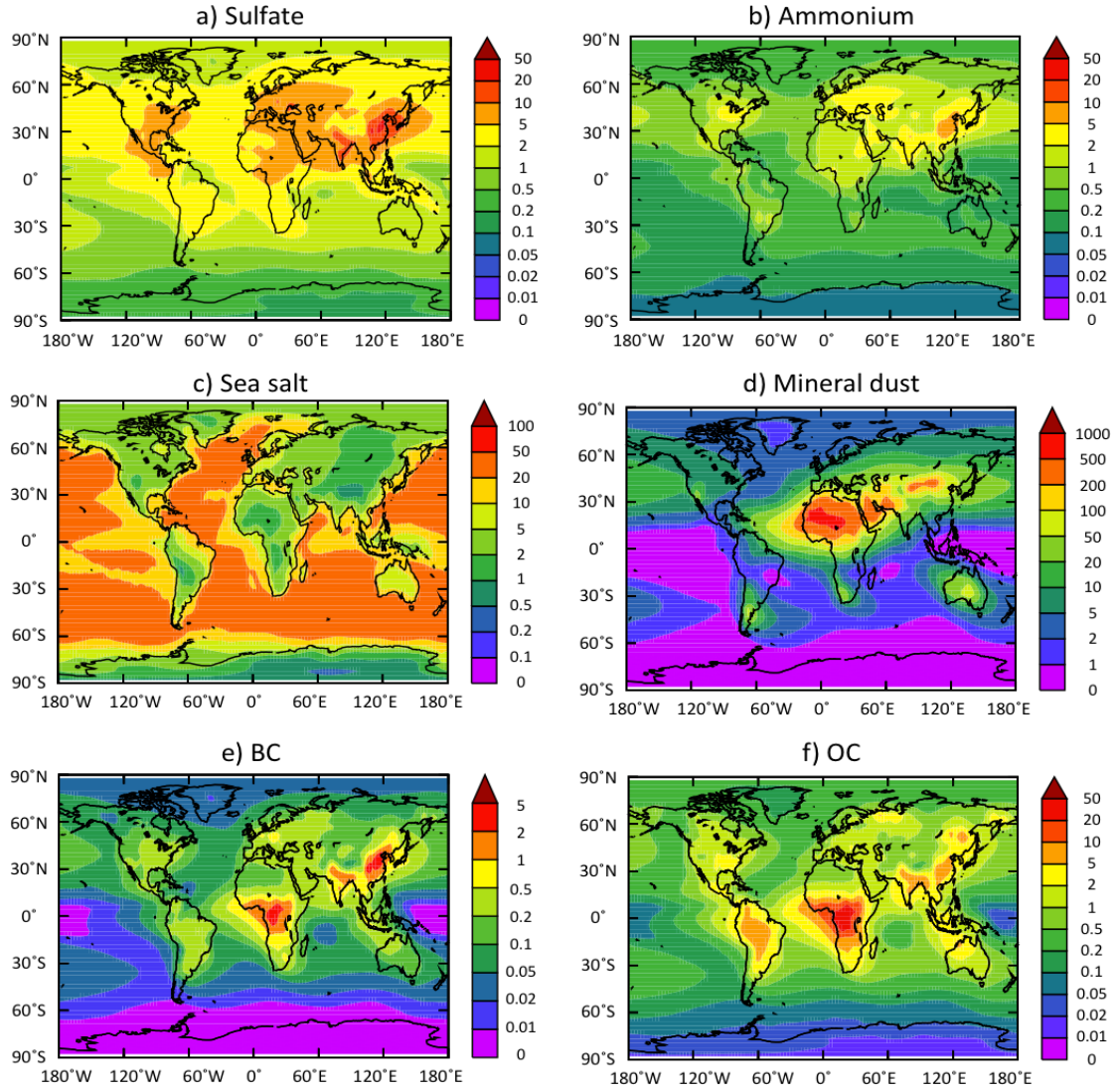

Figure 5.5: Global distributions of the annual mean total aerosol column burden (unit=mg/m^2) for (a) sulfate, (b) ammonium, (c) sea spray, (d) mineral dust, (e) BC, and (f) OC for ST-STN.

Table 5.2: Summary of location and dominant aerosol types in the selected regions over the continents (CRs).

Selected Continental Regions		Location	Dominant aerosol types
CR1	India and China	(80°E :130°E , 10°N : 40°N)	SO_4 (DU, NO_3^-, NH_4^+, OC, BC)
CR2	Central Africa	(0 : 40°E , 20°S : 15 °N)	OC (BC, NO_3, NH_4^+)
CR3	Europe	(0 : 80°E , 40°N : 60°N)	SO_4 (NH_4^+, BC)
CR4	North Africa and Arabian peninsula	(10°W : 60°E , 15°N : 40°N)	DU (SO_4, NH_4^+)
CR5	Brazil (Central South America)	(40°W : 80°W , 30°S : 10°N)	OC (BC, NO_3)
CR6	Sub Arctic and Siberia	(30°E : 120°E , 60°N : 75°N)	SO_4 (NH_4^+, BC)

5.4 Regional distributions

To understand aerosol-cloud feedback in response to different aerosol compositions, six regions over the continents are selected (hereafter, CR); in these six regions, aerosol components are characterized by specific species or air pollution levels (see Fig. 5.3). Selection is based on the global distributions of the annual means of the total aerosol column burden for sulfate, ammonium, sea spray, mineral dust, BC, and OC (see Fig. 5.5 for ST-STN and Fig. F.10 for ST-HYB). The aerosol column burden is similar to the aerosol distribution in Pringle et al. (2010a; see Fig. 6 and Fig. 7 in the paper), in which the aerosol distribution has been evaluated with the observations. The dominant aerosol species and compositions are summarized in Table. 5.2.

The activated aerosol fractions in the selected continental regions show distinct patterns for ST-STN and ST-HYB (Fig. 5.6); generally, the L-shape for the ST-STN simulations is similar to the global mean pattern (Fig. 5.1a; continental and marine mean pattern), with strong activity for all three mode particles at low latitudes, which decreases with altitude. For the ST-HYB simulations, the vertical profiles differ from region to region; most of the continental regions show low activity near the surface and the activated aerosol fractions increase with altitude. These patterns, which take the form of various funnel and D-shapes, are also distinct from the C-shape of the global mean distribution (Fig. 5.1b), as discussed in Section 5.2. For the RH simulations, the activated fraction is similar to the ST simulations (see Fig. F.15). With the vertical distribution of the activated aerosol fractions, the estimated cloud radiative effects at TOA (SCRE, LCRE and NCRE) in Fig. 5.10 are interpreted with the relevant cloud properties of simulated cloud water, cloud ice, and cloud cover, (see Figs. 5.7, 5.8, and 5.9, respectively). The vertical distributions of the activated aerosols, cloud droplet and ice crystal number concentration are also provided to present distinct patterns of CCN activation (see Figs. F.16, F.17, and F.18 in the Appendix).

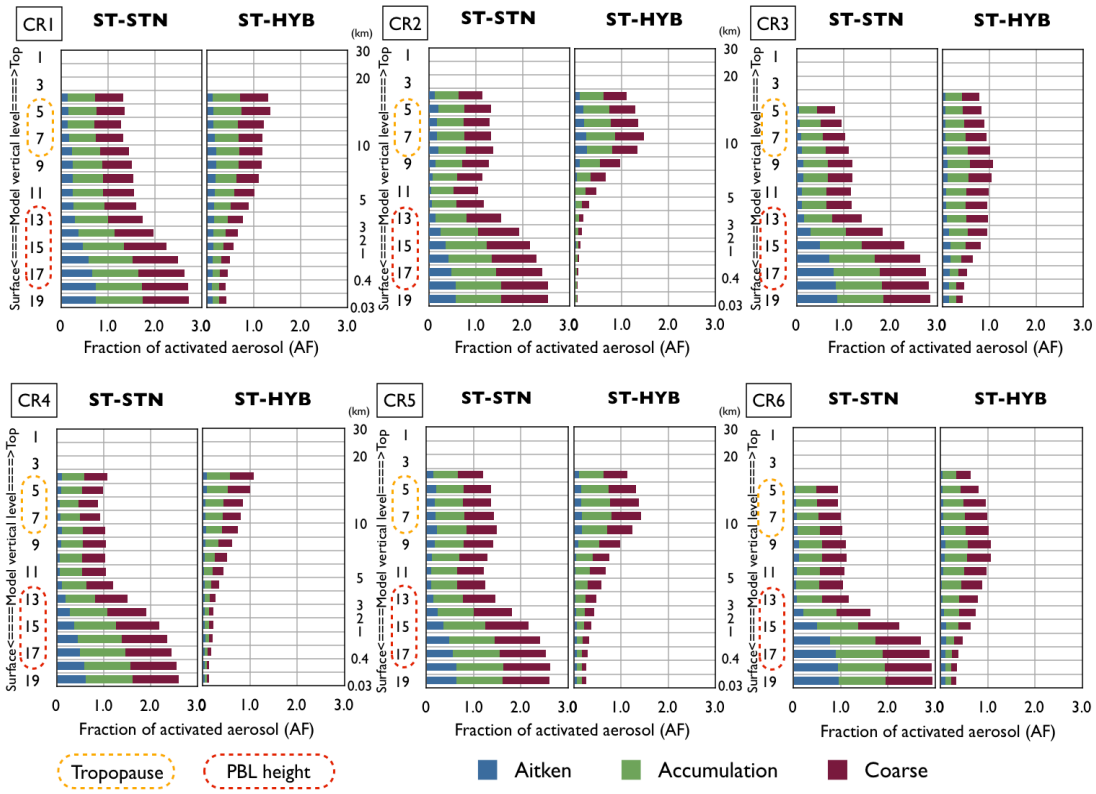

Figure 5.6: Vertical distributions of CCN activation rates for the selected continental regions (CR1 – CR6) for ST-STN and ST-HYB.

5.4.1 Asia (CR1)

The maxima of CCN and CDNC are found over India and China for both the ST-STN and ST-HYB simulations (see Figs F.11, 5.2 and 5.3). India and China both represent high air pollution areas, so they are grouped together into the CR1 region (a white box labeled with the number 1 in Fig. 5.3). In this region, large amounts of anthropogenic aerosols, such as sulfate, nitrate, ammonia, OC and BC (all of which come from growing economies), along with huge amounts of mineral dust (which comes from the desert), are reflected in the simulated aerosol distributions (see Figs. 5.5 and F.10). The fine-mode aerosol particles are also more abundant than in other regions.

As expected from the activated aerosol fraction (see Fig. 5.6a), from the surface to the modeled PBL height, strong CCN efficiencies appear in the STN simulations (ST-STN and RH-STN) together with enhanced cloud cover, and cloud water (Figs. 5.9a and 5.7a). These strong CCN efficiencies enhance cloud optical thickness in low clouds and attribute to strong cloud albedo effects in the STN simulation. In contrast to ST-STN, ST-HYB calculates smaller amounts of low clouds and larger amounts of clouds above the PBL height; these clouds have a higher value of cloud ice water

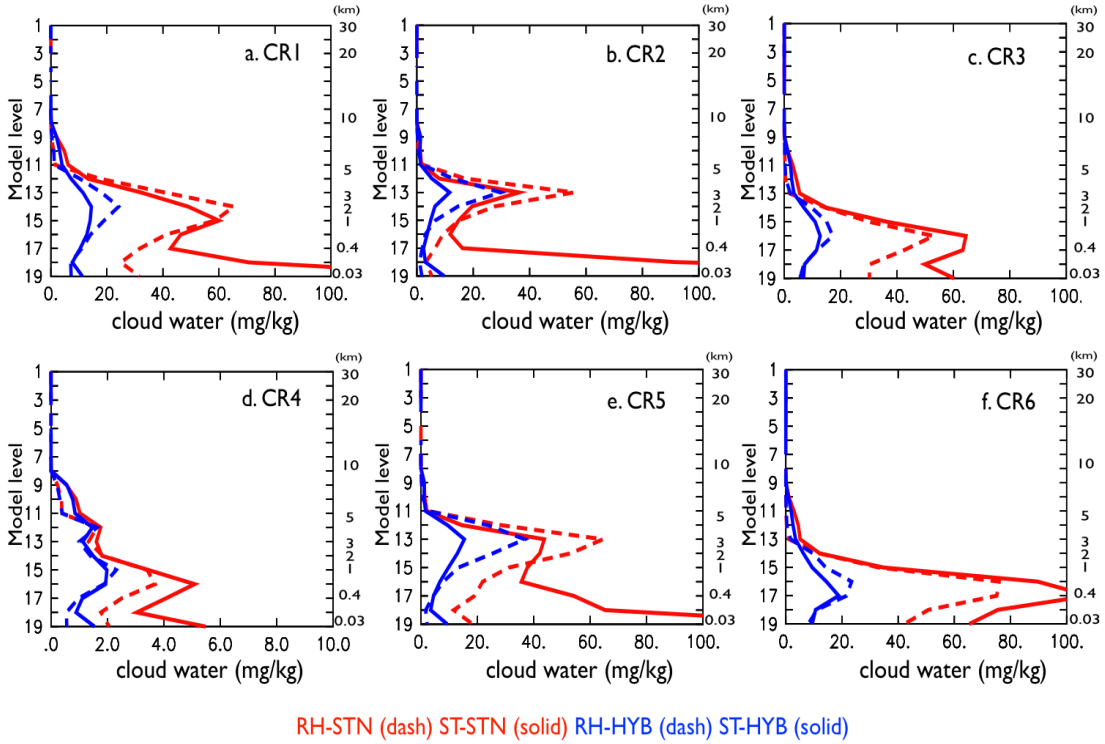

Figure 5.7: Vertical distributions of cloud water in the selected continental regions (CR) for RH-STN, ST-STN, RH-HYB, and ST-HYB.

(Fig. 5.8a). This distinct cloud pattern can be seen in the vertical distribution of cloud cover simulated by the ST-CLC scheme (Fig. 5.9a); an intersection between red and blue solid lines delineates that high clouds in ST-HYB exceed those in ST-STN with a higher value of cloud ice, but this intersection is not shown in the RH simulations (RH-STN and RH-HYB). These distinct patterns of cloud properties depict the sensitivity of cloud cover scheme to the cloud water content as the cloud covers simulated using ST-CLC correspond more sensitively than those simulated by RH-CLC to the distributions of cloud water and ice. In contrast, the RH simulations generally predict larger cloud covers with larger amounts of cloud water than do the ST simulations; the RH simulations also predict much stronger cloud radiative effects (see Fig. 5.10a). The high CDNC in the STN simulations also contributes to strong SCREs, since high CDNC amplifies cloud optical thickness. In Region CR1, the predicted CREs at TOA in the HYB simulations are close to the observations, particularly for the RH-HYB simulation.

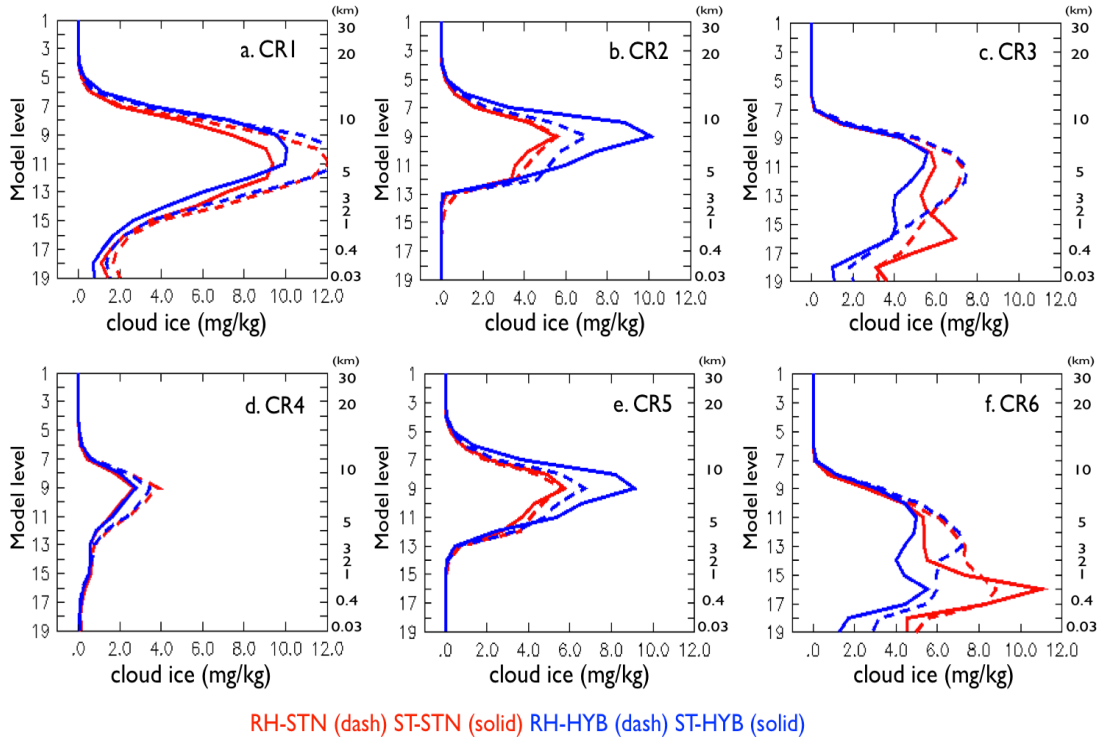

Figure 5.8: Vertical distributions of cloud ice in the selected continental regions (CR) for RH-STN, ST-STN, RH-HYB, and ST-HYB.

5.4.2 Central Africa (CR2) and South America (CR5)

The maxima of OC and BC are found over Central Africa and South America (CR2 and CR5, respectively); these two regions are classified as biomass burning areas (see Figs. 5.5 and A.18). In Central Africa (CR2), fires from both natural ecology and human activity are frequently observed during warm and dry seasons. The emitted aerosols contain soot, nitrates, and organic carbon, all three the results of incomplete combustion during biomass burning (Tyson, 1986; Swap et al., 1996; Eck et al., 2001). Over South America (CR5), aerosol mixtures are largely composed of OC, BC, and ammonia, all of which are produced by biomass burning and deforestation (Davidson and Artaxo, 2004). Both regions show similarity in their vertical distributions of AF, cloud cover, and cloud ice (see Figs. 5.6, 5.9, and 5.8), as well as similarities in their differences in cloud water and relative humidity distributions (see Figs. 5.7 and A.27). Annual surface temperature in these two regions is also similar due to locationally similar latitudes, but relative humidity (RH) shows different patterns (see Fig. A.27). These patterns vary by the annual mean of RH, so Region CR5 shows higher water content than does Region CR2.

In Regions CR2 and CR5 the ST-STN and ST-HYB simulations show contrasting

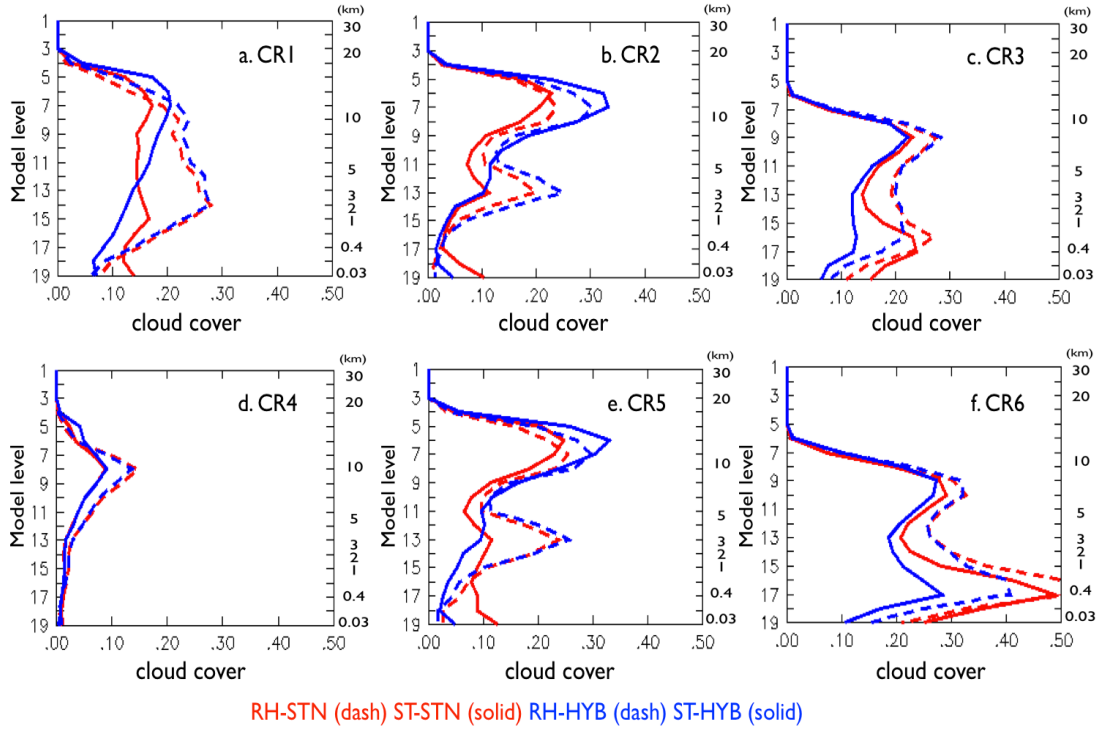

Figure 5.9: Vertical distributions of cloud cover in the selected continental regions (CR) for RH-STN, ST-STN, RH-HYB, and ST-HYB.

patterns of cloud droplet number concentration, as shown by the green boxed areas in Fig. 5.3a and b. The CCN activation in ST-STN is much stronger over the Amazon (in CR5) and Central Africa (CR2), while the ST-HYB simulation shows relatively low CCN efficiency. These different patterns are likely due to the distinct aerosol activities in the CDN scheme, as evidenced by the variations in the hygroscopicity parameters of BC and OC (see Table A.2). Regarding the role of organic components, physicochemical differences play a significant role in the nucleation of droplets, as well as in low water vapor supersaturations and low CCN concentrations (McFiggans et al., 2006; Rose et al., 2007, 2010; and Kreidenweis et al., 2009).

Over South America (CR5), the orographic effects on the aerosol activation are also marked (see Figs. A.19, A.20 and 5.3); over the Andes Mountain area (see Fig. 5.2), all simulations show strong CCN concentrations, with different amplitudes due to the orographically forced updraft velocity. Aerosol activation is determined by the condensation particle rate, which is described using the supersaturations and vertical updrafts. Mountain areas could experience stronger vertical updrafts, which might activate smaller particles (McFiggans et al., 2006). Small particles (i.e., particles with diameters ranging from 40 nm to 140 nm) are particularly activated by strong updrafts

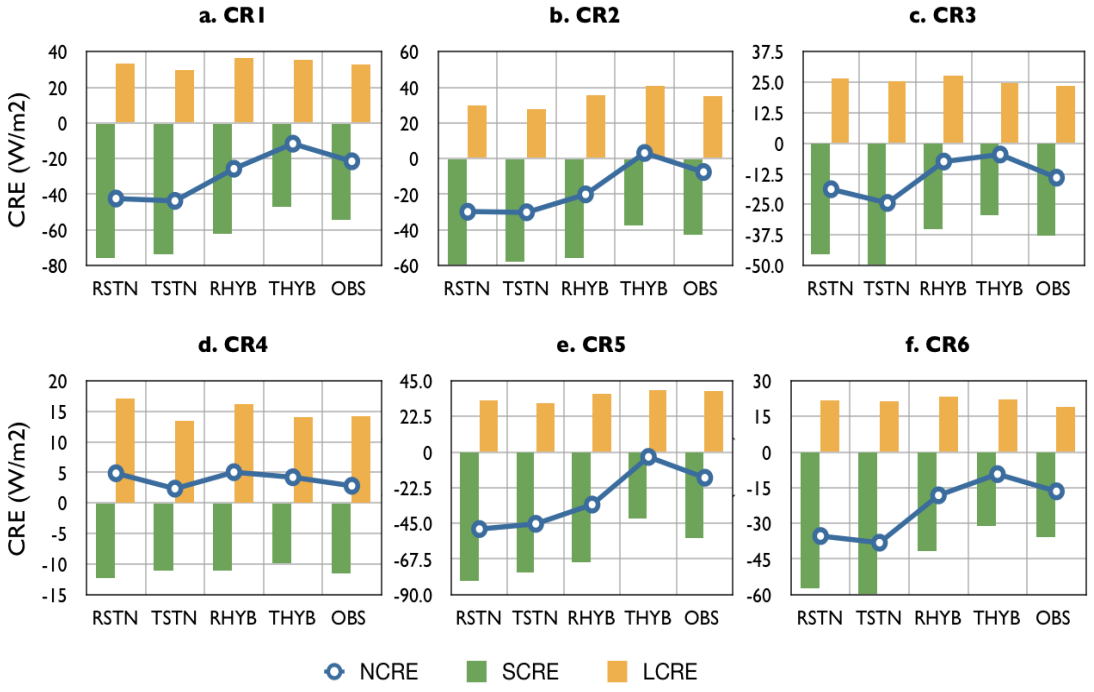

Figure 5.10: Estimated cloud radiative effects in the selected continental regions (CR) for RH-STN (RSTN), ST-STN (TSTN), RH-HYB (RHYB), and ST-HYB (THYB). Green bar, yellow bar, and blue line represent SCRE, LCRE, and NCRE at TOA, respectively.

(see e.g., Hoppel et al., 1996; Leaitch et al., 1996; Flynn et al., 2000; Komppula et al., 2005). These orographic conditions lead to distinct vertical patterns in the accumulated AF, distributions of CDNC, and cloud cover, for both the STN and HYB simulations; both of these simulations also have very similar aerosol distributions.

In Regions CR5 and CR2 aerosol mixtures lead to decrease total aerosol activities with different degrees, particularly near the surface due to the freshly emitted aerosols. Slightly larger amounts of low-hygroscopic particles (BC, OC, DU) and smaller amounts of high hygroscopic particles (SS) appear in region CR2 than in region CR5. These differences strongly impacts cloud radiative effects by changing the cloud vertical structures and optical properties together with the orographical effects (see CREs in Fig. 5.10b and e). The simulations of Region CR5 show relatively larger amounts of clouds, with higher values of cloud droplet number concentration and cloud water than in Region CR2. These differences are substantial for low clouds, intensifying the cloud albedo effect (SCRE) and enhancing the cooling effect for Region CR5 as compared to Region CR2.

Aloft, these low hygroscopic particles could become higher hygroscopic particles via chemical (ageing) processes; these low hygroscopic particles could act as CCNs and INs in the mixed phase and in cold clouds (high clouds). Both regions show two maxima

for simulated cloud cover at the calculated PBL height as low clouds and near the tropopause as high- clouds with different magnitudes (see Fig. 5.9b and e). This is more pronounced in the RH simulations (particularly for low clouds) than in the ST simulations, due to the different cloud water distributions (Fig. 5.7b and e). The HYB simulations predict larger cloud fractions of high clouds, with higher cloud ice content; this results in stronger LCREs than in the STN simulations, since these high clouds exert a greenhouse effect (LCRE) than a cloud albedo effect (SCRE). The integrated NCREs in the STN-simulations show strong cooling effects, as shown by overestimated SCREs and underestimated LCREs. Taking all of these points into consideration, the CREs simulated in ST-HYB are relatively close to the observations.

5.4.3 Western Europe (CR3), and the Sub-Arctic and Siberia (CR6)

A second maximum of sulfate (more than 5 mg/m^2) are found in the simulations over Western Europe (CR3); this maximum also had some nitrates and ammonia (more than 2 mg/m^2) and BC (see Figs. 5.5 for ST-STN and F.10 for ST-HYB). Region CR3 is influenced by marine aerosols (e.g., sea spray) from the Mediterranean Sea and Atlantic Ocean. Aerosol emissions consist of typical anthropogenic aerosols (e.g., ammonium, sulfate and nitrate), since this area is characterized by industry, heavy traffic, and urbanization (Kambezidis and Kaskaoutis, 2008 and Mazzola et al., 2010). In this thesis, Region CR3 represents an area with a medium level of air pollution, with more anthropogenic aerosols more than in Region CR6, but less anthropogenic aerosols than in China and East Asia (CR1).

Over the Sub-Arctic and Siberia (CR6), the aerosol composition is similar to in Region CR3, but number concentrations are smaller. Region CR6 has a relatively lower surface temperature distribution than other regions; this affects droplet activation with increasing water uptake of droplets due to the relatively high RH. This relevance shows in the vertical structure of clouds (Fig. 5.9) which responses to the vertical distribution of RH (Fig. F.19).

Regions CR3 and CR6 show similar L-shaped patterns in the activated aerosol fractions for ST-STN (see Fig. 5.6), but this L-shaped patterns are wider than other regions due to lower surface temperature. These activated patterns depict that most particles are activated at low levels, and above the PBL the fraction decreases exponentially with height. For ST-HYB, the activated aerosol fractions show D-shaped patterns that activated aerosol fraction increases with height until the PBL height, and gradually decreases until the tropopause. Both the ST-STN and ST-HYB simulations demonstrate relatively high activated fraction at low levels than other regions. These aerosol activations allow more clouds to develop close to the surface with large amounts of

cloud water and ice than in other regions.

The vertical distributions of cloud ice and ice crystal number (ICNC) have their maxima at relatively low altitudes: about 5 km (Model level 11) over Europe (CR3) and about 3 km (Model level 13) over the Sub-Arctic and Siberia (CR6; see Figs. 5.8 and F.18). These differences in altitude are likely associated with how temperature and relative humidity are simulated; this influences the condensation process, since particles tend to condense more rapidly with the same amount of cloud water at lower temperatures. This more rapid condensation is due to increased water uptake of droplets, similar to the vertical distributions of the RH (Fig. F.19).

These different vertical distributions of cloud properties affect cloud radiative effects, as a larger cloud fraction of high clouds with higher cloud ice crystal number concentrations enhances the cloud greenhouse effects in Region CR3. In contrast, the larger fraction of low clouds with larger amounts of cloud water and ice, and higher cloud droplet number concentrations, amplify the cloud albedo effects in Region CR6. Overall, Region CR6 has a higher SCRE and smaller LCRE than Region CR3. The STN simulations strongly over-predict the cooling effect (SCRE), while the calculated SCRE in the HYB simulations is reasonably similar to the observed CREs.

5.4.4 North Africa and the Arabian Peninsula (CR4)

High concentrations of mineral dust are found over the Saharan desert and Arabian peninsula in North Africa and the Arabian Peninsula (Derimian et al., 2006; Reeves et al., 2010; Sabbach et al., 2006); North Africa and the Arabian Peninsula constitute Region CR4. Figs. 5.5 and F.10 show high dust concentrations in Region CR4, with an annual mean aerosol column burden of more than 200 mg/m^2. The aerosol column also contains sulfate and ammonium from biomass burning and human activity, such as agriculture.

All simulations predict low CDNC and high clouds in Region CR4 due to the climatologically dry area (small amounts of cloud water) and aerosol composition. The aerosol mixture of mineral dust in CR4 is a principal IN and affects freezing via heterogenous ice nucleation (Richardson et al., 2007). The high clouds in this region are relevant to thin cirrus clouds, which are sensitive to cloud ice and ice crystal number distribution, and which exert a positive net cloud radiative forcing (Chen et al., 2000). The predicted net cloud radiative effects (for CR4) are warming effects in all simulations, with a stronger cloud green house effect (LCRE) than cloud albedo effect (SCRE), see CREs in Fig. 5.10d. The LCREs estimated in the RH simulations tend to be slightly larger than those in the ST simulation due to the larger amounts of cloud ice. In Fig. 5.8d, the RH simulations of CR4 (with the dashed red and blue

lines) show larger values than the ST simulations (with the solid red and blue line). The cloud water and cloud droplet number in the STN simulations are increased with strong aerosol activities at low altitudes; however, the cloud water and cloud droplet number values for CR4 are still much smaller than for other regions (see Figs. 5.7d and F.17d). As a result, the changes in low clouds are not strong enough to significantly change the cloud radiative fluxes, particularly SCRE, since simulated clouds are relatively very small near the surface (see Fig. 5.9d). To sum, the CREs estimated in the ST simulations (ST-STN and ST-HYB) are close to the observations (see Fig. 5.10d).

5.4.5 Regional sensitivity to CCN

To quantify the propagated effect of CCN on cloud properties in the STN and HYB simulations, I calculate a conversion factor (α) with the simple linear function of $[\frac{CDNC_{STN}}{CDNC_{HYB}} = \alpha \times \frac{CCN_{STN}}{CCN_{HYB}}]$ for CDNC, and $[\frac{LWC_{STN}}{LWC_{HYB}} = \alpha \times \frac{CCN_{STN}}{CCN_{HYB}}]$ for LWC. This linear function has been calculated for each model vertical level (ML), from the surface to 5km (i.e., from ML19 to ML11), and for each selected continental region (CR). The α in the equation represents an amplifying coefficient, which transforms changes in CCN to changes in CDNC and LWC (see Figs. 5.11 and 5.12). If $\alpha < 1$ ($\alpha > 1$), the effect of changes in CCN are dampened (amplified) regarding their effects on changes in CDNC and LWC. The α is calculated separately for the ST and RH simulations due to their different sensitivities in responding to changes to both cloud properties and CCN, as shown and discussed in the previous sections.

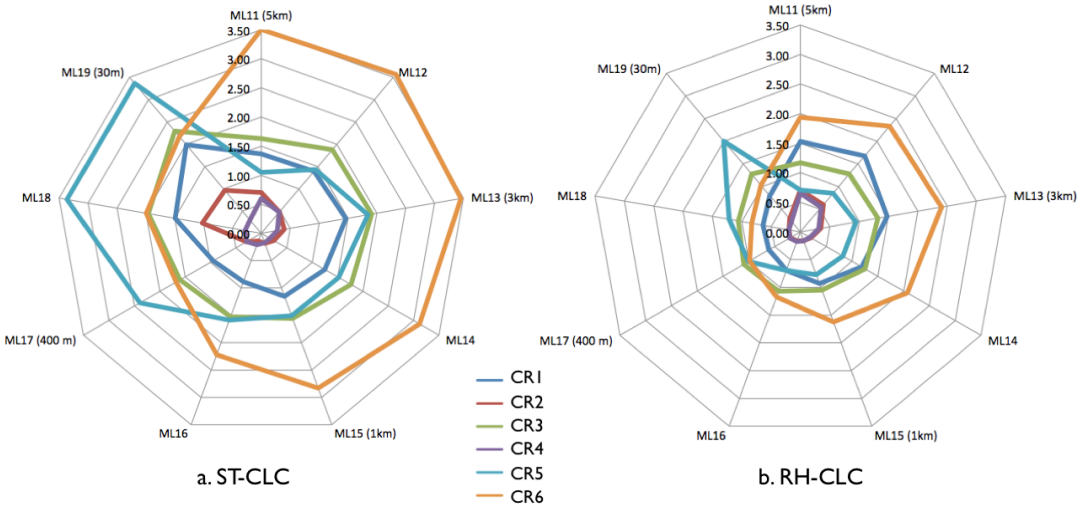

Figure 5.11: Regional sensitivity of CCN to cloud droplet number concentration (CDNC) for STN and HYB by altitude using a conversion factor (α) in $\frac{CDNC_{STN}}{CDNC_{HYB}} = \alpha \times \frac{CCN_{STN}}{CCN_{HYB}}$.

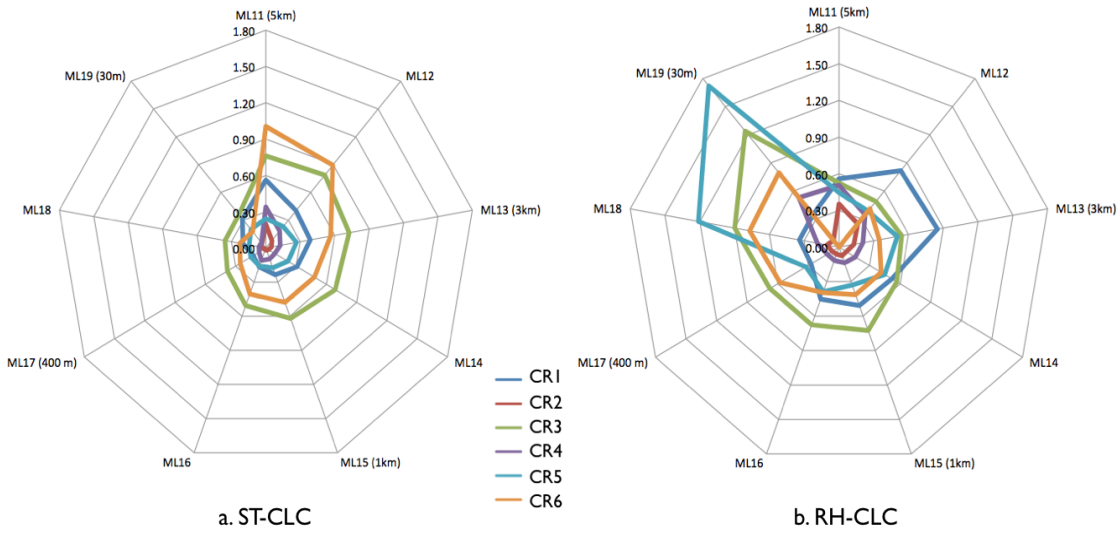

Figure 5.12: Regional sensitivity of CCN to liquid water content (LWC) for STN and HYB by altitude using a conversion factor (α) in $\frac{LWC_{STN}}{LWC_{HYB}} = \alpha \times \frac{CCN_{STN}}{CCN_{HYB}}$.

The effect of CCN on CDNC is not linear, and varies by region and altitude (see Fig. 5.11). If the α is proportional to changes in CCN and CDNC, the α patterns in the diagrams would be a consistent shape and would overlap, with the calculated α of the CRs. This effect of CCN on CDNC could also vary by the simulated variables. Comparing the α patterns in Figs. 5.11 and 5.12, the conversion factors (α) in LWC are generally smaller than in CDNC, with distinct patterns in each region. These distinct patters of α for LWC depict the difficulties of the quantification of climate sensitivity to CCN using a single value.

Sensitivity is heterogeneous with altitude, as shown by the diverse shapes of α, which also relies on the choice of the cloud cover scheme. In the RH simulations, the α for CDNC (see Fig. 5.11) does not exceed 2.5 for all regions and vertical ranges. This could be understood as meaning that the sensitivities in the RH simulations have a more narrow range as compared to the ST simulations. In the tropics (CR2, red; CR4, purple), α is less than 1, which means that increases in CCN have relatively small impacts on changes in CDNC, relative to the other regions. In contrast, the Sub-Arctic region (CR6) show the strongest sensitivities, particularly at from 1km to 5km. As discussed above, the environmental conditions are also an important control factor in aerosol–cloud interactions.

To estimate the regional sensitivity to the cloud radiative effects at TOA in the selected continental regions (CR), the relative differences of the SCRE and LCRE at TOA (see Fig. 5.10) between the STN and HYB simulations are calculated using the

Table 5.3: Relative differences between the STN and HYB simulations of estimated cloud radiative effects in the selected continental regions (CR) for SCRE and LCRE at TOA (corresponding to Fig. 5.10) [Rdiff=$\frac{STN-HYB}{HYB}\times100$ (%)]. Sensitivity of the CLC scheme, defined as the ratio of relative differences [Sensitivity=Rdiff$_{ST}$/Rdiff$_{RH}$].

	SCRE		LCRE		Sensitivity	
	Rdiff$_{RH}$ (%)	Rdiff$_{ST}$ (%)	Rdiff$_{RH}$ (%)	Rdiff$_{ST}$(%)	SCRE	LCRE
CR1	21.6	56.5	-8.9	-15.5	2.6	1.7
CR2	6.8	53.8	-16.7	-32.2	7.9	1.9
CR3	29.3	69.9	-3.8	2.5	2.4	-0.7
CR4	10.5	13.1	6.1	-4.1	1.2	-0.7
CR5	17.1	81.2	-9.8	-21.0	4.8	2.2
CR6	37.6	90.8	-6.2	-2.1	2.4	0.3

equation [Rdiff=$\frac{STN-HYB}{HYB}\times100$ (%)]. Furthermore, the sensitivity of the CLC scheme is measured by the ratio of relative differences [Sensitivity=Rdiff$_{ST}$/Rdiff$_{RH}$]. The relative differences for STN and HYB vary strongly for the variables (SCRE and LCRE), the regions (CR1 – CR6), and the cloud cover schemes (RH-CLC and ST-CLC), as summaried in Table 5.3. In general, these variations are more pronounced in the ST simulations than in the RH simulations, and between the SCRE and LCRE; the difference in simulated SCRE varies much more by CDN scheme than that in simulated LCRE. Regarding regional differences, the strongest changes in SCRE (LCRE) are indicated in CR6 (CR2). Overall, the sensitivity of the cloud cover scheme is most pronounced in CR2 for SCRE and in CR5 for LCRE, as can be seen in a concise sensitivity index for SCRE and LCRE, which ranges from 2.4 – 7.9 for SCRE (except for in CR4) and which is about 2 for LCRE in Region CR5, CR2, and CR1.

To sum, the sensitive response to aerosol activation is influenced by spatiotemporal aerosol composition, as well as by particle size and number distribution under the different meteorological and orographical conditions. This influence is evident in the regionally and vertically distinct patterns of the aerosol activation, cloud properties, and radiative effects. The aerosol-cloud interactions are not simple linear relationships that change in response to aerosol activation and CDNC; rather, these interactions vary by region. These changes influence atmospheric fluxes of energy and mass, by altering vertical motions (dynamics). The influence of these changes is also found in changes in convection and its feedbacks; this will be discussed further in Section 6.4.

5.5 Conclusion

The spatial-temporal aerosol properties of particle size, number and composition affect clouds and climate, with distinct CCN activation under the regional meteorological and geographical conditions. Through a sensitive analysis of droplet activation, both the STN and HYB simulations present not only particle size matters (i.e., higher activity (AF) in larger particles), but also that aerosol chemistry is strongly sensitivity to the size of particles, especially for the Aitken mode. Concerning the number concentration of particles, Aitken particles are a major component of the total aerosol and CCN number concentration; their activation therefore strongly contributes to the cloud droplet formation. At low altitudes, for freshly emitted particles, the chemical composition is likely to be important for the hygroscopic growth of droplets. This distinct aerosol activation in low clouds strongly influences overall cloud properties, and substantially influences cloud radiative effects.

To sum, sensitive simulations of the responses to aerosol activation indicate regionally varying effects on clouds and climate, with findings strongly influenced by the choice of cloud droplet nucleation scheme (STN or HYB). The magnitudes of the effect of aerosol activation are influenced by the cloud cover schemes used (RH-CLC or ST-CLC). Further analysis of the effects of the CLC schemes can be found in Chapter 7.

Chapter 6

Aerosol-cloud feedback effects

In the EMAC model, the prognostic CDN schemes of STN and HYB are designed to represent aerosol feedback effects (i.e., aerosol indirect effect; AIE) on clouds. The different CCN efficiencies in the STN and HYB simulations are discussed in Chapter 5 and the simulations are evaluated with the observations in Chapter 4. In Chapter6, the STN and HYB simulations are compared with the REF simulations in order to investigate the effects (e.g., changes in CDNC, CREs, and precipitation) of aerosol-cloud interactions on clouds and climate. Note that the REF simulations do not make use of aerosol-cloud feedbacks such as a prognostic cloud droplet nucleation process, as is used in the STN and HYB simulations; rather, the REF simulations use a prescribed cloud droplet number concentration based on a single moment cloud microphysics, see the Appendix for more information.

6.1 Annual global mean

Table 6.1 compares differences in the changes in the annual global means of cloud properties, water budgets, TCC, and CREs for the REF simulations versus the STN and HYB simulations. These changes depict the effects of aerosol-cloud feedbacks on cloud properties and on climate relevant parameters. In general, the most substantial changes are found for cloud droplet number concentration (N_d), cloud water content (LWP), and cloud radiative effects (NCRE, SCRE); the rest of the simulated parameters are less sensitive to changes in aerosol-cloud coupling.

CCN activation results in aerosol-cloud feedbacks and contributes to substantial changes in N_d. This occurs because activated aerosols (CCN) are a major source of total cloud droplet number concentration as discussed in Chapter 4. Enhanced N_d is more pronounced in the STN simulations than in HYB simulations, as the aerosol activation algorithms (osmotic coefficient model) used for STN had stronger aerosol

Table 6.1: Global mean changes in cloud properties, hydrological cycle, cloud radiative effects at TOA (CREs), and aerosol optical depth (AOD) after including aerosol feedback effects.

CDN effect of	RH-simulations				ST-simulations			
	STN (ARG)		HYB (ARG-κ)		STN (ARG)		HYB (ARG-κ)	
	Dev.	RDiff.	Dev.	RDiff.	Dev.	RDiff.	Dev.	RDiff.
ΔLWP (g/m^2)	48.9	110.4 %	16.9	38.1 %	50.5	202.8 %	13.2	53.0 %
ΔIWP (g/m^2)	0.9	3.1 %	0.4	1.4 %	2.3	11.0 %	1.3	6.2 %
$\Delta N_d(10^{10}/m^2)$	7.2	331.7 %	2.12	97.2 %	8.0	465.7 %	1.7	99.4 %
ΔN_i ($10^{10}/m^2$)	0.01	2.5 %	0	0.0 %	0.02	5.3 %	0.01	2.6 %
ΔWVM (kg/m^2)	-0.5	-1.9 %	-0.1	-0.4%	-0.8	-3.1 %	0	0.0 %
ΔTCC (%)	1	1.5 %	0.3	0.4 %	6.6	11.9 %	1.8	3.2 %
ΔP_{total} (mm/day)	-0.05	-1.7 %	-0.01	-0.3 %	-0.02	-0.7 %	0	0.0 %
ΔSCRE (W/m^2)	-11.3	20.0 %	-3.7	6.5 %	-18.5	55.1 %	-5.3	15.8 %
ΔLCRE (W/m^2)	0.2	0.7 %	0.1	0.4 %	1.2	4.9 %	0.4	1.6 %
ΔNCRE (W/m^2)	-11.1	39.5 %	-3.6	12.8 %	-17.3	186.0 %	-4.9	52.7 %
Δ AOD	0.03	15.0 %	0.01	5.0 %	0.03	15.8 %	0.0	0.0 %

activity than the κ-method (which is used for HYB). These changes strongly influence relevant cloud properties and climate relevant parameters.

Changes in the liquid water path correspond to substantial changes in N_d since the distribution of LWP is tightly linked with cloud droplet properties, and is positively correlated with cloud droplet number concentration, which also relates to the precipitation formation efficiency. The strongest changes therefore appear in the STN simulations, and changes are more notable when the ST-CLC scheme is coupled (i.e., ST-STN). This different changes can be explained by the effects of cloud cover schemes. The choice of cloud cover scheme is likely to amplify or attenuate aerosol-cloud coupling effects, as cloud cover scheme impacts both cloud water and cloud distribution. However, when CDNC is very high (as is the case in the STN simulations) the effects of cloud cover scheme are somewhat moderated. In general, cloud properties in the ST simulations are more sensitive to local changes in activated aerosols and cloud water than they are in the RH simulations. This difference in sensitivity is demonstrated through sensitive simulations and comparisons in Chapter 4 and 5. This difference in sensitivity can also be found in the variations of ΔLWP. The enhanced cloud droplet number concentrations (ΔN_d) are similar in both the RH and ST simulations, (ΔN_d for RH-HYB = 97 %; ΔN_d for ST-HYB = 99 %). However, the increases in liquid water path varied more between the different CLC schemes (ΔLWP for RH-HYB = 38 %; ΔLWP for ST-HYB = 53 %).

Variations in the ice crystal number concentration (ICNC) and ice water path (IWP)

are also associated with enhanced CDNC and cloud microphysics, but did not change as much as did CDNC and LWP. The ice nuclei (IN) process is more complex than CCN processes in warm clouds. Cloud droplets can become ice crystals by homogeneous or heterogenous freezing processes (contact and immersion). In the both freezing processes, temperature is an important factor in determining the freezing rate of cloud droplet, which means that cloud droplets are need to be located at freezing level or be exposed to low temperatures. The degree of the cloud vertical development is therefore an important condition to approach freezing levels, and is related to convection, vertical atmosphere structure, and vertical motion.

Variations in total water vapor mass (WVM) are insignificant in the present study, since WVM is related to the climatological water budget, rather than to aerosol-cloud feedback or cloud cover coupling. Changes in the global annual mean of total precipitation (P_{total}) also do not vary substantially between the simulations. One reason for this lack of variation is that total precipitation is largely controlled by oceanic evaporation, and all the simulations are used a prescribed SST and SIC. While aerosol-cloud feedbacks (CDN effects) have some effect on large-scale cloud and on stratiform precipitation over ocean and land, this effect is not strong enough to overcome constrained changes over the ocean. A more detailed analysis of precipitation are found in Section 6.5.

Changes in the annual global mean of TCC depend sternly on their coupling with different cloud cover schemes. In the RH simulations, changes in TCC are not noticeable; this is, in part, due to the robust performance of the RH-CLC scheme, which is less sensitive to local variances as discussed in Chapter 4. The ST simulations do show variations in TCC in response to aerosol-cloud interactions, but these variations are relatively small as compared to changes in CDNC. For example, ST-STN simulates a TCC that is 11.9 % larger than that produced by ST-REF; in comparison, ST-REF simulates a CDNC that is more than 5 times higher.

Overall, these changes in cloud properties significantly affect cloud radiative fluxes (see Table 6.1). Compared to the REF simulations, the STN simulations give SCRE values that are about 55 % (in ST-STN) and 20 % (in RH-STN) higher, with strong enhancements in CDNC. Compared to the REF simulations, the HYB-simulations estimate SCRE to be about 7 % (for RH-HYB) and 16 % (for ST-HYB) higher, with a CDNC that is about twice as high. The LCRE is also enhanced by aerosol coupling, but its magnitude is relatively small compared to SCRE, which only moderates enhanced SCRE.

6.2 Zonal distribution

Aerosol-cloud interactions are generally recognized as the elevated cloud droplet number concentration in zonal distributions of changes in CDNC (N_d). Marked increases in CDNC are found at middle latitudes (from 30 °N to 60 °N) in the Northern Hemisphere (NH) for both the STN and HYB simulations, as are increases in LWP and TCC (see Fig. 6.1). Similarly, the zonal distributions of ICNC and IWP vary greatly in the NH. This variation in zonal mean distributions is likely due to the greater amounts of emissions from the NH, which has a much larger fraction of land-covered surface than does the Southern Hemisphere (SH). In the SH, changes in the cloud liquid and ice water budget (LWP and IWP) are more sensitive to small changes in CDNC, since the SH is generally a cleaner area, with lower CCN concentrations (Koch et al., 2011).

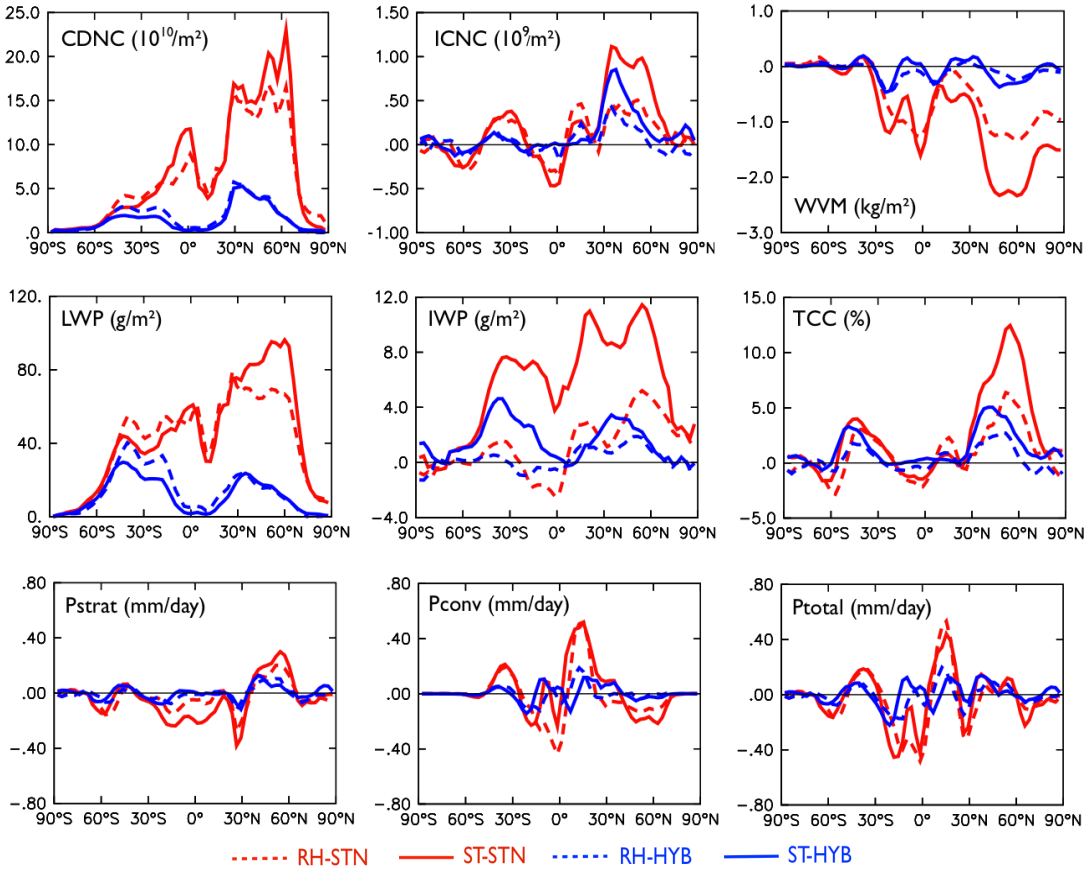

Figure 6.1: Zonal means distribution of changes after including aerosol-cloud feedbacks in the cloud droplet number concentration (CDNC; unit = $10^{10}m^{-2}$); ice crystal number concentration (ICNC; unit = $10^{9}m^{-2}$); water vapor mass (WVM; unit =kg/m^2); stratiform, convective, and total precipitation (P_{strat}, P_{conv}, and P_{total}; unit = mm/day); total cloud cover (TCC; unit = %); and liquid and ice water path (LWP, IWP; unit =g/m^2).

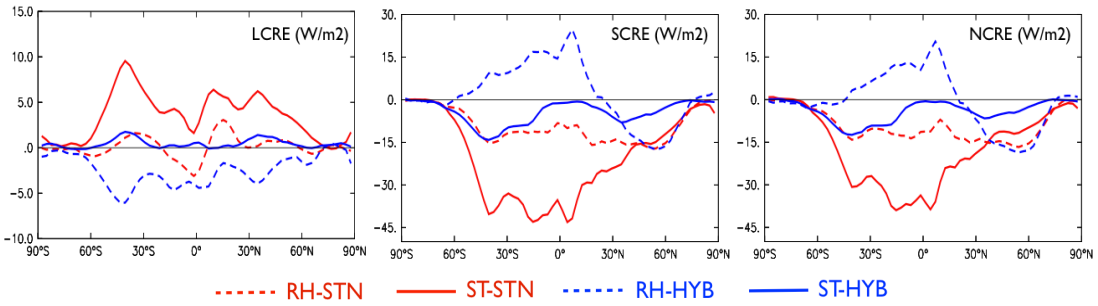

Figure 6.2: Zonal mean distributions of the variances induced in the cloud radiative effect (ΔLCRE, ΔSCRE, and ΔNCRE; unit = W/m^2]) by including aerosol-cloud feedbacks.

The strongest increases in CDNC are generally accompanied by a larger fraction of TCC, as well as by substantial increases in LWP and IWP. In the STN simulations, the second maximum of CDNC is found in the tropics, which contradicts to the zonal distribution of CDNC in the HYB simulations. This difference stems from the different CCN efficiencies in Central Africa and Northern South America (see Chapter 5). High CCN concentrations in clouds could delay warm rain formations as smaller droplets and non-precipitable clouds develop vertically. This delayed rain formation allows more cloud droplets to reach supercooled levels, thereby increasing ICNC. This enhanced ICNC can be diminished by changes in convection. Overall, these changes enhance cloud optical properties, and intensify cloud albedo effects, and cool the Earth's surface. This process is sufficient to compensate invigorated convection processes of phase changes, and decreases the strength and frequency of convection by changing in atmospheric energy fluxes, particularly in the STN simulations. This will be discussed more in Section 6.4. Increases in ICNC are mostly relevant for high (cirrus) clouds, which are estimated to have a warming effect; however, this effect is relatively small compared to the cooling effects of low clouds, and hence has only moderate cooling effects.

Changes in convective activity also affect associated precipitation, as shown by decreases in convective precipitation, which correspond to increases in stratiform precipitation. The detrainment of convective water is used for the large-scale cloud water, which is relevant to the hydrologic cycle in the modeling system. However these changes differ over land and over ocean, and it is therefore difficult to understand the effects of aerosol-cloud interactions on precipitation based on the zonal mean distribution. More detailed discussion will be found in the following sections.

In Fig. 6.2, changes in CREs are highly correlated with the changes in LWP and CDNC demonstrated in Fig. 6.1. Changes in total cloud fraction and mass are also important in determining the cloud radiative effects with their vertical distribution (see Fig. F.2). As discussed in Chapter 4, clouds can exert both cooling and warming

effects (known as the cloud albedo effect and cloud greenhouse effect). Clouds' effects are likely to depend on their altitudes and optical properties: thin high clouds are closely related with LCRE, and low thick clouds are more associated with SCRE.

6.3 Global distributions

The global distributions of differences in the cloud droplet number concentration, total cloud cover, precipitation, net cloud radiation effects and surface temperature when comparing the REF-simulations to the STN and HYB simulations are shown in Figs. 6.3, 6.4, 6.7, 6.5, 6.6, and 6.7, respectively.

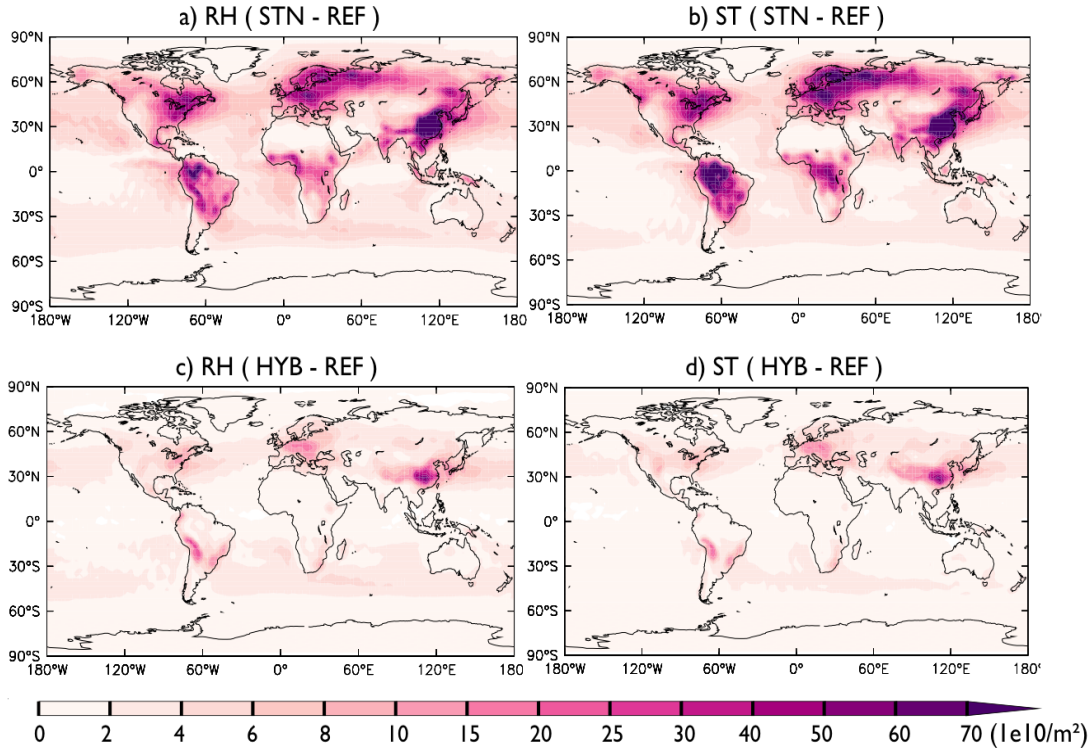

Figure 6.3: Differences in CDNC burden between the STN/HYB simulations and the REF simulations (unit = $10^{10}/m^2$) for a) RH-STN – RH-REF, b) ST-STN – ST-REF, c) RH-HYB – RH-REF, and d) ST-HYB - ST-REF.

The global patterns of enhanced CDNC (the aerosol activation) are strongly relevant to the cloud droplet nucleation algorithms (see Fig. 6.3). Compared to the REF simulations, the STN simulations predict considerably higher CDNC over North and South America, Europe, Central Africa and Asia. In the HYB simulations, enhanced CDNC is also found over these same regions, but the number concentration is much smaller than in the STN simulations. These patterns are similar to the RH and ST

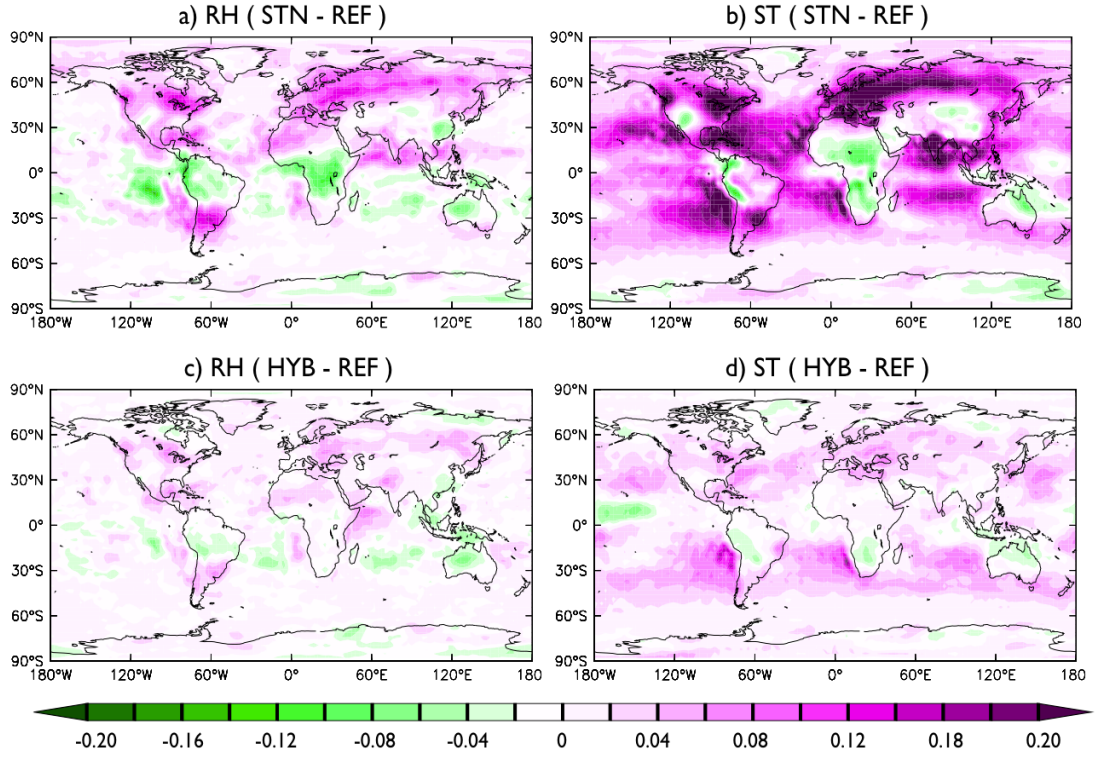

Figure 6.4: Differences in total cloud cover (TCC) between the STN/HYB simulations and the REF simulations (unit = -) for a) RH-STN – RH-REF, b) ST-STN – ST-REF, c) RH-HYB – RH-REF, and d) ST-HYB – ST-REF.

simulations, but the magnitudes are slightly different depending on the CLC schemes.

Increased total cloud fractions correspond to increases in CDNC (see Fig. 6.4). In contrast to changes in CDNC, the simulated TCCs are dependent on the cloud cover schemes. Comparing the distinct patterns of changes in the simulated TCC using ST-CLC and RH-CLC, the ST simulations (the left-hand column of Fig. 6.4b and d) show more noticeable changes for a similar change in CDNC than do the RH simulations (Fig. 6.4a and c). This different sensitivity again confirms that the ST-CLC scheme seems to be tightly connected with local changes in cloud properties (Tompkins, 2005; Lohmann et al., 2007; and Hoose et al., 2008). In general, aerosol coupling induces higher cloud fractions over all ocean and continental regions. Particularly over land, increases in TCC show regionally dependent patterns in response to CCN efficiency. This only exception to these regionally dependent patterns is Central Africa (as discussed in Chapter 5), as due to the arid areas of this region, the simulated TCC in the STN simulations is not positively correlated with enhanced CDNC.

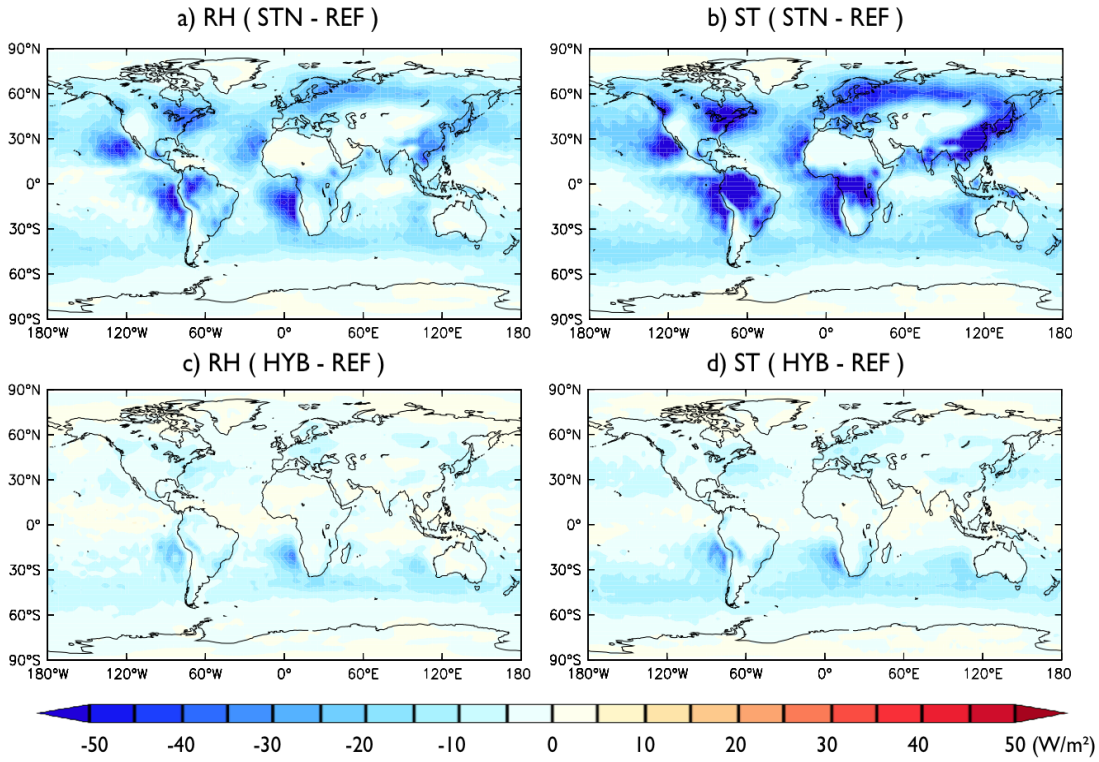

Figure 6.5: Deviations of net cloud radiative effect (NCRE) at the top of the atmosphere (unit = W/m^2) between the STN/HYB simulations and the REF simulations for a) RH-STN – RH-REF, b) ST-STN – ST-REF, c) RH-HYB – RH-REF, and d) ST-HYB – ST-REF.

These overall changes lead to regionally variable cloud cooling effects (see Fig.6.5). These cooling effects are more pronounced over continents and coastlines influenced by the outflow of aerosol originated from the continents, particularly in the STN-simulations. The high CDNC in areas with high air pollution intensifies cloud albedo effects in both the STN and HYB schemes; this leads to cooling effects of about -5 to -15 W/m^2. Over oceans, this cooling effect is mostly due to increases in LWP, and over land it is due mostly to increases in CDNC, with enhanced LWP. Further comparisons of the simulated CREs and the observations are found in the Appendix (E.1.1).

The changes in NCRE at TOA affect the surface temperature (T_{surf}) on the continents (Fig. 6.6); however, over ocean, the changes in temperature are hardly detectable. This is because the present model uses a climatological SST and SIC rather than coupling the ocean model; changes therefore do not fully take into account air-sea interactions. The thermal conductivity of land is also smaller than that of oceans. The continental regions with high aerosol activations have decreased surface temperature (see Fig. 6.6). The aerosol-cloud feedback on climate could be understood as having

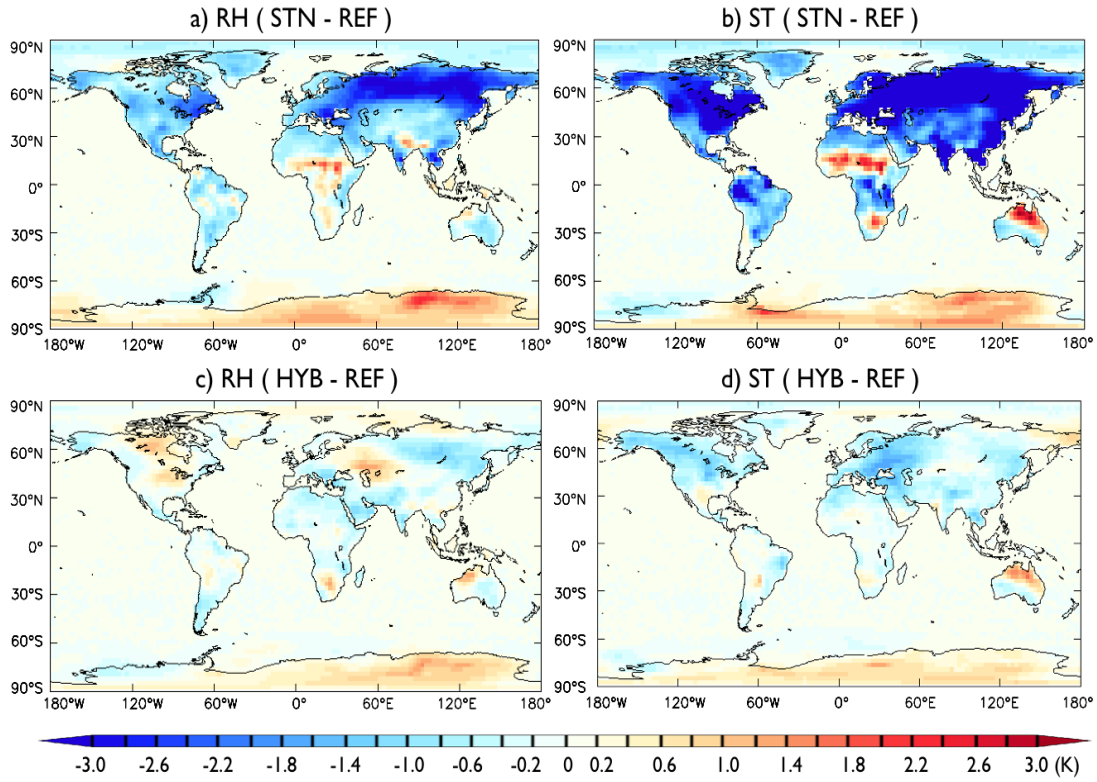

Figure 6.6: Deviations of the surface temperature (T_{surf}; unit = $°C$) between the STN/HYB simulations and the REF simulations for a) RH-STN – RH-REF, b) ST-STN – ST-REF, c) RH-HYB – RH-REF, and d) ST-HYB – ST-REF.

a cooling effect over most of the continents. These decreased surface temperatures attenuate convective activity (in terms of CAPE and CTH) by increasing atmospheric stability. This changes in convection also affects associated precipitation (convective clouds). A more detailed analysis of the convective activity and precipitation in response to aerosol-cloud feedback is found in Section 6.4.

Changes in total precipitation (Fig. 6.7) are difficult to explain, since different trends in precipitation respond differently to increased CDNC; these different responses are due to the many processes at work, from cloud microphysics to atmospheric dynamics. Total precipitation is also largely controlled by the amount of evaporation over ocean. The global mean of total precipitation is not much changed by aerosol coupling (see Table 6.1). As discussed above and in previous chapters, the current model does not fully take into account land-sea interactions, with the analysis is focused on continental precipitation. The enhanced cloud droplets (N_d) are likely to suppress weak stratiform precipitation over land due to decreases in the efficiency of precipitation formation, one of the results of aerosol-cloud interactions. The changes in cloud optical properties

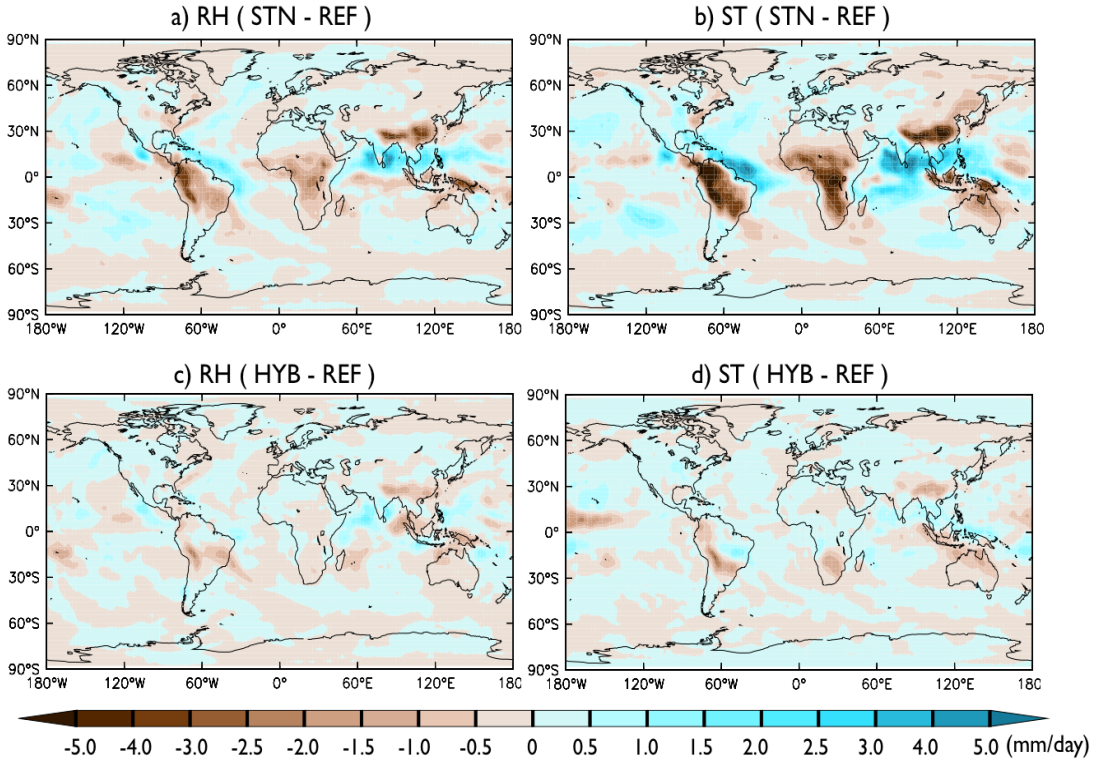

Figure 6.7: Difference of total precipitation (P_{tot}; unit = mm/day) between the STN/HYB simulations and the REF simulations for a) RH-STN – RH-REF, b) ST-STN – ST-REF, c) RH-HYB – RH-REF, and d) ST-HYB – ST-REF.

increase cloud radiative effects (particularly SCRE) and enhance atmospheric stability, thereby reducing convective activity, which then reduces associated precipitation over land (these changes in convective activity and their influence on precipitation will be discussed more in Section 6.4 and 6.5). The overall effects of aerosol-cloud feedbacks redistribute precipitation from land to ocean, and may also change precipitation type from convective to stratiform. These changes of precipitation are regionally dependent; strong decreases are found (indicated by notable dark brown spots) in South America, Central Africa, and China, while over the ocean, along the coastlines of the Atlantic ocean and tropics, and over the Indian and Pacific ocean there are increases in total precipitation (indicated by blue areas; see Fig. 6.7b). This increased precipitation is due in part to increases in convective precipitation caused by increased CAPE. Further analysis of precipitation patterns is found in Section 6.5.

To sum, the activated aerosols (in the form of CCNs) change cloud properties and influence both the radiation balance and precipitation, which is relevant to cloud lifetime effect. The STN simulations predict that large amounts of cloud droplets are

formed in the nucleation process; these simulations also show the largest aerosol indirect effects (AIE). The HYB simulations also show AIEs, but are smaller than those in the STN simulations.

6.4 Convective activity

The mutual effects of aerosol-cloud interactions also influence atmospheric fluxes in energy and mass by altering atmospheric dynamics. Aerosol activation introduces more cloud droplets into clouds; during this process, energy exchanges are accompanied by phase changes, known as latent heat (LH). By increasing CCN, there are more smaller cloud droplets, which suppresses the efficiency of warm rain formation. Delayed of precipitation can cause clouds to develop vertically, giving cloud droplets more of a chance to supercool (Andreae et al., 2004; Diehl et al., 2007). At the upper levels of clouds, the droplets can be turned into ice nuclei (IN) by freezing and releaseing their latent heat; at low levels, the droplets re-absorb heat when they melt. Overall, these energy exchanges during the phase changes of cloud droplets could invigorate convection by taking converted kinetic energy from enhanced static energy for the same amount of surface precipitation (Khain et al., 2005; Rosenfeld 2006).

Elevated number of CCN increases CDNC, which is strongly associated with the development of low clouds with high values of LWC over land. These low clouds effectively reflect incoming solar radiation and cool the surface, which increases atmospheric stability and suppresses thermal convection. These low-cloud effects could compensate for or overcome invigorated convection caused by phase changes. In comparing two different types of convective activity–the convective available potential energy (CAPE) and convective cloud top height (CTH)–the continental means of CTH and CAPE in the REF simulations decrease with aerosol-cloud coupling (i.e., the STN and HYB simulations; see Table 6.2). Aerosol activation and its corresponding heat fluxes due to the releasing of latent heat by condensed cloud droplets are only considered in the context of large-scale cloud microphysics in the current model setups, which is not accounted for convective clouds. Instead of that, convective clouds and the associated convective precipitation are influenced by changed convective activity resulting from strongly enhanced cloud cooling effects.

Reduced convective activities are more pronounced in the STN simulations than in the HYB simulations due to the strong CCN efficiency of the STN simulations. There is also relatively strong suppression of thermal convection in the STN simulations as compared to the HYB simulations (see Fig. 6.8). The estimates of CTH and CAPE are based on daily (24h) means. These means have a wide diurnal range, and are there-

Table 6.2: Global means of convective cloud top height (CTH; unit = m) and convective available potential energy (CAPE; unit = J/kg) over land and ocean, based on daily (24h) means.

Continental						
LAND	RH-REF	RH-STN	RH-HYB	ST-REF	ST-STN	ST-HYB
CTH (m)	1346	1229	1323	1395	1179	1381
CAPE(J/kg)	24.41	18.70	23.26	32.59	20.91	31.19
LAND	RH	Δ(STN-REF)	Δ(HYB-REF)	ST	Δ(STN-REF)	Δ(HYB-REF)
Relative	CTH	-8.69%	-1.71%	CTH	-15.48%	-1.00%
difference	CAPE	-23.39%	-4.71%	CAPE	-35.84%	-4.30%
Marine						
OCEAN	RH-REF	RH-STN	RH-HYB	ST-REF	ST-STN	ST-HYB
CTH (m)	1234	1271	1249	1084	1165	1097
CAPE(J/kg)	32.41	34.35	32.93	27.61	32.22	28.04
OCEAN	RH	Δ(STN-REF)	Δ(HYB-REF)	ST	Δ(STN-REF)	Δ(HYB-REF)
Relative	CTH	3.00%	1.22%	CTH	7.47%	1.20%
difference	CAPE	5.99%	1.60%	CAPE	16.70%	1.56%

fore markedly decreased by low nighttime values; these means also include all shallow convection. These phenomena are generally accompanied by changes in convective precipitation (P_{conv}; see Table 6.3). Over land, convective precipitation (P_{conv}) in the REF simulations decreases with aerosol-cloud feedbacks (in the STN and HYB simulations).

Fig. 6.8 shows the global distribution of differences in CTH for the STN and HYB simulations; a reduction in the strength of convection is clearly associated with elevated number of CCN and CDNC in low-clouds over land (see Figs. F.11c and F.12c). Over continents, the lower values of the CTH in the STN simulations are sectionally correlated with large amounts of CCN and CDNC in areas such as Central and South Africa; Brazil; Northern South America; and East Asia, including China and Korea. Over these regions, decreases in upward mass fluxes are also indicated similar to the distribution of CTH and CAPE (not shown here), since the entrainment and detrainment organised by convection are influenced by changes in CAPE. Entrainment and detrainment also mutually affect convective heating and moistening (Roeckner et al., 2003). This tendency is also found in the regional means of CTH and CAPE, with varying magnitudes (see Table F.3). Over land, the estimated CTHs in the HYB simulations are higher than in the STN simulations ($CTH_{HYB} > CTH_{STN}$); when comparing the CLC schemes, the ST simulations yield higher CTHs than ones in the RH simulations ($CTH_{ST-HYB} > CTH_{RH-HYB}$).

The annual means of CTH and CAPE could diminish their sensitive response to aerosol-cloud interactions, such as in a seasonal variation. The frequency test of CTH

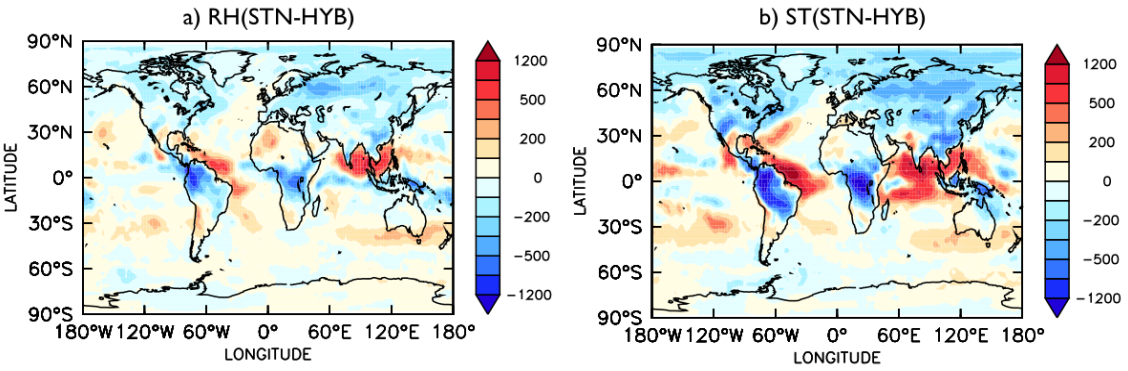

Figure 6.8: Differences of convective cloud top height (CTH; unit=m) between (a) RH-STN and RH-HYB and (b) ST-STN and ST-HYB.

over land therefore has conducted for the boreal winter (DJF: December, January, February) and the boreal summer (JJA: June, July, August). In general, the winter period has both the lowest CTH mean and maxima values, and lower frequencies of higher CTH; the summer period has both the highest CTH mean and maxima values, and higher frequencies of higher CTH. High frequencies of high CTH values in the STN simulations are found at lower CTH values (i.e., less than 1500m), while high frequencies of high CTH values in the HYB simulations are spread widely over higher CTHs in both seasons (see Fig. F.14).

In contrast to the behavior of convection over land, convective activity over ocean is invigorated by aerosol-cloud coupling (see Table 6.2), since changes in marine surface temperature are limited to the vertical heat transfer within the atmosphere, due to the choice of to use a prescribed SST. Condensed cloud droplets release latent heat in large-scale clouds and enhance convective activity. The tropics and other regions influenced by continental outflows show strong convection, with high number concentrations of CCN in the STN simulations (see Fig. 6.8). The ST-STN setup shows the strongest changes in convective activity in response to the aerosol-cloud coupling over land and ocean.

To sum, a higher CCN impacts the frequency and intensity of convection via invigorating or suppressing processes in response to aerosol-cloud feedbacks. A higher CCN can thereby influence the water cycle, and by extension, climate, underlining the importance of the parameterization of aerosol-cloud interactions in the climate model.

6.5 Precipitation

Simulated precipitation results in a complexly related processes such as cloud microphysics, growth of particles, radiation, atmospheric dynamics, and heterogenous surface interactions. In the current model setup, convective clouds do not explicitly take into account aerosol-cloud interactions, but changes in convective activity can affect convective precipitation determined by instant convective updrafts and its detrainment assort large-scale cloud waters. This has been also discussed in Hagemann et al. (2006) has also discussed how convective cloud formation and precipitation are largely controlled by surface radiation. Regarding large-scale precipitation, local variations are associated with local variances in the autoconversion of cloud droplets (related to cloud droplet number concentration), accretional growth (depending on droplet size), and evaporation rate (relevant to cloud cover), and the melting rate of snow (associated with temperature), (Roeckner et al., 2003).

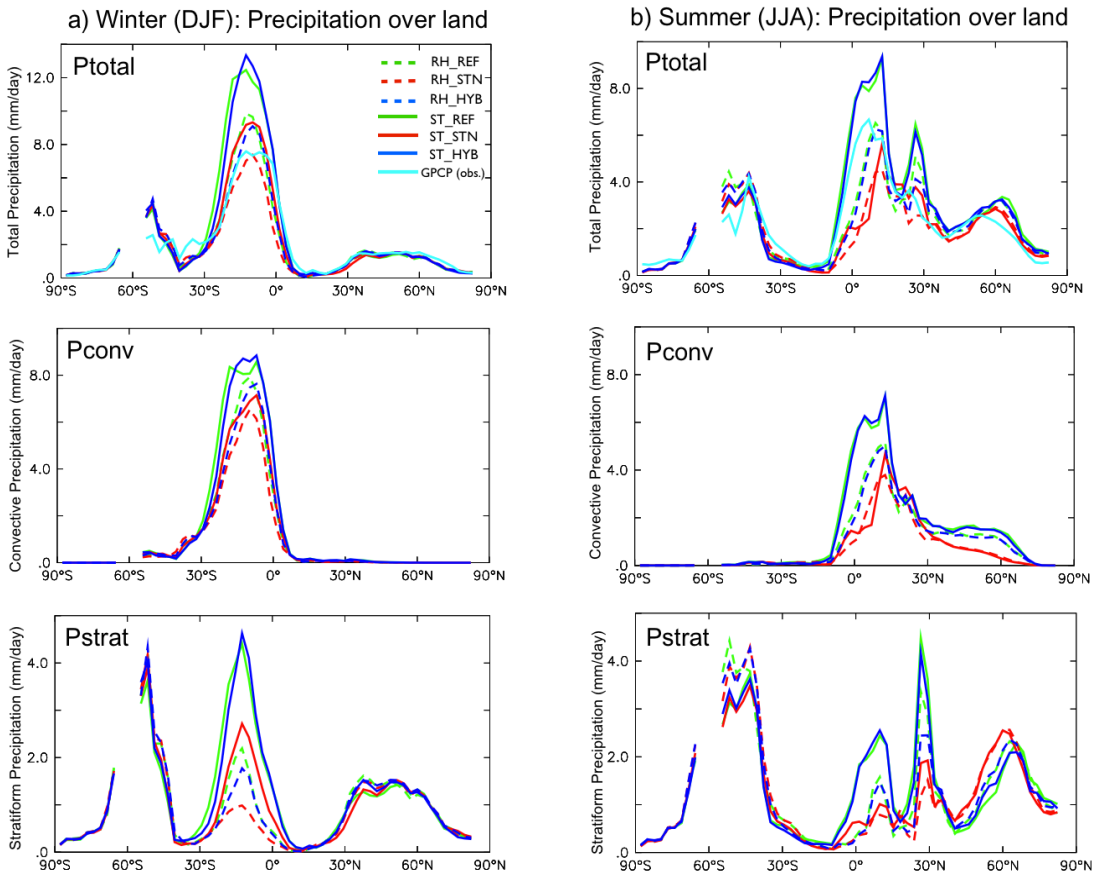

Figure 6.9: Zonal mean distributions of precipitation over land during (a) boreal winter and (b) boreal summer (unit= mm/day)

Table 6.3: Global (land and ocean) mean of total, convective, and large-scale precipitation (unit:mm/day) and percent for the ratio of convective and total precipitation (%) and the ratio of precipitation over land to over ocean ($\frac{Land}{Ocean}$) for each precipitation types.

	RH-simulations			ST-simulations			Observation
Regions	RH-REF	RH-STN	RH-HYB	ST-REF	ST-STN	ST-HYB	OBS
Gobal							
P_{total} (mm/day)	3.01	2.96	3.00	2.97	2.95	2.97	2.68
P_{conv} (mm/day)	1.87	1.86	1.87	1.75	1.80	1.76	-
P_{strat} (mm/day)	1.14	1.11	1.13	1.22	1.15	1.21	-
$P_{conv}/P_{total}(\%)$	62.1	62.8	62.3	58.9	61.0	59.3	-
Ocean only							
P_{total} (mm/day)	3.35	3.44	3.37	3.04	3.32	3.07	2.90
P_{conv} (mm/day)	2.13	2.24	2.15	1.80	2.09	1.83	-
P_{strat} (mm/day)	1.22	1.20	1.22	1.24	1.23	1.24	-
$P_{conv}/P_{total}(\%)$	63.5	65.1	63.8	59.2	63.0	59.6	-
Land only							
P_{total} (mm/day)	2.14	1.75	2.07	2.79	2.00	2.72	2.12
P_{conv} (mm/day)	1.21	0.89	1.16	1.63	1.06	1.58	-
P_{strat} (mm/day)	0.93	0.87	0.91	1.15	0.94	1.14	-
$P_{conv}/P_{total}(\%)$	56.6	50.6	56.0	58.6	50.6	58.1	-
$\frac{Land}{Ocean}$ (Ratio)							
for P_{total}	0.64	0.51	0.61	0.92	0.60	0.89	0.73
for P_{conv}	0.57	0.40	0.54	0.91	0.51	0.86	-
for P_{strat}	0.76	0.73	0.75	0.93	0.76	0.92	-

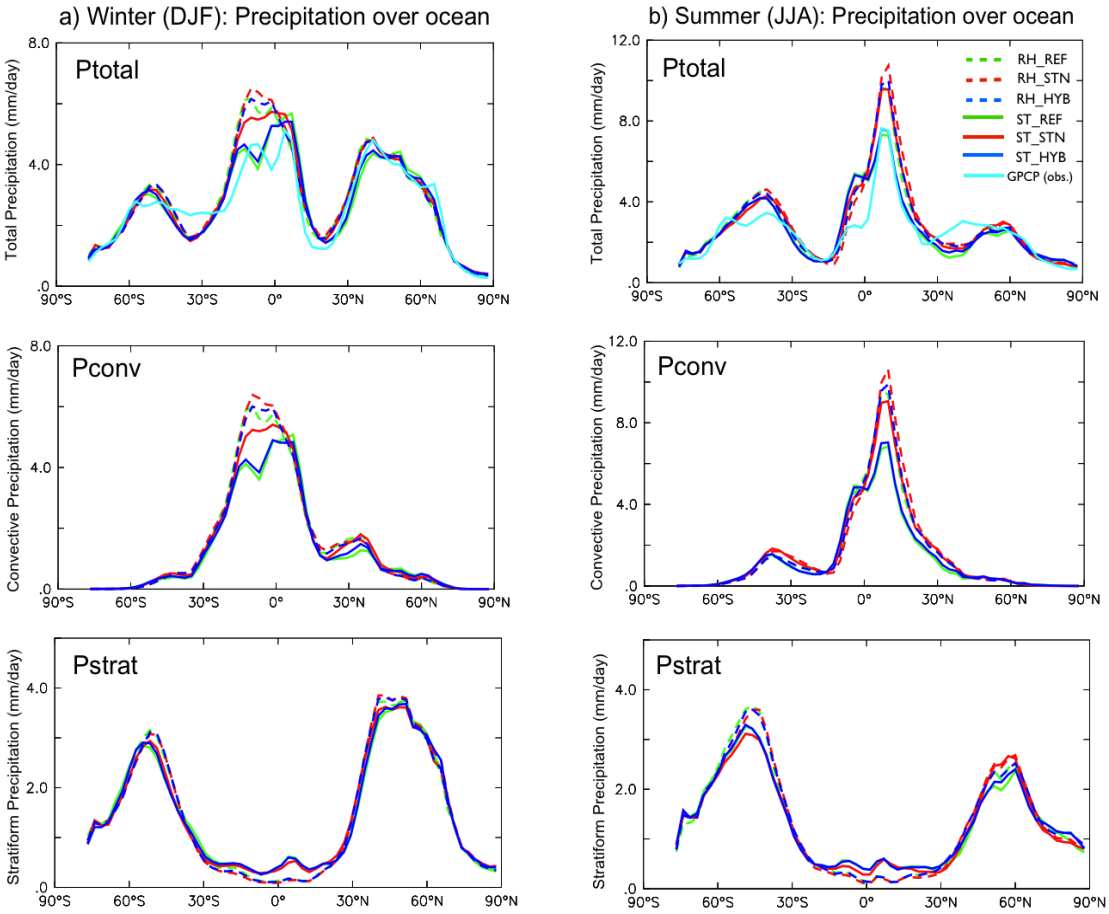

Figure 6.10: Same as in Fig. 6.9, but for precipitation over ocean.

Table 6.3 shows an overview of simulated precipitation patterns, separated by ocean and land, and by convective and stratiform. The global mean values of total precipitation do not vary strongly among the simulations depending on aerosol-cloud coupling (STN and HYB), since total precipitation is largely controlled by the amount of evaporation over ocean, and the surface heat budget is closed due to the choice to use a prescribed SST and SIC. The variations in the mean values of continental and marine precipitation show more notable effects for aerosol-cloud feedbacks, especially over land. Changes in the cloud droplet size and number distributions can influence the efficiency of precipitation formation and convection by changes in energy fluxes (i.e., latent heat (LH) and cloud albedo effect). These effects of changes in the cloud droplet size and number distributions can shift (rearrange) the location of precipitation (e.g., from land to ocean), as well as change the precipitation type (e.g., from convective to stratiform). These processes actively occur over land due to CCN abundance and active energy exchanges between the land surface and air, in contrast to processes over

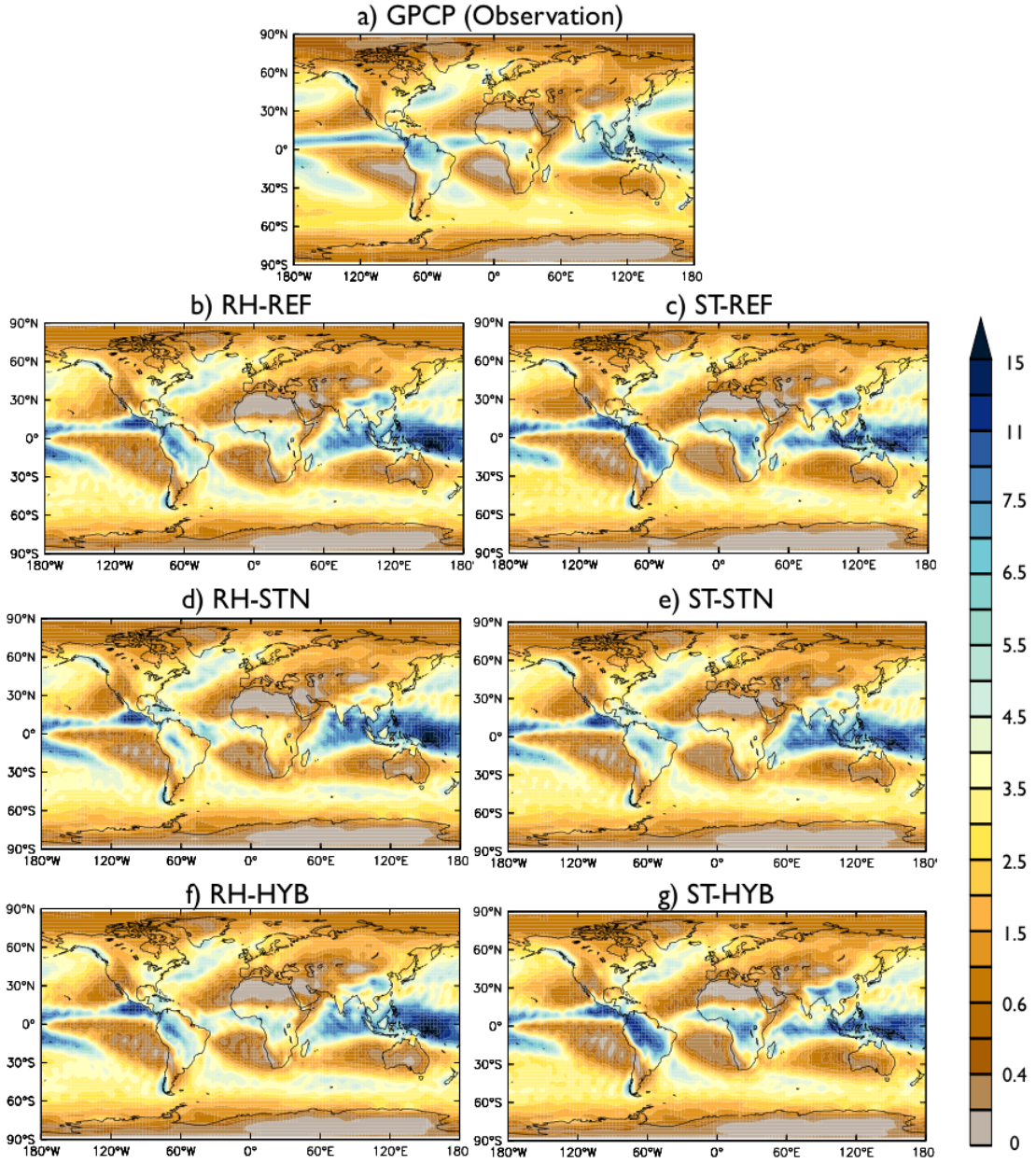

Figure 6.11: Global distribution of simulated and observed total precipitation (unit = mm/day).

the ocean. For this reason, changes in precipitation are more pronounced in the STN simulations than in HYB simulations, while the simulated precipitation in the HYB simulations differs little from that in the REF simulations.

Concerning the proportion of precipitation over land and over ocean, the precipitation ratio ($\frac{Land}{Ocean}$) indicates that more total precipitation occurs over ocean than over land (see Table 6.3). This seems to result in a higher frequency and larger amounts of convective precipitation over oceans in the tropics, especially the Inter-Tropical Convergence Zone (ITCZ). Since energy exchanges between air and ocean are constrained by the prescribed SST and SIC, the aerosol-cloud feedbacks mainly lead to invigorated convection due to induced latent heat via phase changes (i.e., the continental outflow effect), as discussed above. Stronger convection accompanies larger amounts of convective precipitation and results in more precipitation over the ocean; this increased precipitation is more pronounced in the RH simulation, as shown by the $\frac{Land}{Ocean}$ for P_{conv} (0.57 in RH-REF vs. 0.40 in RH-STN; 0.91 in ST-REF vs. 0.51 in ST-STN). This higher fraction of continental precipitation is also indicated by the high fraction of convective precipitation relative to total precipitation (65 % in RH-STN) compared to the other simulations. For stratiform precipitation, the mean values over the ocean do not differ notably between the simulations.

Over land, the magnitude of convection is influenced by surface heat energy exchanges between land and air, which are strongly controlled by aerosol-cloud feedback, i.e., invigorated by LH and weakened by cloud albedo effect. These phenomena are more obvious in convective precipitation, as shown by the changes in convective activity given in Table 6.2; decreases in convective activity over land correspond to decreases in convective precipitation over land and smaller amounts of total precipitation over land. This is clearly demonstrated by comparing between the STN and REF simulations: convective precipitation (P_{conv}) is decreased by 25% in RH-STN, and by 35% in ST-STN, and the proportion of convective precipitation to total precipitation (P_{conv}/P_{total} for land) is also decreased by 8% in ST-STN and by 6% in RH-STN, as compared to the REF simulation. These decreases in convective precipitation are comparable to the effect of increasing the horizontal resolution from T21L19 to T85L19 (T42L19) based on the global annual mean of total precipitation that relates to difference of atmospheric radiative cooling by changes in the clear-sky LW cooling effects (Hagemann et al., 2006). Extreme increases in CDNC can suppress and postpone the formation of stratiform precipitation, as discussed above. Compared to the REF simulations, stratiform precipitation is 10% lower for both ST-STN and RH-STN. This means that both stratiform and convective precipitation over land are decreased by aerosol-cloud

coupling.

Aerosol-cloud interactions show regional variability, as discussed above and in Section 5.4, and similarly the corresponding effects and changes also show regional variability, see Fig. 6.12. As expected from much stronger changes in cloud radiative effects calculated by the STN and HYB simulations, compared to the REF simulation, changes in precipitation, and changes in other relevant properties (i.e., total cloud cover and surface temperature; see Fig. F.5 in Appendix) are more pronounced in the STN simulations. Among the selected continental regions in the STN simulations, Regions CR2 and CR5 show relatively strong changes in both LCRE and SCRE and larger decreases in both convective and stratiform precipitation (see Fig. 6.12) than other regions. In general, strong changes in cloud radiative effects respond to large variations in precipitation, but these responses are not linear as so many processes are involved. These regional variations also vary depending on the simulated variables, the cloud droplet nucleation scheme, and the cloud cover scheme, see the Appendix.

Fig. 6.9 shows the zonal distribution of simulated and observed total precipitation over land for boreal winter (DJF) and boreal summer (JJA); Fig. 6.9 also shows the zonal mean distribution of simulated convective and stratiform precipitation. All simulations generate maximum values at 10°S for boreal winter (DJF) and at 10°N for boreal summer (JJA), which seems to be associated with higher values of convective precipitation. Fig. 6.9 indicates another peak at 50°S, which is mainly associated with the distribution of stratiform precipitation. This peak at 50°S is likely to relate to orographic precipitation over South America (Hagemann et al., 2006).

During boreal winter, most of the simulated total precipitations at 0° to 30°S is higher than the observed precipitation, except for in the RH-STN simulation. The largest differences are found in the ST-REF and ST-HYB simulations. These differences seem to relate to high convective and stratiform precipitation; the simulated CDNC is not high enough to suppress stratiform precipitation and allows relatively high convection due to a lower cloud albedo effect and less latent heat than in the STN simulations. In the northern hemisphere, the distributions of simulated precipitation are close to the observations. During boreal summer (JJA), simulated precipitation in RH-REF and RH-HYB is close to the observations; simulated precipitation is underestimated in the STN simulations, and is overestimated in the ST-REF and ST-HYB simulations. The overestimated convective precipitation in ST-REF and ST-HYB is related to convection, which is stronger in these two simulations than in the ST-STN simulations.The results of a frequency test of CTH indicate that this effect could be more pronounced during boreal summer than during boreal winter (Fig. F.14).

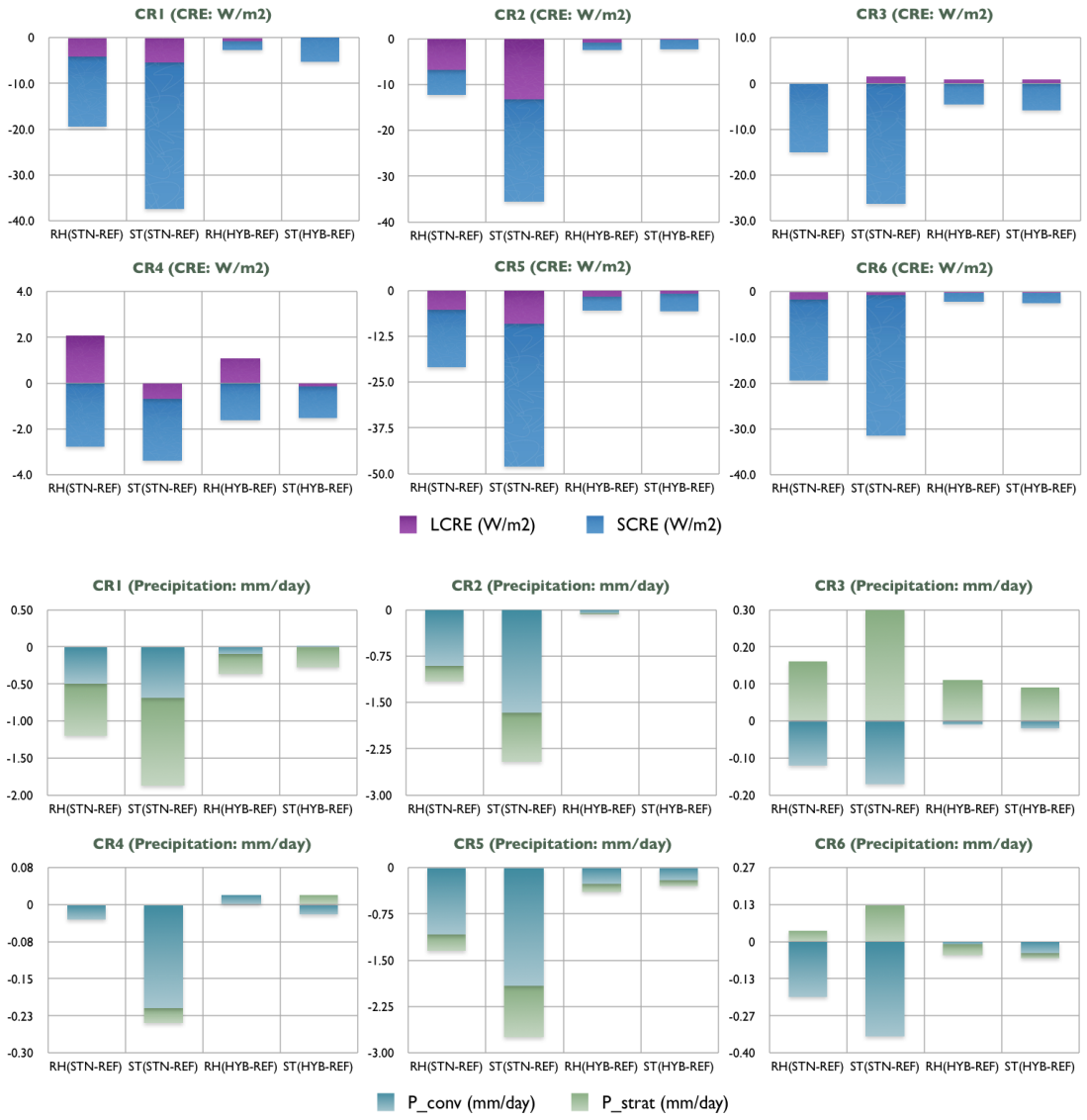

Figure 6.12: Regional variability of changes in cloud radiative effects (SCRE and LCRE; unit = W/m^2) and in convective and stratiform precipitation (P_{conv} and P_{strat}; unit = mm/day) after including nucleated cloud droplets.

Over ocean, the change is not as strong as that of continental precipitation, due to the use of a prescribed SST and SIC. Variations in total precipitation are found mainly in the tropical regions, which are influenced by changes in convection. Thee variations seem to be associated with the estimated precipitation over the western Indian Ocean and over the western and central Pacific Ocean; both of these areas are strongly influenced by the Madden-Julian oscillation (MJO). The global distribution of precipitation indicates that all simulations systematically overestimate precipitation in warm pool over those regions; these overestimations are more pronounced in the RH simulations than in the ST simulations (Fig. 6.11). One reason for this overestimation is that the intraseasonally (30 – 90 day) variations in MJO are difficult to predict using GCMs and the current model does not consider this effect.

To sum, changes of precipitation by including aerosol-cloud coupling (from the REF simulations to the STN and HYB simulations) are more substantially over land than over ocean, and both stratiform and convective precipitation are strongly influenced by changes in cloud droplet number concentration (i.e., aerosol-cloud feedbacks).

6.6 Conclusion

This chapter shows that the inclusion of prognostic cloud droplet nucleation schemes (which represent aerosol-cloud interactions) significantly affects cloud properties and climate relevant parameters. Quantification of cloud droplet nucleation effects also varies regionally and seasonally, depending on the variables used, such as cloud water paths (LWP and IWP), TCC, CREs, and precipitation. This chapter also confirms the effect of aerosol-cloud interactions on convection, with increases in CDNC weakening or invigorating convective activity. Aerosol-cloud coupling generally induces stronger cloud cooling effects (cloud albedo effects) over land, which overcomes the released latent heat and weakens convection. In contrast, over ocean, vertical heat transfer is constrained by the use of a climatological sea surface temperature; released latent heat then invigorates convection.

Chapter 7

Cloud cover scheme effect

The cloud cover scheme determines fractional clouds in a grid box with cloud droplet number concentration and cloud water budget under atmospheric conditions. The estimated cloud cover directly influences cloud properties such as nucleation, evaporation of cloud droplets, and sublimation of ice crystals; together, these properties determine cloud optical properties. As discussed in the previous chapters, the effects of aerosol-cloud interactions on clouds and climate differ depending on the cloud cover scheme, since the simulated cloud properties (particularly cloud water) and cloud radiative effects are closely related to cloud distribution and amount. Chapter 7 addresses the impact of the cloud cover scheme on the simulated cloud properties and climate relevant parameters by comparing the RH simulations (RH-REF, RH-STN, RH-HYB) and the ST simulations (ST-REF, ST-STN, ST-HYB).

7.1 Cloud distributions and cloud radiative effects

Simulated total cloud cover is generally larger in the RH simulations than in the ST simulations. The larger cloud fractions are more pronounced over ocean than over land, particularly in the tropics and subtropics. These larger cloud fractions lead to stronger cooling effects with accompanied changes in relevant cloud properties (see Fig. 7.1). As discussed in Chapter 6, a cooled surface stabilizes the atmosphere and reduces convective activity; this decreases convective precipitation, which affects the hydrological cycle and the distribution of total cloud cover. The larger cooling effect in the RH simulations is associated with more total cloud water, particularly over ocean. Over land, differences in cloud droplet number concentration are also tightly linked with cloud optical properties and show distinct trends of cloud radiative effects, as demonstrated by the changes in NCRE over land and ocean, particularly for the STN

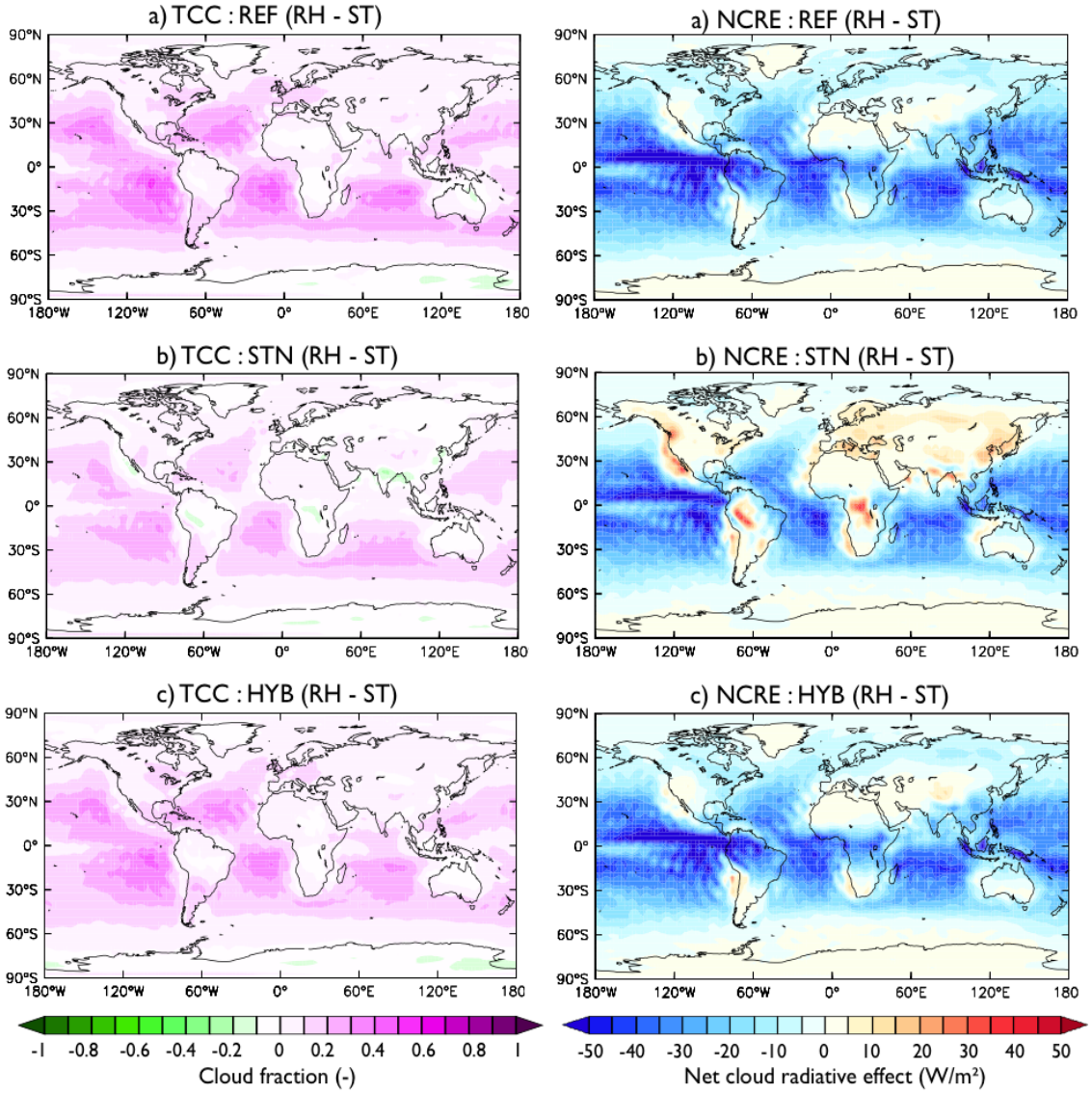

Figure 7.1: Deviations of simulated TCC (unit = -) and NCRE (unit = W/m^2) between the RH and ST simulations for a) the REF, b) the STN, and c) the HYB simulation.

simulations.

These enhanced cooling effects also relate to changes in simulated clouds according to altitude, with the activated aerosols and total cloud water distribution. There are distinct patterns of changes in simulated low, middle, and high clouds, as classified by the ISCCP simulator: high-level clouds occurs above 440 mb and mainly include cirrus, cirrostratus, and deep convection; middle-level clouds appear between 440 mb and 680 mb and are mainly altocumulus, altostratus, and nimbostratus; low-level clouds are formed near the surface, from 1000 mb to 680 mb (see Fig. 7.2)

At low altitudes over the ocean, the RH simulations calculate larger cloud fractions than the ST simulations for both the STN and HYB scheme couplings. These larger marine clouds develop continuously from the surface to mid-altitudes. This overestimation in the calculation of cloud fractions may be related to the general tendency of the RH-CLC scheme to overestimate fog and haze. Over continents, at most of the high latitudes and regions with simulated high CCN concentrations, changes in the STN simulations are different from changes in the HYB simulations. In the HYB simulations, the RH-CLC scheme calculates a larger cloud fraction from the surface to middle latitudes than does the ST-CLC scheme; in contrast, in the STN simulations, clouds are enhanced by the more abundant CCN concentrations pronounced by coupling with the ST-CLC scheme, as opposed to with the RH-CLC scheme. At high altitudes, both the STN and HYB simulations show larger cloud fractions in the ST simulations than in the RH simulations. In Fig. 7.2(a) and (b), notable negative deviations occur over the ITCZ (denoted with strong blue signals). These high clouds can contribute to an increase in cloud warming effects at TOA in the ST simulations, however their waring effects are relatively small compared to the enhanced cloud albedo effects in low clouds. Since the amount of the total cloud water decreases exponentially with height, high clouds are mostly optically thin and have relatively low temperatures due to high altitudes. High clouds therefore have smaller cloud radiative effect than low clouds.

Large values of liquid water content are the largest contributor to increased in cloud albedo in the RH simulations. This is clearly demonstrated in the distribution of liquid water contents (see Fig. 7.3). Lower values of liquid water content occur more often in the ST simulations than in the RH simulations. This distribution is also dependent on cloud droplet number concentration for the REF, HYB, and STN simulations; higher CDNC in the STN simulations more frequently accompanies higher values of liquid water content than does lower CDNC in the REF simulations. In the REF simulations, most of simulated liquid water content is lower than 120 g/m^2. The ranges of simulated liquid water content widen after taking into account aerosol-cloud

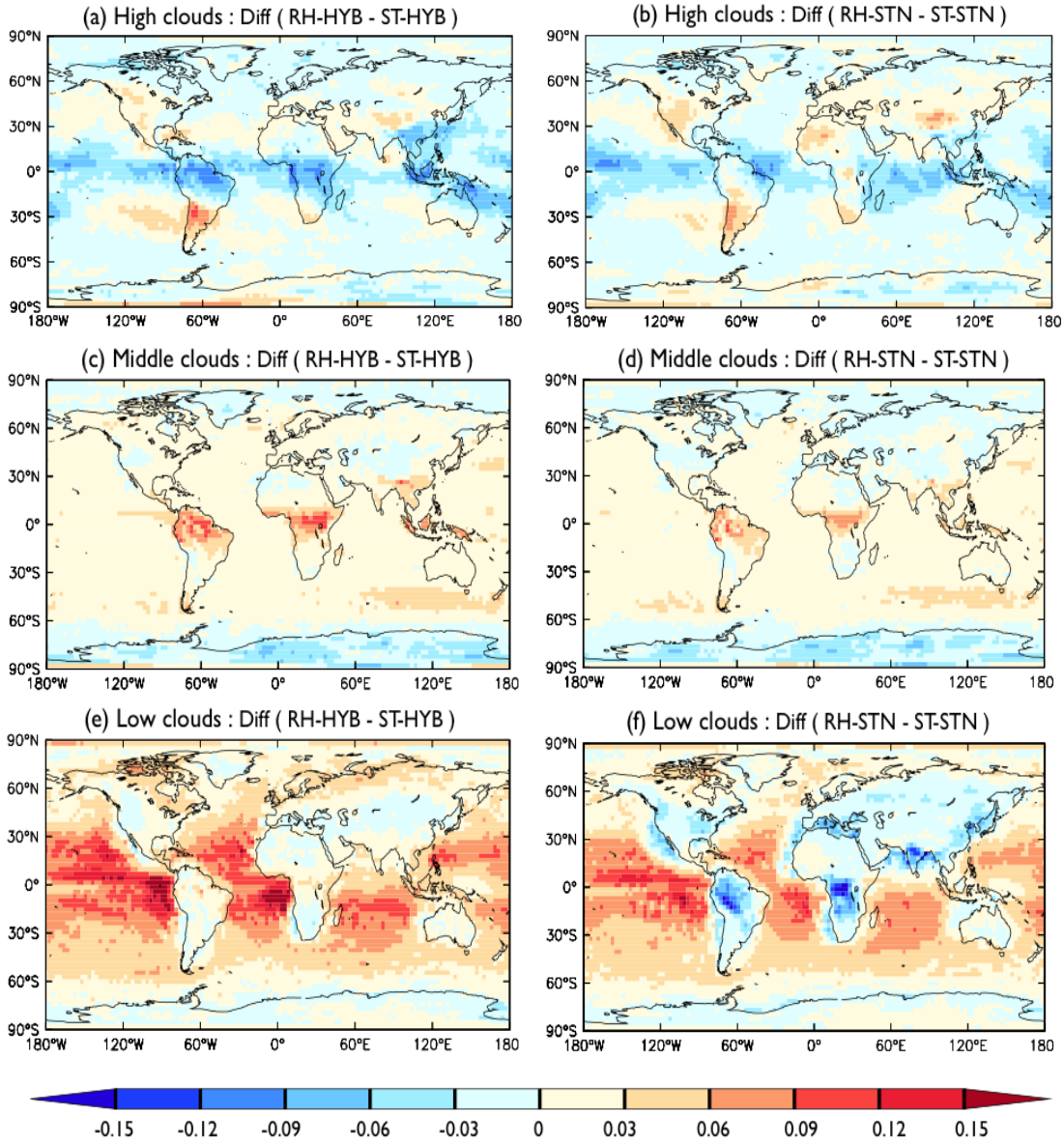

Figure 7.2: Deviations of simulated cloud cover at low, middle, and high altitudes between the RH and ST simulations for the HYB and the STN simulations.

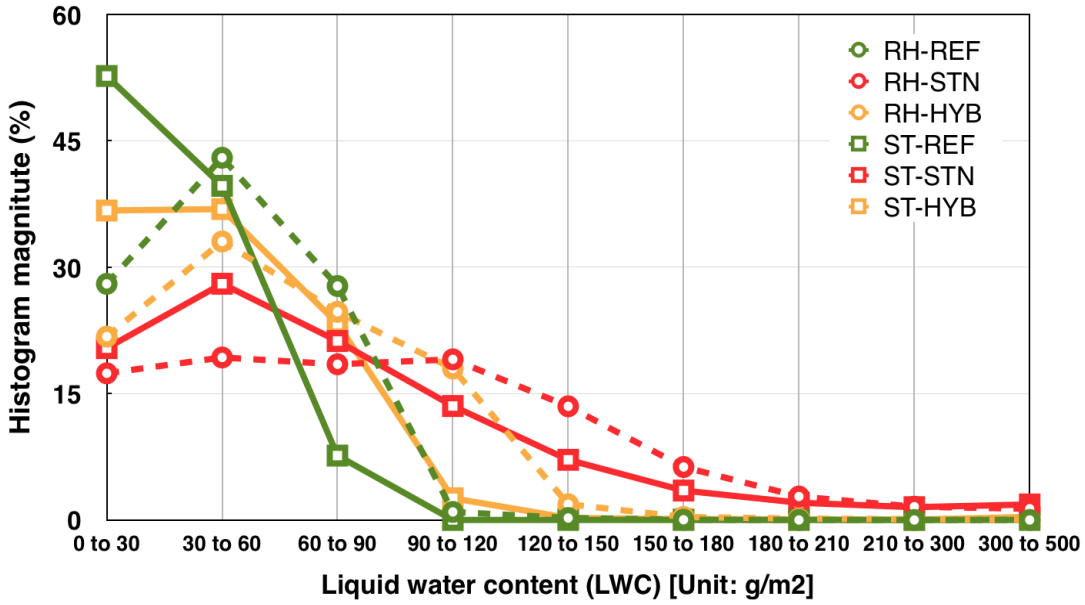

Figure 7.3: Histogram of the occurrence of particular liquid water content for the RH-simulations (dashed line with circles), and for the ST simulations (solid line with squares).

feedbacks (HYB, STN), particularly when these simulations are coupled with the RH-CLC scheme; this means that higher CDNC are generally accompanied by higher liquid water content. This effect is similar to regionally variations in the sensitivity of liquid water content to aerosol-cloud interactions (see Fig. 5.12 and Table 5.3).

The differences between the simulated clouds in the RH and ST simulations are also evident in the histogram of the occurrence of cloud fractions (see Fig. 7.4). This frequency test is based on the annual mean data between 60°N and 60 °S and is separated for global, land, and ocean distributions. The derived TCC from MODIS shows a negatively skewed distribution that the global, marine and continental mean values are greater than their medians. The distribution of predicted TCC in the RH simulations is close to the observed TCC distribution, while the ST simulations are positively skewed distributions as a systematic underestimation of larger cloud fractions, particularly in the tropics. These skews are consistent with those reported in Weber et al. (2011), which evaluated the performance of the ST-CLC scheme in the ECHAM5 using satellite data. Weber et al.'s (2011) study presented positively biased skewness of the simulated cloud cover in the tropics, as well as smaller variances, as compared to MODIS data. The ST simulations predict smaller fractions of cloud cover (from 10% to 50%) more often compared to the observations (see Fig. 7.4a). These high frequencies

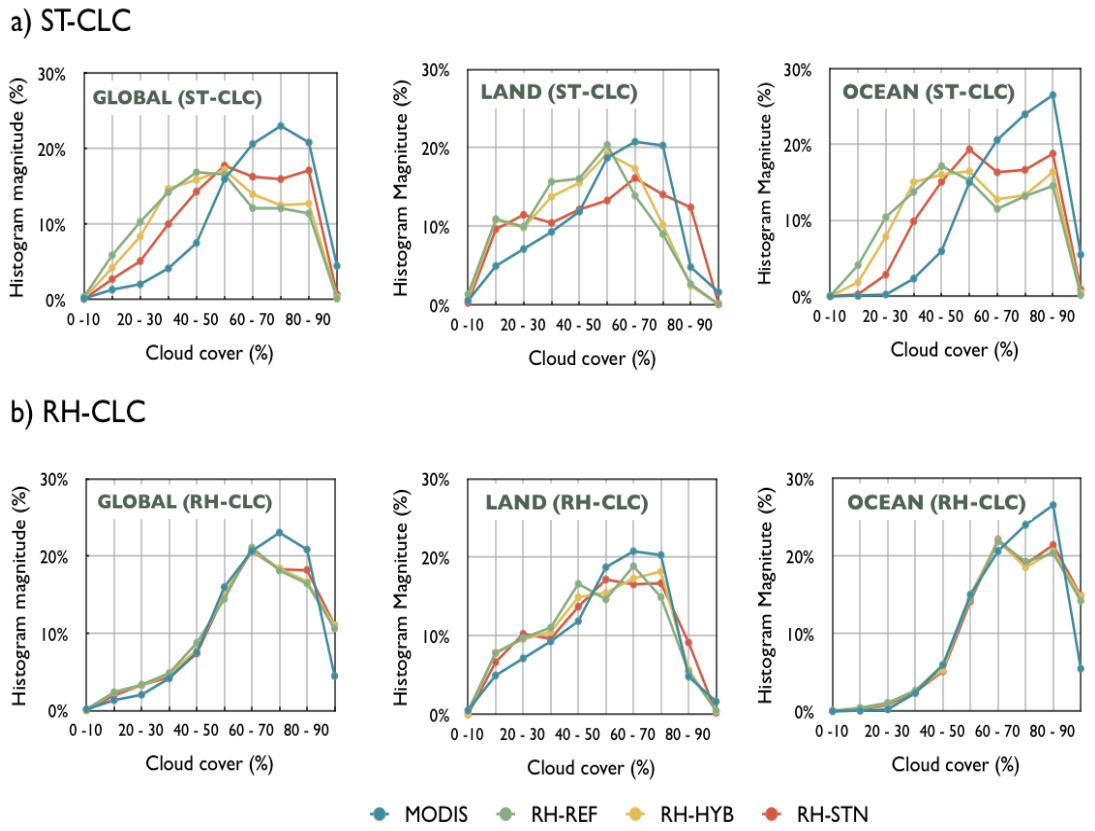

Figure 7.4: Histogram comparing cloud factions distributed over the latitudes 60to 60for observations (MODIS) and a) the ST simulations and b) the RH simulations.

of smaller cloud fractions are mainly contributed by higher occurrences of the smaller fraction of marine clouds, which leads to smaller mean TCC. The largest discrepancy mostly originates from strongly underestimated marine shallow cumulus clouds over the ITCZ (see Fig. 7.2). This underestimation of marine cloud is likely associated with low convective activity resulting from the strong sensitivity of the ST-CLC scheme to regional variations in cloud water and cloud droplets. This will be discussed in detail below (Section 7.2). The ST simulations most frequently predict smaller cloud fractions (by 50 – 60 %) than the observations, which show maximum values at fractions between 70 % and 80 %. In the RH simulations (Fig. 7.4b), the occurrence of TCC steeply increases from smaller cloud fractions to larger cloud fractions, and is maximized at larger cloud fractions. The RH simulations generate frequency patterns for TCC that are similar to the observations, but that are less sensitive to different cloud droplet number concentrations. Particularly over ocean, the occurrence of TCC shows very similar patterns in all RH simulations as compared to the observations. This consistency indicates the robust performance of the RH-CLC scheme in simulating cloud cover both

with and without aerosol-cloud feedbacks.

7.2 Convective activity

As discussed in Section 6.4, convective activity is changed by CCN efficiency due to changes in atmospheric stability resulting from cloud albedo effects. This change occurs because cloud droplet size and number distribution is closely associated with cloud optical properties. For a high CCN efficiency in the STN simulations, strongly enhanced cloud albedo effects over land reduces convective activity.

Similarly, larger cloud fractions and high amounts of cloud water also increase cloud optical properties, thereby stronger cloud albedo effects (see Fig. 7.1). This enhanced cloud albedo effect influences convective activity and the corresponding vertical mass fluxes. Particularly, in the tropics and subtropics these influences are more pronounced than other regions, since the largest amounts of total water path and the most frequent convection are appeared over these regions.

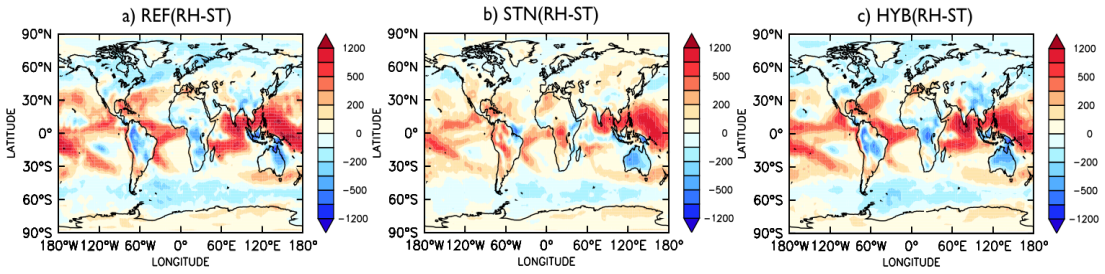

Figure 7.5: Differences of convective cloud top Height (CTH; unit= m) between (a) RH-REF and ST-REF, (b) RH-STN and ST-STN, and (c) RH-HYB and ST-HYB.

The most noticeable differences in convective cloud top height (CTH) between the RH and ST simulations are found in the tropics, see Fig. 7.5. In general, convective cloud top height (CTH) is lower in the tropics and subtropics over ocean in the RH simulations than in the ST simulations, similarly to differences in CAPE (see Fig. F.25). This different convective activity in the tropics is also found in the frequency test of the simulated CAPE over land and ocean between 30°N and 30°S (see Fig. 7.6). The frequency test is based on the annual mean of daily mean CAPE, making CAPE values much lower that those that accompany typical deep convection in the tropics. Low CAPE values occur more often over ocean in the ST simulations than in the RH simulations. The marine mean values of CAPE between 30°N and 30°S are higher with the RH-CLC scheme than with the ST-CLC scheme; i.e., about 20% higher for the HYB simulations, and about 10 % higher for the STN simulations. In contrat,

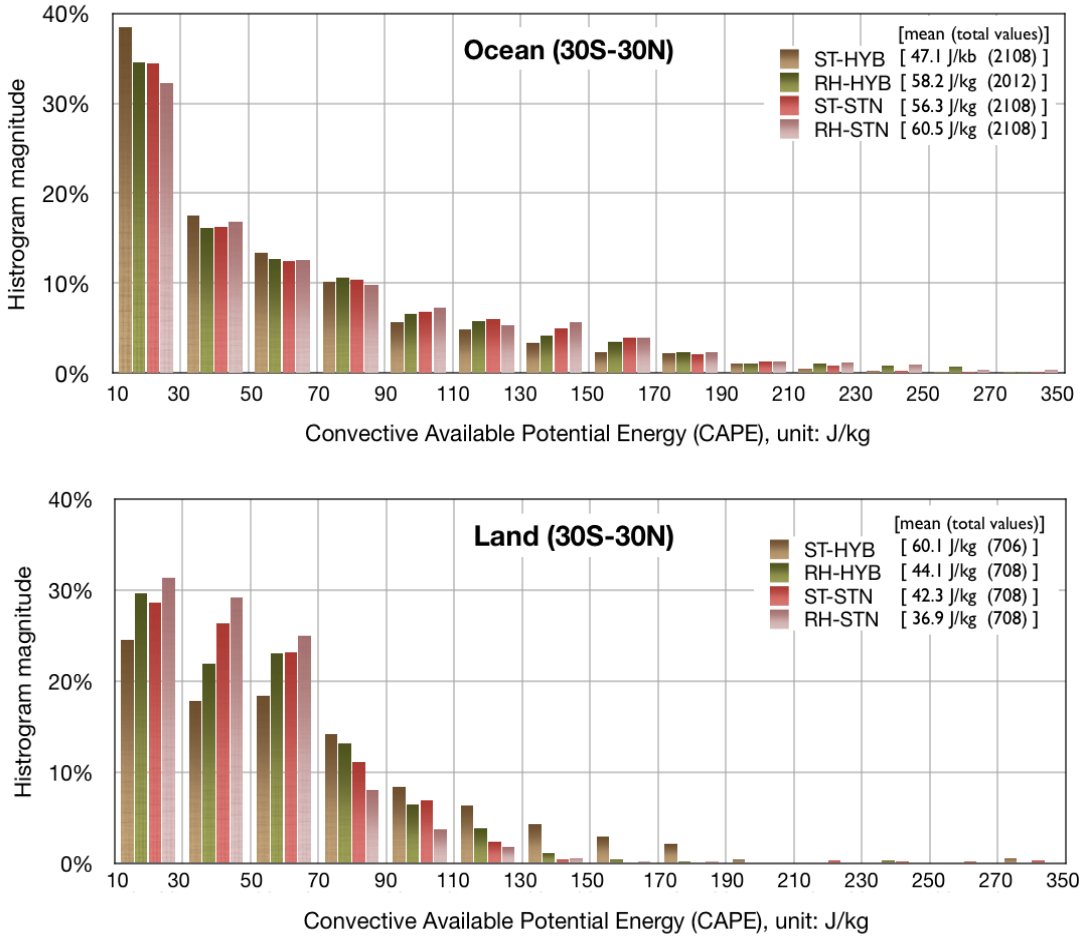

Figure 7.6: Histogram of convective available potential energy (CAPE; unit = J/kg) for land and ocean in the tropic and subtropic (between 30°S and 30°N).

the continental mean values of CAPE are lower in the RH simulations than in the ST simulations. This results from stronger cooling effect over lands in the RH simulations, leading to more frequent low CAPE values than those in the ST simulation.

Cloud cover scheme is also important for vertical movements of air and associated mass fluxes, since simulated CAPE is influenced by the cloud cover scheme and is tightly linked with convective mass transport, i.e., updraft and downdraft. Figs. 7.7 and 7.8 show the deviation of zonal mean updraft and downdraft mass fluxes in the RH simulations as compared to those in the ST simulations. These vertical fluxes exchange moist air from the surface to the upper level in the planetary boundary layer by updraft, and dry air from the upper level of the atmosphere to the lower level of the atmosphere by downdraft. At the low latitudes stronger vertical updrafts transport more water upward in the ST simulations than in the RH simulations (see Fig. 7.7).

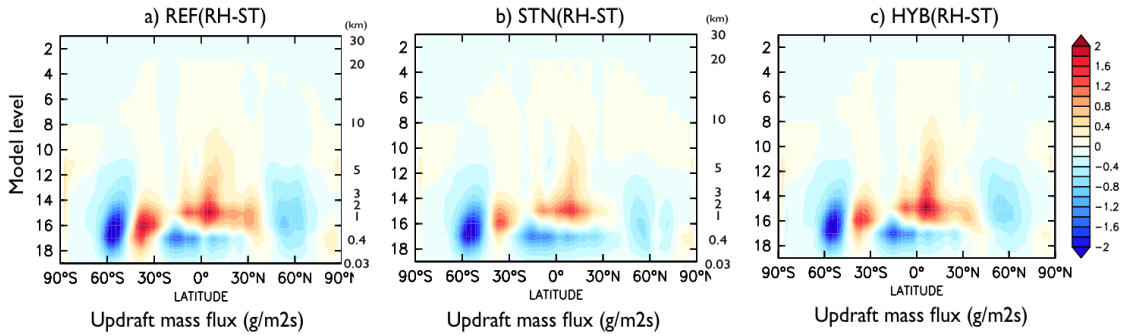

Figure 7.7: Differences of updraft mass flux (unit = g/m^2s) between (a) RH-REF and ST-REF, (b) RH-STN and ST-STN, and (c) RH-HYB and ST-HYB.

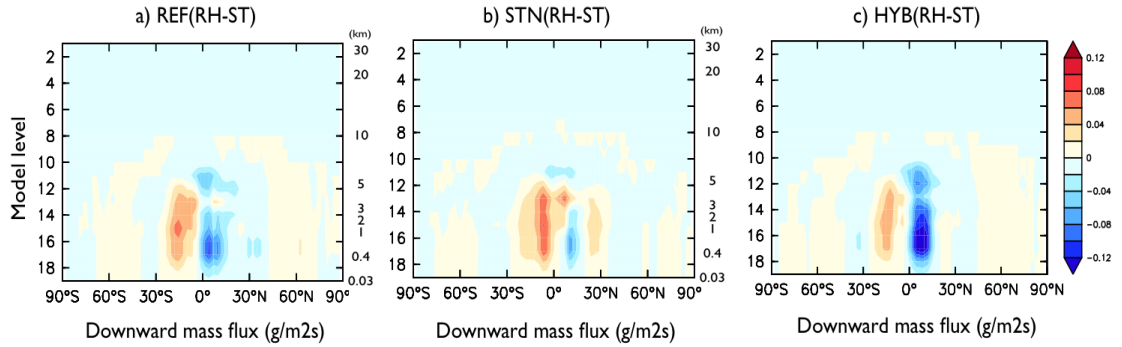

Figure 7.8: Differences of downward mass flux (unit = g/m^2s) between (a) RH-REF and ST-REF, (b) RH-STN and ST-STN, and (c) RH-HYB and ST-HYB.

Fig. 7.8 shows stronger downward mass fluxes at low latitudes, particularly between 0 to 30°N in the Pacific Ocean. These stronger downward mass fluxes are expected based on global distributions of deviations in CTH and CAPE (see Figs. 7.5 and F.25). This transported dry air makes the atmosphere drier at low altitudes in the ST simulations, and could lead to relatively lower values of total cloud cover than those in both the RH simulations and in the observations. Downdraft mass fluxes are one order of magnitude smaller than updraft mass fluxes. In Weber et al. (2011), the overall trends of vertical movements in the ST simulations are in line with the negatively skewed distribution of the total water mixing ratio. Low water mixing ratios occur more frequently at lower altitudes, and seem to be associated with an underestimation of stratiform clouds over the oceans at low latitudes. In the current cloud cover scheme, the distribution of total water mixing ratios is not treated with the prognostic calculation of skewness. Such a prognostic calculation would help to improve the performance of the ST-CLC scheme (Weber et al., 2011).

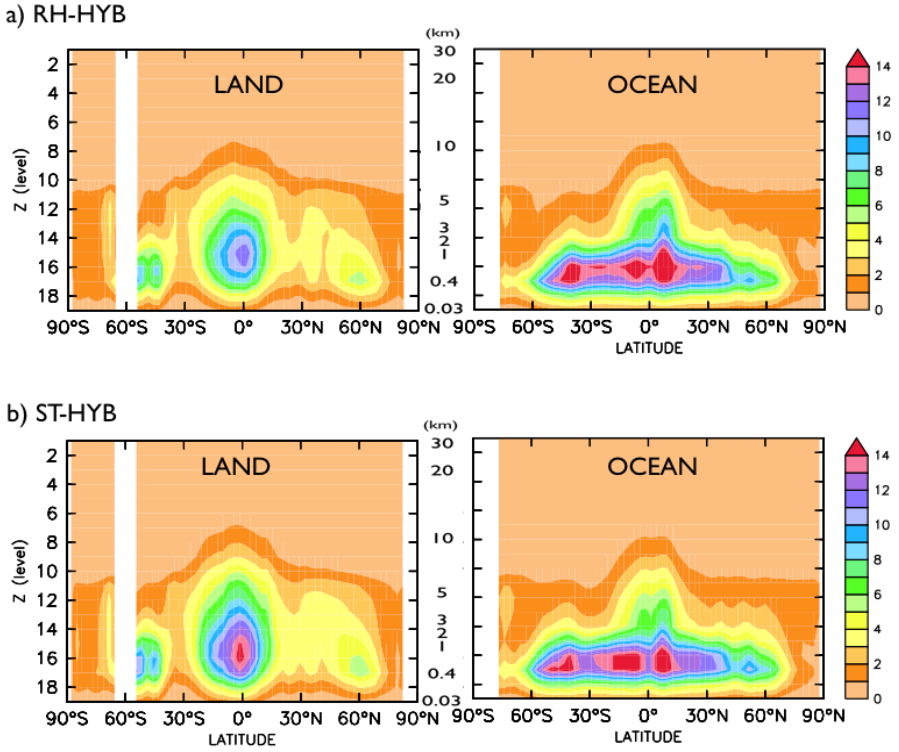

Figure 7.9: Updraft mass flux (unit = g/m^2s) over land and ocean for (a) RH-HYB (b) ST-HYB.

The zonal mean distributions of updraft mass fluxes over land and ocean are presented in detail for the HYB and STN simulations in Figs. 7.9 and 7.10. In both simulations the largest volume of updraft mass occurs in the tropics and in the regions between 30°S to 60°S at low altitudes. The largest amounts of updraft marine mass fluxes are concentrated at low altitudes between 60°S to 60°N, and in the tropics, and extended into the upper troposphere. Over land, differences between the STN and HYB simulations are more pronounced in the tropics. The updraft mass is much smaller in the STN simulations than in the HYB simulations due to the reduced convective activity, as discussed above and in previous chapters.

7.3 Hydrological cycle

The hydrological cycle is associated with the atmospheric energy budget on both local and global scales; the hydrological cycle is affected by condensed water vapor such as the liquid or ice phase in clouds and precipitation. The conversion of water vapor to liquid or ice is affected by the concentration and chemical composition of ambient

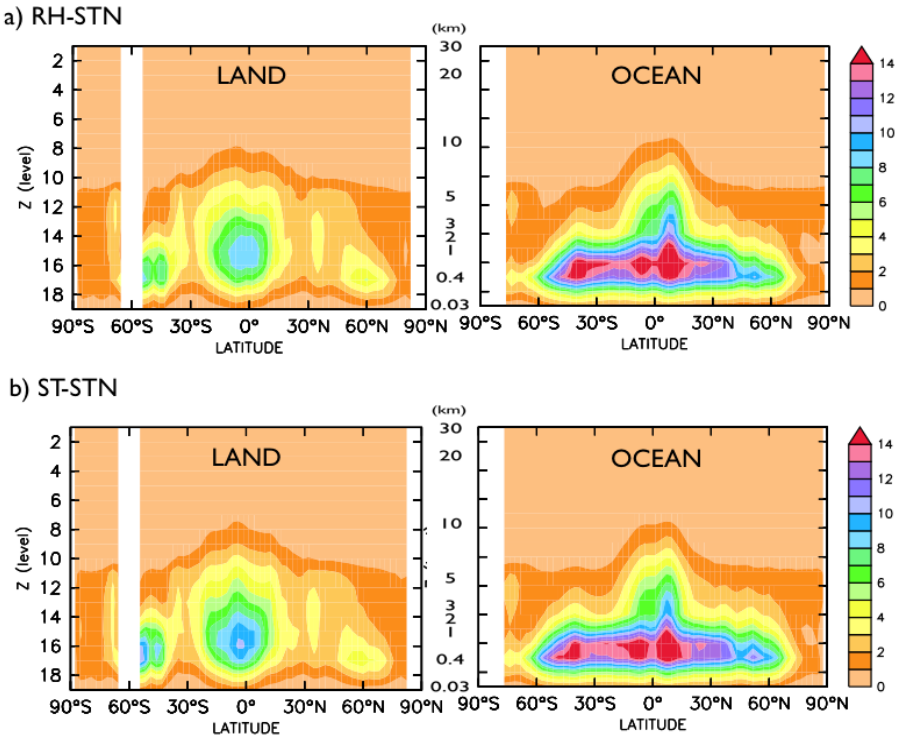

Figure 7.10: Updraft mass flux (unit = g/m^2s) over land and ocean for (a) RH-STN (b) ST-STN.

aerosol particles. The statistical cloud cover scheme is therefore more sensitive to cloud properties than the relative humidity threshold cloud cover scheme.

Liquid water path (LWP) shows particularly large variations depending on cloud drop number concentration and cloud cover, since simulated LWPs are directly linked with cloud droplet nucleation and cloud cover schemes. The large amounts of cloud water content and cloud cover in the RH simulations influence the formation of precipitation, which is driven by a number of processes, including cloud microphysics, radiative transfer, and atmospheric dynamics (see Table 7.1 for summary). Both liquid and ice water paths in the RH simulations are larger for both land and ocean than in the ST simulations, except for the STN simulations over land. This exception is associated with CCN abundance, which is sufficient to attenuate the general trend of the RH-CLC scheme. The large amounts of liquid and ice water path interact reciprocally, with large fractions of total cloud cover. The magnitudes of changes in simulated TCC are relatively smaller than those associated with cloud water budget, and vary regionally due to the influences of atmospheric conditions.

Total precipitation is largely determined by the amount of evaporation over ocean.

Table 7.1: Relative differences between the RH and ST simulations for the convective available potential energy (CAPE); total cloud cover (TCC); and convective, stratiform, and total precipitation ($P_{conv}, P_{strat}, P_{total}$) [Rdiff=$\frac{(RH-ST)}{ST}$ $\times 100(\%)$]. Separately by land and ocean, based on annual mean.

Continental

Rdiff(%)	CAPE	TCC	P_{conv}	P_{strat}	P_{total}	WVM	LWP	IWP
REF(RH-ST)	-25.1%	7.5%	-25.8%	-19.1%	-23.3%	-3.1%	57.6%	25.4%
STN(RH-ST)	-10.6%	1.4%	-16.0%	-7.5%	-12.5%	1.7%	-8.7%	19.4%
HYB(RH-ST)	-25.4%	6.7%	-26.6%	-20.2%	-23.9%	-3.0%	42.9%	19.2%

Marine

Rdiff(%)	CAPE	TCC	P_{conv}	P_{strat}	P_{total}	WVM	LWP	IWP
REF(RH-ST)	17.4%	28.6%	18.3%	-1.6%	10.2%	2.0%	82.4%	44.3%
STN(RH-ST)	6.6%	15.0%	7.2%	-2.4%	3.6%	2.0%	39.7%	33.2%
HYB(RH-ST)	17.4%	24.1%	17.5%	-1.6%	9.8%	1.8%	65.5%	38.4%

Total global mean precipitation therefore dose not substantially vary with the coupling of cloud cover scheme (see, Table 7.2). This stability in global mean precipitation is due to the use of a set SST and SIC, as discussed in previous chapters. The analysis is therefore separated for ocean and land, as well as for precipitation types, since convective and stratiform precipitation show distinct behaviors in response to both the aerosol-cloud interactions and cloud cover scheme effects. These distinct behaviors are in part due to the different processes by which precipitation is formed: convective precipitation is largely governed by simulated convection, while cloud droplet size and number distribution, and aerosol activity are not considered; in contrat, stratiform precipitation mutually interacts with aerosol activation and the accompanying energy exchanges (e.g., latent heat), similar to large-scale clouds.

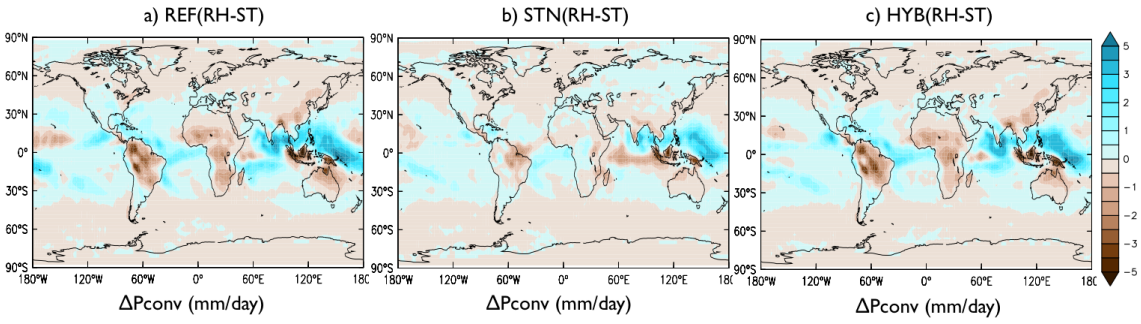

Figure 7.11: Differences in convective precipitation between (a) RH-REF and ST-REF, (b) RH-STN and ST-STN, and (c) RH-HYB and ST-HYB.

The reduced convective activity over land decreases convective precipitation over land and shifts more convective precipitation from the land to the ocean. The RH-

CLC scheme therefore yields lower convective precipitation over land than does the ST-CLC scheme. Fig. 7.11 shows the changes in simulated convective precipitation due to the coupling of cloud cover schemes. The RH simulations show stronger convective precipitation in the ITCZ over ocean, and decreased precipitation over land, which corresponds to changes in convective top height (CTH) and convective available potential energy (CAPE) (see Figs. 7.5 and F.25). In the STN simulations, these trends in the CLC scheme effects are less marked in CCN abundant regions such as Central Africa. Over ocean, higher convective precipitation in the tropics is simulated in the RH simulations than in the ST simulations. In the tropics, convection and convective precipitation occur more frequently than at other latitudes and therefore the changes in convection and convective precipitation are more pronounced. Total water path has larger values over ocean and lower values over land in the RH simulations as compared to in the ST simulations (not shown).

The overall differences between the ST and RH simulations (separated into land and ocean) are summarized in Table 7.1. In the ST simulations, the large amount of continental precipitation leads to decreased total water vapor and removes more cloud water from clouds. This larger continental precipitation also triggers a higher removal rate of aerosols, which decreases the aerosol optical depth in the ST simulations. Over ocean, decreases in CAPE reduce detrained cloud water and water vapor from convection, and thereby lower large-scale cloud water, which leads to smaller cloud fractions over the ocean.

7.4 Global mean changes in cloud properties and climate

The simulated cloud properties are strongly affected by CLC scheme, with different magnitudes depending on variables and regions. Table 7.2 summarizes the global mean differences of the simulated cloud properties, hydrological cycle, cloud radiative effects at TOA, and aerosol optical depth for the RH simulations as compared to the ST simulations. Strong variations are found in the cloud water budget and cloud radiative effects. Cloud water distribution is one of key factors in determining cloud fractions, and the determined cloud cover strongly influences cloud radiative effects.

The simulated cloud droplet number concentration is higher with the RH-CLC scheme due to larger cloud fractions, expect for the STN simulations. Globally, high CCN efficiency in the STN simulation is not much influenced by larger cloud coverage. The changes in LWP are exceptionally large and accompany changes in the hydrological cycle. The changes in LWP are strongly dependent on cloud cover scheme, but this

Table 7.2: Global mean changes between the RH and ST simulations for simulated cloud properties, hydrological cycle, cloud radiative effects at TOA, and aerosol optical depth from using deviations (Dev.) and relative differences (RDiff) [RDiff= $\frac{(RH-ST)}{ST} \times 100$ (%)].

CLC effects on Change from	REF-simulations [RH-REF to ST-REF]		STN-simulations [RH-STN to ST-STN]		HYB-simulations [RH-HYB to ST-HYB]	
	Dev.	RDiff.	Dev.	RDiff.	Dev.	RDiff.
ΔLWP (g/m^2)	19.4	77.9 %	17.8	23.6 %	23.1	60.6 %
ΔIWP (g/m^2)	8.1	38.8 %	6.7	28.9 %	7.2	32.4 %
ΔN_d ($10^{10}/m^2$)	0.46	26.7 %	-0.32	-3.3 %	0.87	25.4 %
ΔN_i ($10^{10}/m^2$)	0.02	5.3 %	0.01	2.5 %	0.01	2.6 %
ΔWVM (kg/m^2)	0.2	0.8 %	0.5	2.0 %	0.1	0.4 %
ΔTCC (%)	12.7	22.8 %	7.1	11.4 %	11.2	19.5 %
ΔP_{total} (mm/day)	0.04	1.3 %	0.01	0.3 %	0.03	1.0 %
ΔP_{strat} (mm/day)	-0.08	-6.6 %	-0.04	-3.5 %	-0.08	-6.6 %
ΔP_{conv} (mm/day)	0.12	6.9 %	0.06	3.3 %	0.11	6.3 %
ΔSCRE (W/m^2)	-23.0	68.5 %	-15.8	30.3 %	-21.4	55.5 %
ΔLCRE (W/m^2)	4.2	17.3 %	3.2	12.5 %	3.9	15.8 %
ΔAOD	0.01	5.3 %	0.01	4.5 %	0.02	10.5 %

change can be counteracted by overly high CDNC (STN). Higher CDNC and higher amounts of cloud water lead to larger cloud cover (Lohmann et al., 2007), as is found in the RH simulations. Overall, these values are closely associated with cloud optical properties, and have strong impacts on cloud radiative effects. The shortwave cloud radiative effects, which reflect more incoming solar radiation, show more pronounced changes than do the longwave cloud radiative effects, which trap more heat reflected from the surface. The changes in cloud radiative effects affect atmospheric energy and influence precipitation. Global mean total precipitation is not much influenced by cloud cover scheme, as increases in convective precipitation are compensated for by decreases in stratiform precipitation in the RH simulations as shown by the differences in simulated stratiform and total precipitation in Fig. F.27. Changes in precipitation can also influence aerosol optical depth, particularly over land, due to a large aerosol loading. Over land, decreases in precipitation through changes in convection and/or delayed precipitation caused by high CDNC, can lead to higher LWP loading. This higher LWP loading could reduce the wet scavenging rate of aerosols as a removal process (Lohmann and Feichter, 1997; and Lohmann et al., 2007). This leads to relatively higher aerosol optical depth in the RH simulations as compared to the ST simulations.

7.5 Conclusion

The simulated clouds depend strongly on the cloud cover scheme, and have different sensitivity to aerosol-cloud coupling. In the comparison of the simulated clouds properties

and relevant climate parameters, differences between the RH and ST simulations shows large distances due to the opposite directions in which they tend to simulated clouds. In general, the RH simulations calculate negatively skewed distributions of cloud fractions and relevant cloud water, which leads to larger mean values; in contrast, the ST simulations yield positively skewed distributions of cloud fractions and relevant cloud water, which leads to lower mean values. These different skews stem from underestimated marine clouds, in particular over the ITCZ. This positively skewed distribution seems to be systematically deficient, since the skewness is prognostically calculated in the ST-CLC scheme and negative skewness is constrained by the current scheme settings. This calculated skewness could be improved by tuning the skewness parameters. Tompkins (2008) recommended modifying the skewness to promote simulating negative skewness, but positive skewness still appears in the tropics. The distributions in the RH simulations are more realistic than those in the ST simulations. However, the global annual mean values of cloud water in the ST simulations are relatively close to the observations than are the RH simulations (see Table 4.1). The overestimation of cloud cover and relevant cloud and climate parameters in the RH simulations could be associated with the coarse resolution (T42L19) that is used. The RH-CLC scheme depends on the model resolution (Tompkins, 2005), since this scheme determines cloud fractions with the variance of humidity within the grid box. The overestimated cloud cover could therefore be attenuated by applying a higher resolution.

Chapter 8

Conclusion and outlook

This thesis focuses on the effects of aerosols on clouds and climate using the chemistry-climate EMAC model, with a particular focus on aerosol chemical composition effects on warm cloud formation (see **Chapter 1**). The cloud droplet nucleation scheme, which represents an important contributor to aerosol and cloud interactions in the EMAC model, is used to calculate the CCN efficiency of aerosols. The simulated cloud properties and climate status are integrated with the results of cloud droplet nucleation schemes and cloud cover schemes based on double moment cloud microphysics parameterization. The different aerosol activation results in a distinct cloud droplet size spectrum, which corresponds to the aerosol composition effects for each STN and HYB cloud droplet nucleation scheme (see **Chapter 2**). The κ-method is for the first time incorporated into an existing cloud droplet nucleation scheme to calculate hygroscopicity and critical supersaturation of aerosols (HYB), and the performance of the modified scheme is compared with the osmotic coefficient model (STN). The experiments are designed to enable a comprehensive understanding of aerosol-cloud interactions, and to understand the significance of the interactions among the simulated clouds and climate system (see **Chapter 3**). In addition, since the calculated cloud coverage is an important determinant of cloud radiative effects (in addition to cloud droplet size and number distribution) and is influencing the nucleation process two cloud cover schemes (RH-CLC and ST-CLC) have been examined and their effects on the simulated cloud properties and relevant climate parameters have been investigated.

Evaluation of performance (Chapter 4)

In Chapter 4, the performance of both cloud droplet nucleation parameterizations and cloud cover schemes in the EMAC model are evaluated using the observations. The assessment of general performance, using Taylor diagram and skill scores (Taylor, 2001),

is based on spatial pattern similarity and variation between the simulations and observations.

- The current EMAC model set-ups perform better over continents with all combinations of the cloud droplet nucleation and cloud cover schemes. Over oceans, the simulated cloud and climate parameters have larger variations than the observed variability, and relatively lower pattern correlations with observations than the continental simulations. Larger centered root mean square (CRMS) errors (ranging from 0.55 to 1.0) also appear when comparing marine parameters to the calculated skill scores. More than 83% of the simulated continental parameters in the present study approach higher than "Good" skill performance, with skill scores over 0.8500. Over the oceans, the overall skill scores are relatively lower than ones in the continental parameters; nevertheless, the simulated TCC and LCRE are relatively skillful (mostly "Very good", i.e., higher than 0.9000), with the rest of the simulated TCC and LCRE mostly rated as "Fair" (ranging from 0.8499 to 0.7500). The rating of overall performance is, on average, about 25% higher for continental than for marine values. This is in part due to the constrained feedbacks between ocean and air caused by using a prescribed sea surface temperature.

- To consider the aerosol-cloud feedback, the HYB scheme applies the κ-method to the ARG cloud droplet nucleation scheme. This is found to be a better method for predicting cloud and climate parameters for both cloud cover schemes over land than the standard ARG scheme (osmotic coefficient model). Although it is difficult to conclude which model setup performs better over the ocean, due to the constraints of the prescribed SST and SIC, the skills scores generally indicate that the model performs higher than "Fair" to "Good".

- The relative humidity threshold cloud cover scheme (RH-CLC) offers a better simulation of total cloud cover and the relevant parameters than the statistical cloud cover scheme (ST-CLC), with the HYB activation scheme and single moment microphysics (REF); in general, the ratings for the RH simulations are more than 10% higher than the ST-simulations. The ST-CLC scheme seems to more sensitively simulate the cloud properties and climate parameters corresponding to aerosol-cloud interactions than the RH-CLC scheme.

Main results from this study

- **Aerosol activation (Chapter 5)**
  The simulations are sensitive to aerosol activation, which is strongly governed by the cloud droplet nucleation schemes (STN and HYB; i.e., the activated aerosol fractions in the accumulation and coarse modes (about 60% for STN, about 40% for HYB) and in the Aitken mode (about 20% for STN, about 12% for HYB). This distinct aerosol activation shows sensitivity to aerosol chemical composition for all particle sizes, especially for the Aitken mode. As Aitken particles are the major component of the total aerosol number concentration, the activity of Aitken particles strongly contributes to the total cloud droplet formation and spectrum, and thereby affecting cloud structure and peroperties. The total cloud droplet number concentration (N_d) in the HYB simulations is about 50% lower than in the STN simulation. The differences are more pronounced at low altitudes than at high altitudes, since the chemical composition is likely to be important for the hygroscopic growth of droplets for freshly emitted particles. Furthermore, since environmental conditions are an important control factor for aerosol-cloud interactions, the cloud droplet number concentration and liquid water content show distinct sensitivity to region and altitude. For example, the Sahara desert, an extremely dry area where evaporation is more than twice the amount of rainfall, is less influenced by increases in CCN; in contrast, the subarctic regions show the strongest sensitivity, as the lower surface temperature amplifies the effects of the activated aerosols more than in other regions. These comprehensive changes exert regionally varying effects on climate status. The strongest cloud albedo effects are found in the Sub Arctic and Siberia, and the smallest effects were found in the Sahara desert. The overall effects of aerosol and cloud interactions are simulated with two different cloud cover schemes (RH-CLC and ST-CLC; see Chapter 7). Aerosol chemical composition is found to have a profound effect on cloud formation, which in turn affects cloud properties and climate parameters.

- **The effect of cloud droplet nucleation (Chapter 6)**
  The cloud droplet nucleation effects vary according to variables such as cloud water paths, cloud cover, cloud radiative effects, and precipitation. The strongest changes are found for cloud droplet number concentration (CDNC) and cloud water (LWP); compared to the reference simulations, the global mean of CDNC increased 38 – 203 %, and the global mean of LWP increased 97 – 331 % in the prognostic CDN simulations. These strong increases in CDNC decrease the efficiency of the formation of weak stratiform precipitation by up to 18 % over

land (6 % globally) and enhance cloud water loading. These large-scale changes lead to larger cloud cover and longer cloud lifetime, and contribute to high optical thickness and strong cloud cooling effects. This cools the Earth's surface, increases atmospheric stability, and reduces convective activity. The ability of an elevated CDNC to weaken or invigorate convective activity over both land and ocean is well demonstrated; in general, the enhanced cloud cooling effects over land are stronger than the released latent heat produced by condensation. This weakens convection and decreases convective precipitation over land. Over land, the convective available potential energy (CAPE) is reduced by 4 – 36 %, and the convective precipitation is decreased by 1 – 18 %. Over ocean, the latent heat is a major change in energy fluxes, as vertical heat transfer in constrained by using a prescribed sea surface temperature; this latent heat invigorates convection by 2 – 17 %, and increases convective precipitation by 1 – 16 %. The present investigation shows the important roles of aerosols and cloud interaction for cloud and climate simulations.

- **The effect of cloud cover scheme (Chapter 7)**
  The simulated clouds show a strong dependency on the cloud cover scheme, and different sensitivity to aerosol-cloud coupling. The statistical cloud cover scheme (ST-CLC) seems to be more sensitive to aerosol-cloud coupling, since this scheme uses a tighter linkage of local dynamics and cloud water distributions in the cloud formation process than the relative humidity threshold cloud cover scheme (RH-CLC). In general, the RH simulations calculate negatively skewed distributions of cloud fractions and relevant cloud water, which lead to larger mean values, while the ST simulations yield positively skewed distributions resulting in lower mean values; based on the global annual mean values, RH-CLC simulates larger total cloud cover (up to 23 % higher), higher liquid water path (up to 78 %), and stronger cloud albedo effect (up to 69 %) than does ST-CLC. This negative skew underestimates marine clouds in the ST simulations, particular over the intertropical convergence zone (ITCZ). This underestimation of total cloud cover may relate to systematic deficiency in the way that skew is calculated in the statistical cloud cover scheme (ST-CLC). For the RH simulations, the distributions of simulated clouds are relatively closed to those of the observations as compared to the ST simulations, but the overall properties (e.g., total cloud cover, cloud water content) are overestimated. The overestimation may be attenuated with higher resolution. This analysis depicts the importance of cloud cover scheme on simulating clouds and climate.

Further studies and open questions

To confirm the effects of aerosols and cloud interactions presented in this thesis, further studies would contribute to a better understanding of the effect of aerosol chemical composition on clouds and climate with the major types of large (i.e., mineral dust particle) and small (i.e., organic compounds) particles in the atmosphere.

- **Dust aerosol parameterization**
  In the GCM, dust particles are associated with a single variable to represent chemical compositions (i.e., species); uncertainties could therefore arise in the simulated properties. In calculating CCN activation, a set of sensitivity tests could assess different effective hygroscopicity values for dust (κ_{DU}), to represent the different chemical compositions of mineral dust. This could give a better understanding of the effect of the chemical composition of dust particles on clouds and climate.

- **Organic compound aerosol parameterization**
  For the regional and global climate modeling study, the total amount of OC is calculated from the total emission of organic matter, and the soluble composition fraction (WSOC) is estimated with an empirical parameter. This parameter also affects the CCN activation, cloud properties, and radiative effects on clouds and climate by changing the effective hygroscopicity parameter (κ) of each mode. This determines also the number concentration and the composition of soluble OC particles. A two-part sensitivity experiment for OC could assess the hygroscopicity of OC (κ_{OC}) and the conversion parameter of WSOC. Such an experiment could help decreases the uncertainty regarding the impact of OC particles on climate.

Appendix A

Abbreviations used in the dissertation

AOD Aerosol Optical Depth

AIE Aerosol Indirect Effect

AI Accumulation Insoluble mode

ARG Abdul Razzak and Ghan scheme

CAPE Convective Available Potential Energy

CCN Cloud Condensation Nuclei

CDN Cloud Droplet Nucleation

CDNC Cloud Droplet Number Concentration

CERES Clouds and the Earth's Radiant Energy System

CI Coarse Insoluble mode

CLC CLoud Cover scheme

CRE Cloud Radiative Effect

CS Coarse Soluble mode

CTH Convective cloud Top Height

DJF December-January-February

EBAF Energy Balanced And Filled

HYB Hybrid ARG CDN scheme (ARG-κ)

ICN Ice Crystal Number

IN Ice Nuclei

IPCC Intergovernmental Panel on Climate Change

ISCCP International Satellite Cloud Climatology Project

IWP(C) Ice Water Path (Content)

JJA June-July-August

LCRE Long wave Cloud Radiative Effect

LWP(C) Liquid Water Path (Content)

MODIS Moderate Resolution Imaging Spectroradiometer

NCRE Net Cloud Radiative Effect

NI Nucleation Insoluble mode

NS Nucleation Soluble mode

RH-CLC Relative Humidity threshold Cloud Cover scheme

SCRE Short wave Cloud Radiative Effect

STN Standard ARG CDN scheme

ST-CLC Statistical Cloud Cover scheme

TCC Total Cloud Cover

TOA the Top Of the Atmosphere

WVM Water Vapor Mass

Appendix B

Submodels

B.1 Aerosol dynamics and thermodynamics (GMXe)

The size and number distribution of aerosol are determined with the parameters in TableB.1.

Table B.1: Description of aerosol size and number with seven aerosol modes and standard deviation (σ)

Aerosol Mode		Range of radius	sigma (σ)
Hydrophilic			
Nucleation	(NS)	$< 0.005\mu m$	1.59
Aitken	(KS)	$0.005\ \mu m \leq r < 0.06\mu m$	1.59
Accumulation	(AS)	$0.06\ \mu m \leq r < 0.5\mu m$	1.59
Coarse	(CS)	$\geq 0.5\mu m$	2.00
Hydrophobic			
Aitken	(KI)	$0.005\ \mu m \leq r < 0.06\mu m$	1.59
Accumulation	(AI)	$0.06\ \mu m \leq r < 0.5\mu m$	1.59
Coarse	(CI)	$\geq 0.5\mu m$	2.00

B.2 Convection (CVTRANS and CONVECT)

Convection is an important process to vertically transport and exchange the energy and airmass including the change in the hydrological cycle and thereby influencing the general atmospheric thermodynamics. The intensity of convection determines the convective cloud top height, vertical extension, and convective precipitation, and influences on the vertical exchange of air mass flux. The strength depends on the atmospheric stability and generally measured by CAPE (Convective Available Potential Energy) in J/kg. It is calculated by vertically integrating the local buoyancy of air parcel from the

level of free convection (LFC) to the equilibrium level (EL). The model has several options to calculate the convection and relevant parameters in the submodel CONVECT, and the current study uses the Tiedtke scheme (Tiedtke, 1989). In the model, CAPE is considered as the effect of the liquid water (l) and defined with

$$CAPE = \int_{z_{LFC}}^{z_{EL}} g(\frac{T_{v,parcel} - T_{v,env}}{T_{v,env}} - l)dz \tag{B.1}$$

where z_{LFC} is the height of LFC, z_{EL} is the height of EL, $T_{v,parcel}$ is the virtual temperature of the air parcel, $T_{v,env}$ is the virtual temperature of the environment, and the g is the gravitational acceleration. With the estimated values, the submodel CVTRANS calculates the entrainment and detrainment of the air mass flux in each vertical model layer as well as water flux.

B.3 Emission (OFFLEM/ONLEM, LNOX and TNUDGE)

Emissions of gases and aerosols are treated by two parts for prescribed and online-calculated emission in the submodel OFFLEM and ONLEM, respectively. OFFLEM calculates offline emissions and stored data to simulated model such as GHGs (green house gases, i.e., $N_2O, CH_4, CFCs$), and $NO, CO, HCHO, HCOOH$, higher hydrocarbons (e.g., C_2H_4, C_2H_6, C_3H_6 and etc.), NH_3, the volcanic SO_2 emission and anthropogenic SO_2, NO_x, and the aerosol which is relatively constant such as dust (DU), sea spray (SS), and etc. ONLEM treats the aerosols and gases which are strongly dependent on the meteorological condition or time as calculating tendencies or fluxes of emissions at each time step during simulations, i.e., DMS, BC, OC, and the biogenic NO. TNUDGE treats the pseudo-sources/sinks using trace nudging method for CH_4. These three submodels presented and described in Kerkweg et al. (2006) and are coupled with the aerosol submodel GMXe. LNOX calculates the production of NO_x by lighting and the detailed description is found in Tost et al. (2007b).

B.4 Classification of cloud type (SATSIMS)

This submodel diagnoses cloud types with the classification of simulated clouds into 49 number of types with the aerosol optical thickness and cloud top pressure (See figure B.1). The classification is based on the International Satellite Cloud Climatology Project (ISCCP) simulator. The individual 49 small boxes represent 49 classifications,

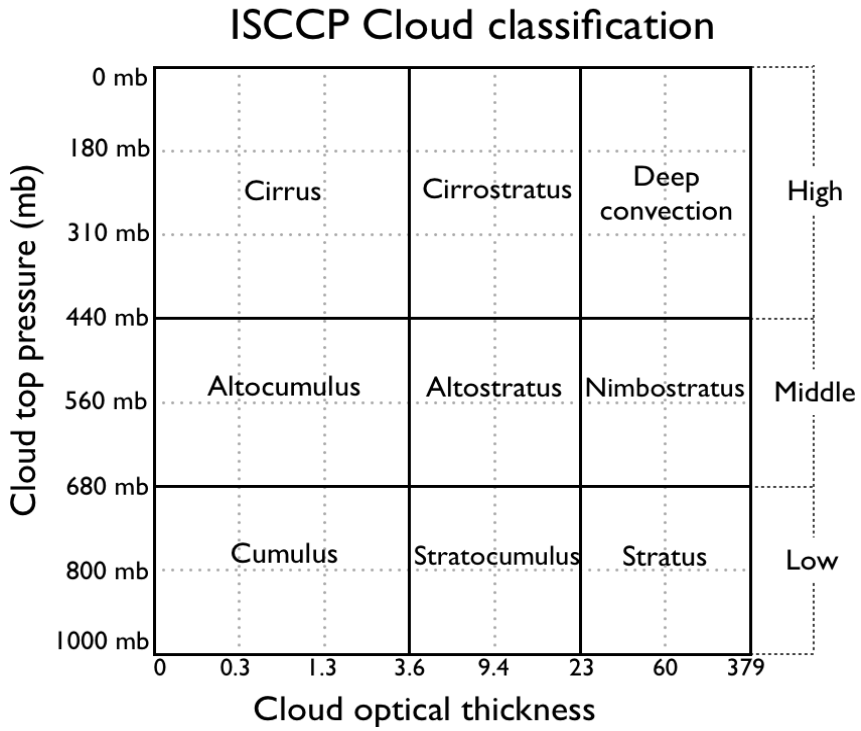

Figure B.1: ISCCP cloud classification

and are consisted of nine cloud types. These speciated cloud types are largely divided into the high-, middle- and low-level clouds by cloud height and separated nine types of clouds by cloud optical thickness. High-level clouds occurs above 440 mb and mainly include cirrus, cirrostratus and deep convection. Middle-level clouds appear in between 440 mb and 680 mb and represent with altocumulus, altostratus and nimbostratus. Low-level clouds are formed near the surface from 1000 mb to 680 mb. The ISCCP simulator has been evaluated with the ground-based data by Gerald at el.(2010).

B.5 Radiation for all wavelengths (RAD4ALL)

This submodel purpose to calculate the radiative transports regards with radiative active chemical species, aerosol and cloud properties. The energy fluxes are dependent on the composition of atmosphere, of aerosol and gases, cloud water budget and cloud cover as well. In this study, the radiative active chemical species are considered as $CO_2, CH_4, O_3, NO_2, CFC_{11}$ and CFC_{12} using uniform volume mixing ratio of the year of 2000; the integrated effects of aerosol and cloud properties are given prognostic cloud cover, specific humidity, cloud water and ice and cloud droplet/ice number (Rockel et al., 1991). The shortwave are diagnosed by the single scattering properties based on

Mie calculations with idealized cloud droplet and ice crystals size distributions (Stier et al., 2005, 2006).

B.6 Aerosol optical properties (AEROPT)

The submodel AEROPT calculates the optical properties of aerosols such as $POM, BC, DU, SS, WASO$ (i.e., $NH_4^+, SO_4^{2-}, HSO_4^-, NO_3^-$, etc.) with the extinction coefficient σ for the short and longwave spectrum.

B.7 Other submodels

- overall atmospheric chemical reactions in troposphere and stratosphere are calculated by the submodel MECCA1 (Sander et al., 2005).
- the model treats online-calculated the photolysis rates in the submodel JVAL (Jöckel et al., 2006)
- NO_x production by lighting in the submodel LNOX (Tost et al., 2007b), respectively.
- the heterogeneous reaction rates on stratospheric and tropospheric aerosols are provided by submodel HETCHEM (Jöckel et al., 2006).
- the relevant atmospheric structure of tropopause such as the height of the planetary boundary layer is determined in the submodel TROPOP (Jöckel et al., 2006)
- the processes of dry and wet deposition are treated in the submodel DRYDEP and SCAV, respectively; the submodel SCAV describes the scavenging processes of gases or aerosol by precipitation fluxes as wet deposition and liquid phase chemistry in large-scale (the submodel CLOUD) as well as in convective clouds and precipitations (the submodel CONVECT).
- the sedimentations of aerosol particles and components are estimated in the submodel SEDI.

The further information could be found the reference papers of each submodels in Table 2.1.

Appendix C

Cloud droplet nucleation (CDN) parameterizations

C.1 Diagnostic CDNC parameterizations

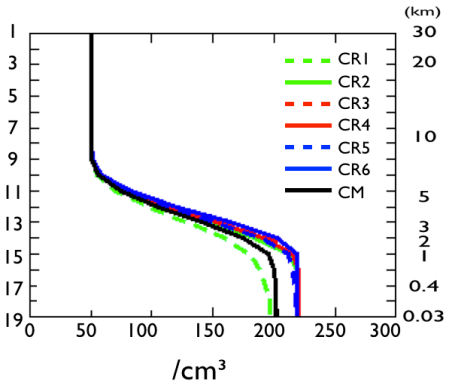

Figure C.1: Vertical distribution of CCN (unit = cm^{-3}) and mean values (CM) in the REF simulations for the continental regions CR1 – CR6. Based on Lohmann and Roeckner (1996)

CP1 Lohmann and Roeckner(1996)

the function of CDNC is pressure initial condition of land (220) and ocean (80)

CP2 Rotstayn(1997)

$\mathrm{CDNC}_{land} = 173.8 \times 10^6 \times \mathrm{M}_{sulfate}{}^{0.26}$

$\mathrm{CDNC}_{ocean} = 114.8 \times 10^6 \times \mathrm{M}_{sulfate}{}^{0.48}$

$\mathrm{CDNC} = \mathrm{CDNC}_{land} \times \mathrm{F}_{slf} + \mathrm{CDNC}_{ocean} \times (1\text{- } \mathrm{F}_{slf})$

CP3 sulfate, reference from Jones et al., (2001)
CDNC = 3.75 × 10^8 × (1 - exp (-2.5 × 10^{-9})) × $N_{sulfate}$

CP4 sulfate, sea salt, organic matters, reference from Menon et al., 2002
$CDNC_{land}$ = $M_{sulfate}$× $M_{OM}{}^{0.13}$ × 257.04 × 10^6
$CDNC_{ocean}$ = $M_{sulfate}{}^{0.5}$ × $M_{OM}{}^{0.13}$ × $M_{SS}{}^{0.05}$ × 257.04× 10^6
CDNC = $CDNC_{land}$ × F_{slf} + $CDNC_{ocean}$ × (1- F_{slf})

$M_{sulfate}$: mass of sulfate, M_{OM}: mass of organic matter, M_{ss}: mass of sea spray, $N_{sulfate}$: number of sulfate, F_{slf}: fraction of land and sea

C.2 Prognostic CDN parameterization

C.2.1 Numerical solution of S_{max} in ARG scheme

The change of S dependent on time during adiabatically rising air parcel with uniform updraft (V) can be defined by follows (Leaitch et al., 1986);

$$\frac{dS}{dt} = \alpha V - \gamma \frac{dw}{dt} \tag{C.1}$$

where α and γ are size invariant coefficients that are influenced by temperature (T) and the water vapor pressure (e_s) and expressed by

$$\alpha = \frac{gM_wL}{C_pRT^2} - \frac{gM_a}{RT} \tag{C.2}$$

$$\gamma = \frac{RT}{e_sM_w} + \frac{M_wT}{C_ppM_aT} \tag{C.3}$$

where g: gravity, M_w: molecular weight of water, M_a: molecular weight of aerosol, L: latent heat of evaporation, R: gas constant for dry air, T: temperature, C_p: heat capacity of air, V: updraft velocity, p: pressure, e_s: saturation vapor pressure at temperature T.

The condensation rate (dw/dt) of the activated droplets is calculated with the sum of the hygroscopic growth of particles during the changes of S_c and can be expressed with

$$\frac{dw}{dt} = 4\pi\rho_w \sum_{i=1}^{7} \int_0^S r_i^2 \frac{dr_i}{dt} \frac{dn_i(S_c)}{dr_{d,i}} dS_c \tag{C.4}$$

where r_i is the radius of the forming droplet in aerosol mode (i) and $n_i(S_c)dS_c$ is the

number concentration of activated particles over the dry radius in aerosol mode (i) between S_c and $S_c + dS_c$.

The growth of particle can be determined by the change of the droplet radius over time ($\frac{dr_i}{dt}$) that is derived by Leaitch et al. (1986);

$$\frac{dr_i}{dt} = \frac{G}{r_i}\left(S_i - \frac{A}{r_i} + \frac{Br_{d,i}^3}{r_i^3}\right) \tag{C.5}$$

where the size dependent growth coefficient (G) denotes the diffusion of heat and moisture to the particle and the chemical composition effect (B), and r_i is a radius and $r_{d,i}$ is a dry radius in aerosol mode (i).

In order to use numerical solutions for estimates S_{max}, the same assumption in Abdul-Razzak and Ghan.,[1998, 2000] are taken that S_c is relative small to S_{max} (i.e. $S_c \ll S_{max}$ and $r_c \ll r_{min}$), therefore the subsequent growth terms are negligible under these conditions and derived by

$$S_{max} = \left[\sum_{i=1}^{7} \frac{1}{S_{c,i}^2}\left(f_i\left(\frac{\varsigma}{\eta_i}^{\frac{3}{2}}\right) + g_i\left(\frac{S_{c,i}^2}{\eta_i + 3\varsigma}\right)^{\frac{3}{4}}\right)\right]^{-\frac{1}{2}} \tag{C.6}$$

where f_i and g_i are hired to solve this equation numerically with an error range in less than 25% and are expressed

$$f_i \equiv 0.5\exp(2.5\ln^2\sigma_i) \tag{C.7}$$

$$g_i \equiv 1 + 0.25\ln\sigma_i \tag{C.8}$$

ζ and η_i are dimensionless parameters to design for the neglecting terms of curvature, solute and gas kinetic effects, with adjusting coefficients in order to eliminate errors caused by simplifying assumptions and given by

$$\zeta \equiv \frac{2A}{3}\left(\frac{\alpha V}{G}\right)^{\frac{1}{2}}, \eta_i \equiv \frac{\left({}^{\alpha V}/_{G}\right)^{\frac{3}{2}}}{2\pi\rho_w\gamma N_i} \tag{C.9}$$

where V is the constant vertical updraft, and G is expressed the growth coefficient in terms of diffusion of heat and moisture to the particles as a size-dependent term, and α and γ are hired to express the supersaturation rate on time dependent as size-invariance coefficients.

The activated aerosol fractions (AF) is expressed by the ratio of the number of activated aerosol (N_i) to the total number of available aerosol particles ($N_{a,i}$) in each

aerosol mode (i) and can estimate with

$$AF_i = \frac{1}{2}[1 - erf(u_i)], N_i = AF_i \times N_{a,i} \tag{C.10}$$

where u_i is defined with the geometric standard deviation σ_i of aerosols in mode (i) and given by

$$u_i \equiv \frac{\ln\left({}^{r_{c,i}}/_{\bar{r}_i}\right)}{\sqrt{2}\ln\sigma_i} = \frac{\ln\left({}^{S_{c,i}}/_{S_{max}}\right)}{3\sqrt{2}\ln\sigma_i} \tag{C.11}$$

and originated from Leaitch et al. (1986). These all equations and values are described in detail by Abdul-Razzak and Ghan (1998, 2000).

C.3 Hygroscopicity and relevant parameters in STN and HYB

For the multi-compounds aerosols (i.e., DU, BC, and OC), the empirical variables are applied to the calculation of B_j; the Osmotic coefficient (ϕ_{DU}) is based on east Asian dust observed by Nishikawa et al. (1991) and Nishikawa (1993). To simpler calculation of water uptake, the fixed parameters of ϕ_j and B_j are applied, which could be varied depending the solution. The density (ρ_{DU}) and molecular weight (M_{DU}) of soil dust are based on the chemical composition of $CaSO_4$ in the aerosol submodel GMXe.

The individual κ values for aerosol particles (κ_j) are mainly from the the hygroscopic parameters in Petters and Kreidenweis (2007); 0.61 for $(NH_4)_2SO_4$, 0.67 for NH_4NO_3, 1.28 for $NaCl$, 0.90 for H_2SO_4, 0.88 for $NaNO_3$, 0.91 for $NaHSO_4$, 0.80 for Na_2SO_4, and 0.65 for $(NH_4)3H(SO_4)_2$; 0.0 for black carbon (BC) and 0.1 for organic carbon (OC) (Wang et al., 2008; Gunthe et al., 2009; Pöschl et al., 2009; Dusek et al., 2010; King et al., 2010; Pringle et al., 2010); 0.03 for dust particle (DU), recommended as a global mean of κ_{DU} in Koehler et al., 2009. The calculated κ is comparable to derived values from measurement for estimate the CCN activity according to Rose et al. (2010) and Gunthe et al. (2009).

Table C.1: Hygroscopicity of aerosol components, including the number of ions the salt dissociates into water (μ), the osmotic coefficient (ϕ), the mass fraction of soluble material (ϵ), the density (ρ_a) and the molecular weight (M_a) of the aerosols.

Component (j)	μ_j	ϕ_j	ϵ_j	ρ_j	M_j	B_j	κ_j
Ammonium sulfate	3.0	0.7	1.0	1.77	132.17	0.51	0.61
Sea salt	2.0	1.0	1.0	2.17	58.44	1.16	1.28
Soil dust	2.0	0.45	0.13	2.65	40.08	0.14	0.03
Organic carbon	1.0	1.0	0.047	2.0	12.11	0.14	0.1
Black carbon	1.0	1.0	1.7e-07	2.0	12.11	0.5e-7	0.0

Appendix D

Statistical analysis

D.1 Weighted average

In this thesis, all global and regional mean values are based on area weighted averaging calculation due to uneven gridbox size as shown by zonal distribution of the proportion of grid box area over total grid area (Fig. D.1). The vertical mean is used to base on volume-weighted or mass-weighted averaging calculation depending on variables. The vertical variation of gird values are shown by Table D.1.

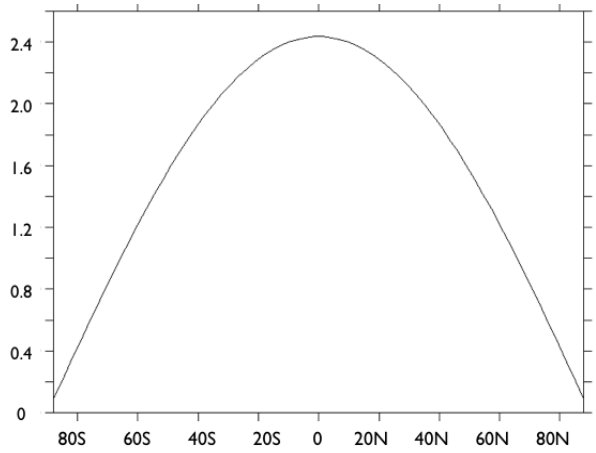

Figure D.1: Zonal distribution of the proportion of gridbox area over the total grid area.

D.2 Taylor Diagram

Taylor diagram based on Taylor (2001, 2005) summarizes a pattern resemblance between two patterns (e.g., simulation and observation) with statistical values (i.e., the

Table D.1: Vertical distribution of grid values: global means of grid volume (GRVOL; unit = m^3), grid mass (GRM; unit =kg), grid mass of dry air (GRMD; unit = kg), and proportion of total corresponding values for P-GV, P-GRM, and P-GRMD (unit = %).

Model Level	GRVOL (m^3)	GRM (kg)	GRMD (kg)	P-GV (%)	P-GRM (%)	P-GRMD (%)
1	1.019E+15	1.554E+13	1.554E+13	34.33	2.026	2.020
2	3.153E+14	1.554E+13	1.554E+13	10.62	2.026	2.020
3	1.891E+14	1.616E+13	1.616E+13	6.37	2.106	2.100
4	1.540E+14	1.959E+13	1.959E+13	5.19	2.553	2.546
5	1.444E+14	2.567E+13	2.567E+13	4.87	3.346	3.336
6	1.420E+14	3.359E+13	3.359E+13	4.79	4.377	4.364
7	1.385E+14	4.250E+13	4.250E+13	4.67	5.539	5.523
8	1.339E+14	5.156E+13	5.157E+13	4.51	6.720	6.701
9	1.275E+14	5.990E+13	5.992E+13	4.30	7.806	7.786
10	1.188E+14	6.664E+13	6.669E+13	4.00	8.685	8.666
11	1.079E+14	7.099E+13	7.108E+13	3.64	9.251	9.236
12	9.533E+13	7.223E+13	7.240E+13	3.21	9.414	9.408
13	8.171E+13	6.989E+13	7.014E+13	2.75	9.108	9.114
14	6.732E+13	6.374E+13	6.409E+13	2.27	8.307	8.327
15	5.266E+13	5.403E+13	5.443E+13	1.77	7.041	7.073
16	3.816E+13	4.154E+13	4.192E+13	1.29	5.414	5.447
17	2.444E+13	2.766E+13	2.796E+13	0.82	3.605	3.633
18	1.271E+13	1.469E+13	1.485E+13	0.43	1.914	1.930
19	5.028E+12	5.873E+12	5.940E+12	0.17	0.765	0.772

centered root mean squared (RMS) difference, the spatial pattern correlation, and the standard deviation). In this thesis, the diagram uses to evaluate the model performances by presenting the pattern similarities with the model results and the observations. Taylor diagram can be described with the following formula (Taylor, 2001):

$$E'^2 = {\sigma_x}^2 + {\sigma_r}^2 - 2\sigma_x\sigma_r R, \tag{D.1}$$

where R is the correlation coefficient, E' is the centered RMS difference between the model results and the observations (or reference data), and σ_x and σ_r are the standard deviations of the model results and the observations (or reference data), are given by;

$$R = \frac{\frac{1}{N}\sum_{n=1}^{N}(x_n - \bar{x})(r_n - \bar{r})}{\sigma_x\sigma_r} \tag{D.2}$$

$$E'^2 = \frac{1}{N}\sum_{n=1}^{N}[(x_n - \bar{x}) - (r_n - \bar{r})]^2 \tag{D.3}$$

$$\sigma_x^2 = \frac{1}{N}\sum_{n=1}^{N}[(x_n - \bar{x})]^2, \sigma_r^2 = \frac{1}{N}\sum_{n=1}^{N}[(r_n - \bar{r})]^2 \tag{D.4}$$

To plot different variables (i.e., the relevant cloud and climate parameters) on a

same digram, the simulated standard deviation and centered RMS error are normalized by the corresponding observed standard deviation (σ_r). Note that, the correlation coefficient (R) is not changed by a normalization. The normalized statistical variables are calculated with the following equation;

$$\hat{E'} = \frac{E'}{\sigma_r}, \hat{\sigma_x} = \frac{\sigma_x}{\sigma_r}, \hat{\sigma_r} = 1 \tag{D.5}$$

D.3 Skill score

To evaluate the performance of the CDN and CLC parameterization in the EMAC model, a relative skill score is calculated with by the simple formula (S),which is based on Taylor (2001);

$$S = \frac{4(1+R)}{(\hat{\sigma_x} + \frac{1}{\hat{\sigma_x}})^2(1+R_0)} \tag{D.6}$$

where R_0 is the maximum correlation coefficient (0.9976) in this study. This model skill score is determined by their pattern variability and correlation with observations. If the simulated standard deviation is close to the observed standard deviation (i.e., $\hat{\sigma_x}$ approaches 1) and the correlation coefficient gets higher (i.e., R is close to R_0), the model skill score (S) gets closer to 1 (most skillful). Note that the RMS error may not necessarily contribute to a high skill score. Further detailed information could be found in Taylor (2001).

D.4 Internal consistency reliability

To avoid misreading the perturbation of the status in which model did not reach the equilibrium. For this reason, I had been validated simulated variables with the repeatability (or test-retest reliability) before evaluating model results with observations. To represent the value with 95% repeatability conditions, the statistical formulae are used the probability if the value followed the σ-distributions. The 95% confidence intervals are calculated with statistical formulae, i.e., standard deviation random errors and systematic error during simulations.

$$E[X] = \mu, \sigma = \sqrt{E[(X-\mu)^2]} \tag{D.7}$$

$$SD(\sigma) = \sqrt{\frac{1}{N-1}\sum_{n=1}^{N}(x_i - \bar{x})^2} \tag{D.8}$$

$$SE = \frac{\sigma}{\sqrt{N}} \tag{D.9}$$

Degree of freedom (df) = N-1 The 95% confidence interval (C.I.) is calculated by

$$95\%C.I. = mean \pm SE \times \alpha \tag{D.10}$$

for small trials, if the value followed the Z distribution (i.e., α=2.262, df=9), the confidence level (α) the degree of freedom (df=N-1)

Appendix E

Cloud radiative effects

This section purposes to assist Chapter 4 with additional model results for cloud radiative effects at the top of the atmosphere.

E.1 Land and ocean

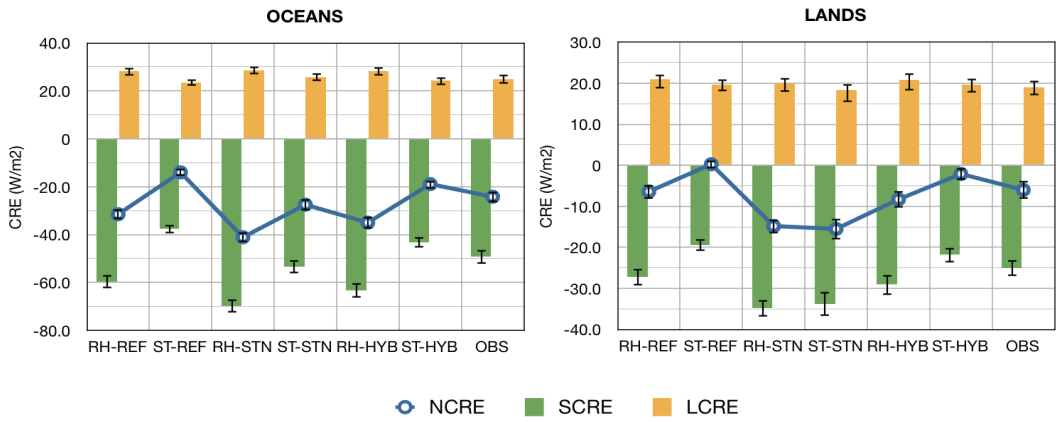

Figure E.1: Cloud radiative effects at the top of the atmosphere (TOA) over land and ocean. Green bar, yellow bar, and blue line represent the SCRE, LCRE and NCRE, respectively

Fig.E.1 shows the calculated marine and continental mean of CREs with the observation. The RH-simulations are generally overpredicted both SCRE and LCRE due to the larger cloud cover and cloud water over ocean as shown by Fig. 6.4 and 6.5. The overestimated CREs are also found in the deviation and relative difference of the net cloud radiation effect, (Fig.4.7 and F.8). The estimated CRE is also related to the vertical distribution of cloud properties such as cloud droplet number concentration, cloud cover, and water. As shown by Fig.F.2, most pronounced differences are indicated at

Table E.1: Summary of dominant aerosol types in the selected regions over oceans, including spatial information.

Regions over oceans		Location	Expected aerosol types
Western North Atlantic	(WA)	31-41N:65-75W	Anthropogenic aerosols
Bay of Bengal	(BB)	9-19N:85-95E	Anthropogenic aerosols
Eastern South Atlantic	(EA)	10-20N:18-28W	Dust(Summer)
Arabian Sea	(AS)	10-20N: 62-72E	Dust(Summer), Anthropogenic aerosols (Winter)
African Biomass	(AF)	3-13S:0-10E	Carbonaceous anthropogenic aerosols
South Indian Ocean	(IO)	10-20N:70-80E	Maritime sea salt (pristine)

low clouds, particularly at the PBL height.

E.1.1 Regional distribution of CREs

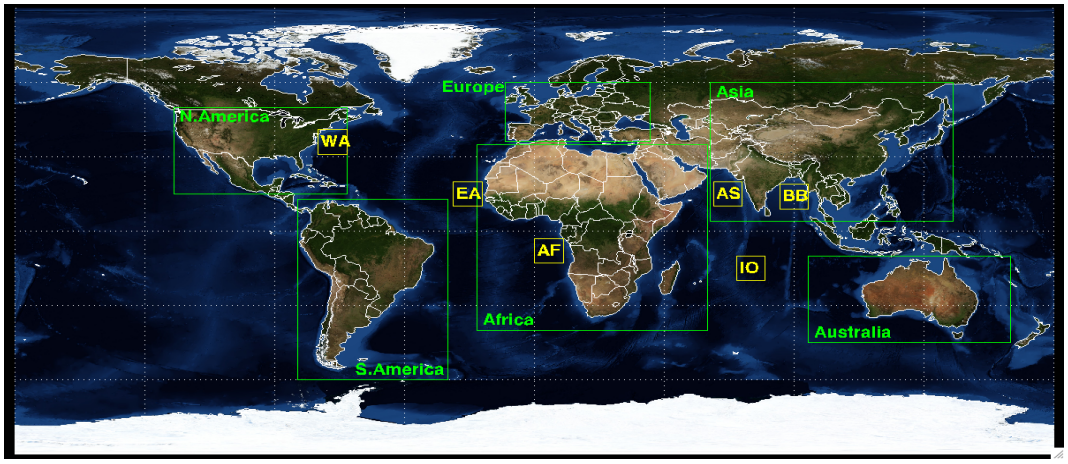

Figure E.2: Summary of the regions used in the regional analysis

Fig. E.2 shows the selected main continental and marine regions to evaluate cloud radiative effects compared to observations. Large green boxes and small yellow boxes represent main continents and marine regions where strongly influenced by continental airflow. The selected marine regions cover 10° × 10° area. Locational information and expected dominant aerosols of marine regions are summarised in TableE.1. This selected regions are based on aerosol column burden distribution and referred to Jones et al., (2009).

The estimated CREs in Australia and Africa depicts the importance of cloud cover distribution in order to estimate CREs. Over these regions, the large differences are found between the observations MODIS and ISCCP (see in Fig. 4.4). The estimated cloud radiative effects also show large differences among the simulations and observations due to large distances (errors) of cloud cover distribution. Coastal regions also

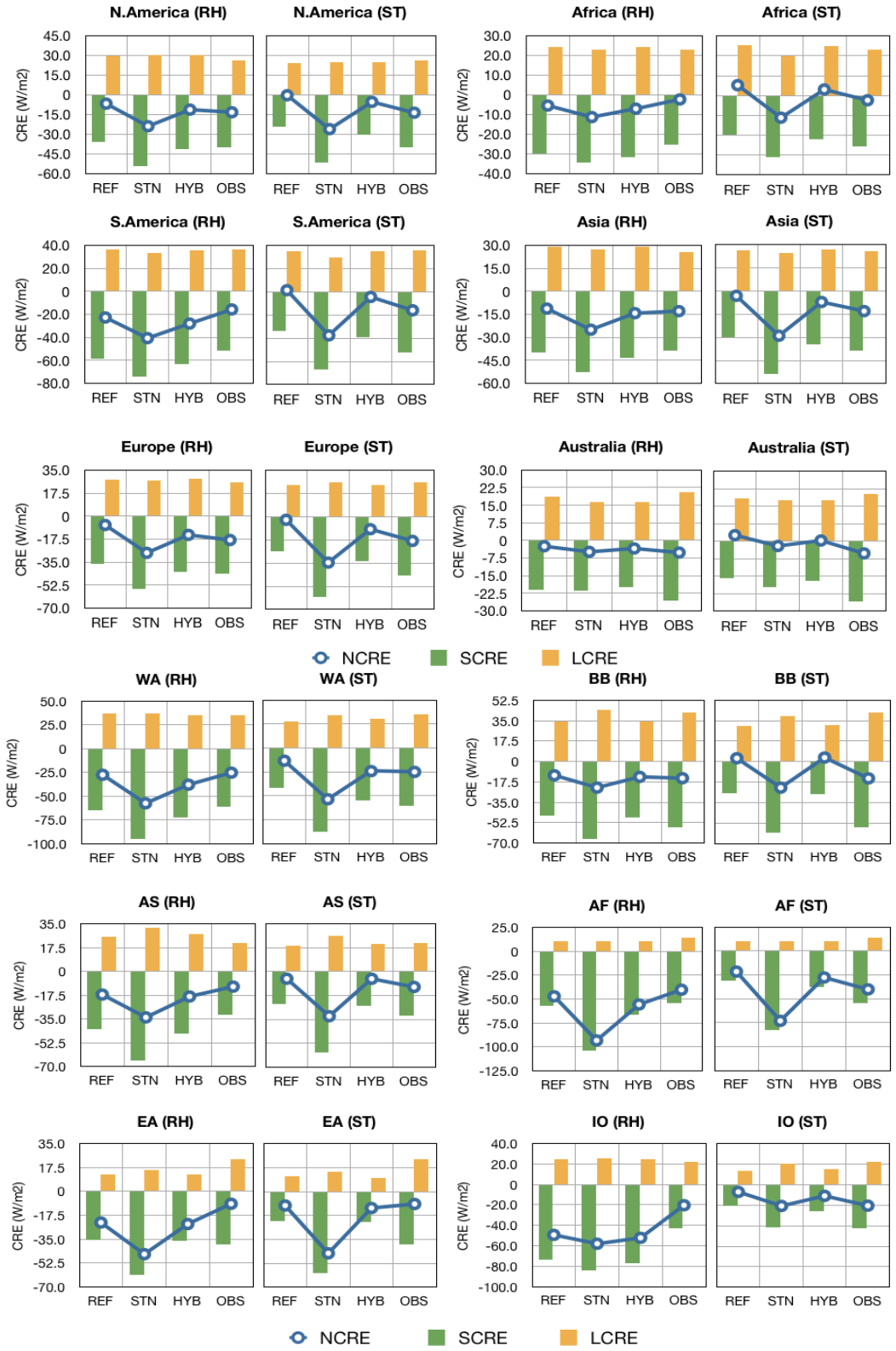

Figure E.3: Cloud radiative effect at the top of the atmosphere over the continents and the ocean (unit = W/m^2).

have difficulties to calculate precise variables due to the low model resolution (T42) (see Fig. 4.7). This coarse horizontal resolution could suppress horizontal variabilities with geographical differences (Pringle et al., 2010b).

All simulations calculate NCRE over Australia reasonably close to the observed NCRE, but the simulated SCRE and NCRE are underestimated. Over South America, ST-STN overestimates SCRE, which seems to be overly sensitive to dominant aerosols BC and POM. As discussed in Chapter 5, the STN simulations calculate high CDNC in this region as compared to the HYB simulation. High CDNC contributes to increase in cloud optical properties and stronger cooling effects. Over Europe and Asia, the HYB simulations performs better to predict CREs in most continental regions. Particularly RH-HYB is the best combination to estimate CREs using the EMAC model. Overall, the HYB simulations show a relative good performance in most continental regions at the limited content to CREs (see Fig. E.3). The distances from the observations are significantly reduced in the HYB simulations compared the STN simulations, particularly for North America, Asia and Europe (see Fig. 4.7).

Over the marine regions, Western North Atlantic (WA) and Bay of Bengal (BB) are directly influenced by North America and India where anthropogenic aerosols are dominant as polluted ocean regions. Both regions are expected similar amount of N_{ccn} (see Fig.5.2), but large differences are found in the calculated CREs in all simulations (Fig. E.3). These large differences in CREs are caused by the different atmospheric conditions, which leads to different cloud properties (e.g, LWP) and thereby significantly different CREs. Both Eastern South Atlantic (EA) and Arabian Sea (AS) are exposed by dust aerosols particularly during summer. The HYB simulations perform better in two regions than the STN simulations (see Fig. E.3). South Atlantic and near Southeast Africa (AF) have the largest carbonaceous aerosols. The obtained CREs in RH-REF, RH-HYB and ST-HYB are close to the observations. Indian ocean (IO) represents a pristine marine region where aerosols are mainly consisted of sea salt. This region seems more influenced by cloud cover scheme than by cloud droplet nucleation scheme. The estimated CREs shows noticeable differences dependent on cloud cover distribution simulated by RH-CLC and ST-CLC (see Figs. 4.5 and 4.6). This confirms the important of cloud cover scheme to simulate marine clouds and the associated properties.

Table E.2: The internal consistency reliability of cloud radiative effects at the top of the atmosphere as simulated by EMAC and as estimated by the observations (CERES EBAF). Values are presented with the standard deviation(SD), the standard error (SE), and the 95% confidence interval (CI) of the free-running simulations with prognostic CDN schemes.

	RH-REF	ST-REF	RH-STN	ST-STN	RH-HYB	ST-HYB	OBS
GLOBAL							
NCRE (MEAN)	-28.05	-9.30	-39.22	-26.59	-31.73	-14.13	-21.05
SD (standard deviation)	0.21	0.10	0.26	0.12	0.14	0.14	0.32
SE (standard error)	0.09	0.04	0.08	0.04	0.05	0.04	0.10
95% CI (confidence interval)	0.26	0.12	0.19	0.08	0.10	0.10	0.23
SCRE (MEAN)	-56.56	-33.53	-67.88	-52.07	-60.29	-38.86	-47.26
SD (standard deviation)	0.29	0.10	0.24	0.13	0.11	0.18	0.25
SE (standard error)	0.13	0.05	0.07	0.04	0.04	0.06	0.08
95% CI (confidence interval)	0.36	0.13	0.17	0.09	0.08	0.13	0.18
LCRE (MEAN)	28.51	24.22	28.66	25.48	28.57	24.74	26.21
SD (standard deviation)	0.09	0.05	0.07	0.06	0.06	0.07	0.19
SE (standard error)	0.04	0.02	0.02	0.02	0.02	0.02	0.06
95% CI (confidence interval)	0.11	0.06	0.05	0.04	0.04	0.05	0.13
OCEAN							
NCRE (MEAN)	-31.50	-14.00	-41.1	-27.5	-35.0	-18.9	-24.2
SD (standard deviation)	2.15	1.51	2.15	2.4	2.58	1.88	2.38
SE (standard error)	0.96	0.68	0.68	0.75	0.81	0.59	0.75
95% CI (confidence interval)	2.67	1.87	1.54	1.69	1.84	1.34	1.70
SCRE (MEAN)	-59.60	-37.60	-69.8	-53.3	-63.2	-43.1	-49.1
SD (standard deviation)	2.82	2.09	2.82	2.87	3.2	2.52	3.1
SE (standard error)	1.26	0.93	0.89	0.91	1.02	0.80	0.98
95% CI (confidence interval)	3.50	2.59	2.02	2.05	2.30	1.80	2.23
LCRE (MEAN)	28.2	23.6	28.7	25.8	28.2	24.2	24.9
SD (standard deviation)	1.90	1.55	1.90	1.83	2.02	1.81	1.96
SE (standard error)	0.85	0.69	0.60	0.58	0.64	0.57	0.62
95% CI (confidence interval)	2.36	1.93	1.36	1.31	1.45	1.29	1.40
LAND							
NCRE (MEAN)	-6.40	0.25	-14.8	-15.5	-8.3	-2.1	-6.0
SD (standard deviation)	1.78	1.10	1.78	2.67	2.11	1.53	2.24
SE (standard error)	0.80	0.49	0.56	0.85	0.67	0.48	0.71
95% CI (confidence interval)	2.21	1.37	1.27	1.91	1.51	1.09	1.60
SCRE (MEAN)	-27.20	-19.40	-34.8	-33.8	-29.0	-21.8	-25.0
SD (standard deviation)	2.17	1.56	2.17	2.98	2.6	1.97	2.05
SE (standard error)	0.97	0.70	0.69	0.94	0.81	0.62	0.65
95% CI (confidence interval)	2.69	1.93	1.55	2.13	1.84	1.41	1.47
LCRE (MEAN)	20.9	19.6	20.0	18.3	20.8	19.7	19.0
SD (standard deviation)	1.54	1.42	1.54	1.54	1.68	1.55	1.88
SE (standard error)	0.69	0.64	0.49	0.49	0.53	0.49	0.60
95% CI (confidence interval)	1.91	1.77	1.10	1.10	1.20	1.11	1.35

Table E.3: Cloud radiative effects (CREs) at the top of the atmosphere over land and ocean.

		No AIE inclusion		Standard CDN scheme		Hybrid CDN scheme		Observation
	Regions	RH-REF	ST-REF	RH-STN	ST-STN	RH-HYB	ST-HYB	CERES
	Ocean only							
NH	SCRF (W/m^2)	-52.5	-32.3	-63.7	-49.7	-54.2	-35.2	-42.9
	LCRF(W/m^2)	26.3	22.3	27.4	25.0	26.5	22.8	23.7
	NCRF(W/m^2)	-26.2	-10.0	-36.3	-24.7	-27.7	-12.3	-19.2
SH	SCRF (W/m^2)	-65.9	-42.3	-75.1	-56.4	-71.2	-50.1	-54.6
	LCRF(W/m^2)	29.9	24.8	29.8	26.5	29.7	25.4	26.0
	NCRF(W/m^2)	-36.1	-17.5	-45.3	-29.8	-41.5	-24.7	-28.6
GL	SCRF (W/m^2)	-59.6	-37.6	-69.8	-53.3	-63.2	-43.1	-49.1
	LCRF(W/m^2)	28.2	23.6	28.7	25.8	28.2	24.2	24.9
	NCRF(W/m^2)	-31.5	-14.0	-41.1	-27.5	-35.0	-18.9	-24.2
	Land only							
NH	SCRF (W/m^2)	-35.2	-25.7	-46.4	-45.7	-37.8	-28.9	-32.1
	LCRF(W/m^2)	25.4	23.7	24.6	22.4	25.6	23.9	22.3
	NCRF(W/m^2)	-9.8	-2.0	-21.8	-23.4	-12.2	-5.0	-9.8
SH	SCRF (W/m^2)	-16.8	-11.1	-19.6	-18.3	-17.6	-12.6	-15.7
	LCRF(W/m^2)	14.9	14.3	14.0	12.9	14.5	14.3	14.8
	NCRF(W/m^2)	-1.9	3.2	-5.6	-5.4	-3.2	1.7	-0.97
GL	SCRF (W/m^2)	-27.2	-19.4	-34.8	-33.8	-29.0	-21.8	-25.0
	LCRF(W/m^2)	20.9	19.6	20.0	18.3	20.8	19.7	19.0
	NCRF(W/m^2)	-6.4	0.25	-14.8	-15.5	-8.3	-2.1	-6.0
	Global							
NH	SCRF (W/m^2)	-46.0	-29.8	-57.2	-48.2	-48.0	-32.8	-38.8
	LCRF(W/m^2)	26.0	22.8	26.4	24.0	26.2	23.2	26.2
	NCRF(W/m^2)	-20.1	-7.0	-30.9	-24.2	-21.9	-9.6	-12.6
SH	SCRF (W/m^2)	-51.8	-33.4	-59.1	-45.4	-55.8	-39.3	-43.5
	LCRF(W/m^2)	25.5	21.8	25.3	22.6	25.4	22.2	25.1
	NCRF(W/m^2)	-26.2	-11.6	-33.9	-22.8	-30.5	-17.1	-18.4
GL	SCRF (W/m^2)	-48.9	-31.6	-58.2	-46.8	-51.9	-36.1	-41.1
	LCRF(W/m^2)	25.8	22.3	25.8	23.3	25.8	22.7	25.6
	NCRF(W/m^2)	-23.1	-9.3	-32.4	-23.5	-26.2	-13.3	-15.5

Appendix F

Figures and tables

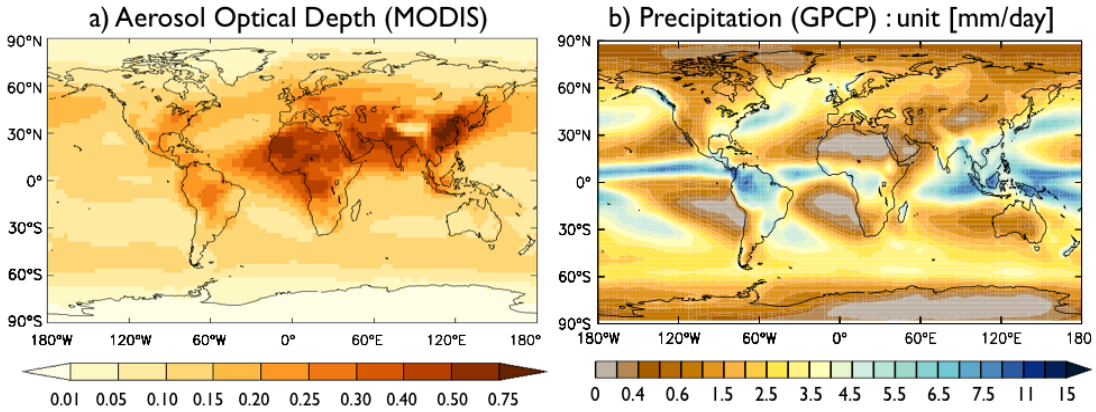

Figure F.1: Global distribution of observation data: a) aerosol optical depth estimated by MODIS for 10 years, b) total precipitation estimated by GPCP data for 10 years

Table F.1: Evaluation of performances (based on skill scores) of the CDN and CLC schemes in the EMAC model.

Continental

	TCC	SCRE	LCRE	PTOT	AOD	SUM	AVE
RH-REF	0.9513	0.9025	0.9479	0.9117	0.8906	4.6040	0.9208
RH-STN	0.9497	0.7778	0.8858	0.8378	0.8729	4.3240	0.8648
RH-HYB	0.9518	0.8901	0.9405	0.9155	0.8646	4.5625	0.9125
	TCC	SCRE	LCRE	PTOT	AOD	SUM	AVE
ST-REF	0.9287	0.8592	0.9319	0.7434	0.9094	4.3726	0.8745
ST-STN	0.9401	0.7603	0.8778	0.9453	0.8893	4.4128	0.8826
ST-HYB	0.9392	0.9111	0.9391	0.7783	0.8852	4.4529	0.8906

Marine

	TCC	SCRE	LCRE	PTOT	AOD	SUM	AVE
RH-REF	0.9205	0.8599	0.9005	0.7950	0.8219	4.2977	0.8595
RH-STN	0.9263	0.8106	0.8998	0.7834	0.7429	4.1630	0.8326
RH-HYB	0.9207	0.8410	0.9032	0.7957	0.7846	4.2452	0.8490
	TCC	SCRE	LCRE	PTOT	AOD	SUM	AVE
ST-REF	0.7975	0.8761	0.9074	0.8477	0.8489	4.2776	0.8555
ST-STN	0.8625	0.8248	0.9266	0.8304	0.8183	4.2625	0.8525
ST-HYB	0.8281	0.8489	0.9091	0.8530	0.8260	4.2651	0.8530

Table F.2: Continental and marine means and corresponding statistical variables: standard deviation (σ)*, spatial pattern correlation coefficient (R), centered root mean square (E')* difference. These variables are used in the spatial pattern comparisons between the model simulations and observations, and their skill scores (S) presented in Fig. 4.8.

	Continental					Marine				
TCC (-)	Mean	σ	R	E'	S	Mean	σ	R	E'	S
1-RH-REF	0.532	0.204	0.903	0.088	0.951	0.715	0.158	0.865	0.079	0.920
2-ST-REF	0.482	0.195	0.855	0.105	0.929	0.539	0.198	0.789	0.122	0.798
3-RH-STN	0.548	0.200	0.898	0.090	0.950	0.722	0.154	0.868	0.077	0.926
4-ST-STN	0.533	0.219	0.900	0.0954	0.940	0.618	0.169	0.786	0.105	0.862
5-RH-HYB	0.539	0.202	0.903	0.090	0.952	0.717	0.157	0.863	0.077	0.921
6-ST-HYB	0.493	0.195	0.876	0.095	0.939	0.563	0.191	0.817	0.105	0.828
Obs. (MODIS)	0.520	0.196				0.7155	0.140			
SCRE (W/m^2)	Mean	σ	R	E'	S	Mean	σ	R	E'	S
1-RH-REF	-35.76	24.36	0.897	11.03	0.903	-64.79	20.59	0.761	13.51	0.860
2-ST-REF	-24.36	14.68	0.854	10.27	0.859	-37.18	19.24	0.764	12.74	0.876
3-RH-STN	-45.40	30.76	0.906	15.51	0.778	-76.74	22.94	0.736	15.54	0.811
4-ST-STN	-43.36	30.76	0.863	17.08	0.760	-55.51	22.26	0.741	14.99	0.825
5-RH-HYB	-38.23	25.38	0.909	15.51	0.890	-68.99	21.90	0.762	15.54	0.841
6-ST-HYB	-27.63	16.54	0.867	17.08	0.911	-43.29	21.59	0.768	14.99	0.849
Obs. (CERES)	-33.00	19.42				-52.84	17.59			
LCRE (W/m^2)	Mean	σ	R	E'	S	Mean	σ	R	E'	S
1-RH-REF	26.07	11.63	0.894	5.336	0.948	29.48	13.24	0.868	6.595	0.900
2-ST-REF	24.98	13.07	0.892	5.912	0.932	23.97	11.87	0.826	6.777	0.907
3-RH-STN	24.77	9.876	0.811	6.752	0.886	30.19	13.19	0.864	6.655	0.900
4-ST-STN	22.51	9.243	0.839	6.275	0.878	26.66	11.89	0.865	5.989	0.927
5-RH-HYB	25.96	11.11	0.881	6.752	0.940	29.59	13.12	0.868	6.655	0.903
6-ST-HYB	25.02	12.87	0.899	6.275	0.939	24.62	11.88	0.830	5.989	0.909
Obs. (CERES)	24.17	11.51				27.09	10.89			
Ptot (mm/day)	Mean	σ	R	E'	S	Mean	σ	R	E'	S
1-RH-REF	2.142	1.975	0.827	1.135	0.912	3.348	2.665	0.833	1.529	0.795
2-ST-REF	2.788	3.000	0.844	1.741	0.743	3.039	2.394	0.825	1.361	0.848
3-RH-STN	1.752	1.419	0.803	1.115	0.838	3.441	2.681	0.814	1.600	0.783
4-ST-STN	1.998	1.792	0.892	0.855	0.945	3.321	2.516	0.8409	1.394	0.830
5-RH-HYB	2.067	1.840	0.829	1.115	0.915	3.366	2.656	0.830	1.600	0.796
6-ST-HYB	2.720	2.876	0.863	0.855	0.778	3.074	2.372	0.8279	1.394	0.853
Obs. (GPCP)	2.118	1.868				2.904	1.817			
AOD (-)	Mean	σ	R	E'	S	Mean	σ	R	E'	S
1-RH-REF	0.217	0.167	0.784	0.108	0.891	0.203	0.084	0.692	0.062	0.822
2-ST-REF	0.202	0.156	0.817	0.095	0.909	0.184	0.076	0.704	0.057	0.849
3-RH-STN	0.236	0.174	0.759	0.117	0.873	0.233	0.099	0.655	0.075	0.743
4-ST-STN	0.227	0.179	0.803	0.108	0.889	0.219	0.094	0.767	0.060	0.818
5-RH-HYB	0.214	0.164	0.729	0.117	0.865	0.215	0.087	0.635	0.075	0.785
6-ST-HYB	0.200	0.155	0.769	0.108	0.885	0.194	0.076	0.658	0.060	0.826
Obs. (MODIS)	0.219	0.159				0.132	0.071			

*The normalized standard deviation ($\hat{\sigma_x}= \frac{\sigma_x}{\sigma_r}$) and CRMS difference ($\hat{E'}=\frac{E'}{\sigma_r}$) by the corresponding observed standard deviation (σ_r) are used in Taylor diagrams (Fig. 4.8).

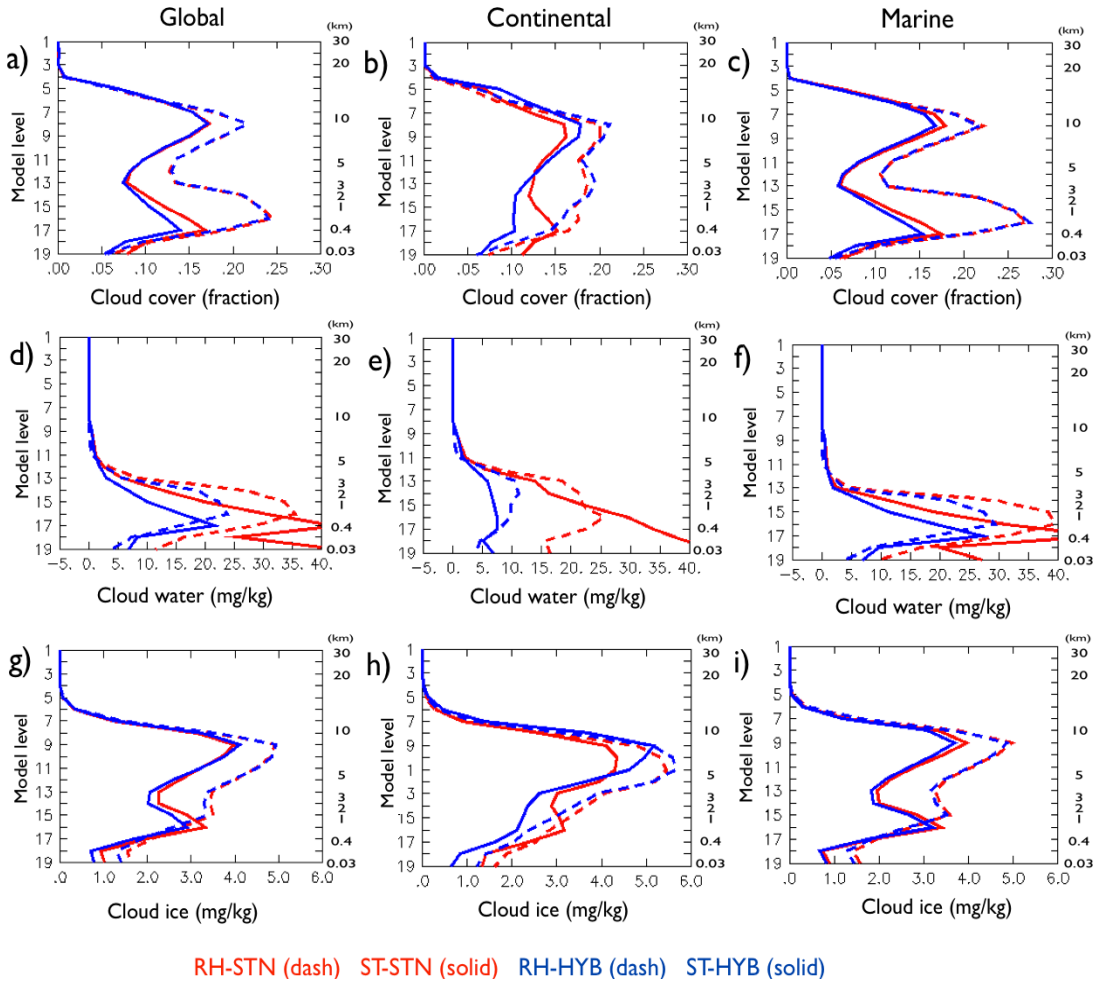

Figure F.2: Vertical distributions of global, continental, and marine mean cloud cover, cloud water, and cloud ice.

Table F.3: Global (continental) and regional means of convective cloud top height (CTH; unit = m) and convective available potential energy (CAPE; unit = J/kg) in the selected regions over the continents (CRs)

	CTH (unit = m)						CAPE (unit = J/kg)					
CLC	RH-CLC			ST-CLC			RH-CLC			ST-CLC		
CDN	REF	STN	HYB	REF	STN	HYB	REF	STN	HYB	REF	STN	HYB
CR1	1606	1432	1578	1710	1426	1733	30.5	22.1	29.3	42.9	26.4	42.3
CR2	2171	1891	2107	2312	1744	2269	56.6	41.7	53.8	67.9	40.4	61.2
CR3	1501	1316	1463	1475	1285	1465	7.0	4.0	6.6	8.0	3.4	8.0
CR4	799	883	834	800	797	822	8.4	8.2	8.8	10.3	7.8	10.3
CR5	2351	2060	2286	2459	1894	2390	75.4	58.5	70.6	100.4	61.8	96.6
CR6	957	740	946	1063	714	1005	4.7	0.9	4.6	8.0	0.6	7.1

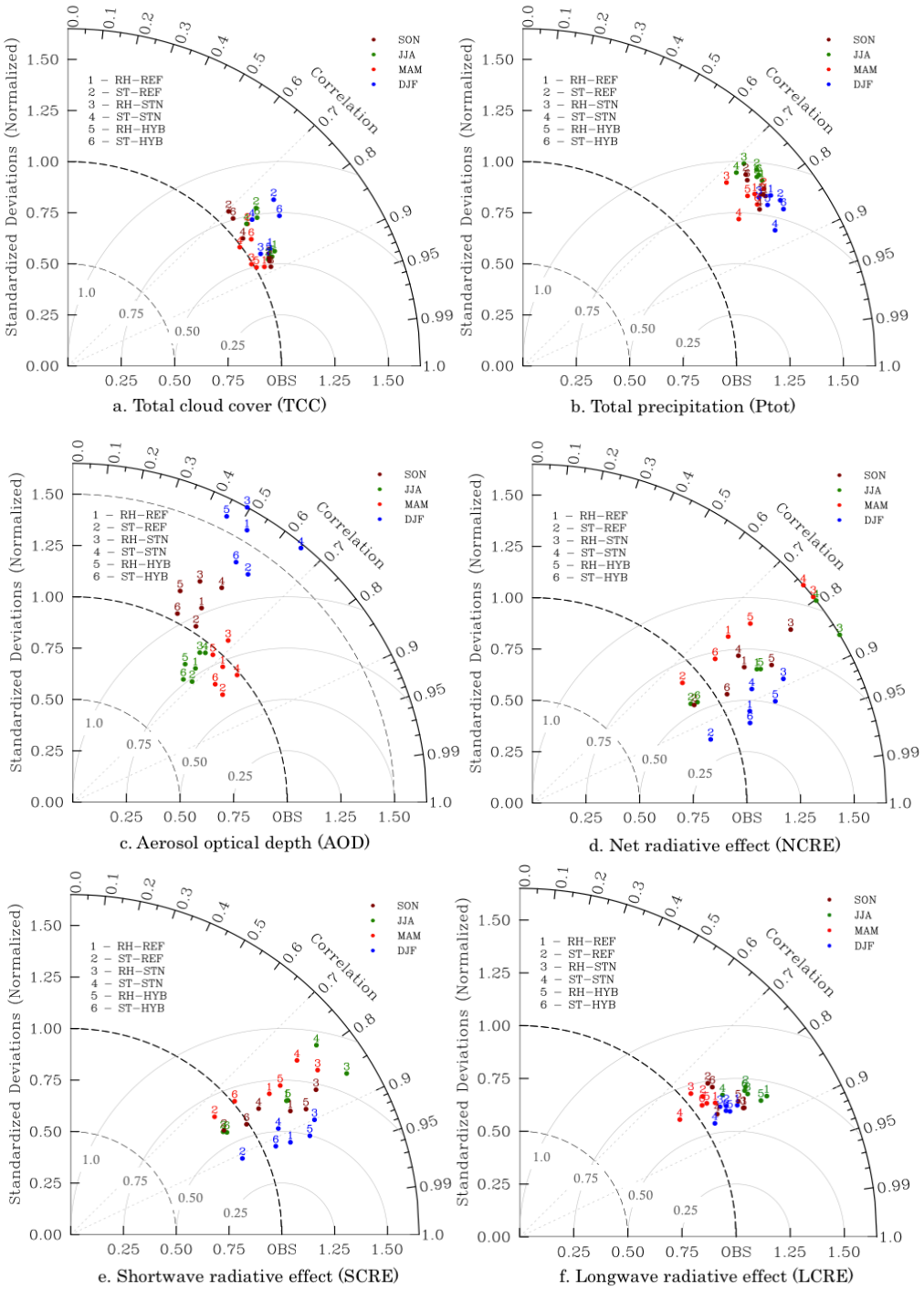

Figure F.3: Taylor diagram for seasonal distributions of a) total cloud cover (TCLC), b) NCRE at TOA, c) total precipitation (P_{tot}) and d) aerosol optical depth (AOD) for all EMAC simulations.

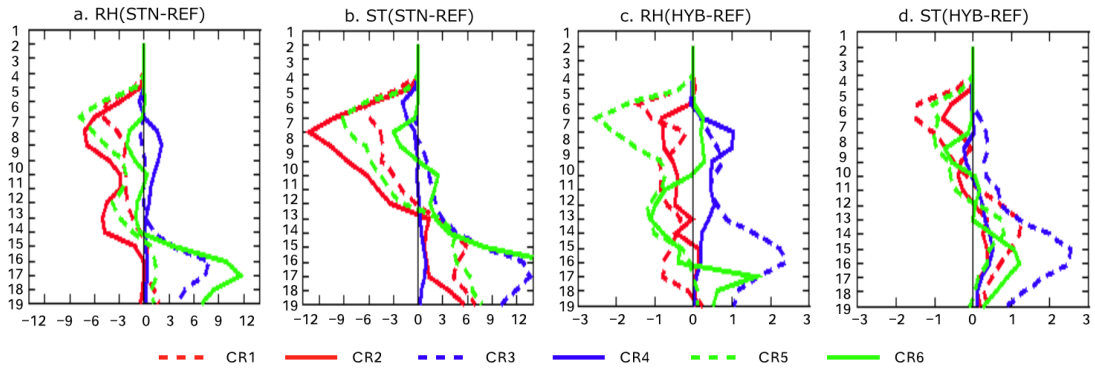

Figure F.4: Vertical distributions of changes in cloud cover (unit = %) for selected continental regions (CRs) after including nucleated cloud droplets.

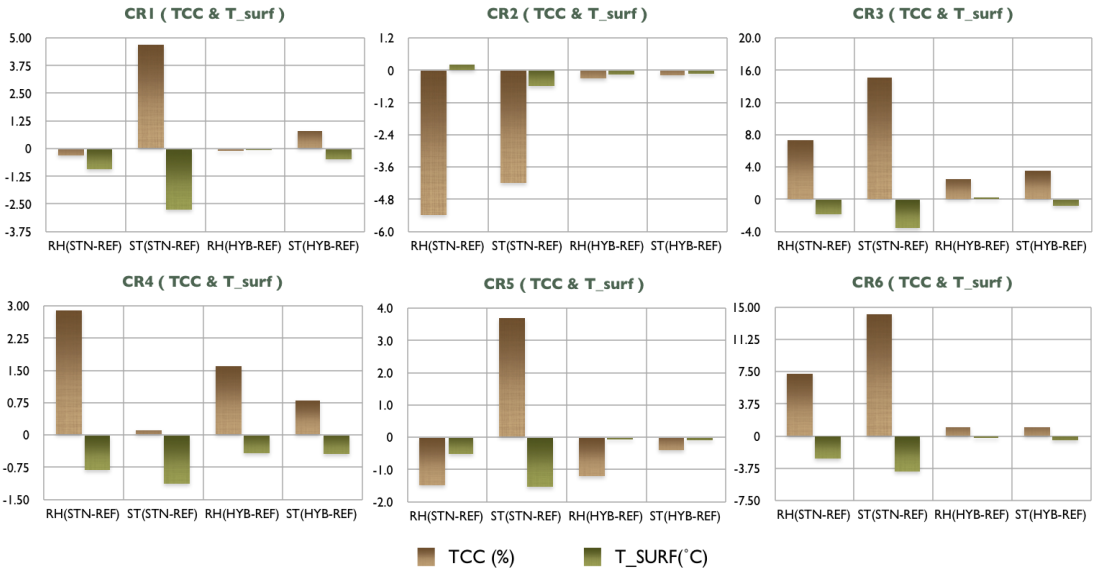

Figure F.5: Regional variability of changes in total cloud cover (TCC, unit = %) and surface temperature (T_{surf},$^\circ C$) after including nucleated cloud droplets.

Table F.4: Regional means of LWP (unit = g/m^2), IWP (unit = g/m^2), WVM (unit = kg/m^2), TCC (unit = %), Pstrat, Pconv, Ptotal (unit = mm/day)for CRs

RH-REF	LWP	IWP	WVM	TCC	P_{strat}	P_{conv}	P_{total}	T_{surf}	SCRE	LCRE	NCRE
CR1	43.1	45.4	26.8	0.63	2.52	1.74	4.26	288.1	-60.5	37.5	-23.0
CR2	44.5	23.1	5.3	0.65	0.47	3.14	3.61	297.6	-54.0	36.5	-17.5
CR3	20.0	39.3	14.6	0.56	0.99	0.31	1.30	282.1	-30.4	26.7	-3.7
CR4	3.8	10.3	17.4	0.24	0.10	0.18	0.29	297.4	-9.5	15.1	5.6
CR5	56.7	23.0	40.2	0.68	0.84	4.07	4.91	297.7	-65.9	38.2	-27.7
CR6	33.2	44.0	10.5	0.79	1.43	0.25	1.68	267.3	-39.6	23.6	-15.9
ST-REF	LWP	IWP	WVM	TCC	P_{strat}	P_{conv}	P_{total}	T_{surf}	SCRE	LCRE	NCRE
CR1	24.1	33.6	27.1	0.58	3.10	2.26	5.36	288.6	-41.8	35.4	-6.3
CR2	22.1	28.6	36.9	0.64	1.33	3.99	5.33	297.1	-35.4	40.9	5.5
CR3	16.8	26.7	15.0	0.49	0.89	0.34	1.24	283.1	-23.3	23.9	0.5
CR4	4.0	7.9	18.6	0.23	0.13	0.39	0.53	297.1	-8.4	14.2	5.7
CR5	26.0	27.1	41.1	0.63	1.90	5.37	7.27	297.4	-37.1	39.8	2.7
CR6	29.1	31.4	11.2	0.73	1.28	0.38	1.66	268.2	-29.0	22.3	-6.6
RH-STN	LWP	IWP	WVM	TCC	P_{strat}	P_{conv}	P_{total}	T_{surf}	SCRE	LCRE	NCRE
CR1	171.3	43.04	25.3	0.63	1.82	1.24	3.06	287.2	-75.8	33.4	-42.4
CR2	102.6	17.61	32.8	0.59	0.22	2.23	2.46	297.8	-59.5	29.7	-29.8
CR3	89.6	43.61	13.7	0.63	1.15	0.18	1.33	280.2	-45.3	26.6	-18.8
CR4	10.9	12.37	16.9	0.27	0.10	0.15	0.26	296.5	-12.3	17.1	4.9
CR5	169.1	19.06	38.2	0.66	0.57	3.00	3.57	297.2	-81.5	32.9	-48.6
CR6	117.5	47.13	8.8	0.86	1.47	0.05	1.52	264.7	-57.3	21.9	-35.3
ST-STN	LWP	IWP	WVM	TCC	P_{strat}	P_{conv}	P_{total}	T_{surf}	SCRE	LCRE	NCRE
CR1	178.5	35.0	24.3	0.63	1.92	1.57	3.49	285.9	-73.7	29.9	-43.7
CR2	112.5	16.9	32.1	0.60	0.54	2.33	2.87	296.5	-57.7	27.6	-30.1
CR3	124.7	40.0	13.2	0.64	1.19	0.17	1.37	279.5	-49.7	25.3	-24.4
CR4	14.3	8.8	16.6	0.23	0.10	0.18	0.28	295.9	-11.1	13.5	2.3
CR5	176.8	18.4	38.0	0.66	1.06	3.46	4.52	295.9	-76.0	30.7	-45.3
CR6	156.3	41.9	8.2	0.87	1.41	0.04	1.44	264.1	-59.6	21.5	-38.1
RH-HYB	LWP	IWP	WVM	TCC	P_{strat}	P_{conv}	P_{total}	T_{surf}	SCRE	LCRE	NCRE
CR1	65.4	45.2	26.4	0.63	2.25	1.63	3.88	288.1	-62.4	36.7	-25.7
CR2	55.9	22.8	34.9	0.64	0.45	3.08	3.53	297.4	-55.7	35.6	-20.1
CR3	37.3	42.1	14.8	0.58	1.10	0.29	1.39	282.3	-35.1	27.6	-7.5
CR4	7.5	11.6	17.6	0.26	0.11	0.20	0.31	296.9	-11.1	16.1	5.0
CR5	90.0	21.9	39.7	0.67	0.71	3.80	4.51	297.6	-69.7	36.5	-33.2
CR6	43.8	42.8	10.7	0.80	1.39	0.24	1.63	267.1	-41.6	23.4	-18.2
ST-HYB	LWP	IWP	WVM	TCC	P_{strat}	P_{conv}	P_{total}	T_{surf}	SCRE	LCRE	NCRE
CR1	48.2	37.4	26.8	0.59	2.82	2.27	5.09	288.1	-47.1	35.4	-11.6
CR2	28.3	28.5	36.7	0.64	1.34	4.00	5.33	297	-37.5	40.7	3.2
CR3	35.2	31.6	14.8	0.53	0.98	0.33	1.30	282.2	-29.2	24.7	-4.6
CR4	8.4	9.0	18.7	0.24	0.15	0.37	0.53	296.6	-9.8	14.1	4.2
CR5	45.7	27.0	40.7	0.62	1.80	5.17	6.96	297.3	-42.0	38.9	-3.1
CR6	37.8	32.2	10.8	0.74	1.26	0.34	1.60	267.7	-31.3	22.0	-9.3

Table F.5: Global (land and ocean) means of total, convective, and large-scale precipitation (unit = mm/day); ratio of convective and total precipitation (unit = %).

	RH-simulations		ST-simulations	
Regions	RH(STN-REF)	RH(HYB-REF)	ST(STN-REF)	ST(HYB-REF)
Gobal				
ΔP_{total}	-1.66 %	-0.33 %	-0.67 %	0.00 %
ΔP_{conv}	-0.53 %	0.00 %	2.86 %	0.57 %
ΔP_{strat}	-2.63 %	-0.88 %	-5.74 %	-0.82 %
Ocean only				
ΔP_{total}	2.69 %	0.60 %	9.21 %	0.99 %
ΔP_{conv}	5.16 %	0.94 %	16.11 %	1.67 %
ΔP_{strat}	-1.64 %	0.00 %	-0.81 %	0.00 %
Land only				
ΔP_{total}	-18.22 %	-3.27 %	-28.32 %	-2.51 %
ΔP_{conv}	-26.45 %	-4.13 %	-34.97 %	-3.07 %
ΔP_{strat}	-6.45 %	-2.15 %	-18.26 %	-0.87 %

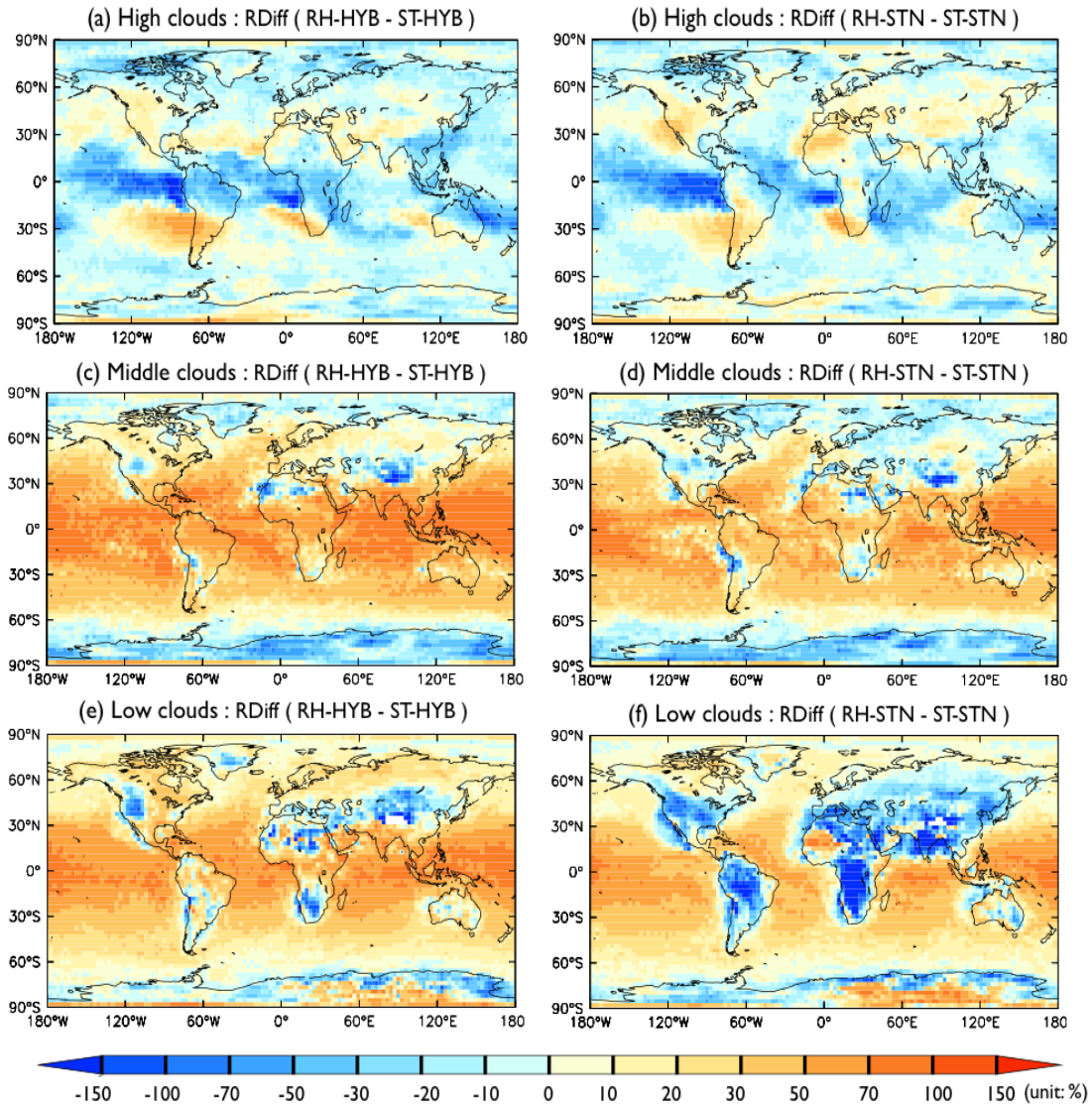

Figure F.6: Relative differences between the estimated cloud covers at low, middle, and high altitudes for RH-CLC and ST-CLC.

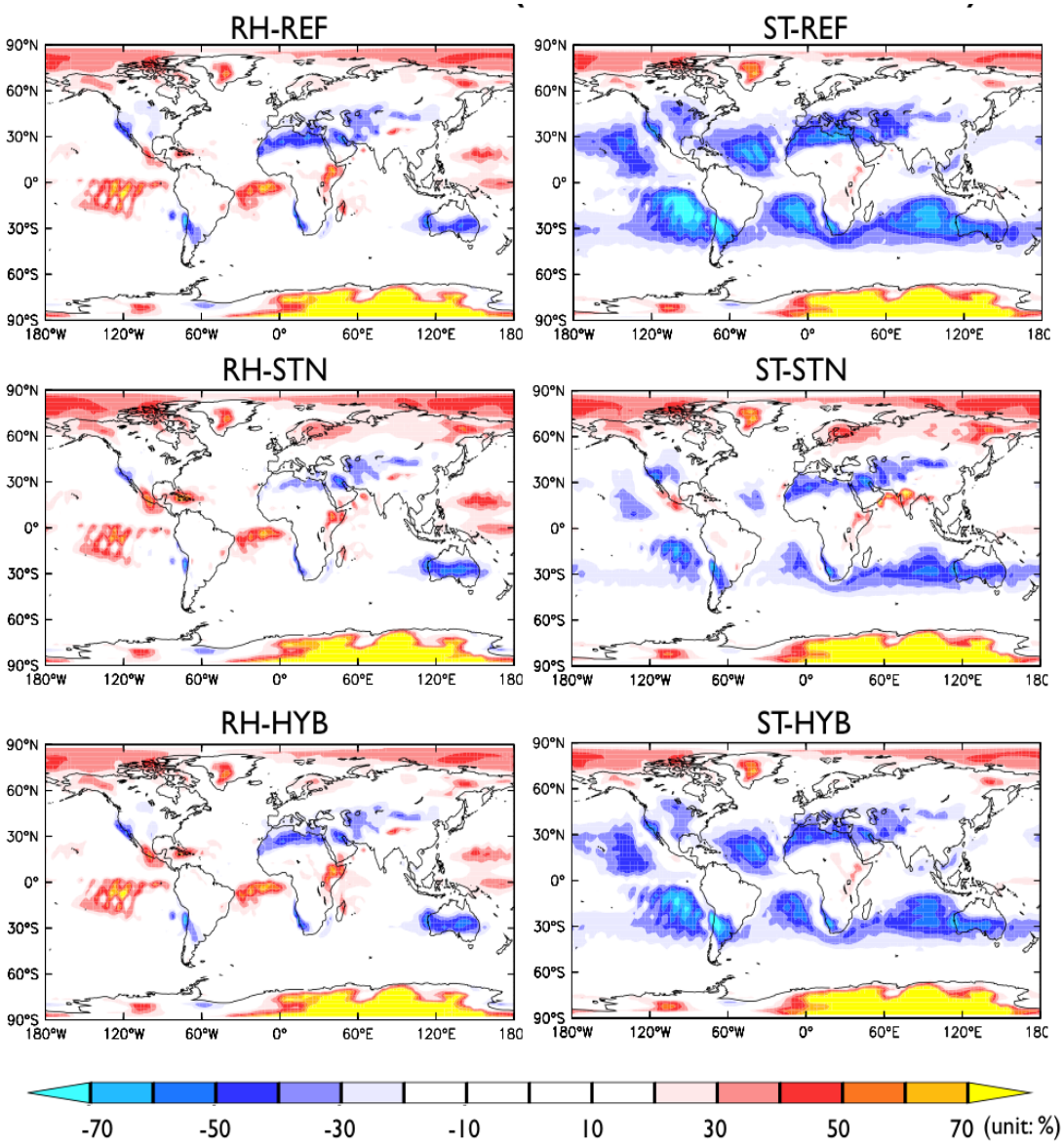

Figure F.7: Relative difference between the simulated clouds and the observations (ISCCP).

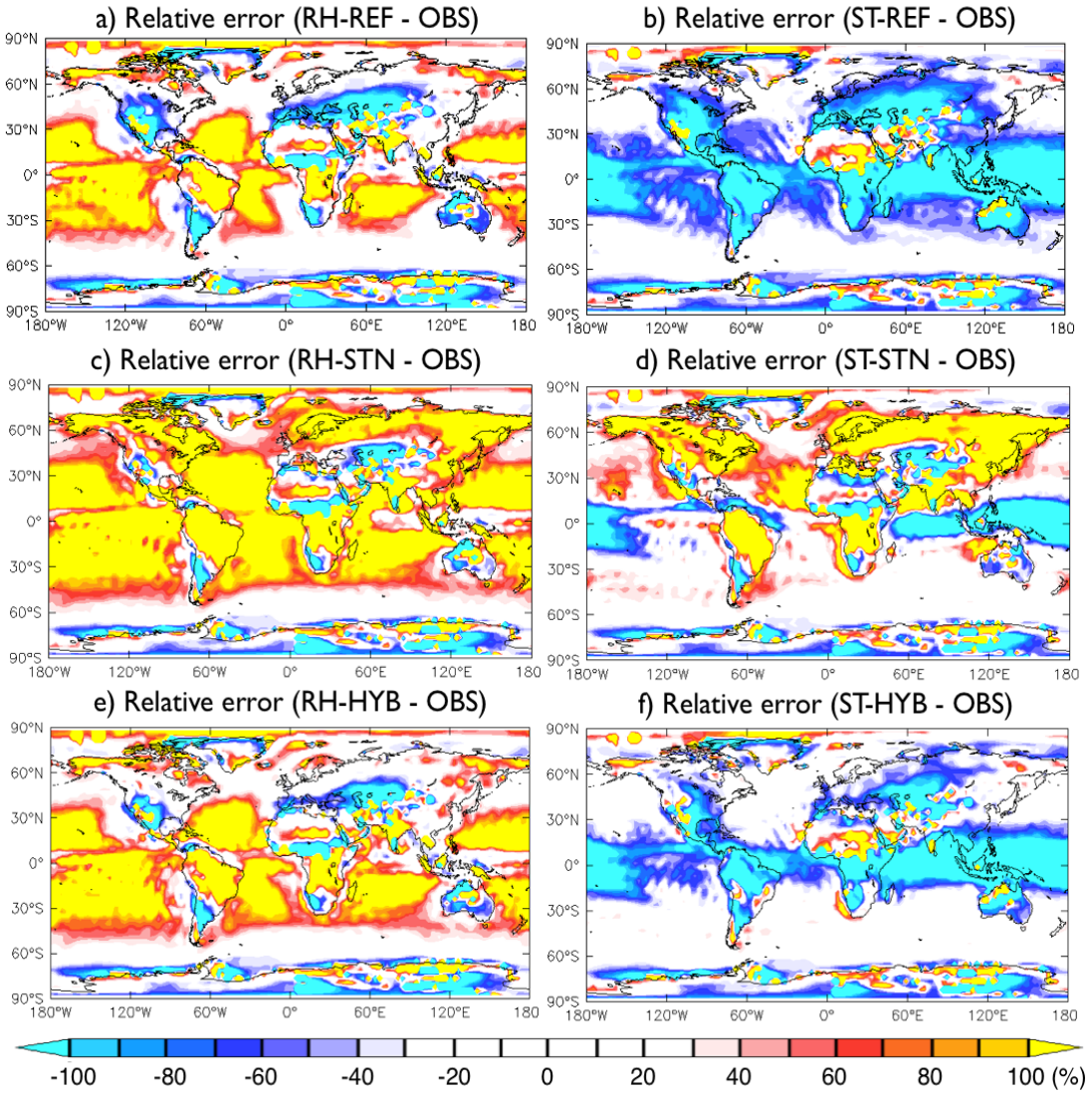

Figure F.8: Relative errors of the estimated NCRE at top of atmosphere (TOA) relative to the observed NCRE at TOA: Relative Error (%) = $\frac{[Model-OBS]}{OBS} \times 100(\%)$

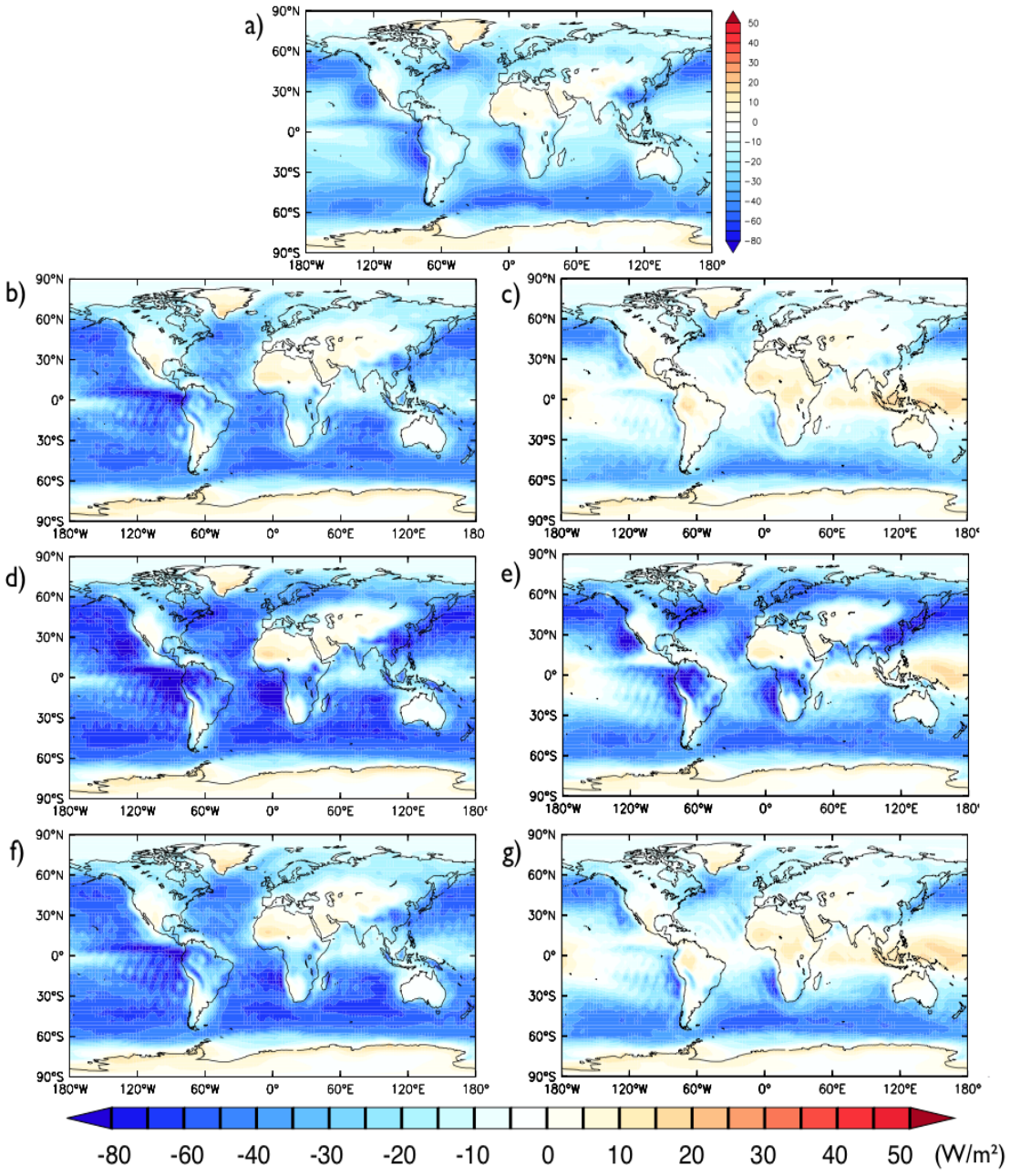

Figure F.9: Global distribution of annual mean net cloud radiative effect (NCRE) at TOA (unit = W/m^2) for the simulations and the observations (CERES EBAF)

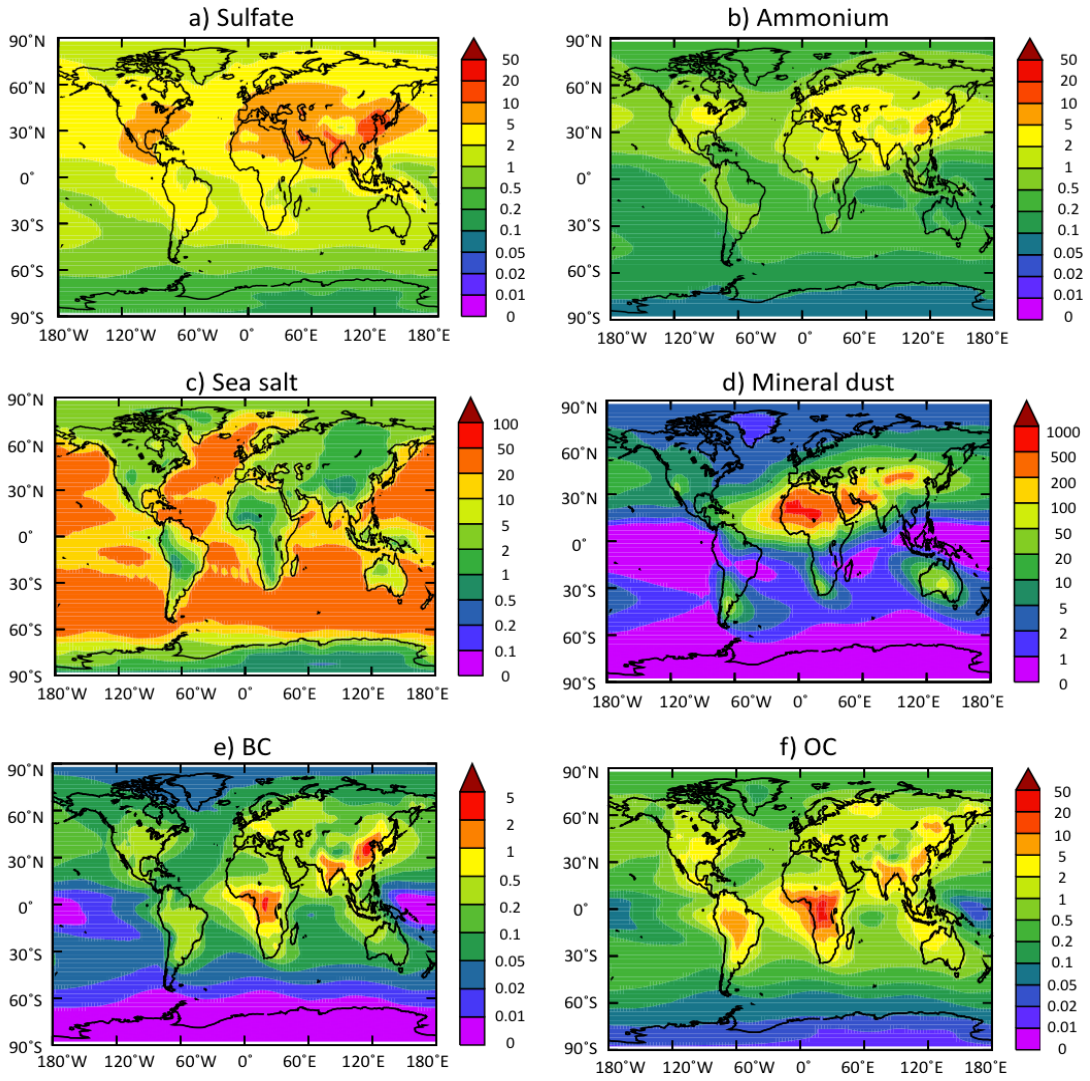

Figure F.10: Global distributions of annual mean total aerosol column burden (unit = mg/m^2): (a) sulfate, (b) ammonium, (c) sea spray, (d) mineral dust, (e) BC, and (f) OC for ST-HYB.

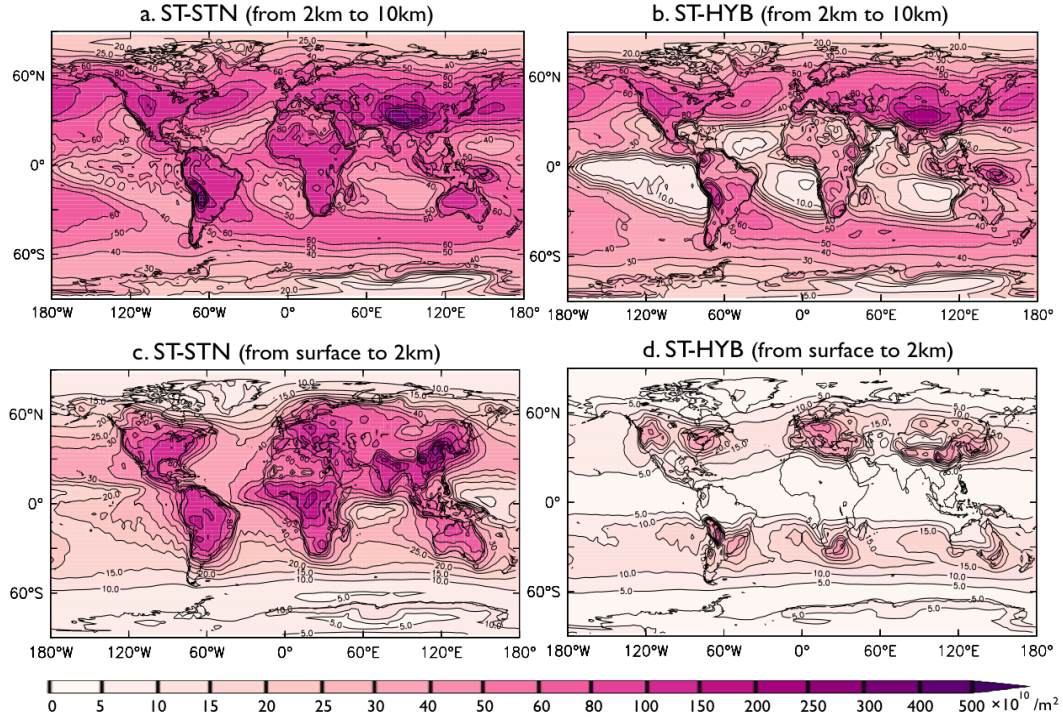

Figure F.11: Global distributions of the vertically integrated CCN number concentration (N_{CCN}) for high altitudes (2 – 10 km) for (a) ST-STN and (b) ST-HYB; for low altitudes (surface – 2 km) for (c) ST-STN and (d) ST-HYB.

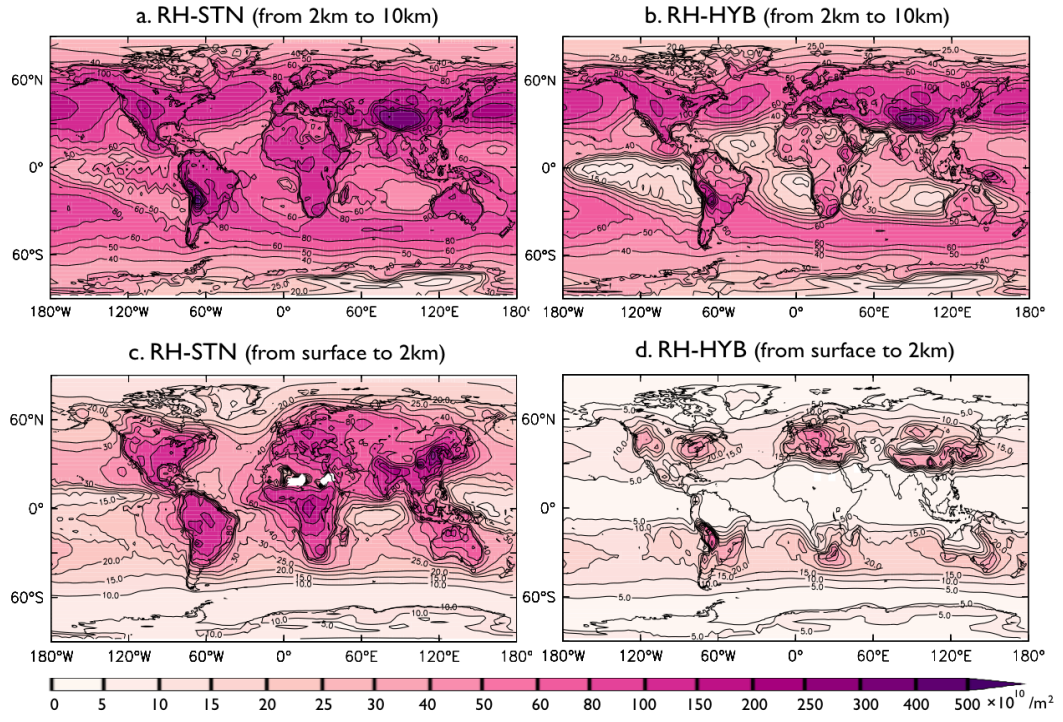

Figure F.12: Same as Fig. F.11 for the RH-simulations (RH-STN and RH-HYB)

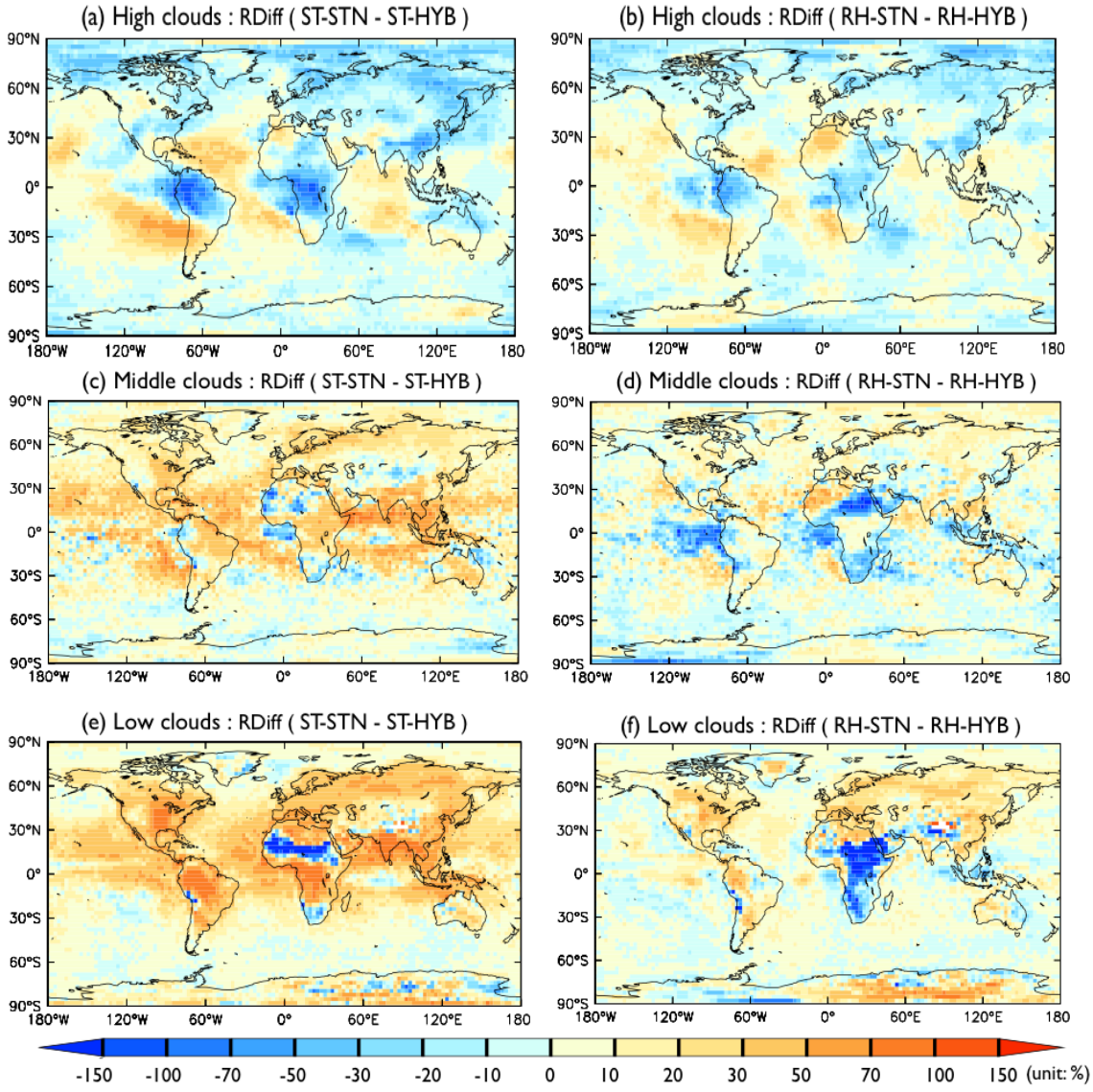

Figure F.13: Relative differences in estimated cloud covers at low, middle, and high altitudes between a) ST-STN and ST-HYB, b) RH-STN and RH-HYB, c) ST-STN and ST-HYB, d) RH-STN and RH-HYB, e) ST-STN and ST-HYB, and f) RH-STN and RH-HYB.

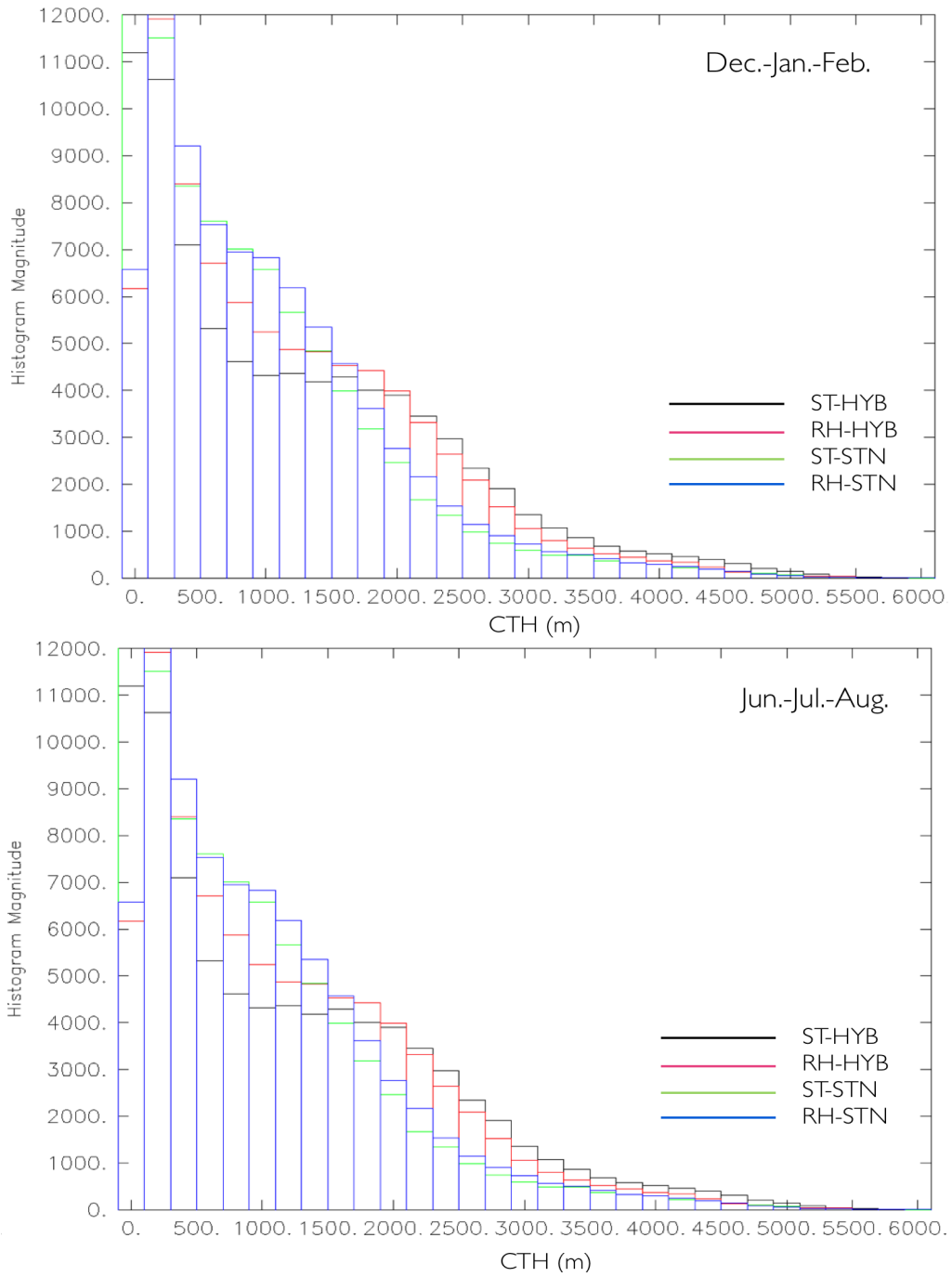

Figure F.14: Frequency of Convective cloud Top Height (CTH) over land for boreal winter (December, January, February; DJF) and boreal summer (June, July, August; JJA).

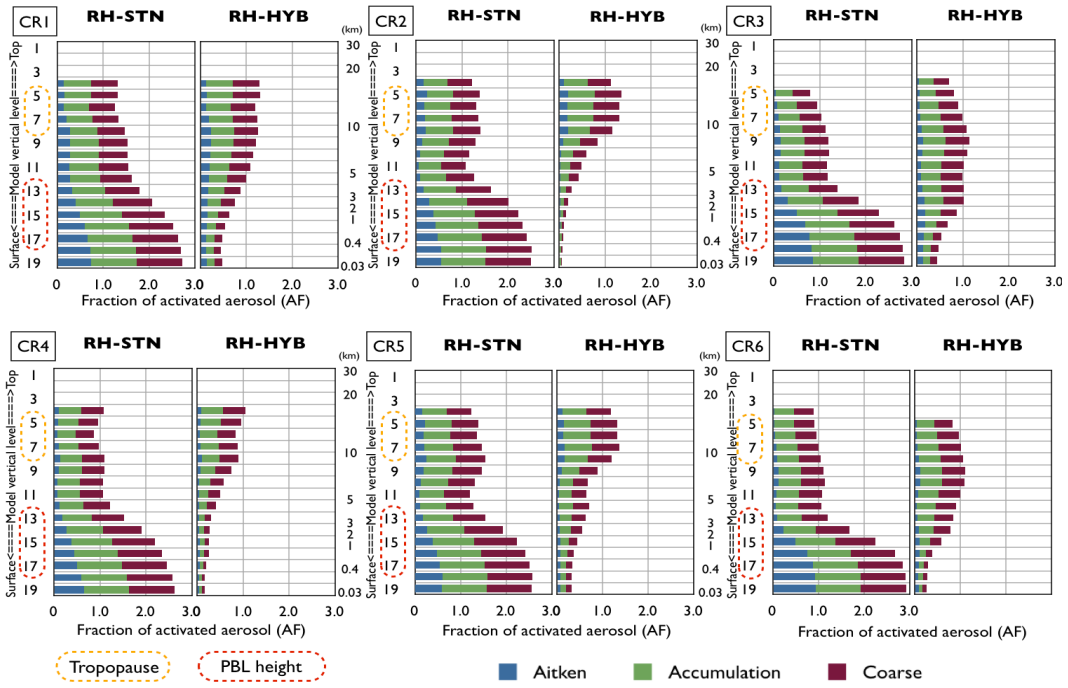

Figure F.15: Vertical distributions of CCN activation rates in the selected continental regions (CR1 – CR6) for RH-STN and RH-HYB.

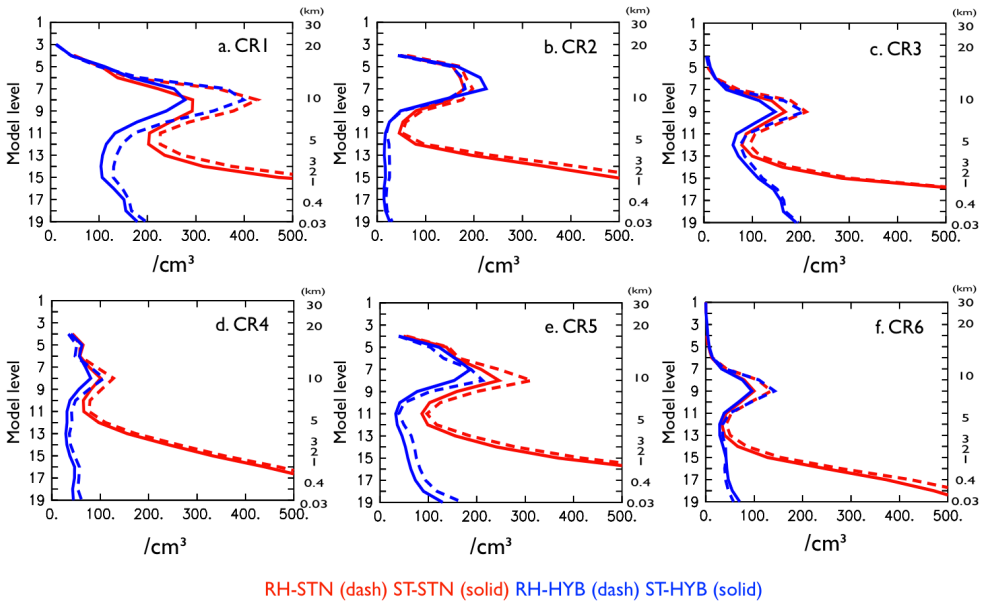

Figure F.16: Vertical distributions of activated aerosol in the selected continental regions (CRs) for RH-STN, ST-STN, RH-HYB, and ST-HYB.

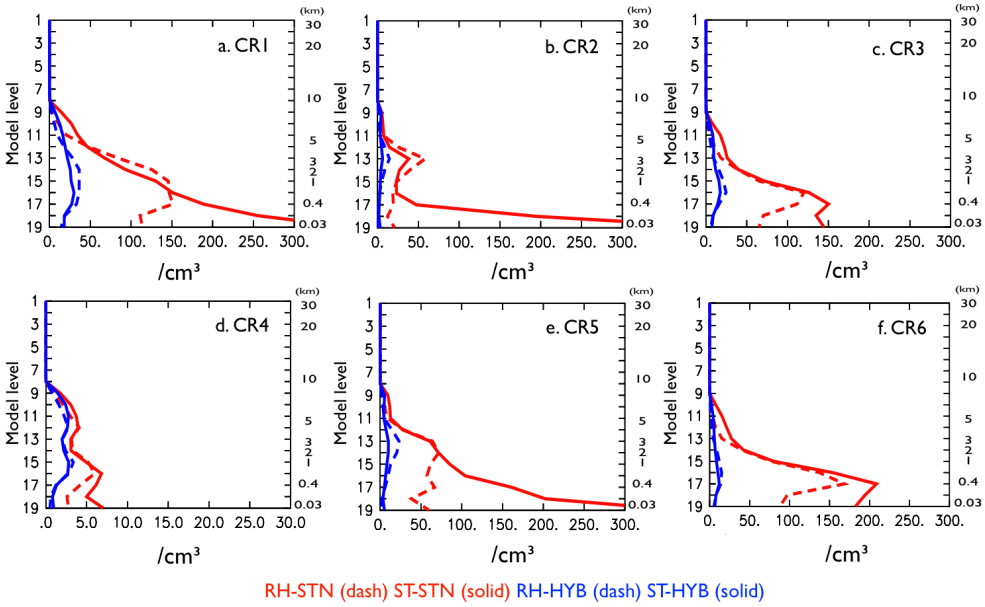

Figure F.17: Vertical distributions of cloud droplet number concentration (CDNC) in the selected continental regions (CR) for RH-STN, ST-STN, RH-HYB, and ST-HYB.

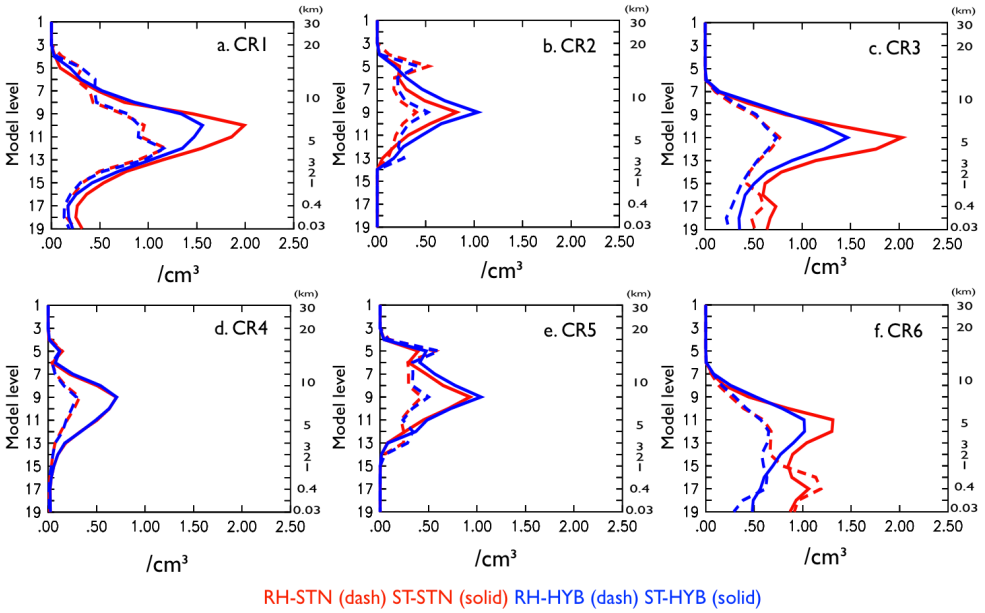

Figure F.18: Vertical distributions of ice crystal number concentration (ICNC) in the selected continental regions (CRs) for RH-STN, ST-STN, RH-HYB, and ST-HYB.

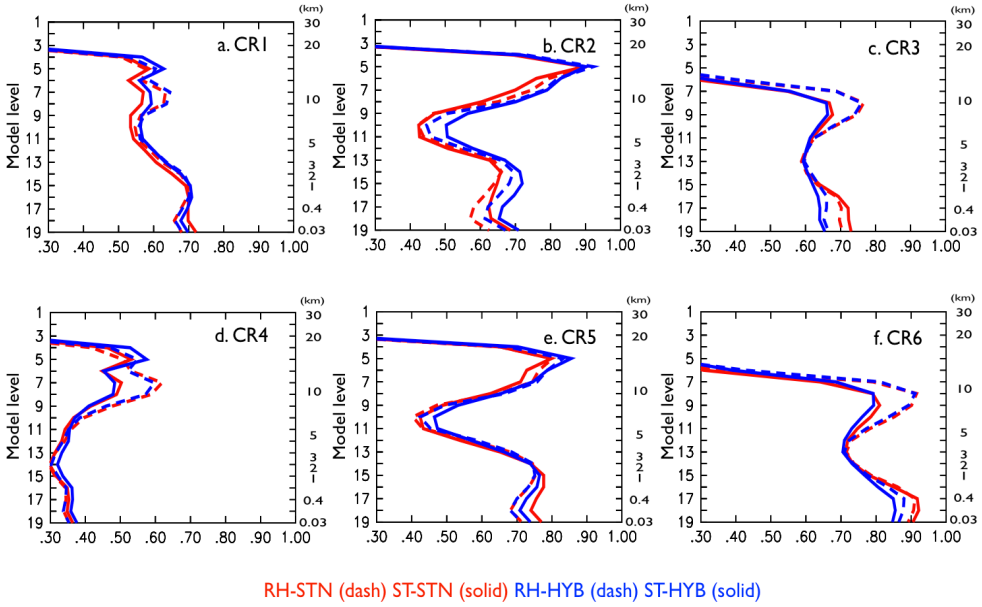

Figure F.19: Vertical distributions of relative humidity in the selected continental regions (CRs) for RH-STN, ST-STN, RH-HYB, and ST-HYB.

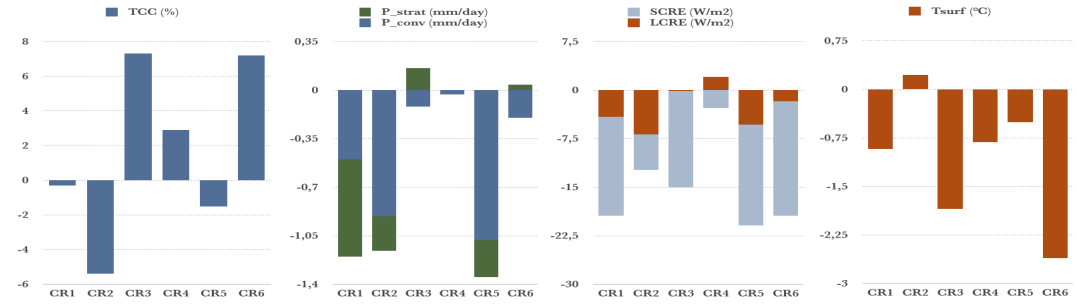

Figure F.20: Regional variability of changes for RH(STN-REF).

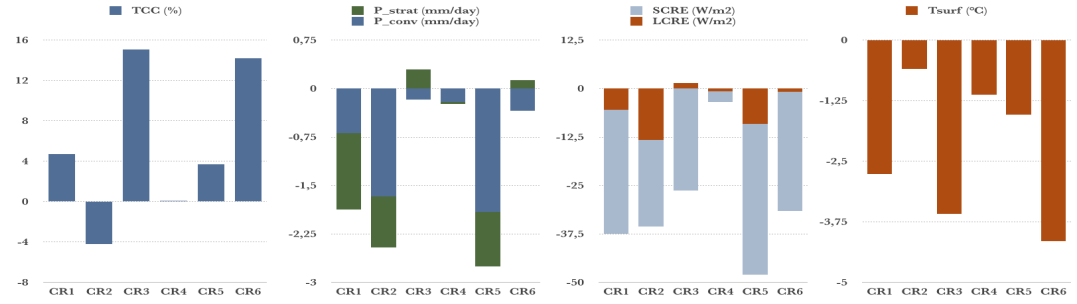

Figure F.21: Regional variability of changes for ST(STN-REF).

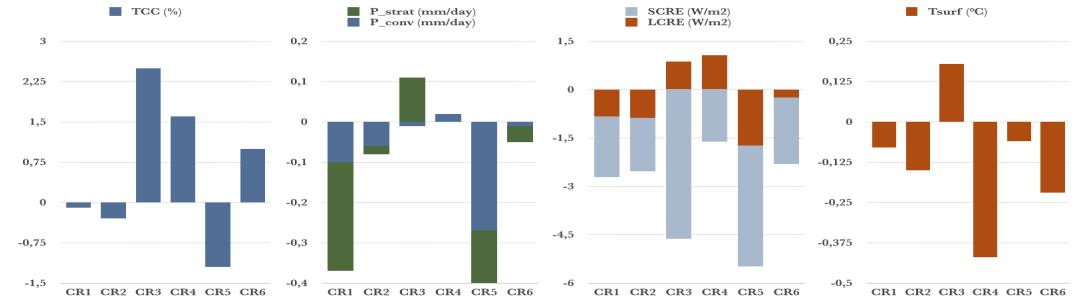

Figure F.22: Regional variability of changes for RH(HYB-REF).

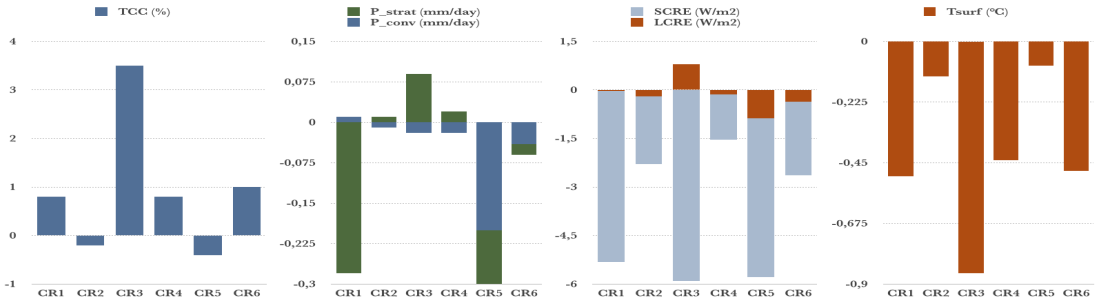

Figure F.23: Regional variability of changes for ST(HYB-REF).

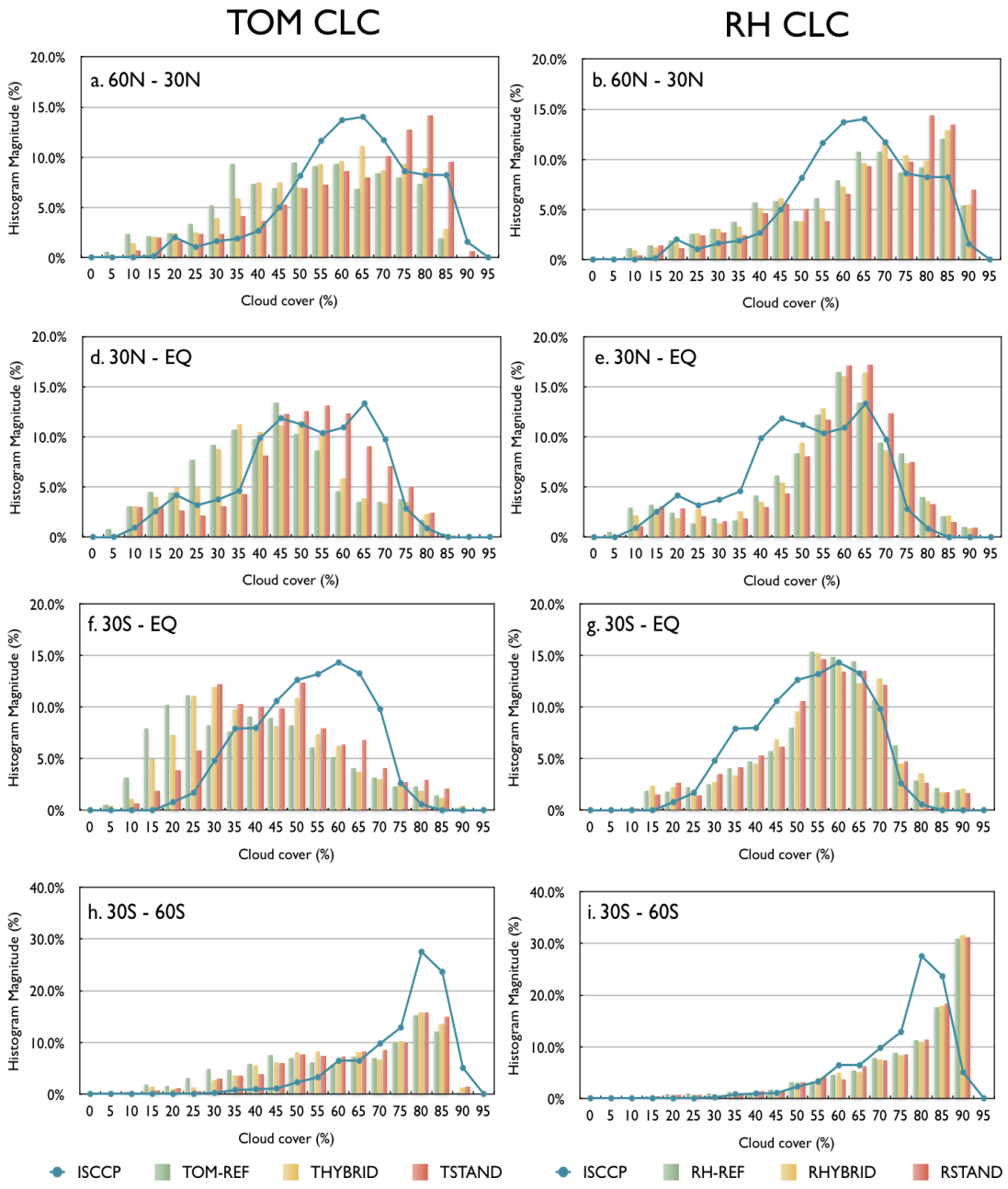

Figure F.24: Histogram of cloud factions distributed by latitude. Histogram magnitude represents the proportion of each cloud fraction simulated in these experiments.

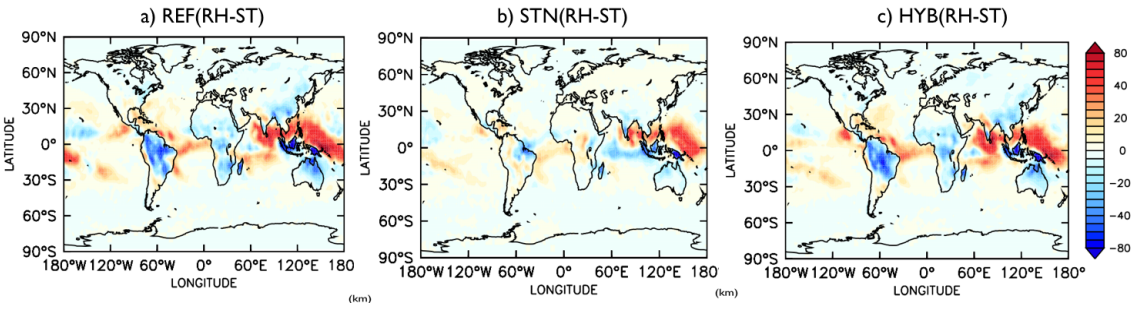

Figure F.25: Differences of Convective Available Potential Energy (CAPE; unit = J/kg) between (a) RH-REF and ST-REF, (b) RH-STN and ST-STN, and (c) RH-HYB and ST-HYB.

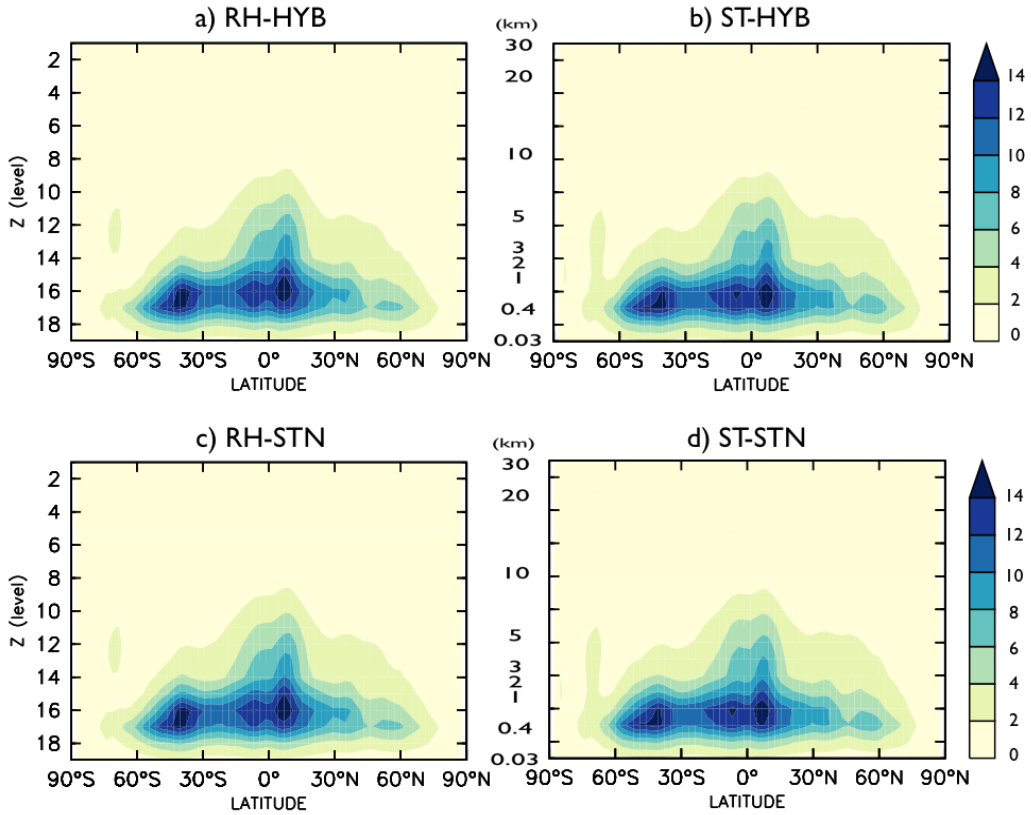

Figure F.26: Zonal mean distribution of updraft mass fluxes (unit = g/m^2s) for (a) RH-HYB, (b) ST-HYB, (c) RH-STN, and (d) ST-STN.

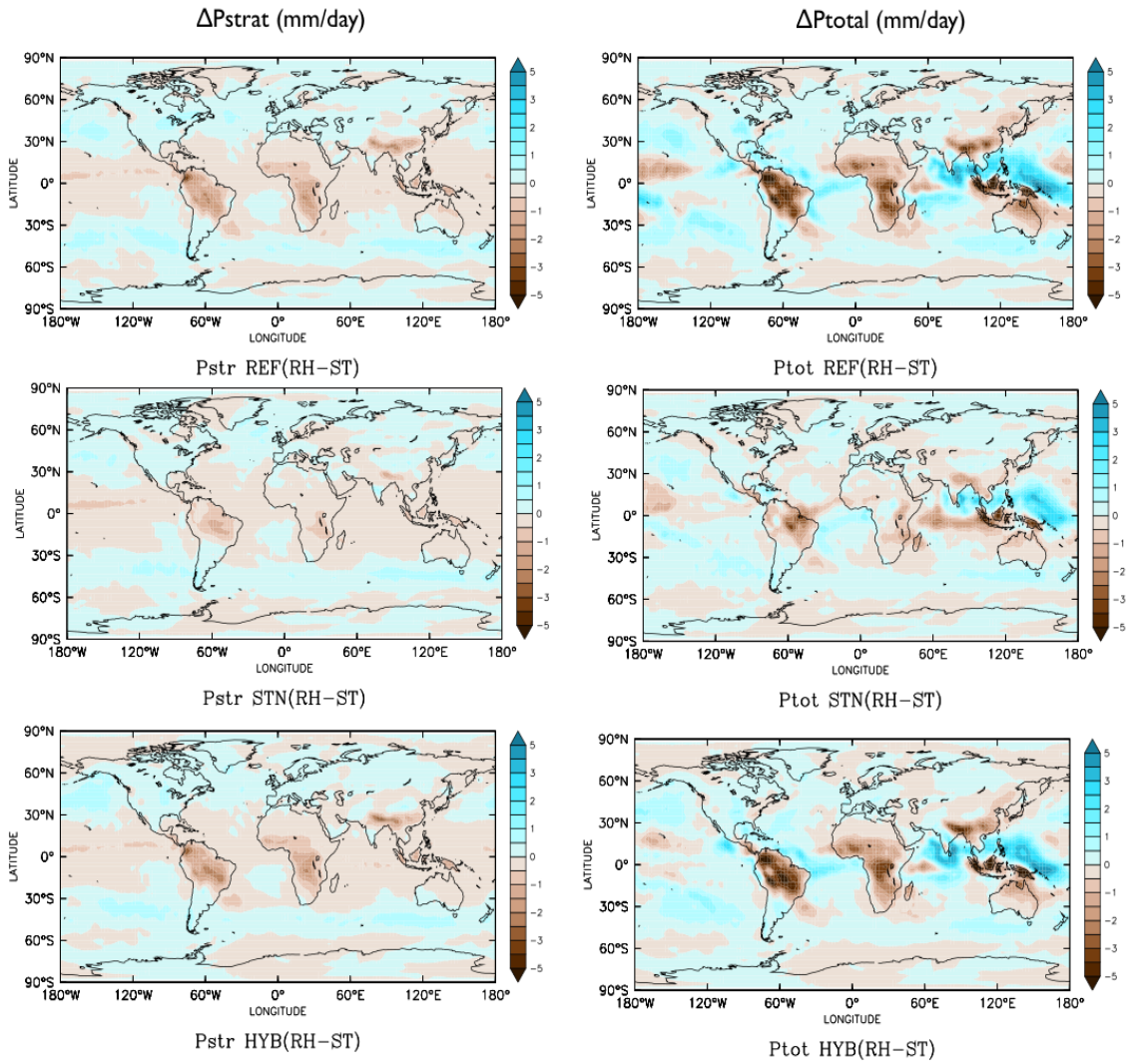

Figure F.27: Differences of simulated stratiform and total precipitation between the RH and ST simulations.

List of Figures

List of Tables

Bibliography

[Abdul-Razzak and Ghan(2000)] Abdul-Razzak, H. and Ghan, S. J.: A parameterization of aerosol activation 2. Multiple aerosol types, J. Geophys. Res., 105, 6837–6844, 2000.

[Abdul-Razzak and Ghan (2002)] Abdul-Razzak, H. and Ghan, S. J.: A parameterization of aerosol activation: 3. Sectional representation, J. Geophys. Res., 107, 4026, 10.1029/2001JD000483, 2002.

[Abdul-Razzak and Ghan(2004)] Abdul-Razzak, H. and Ghan, S. J.: Parameterization of the influence of organic surfactants on aerosol activation, J. Geophys. Res., 109, D03205, 10.1029/2003JD004043, 2004.

[Abdul-Razzak et al.(1998)] Abdul-Razzak, H., Ghan, S. J., and Rivera-Carpio, C.: A parameterization of aerosol activation: 1. Single aerosol type, J. Geophys. Res.,103, 6123–6132, 1998.

[Adler et al.(2003)] Adler, R. F., Huffman, G. J., Chang, A., Ferraro, R., Xie, P., Janowiak, J., Rudolf, B., Schneider, U., Curtis, S., Bolvin, D., Gruber, A., Susskind, J., Arkin, P., and Nelkin, E.: The version-2 global precipitation climatology project (GPCP) monthly precipitation analysis (1979–present), J. Hydrometeorol., 4, 1147–1167, 2003.

[Ackerman et al.(2000)] Ackerman, A. S., Toon, O. B., Stevens, D. E., Heymsfield, A. J., Ramanathan, V., and Welton, E. J.: Reduction of tropical cloudiness by soot, Science, 288, 1042–1047, 2000.

[Albrecht(1989)] Albrecht, B.: Aerosols, cloud microphysics, and fractional cloudiness, Science, 245, 1227–1230, 1989.

[Anderson et al.(2003)] Anderson, T. L., Charlson, R. J., Schwartz, S. E., Knutti, R., Boucher, O., Rodhe, H., and Heintzenberg, J.: Climate forcing by aerosols – a hazy picture, Science, 300, 1103–1104, 2003.

[Andreae(2009)] Andreae, M. O: A new look at aging aerosols, Science, 326(5959), 1493–1494, doi:10.1126/science.1183158, 2009.

[Andreae and Rosenfeld(2008)] Andreae, M. O. and Rosenfeld, D.: Aerosol–cloud-precipitation interactions, Part 1: The nature and sources of cloud-active aerosols, Earth Sci. Rev., 89, 13–41, 10.1016/j.earscirev.2008.03.001, 2008.

[Boucher and Lohmann(1995)] Boucher, O. and Lohmann, U.: The sulfate-CCN-cloud albedo effect: a sensitivity study with two general circulation models, Tellus B, 47, 281–300, 1995.

[Bougiatioti et al.(2009)] Bougiatioti, A., Fountoukis, C., Kalivitis, N., Pandis, S. N., Nenes, A., and Mihalopoulos, N.: Cloud condensation nuclei measurements in the marine boundary layer of the Eastern Mediterranean: CCN closure and droplet growth kinetics, Atmos. Chem. Phys., 9, 7053–7066, 10.5194/acp-9-7053-2009, 2009.

[Cavalli et al.(2004)] Cavalli, F., Facchini, M. C., Decesari, S., Mircea, M., Emblico, L., Fuzzi, S., Ceburnis, D., Yoon, Y. J., O'Dowd, C. D., Putaud, J.-P., and Dell'Acqua, A.: Advances in characterization of size-resolved organic matter in marine aerosol over the North Atlantic. J. Geophys. Res. 109 (D24), D24215. doi:10.1029/2004JD005137

[Chen et al.(2000)] Chen, T., Rossow, W. B., and Zhang, Y.: Radiative effects of cloud-type variations, J. Climate, 13, 264–286, 2000.

[Chen et al.(2007)] Chen, T., Rossow, W. B., and Zhang, Y.: Comparison between measured and predicted CCN concentrations at Egbert, Ontario: Focus on the organic aerosol fraction at a semi-rural site, Atmos. Environ., 41, 8172–8182, 2007.

[Chu et al.(2002)] Chu, D., Kaufman, Y., Ichoku, C., Remer, L., Tanre, D., and Holben, B.: Validation of MODIS aerosol optical depth retrieval over land, Geophys. Res. Lett., 29, 8007, 10.1175/JAS3385.1, 2002.

[Chuang and Penner(1995)] Chuang, C. C. and Penner, J. E.: Effects of anthropogenic sulfate on cloud drop nucleation and optical properties, Tellus B, 47, 566–577, 1995.

[Cohard et al.(2000)] Cohard, J. M., Pinty, J. P., and Suhre, K.: On the parameterization of activation spectra from cloud condensation nuclei microphysical properties, J. Geophys. Res., 105, 11753–11766, 10.1029/1999JD901195, 2000.

[de Meij et al.(2012)] de Meij, A., Pozzer, A., Pringle, K. J., Tost, H., and Lelieveld, J.: EMAC model evaluation and analysis of atmospheric aerosol properties and distribution, Atmos. Res., 114–115, 38–69, 2012.

[Dentener et al.(2006)] Dentener, F., Kinne, S., Bond, T., Boucher, O., Cofala, J., Generoso, S., Ginoux, P., Gong, S., Hoelzemann, J. J., Ito, A., Marelli, L., Penner, J. E., Putaud, J.-P., Textor, C., Schulz, M., van der Werf, G. R., and Wilson, J.: Emissions of primary aerosol and precursor gases in the years 2000 and 1750 prescribed data-sets for AeroCom, Atmos. Chem. Phys., 6, 4321–4344, 10.5194/acp-6-4321-2006, 2006.

[Derimian et al.(2006)] Derimian, Y., Karnieli, A., Kaufman, Y. J., Andreae, M. O., Andreae, T. W., Dubovik, O., Maenhaut, W., Koren, I., and Holben, B. N.: Dust and pollution aerosols over the Negev desert, Israel: Properties, transport, and radiative effect, J. Geophys. Res., 111, D05205, doi:10.1029/2005JD006549, 2006.

[Devasthale et al.(2005)] Devasthale, A., Kruger, O., and Grassl, H.: Change in cloud-top temperatures over Europe, IEEE Geosci. Remote S., 2, 333–336, 10.1109/LGRS.2005.851736, 2005.

[Dusek et al.(2006)] Dusek, U., Frank, G. P., and Hildebrandt, L.: Size matters more than chemistry for cloud-nucleating ability of aerosol particles, Science, 312, 1375–1378, 2006.

[Dusek et al.(2010)] Dusek, U., Frank, G. P., Curtius, J., Drewnick, F., Schneider, J., Küurten, A., Rose, D., Andreae, M. O., Borrmann, S., and Pöschl, U.: Enhanced organic mass fraction and decreased hygroscopicity of cloud condensation nuclei (CCN) during new particle formation events, Geophys. Res. Lett., 37, L03804, 10.1029/2009GL040930, 2010.

[Eck et al.(2001)] Eck, T. F., Holben, B. N., Ward, D. E., Dubovik, O., Reid, J. S., Smirnov, A., Mukelabai, M. M., Hsu, N. C., Oeill, N. T., and Slutsker, I.: Characterization of the optical properties of biomass burning aerosols in Zambia during the 1997 ZIBBEE Field Campaign, J. Geophys. Res., 106, 3425–3448, doi:10.1029/2000JD900555, 2001.

[Feichter et al.(1997)] Feichter, J., Lohmann, U., and Schult, I.: The atmospheric sulfur cycle and its impact on the shortwave radiation, Clim. Dynam., 13, 235–246, 1997.

[Feingold(2003)] Feingold, G.: Modeling of the first sindirect effect: analysis of measurement requirements, Geophys. Res. Lett., 30, 1997, 10.1029/2003GL017967, 2003.

[Feingold and Heymsfield(1992)] Feingold, G. and Heymsfield, A.: Parameterizations of condensational growth of droplets for use in general circulation models, J. Atmos. Sci., 49, 2325–2342, 1992.

[Feingold et al.(2003)] Feingold, G., Eberhard, W. L., Veron, D. E., and Previdi, M.: First measurements of the Twomey indirect effect using ground-based remote sensors, Geophys. Res. Lett., 30, 1287, 10.1029/2002GL016633, 2003.

[Forster et al.(2007)] Forster, P., Ramaswamy, V., Artaxo, P., Berntsen, T., Betts, R., Fahey, D., Haywood, J., Lean, J., Lowe, D., Myhre, G., Nganga, J., Prinn, R., Raga, G. M. S., and Dorland, R. V.: Changes in atmospheric constituents and in radiative forcing, in: Intergovernmental Panel on Climate Change, Cambridge University Press, Cambridge, UK, New York, NY, USA, 130–234, 2007.

[Fountoukis and Nenes(2005)] Fountoukis, C. and Nenes, A.: Continued development of a cloud droplet formation parameterization for global climate models, J. Geophys. Res., 110, D11212, 10.1029/2004JD005591, 2003.

[Gerald et al.(2011)] Gerald, G. M., Houser, S., Benson, S., Stephen, A., Klein, S. A., and Min, Q.: Critical evaluation of the ISCCP simulator using ground-based remote sensing data, J. Climate, 24, 1598–1612, 10.1175/2010JCLI3517.1, 2011

[Ghan et al.(1993)] Ghan, S., Chuang, C., and Penner, J.: A parameterization of cloud droplet nucleation, Part I: Single aerosol species, Atmos. Res., 30, 197–222, 1993.

[Ghan et al.(1995)] Ghan, S., Chuang, C., Easter, R., and Penner, J.: A parameterization of cloud droplet nucleation: 2. Multiple aerosol types, Atmos. Res., 36, 39–54, 1995.

[Ghan et al.(1997)] Ghan, S. J., Leung, L. R., Easter, R. C., and Abdul-Razzak, H.: Prediction of cloud droplet number in a general circulation model, J. Geophys. Res., 102, 21777–21794, 1997.

[Gottwald et al.(2006)] M. Gottwald, H. Bovensmann, G. Lichtenberg, S. Noel, A. von Bargen, S. Slijkhuis, A. Piters, R. Hoogeveen, C. von Savigny, M. Buchwitz, A. Kokhanovsky, A. Richter, A. Rozanov, T. Holzer-Popp, K. Bramstedt, J.-C. Lambert, J. Skupin, F. Wittrock, H. Schrijver, J.P. Burrows: SCIAMACHY, Monitoring the Changing Earth's Atmosphere; Published by DLR, 2006

[Gultepe and Isaac(1996)] Gultepe, I. and Isaac, G. A.: The relationship between cloud droplet and aerosol number concentrations for climate models, Int. J. Climatol., 16, 1–6, 1996.

[Gunthe et al.(2009)] Gunthe, S. S., King, S. M., Rose, D., Chen, Q., Roldin, P., Farmer, D. K., Jimenez, J. L., Artaxo, P., Andreae, M. O., Martin, S. T., and Pöschl, U.: Cloud condensation nuclei in pristine tropical rainforest air of Amazonia: size-resolved measurements and modeling of atmospheric aerosol composition and CCN activity, Atmos. Chem. Phys., 9, 7551–7575, 10.5194/acp-9-7551-2009, 2009.

[Hagemann et al.(2006)] Hagemann, S., Arpe, K., and Roeckner, E.: Evaluation of the Hydrological Cycle in the ECHAM5 Model. J. Climate, 19, 3810–3827, 10.1175/JCLI3831.1, 2006.

[Han et al.(1994)] Han, Q., Rossow, W. B., and Lacis, A. A.: Near-global survey of effective droplet radii in liquid water clouds using ISCCP data, J. Climate, 7, 465–497, 1994.

[Han et al.(1998)] Han, Q., Rossow, W. B., Chou, J., and Welch, R. M.: Global survey of the relationships of cloud albedo and liquid water path with droplet size using ISCCP, J. Climate, 11, 1516–1528, 1998.

[Hänel(1987)] Hänel, G.: The role of aerosol properties during the condensational stage of cloud: a reinvestigation of numerics and microphysics, Beitr. Phys. Atmos., 60, 321–339, 1987.

[Haywood and Schulz(2007)] Haywood, J. and Schulz, M.: Causes for the reduction of uncertainty in estimates of the anthropogenic radiative forcing of climate between IPCC (2001) and IPCC (2007), Geophys. Res. Lett., 34, L20701, 10.1029/2007GL030749, 2007.

[Henning et al.(2010)] Henning, S., Wex, H., Hennig, T., Kiselev, A., Snider, J., Rose, D., Dusek, U., Frank, G. P., Pöschl, U., Kristensson, A., Bilde, M., Tillmann, R., Kiendler-Scharr, A., Mentel, T. F., Walter, S., Schneider, J., Wennrich, C., and Stratmann, F.: Soluble mass, hygroscopic growth and droplet activation during LExNo, J. Geophys. Res., 115, D11206, 10.1029/2009JD012626, 2010.

[Hoose et al.(2008)] Hoose, C., Lohmann, U., Stier, P., Verheggen, B., and Weingartner, E.: Aerosol processing in mixed-phase clouds in ECHAM5-HAM: model description and comparison to observations, J. Geophys. Res., 113, D07210, 10.1029/2007JD009251, 2008

[IAPSAG] IAPSAG: WMO/IUGG International Aerosol Precipitation Science Assessment Group (IAPSAG) Report: Aerosol Pollution Impact on Precipitation: a Scientific Review, World Meteorological Organization, Geneva, 482 pp., 2007.

[IPCC 2007] IPCC core writing team: IPCC, 2007: Climate Change 2007: Synthesis Report, Contribution of Working Groups I, II and III to the Fourth Assessment Report of the Intergovernmental Panel on Climate Change, IPCC, Geneva, Switzerland, 2007.

[IPCC 2013] IPCC core writing team: IPCC, 2013: Climate Change 2013: Synthesis Report, Contribution of Working Groups I, II and III to the Fifth Assessment Report of the Intergovernmental Panel on Climate Change, IPCC, Geneva, Switzerland, 2013.

[Jacobson et al.(2000)] Jacobson, M.C., Hansson, H.-C., Noone, K.J. and Charlson, R.J.: Organic atmospheric aerosols: Review and state of the science. Reviews of Geophysics 38: doi: 10.1029/1998RG000045. issn: 8755–1209, 2000.

[Jiang et al.(2012)] Jiang, J. H., Su, H., Zhai, C., Perun, V., Del Genio, A. D., Nazarenko, L. S., Donner, L. J., Horowitz, L. W., Seman, C. J., Cole, J., Gettelman, A., Ringer, M. A., Rotstayn, L. D., Jeffrey, S. J., Wu, T., Brient, F., Dufresne, J.-L., Kawai, H., Koshiro, T., Masahiro, W., LÉcuyer, T. S., Volodin, E. M., Iversen, T., Drange, H., dos Santos Mesquita, M., Read, W. G., Waters, J. W., Tian, B., Teixeira, J., and Stephens, G. L.: Evaluation of cloud and water vapor simulations in CMIP5 climate models using NASA "A-Train" satellite observations, J. Geophys. Res., 117, D14105, 10.1029/2011JD017237, 2012.

[Jones and Slingo(1996)] Jones, A. and Slingo, A.: Predicting cloud-droplet effective radius and indirect sulphate aerosol forcing using a general circulation model, Q. J. Roy. Meteor. Soc., 122, 1573–1595, 1996.

[Jones et al.(1994)] Jones, A., Roberts, D. L., and Slingo, A.: A climate model study of indirect radiative forcing by anthropogenic sulphate aerosols, Nature, 370, 450–453, 1994.

[Jöckel et al.(2005)] Jöckel, P., Sander, R., Kerkweg, A., Tost, H., and Lelieveld, J.: Technical Note: The Modular Earth Submodel System (MESSy) – a new approach towards Earth System Modeling, Atmos. Chem. Phys., 5, 433–444, 10.5194/acp-5-433-2005, 2005.

[Jočkel et al.(2006)] Jöckel, P., Tost, H., Pozzer, A., Brühl, C., Buchholz, J., Ganzeveld, L., Hoor, P., Kerkweg, A., Lawrence, M. G., Sander, R., Steil, B., Stiller, G., Tanarhte, M., Taraborrelli, D., van Aardenne, J., and Lelieveld, J.: The atmospheric chemistry general circulation model ECHAM5/MESSy1: consistent simulation of ozone from the surface to the mesosphere, Atmos. Chem. Phys., 6, 5067–5104, 10.5194/acp-6-5067-2006, 2006.

[Jöckel et al.(2008)] Jöckel, P., Kerkweg, A., Buchholz-Dietsch, J., Tost, H., Sander, R., and Pozzer, A.: Technical Note: Coupling of chemical processes with the Modular Earth Submodel System (MESSy) submodel TRACER, Atmos. Chem. Phys., 8, 1677–1687, 10.5194/acp-8-1677-2008, 2008.

[Kambezidis and Kaskaoutis(2008)] Kambezidisa, H. D. and Kaskaoutisa, D. G.: Aerosol climatology over four AERONET sites: An overview, Atmos. Environ., 42, 1892–1906, doi:10.1016/j.atmosenv.2007.11.013, 2008.

[Kanakidou et al.(2005)] Kanakidou, M., Seinfeld, J. H., Pandis, S. N., Barnes, I., Dentener, F. J., Facchini, M. C., Van Dingenen, R., Ervens, B., Nenes, A., Nielsen, C. J., Swietlicki, E., Putaud, J. P., Balkanski, Y., Fuzzi, S., Horth, J., Moortgat, G. K., Winterhalter, R., Myhre, C. E. L., Tsigaridis, K., Vignati, E., Stephanou, E. G., and Wilson, J.: Organic aerosol and global climate modelling: a review, Atmos. Chem. Phys., 5, 1053-1123, doi:10.5194/acp-5-1053-2005, 2005.

[Kaku et al.(2006)] Kaku, K. C., Hegg, D. A., Covert, D. S., Santarpia, J. L., Jonsson, H., Buzorius, G., and Collins, D. R.: Organics in the Northeastern Pacific and their impacts on aerosol hygroscopicity in the subsaturated and supersaturated regimes, Atmos. Chem. Phys., 6, 4101-4115, doi:10.5194/acp-6-4101-2006, 2006.

[Kärcher and Lohmann, 2002] Kärcher, B. and Lohmann, U.: A parameterization of cirrus cloud formation: homogeneous freezing including effects of aerosol size, J. Geophys. Res., 107, 4698, 10.1029/2001JD001429, 2002

[Kaufman and Fraser(1997)] Kaufman, Y. J. and Fraser, R. S.: The effect of smoke particles on clouds and climate forcing, Science, 277, 1636–1639, 1997.

[Kaufman et al.(1997)] Kaufman, Y., Tanre, D., Remer, L., Vermote, E., Chu, A., and Holben, B.: Operational remote sensing of tropospheric aerosol over land from EOS moderate resolution imaging spectroradiometer, J. Geophys. Res., 102, 17051–17067, 10.1029/96JD03988, 1997.

[Kaufman et al.(2002)] Kaufman, Y. J., Boucher, O., Tanré, D., Chin, M., Remer, L. A., and Takemura, T.: A satellite view of aerosols in the climate system, Nature 419, 215–223, 2002.

[Kaufman et al.(2005)] Kaufman, Y. J., Tanré, D., Boucher, O.: Aerosol anthropogenic component estimated from satellite data, Geophys. Res. Lett. 32 (17), L17804. doi:10.1029/2005GL023125.

[Kazil et al.(2010)] Kazil, J., Stier, P., Zhang, K., Quaas, J., Kinne, S., O'Donnell, D., Rast, S., Esch, M., Ferrachat, S., Lohmann, U., and Feichter, J.: Aerosol nucleation and its role for clouds and Earth's radiative forcing in the aerosol-climate model ECHAM5-HAM, Atmos. Chem. Phys., 10, 10733–10752, 10.5194/acp-10-10733-2010, 2010.

[Kerkweg et al.(2006a)] Kerkweg, A., Buchholz, J., Ganzeveld, L., Pozzer, A., Tost, H., and Jöckel, P.: Technical Note: An implementation of the dry removal processes DRY DEPosition and SEDImentation in the Modular Earth Submodel System (MESSy), Atmos. Chem. Phys., 6, 4617–4632, 10.5194/acp-6-4617-2006, 2006a.

[Kerkweg et al.(2006b)] Kerkweg, A., Sander, R., Tost, H., and Jöckel, P.: Technical note: Implementation of prescribed (OFFLEM), calculated (ONLEM), and pseudo-emissions (TNUDGE) of chemical species in the Modular Earth Submodel System (MESSy), Atmos. Chem. Phys., 6, 3603–3609, 10.5194/acp-6-3603-2006, 2006b.

[Khain et al.(2005)] Khain, A., Rosenfeld, D., Pokrovsky, A.: Aerosol impact on the dynamics and microphysics of deep convective clouds, Q. J. R. Meteorol. Soc.131 (611), 2639–2663, 2005.

[Khairoutdinov and Kogan(2000)] Khairoutdinov, M. and Kogan, Y.: A new cloud physics parameterization in a large-eddy simulation model of marine stratocumulus, Mon. Weather Rev., 128, 229–243, 2000.

[Khvorostyanov and Curry(2009)] Khvorostyanov, V. I. and Curry, J. A.: Parameterization of cloud drop activation based on analytical asymptotic solutions to the supersaturation equation, J. Atmos. Sci., 66, 1905–1925, 10.1175/2009JAS2811.1, 2009.

[Kim et al.(2008)] Kim, D., Wang, C., Ekman, A. M. L., Barth, M. C., and Rasch, P. J.: Distribution and direct radiative forcing of carbonaceous and sulfate aerosols in an interactive size resolving aerosol climate model, J. Geophys. Res.-Atmos., 113, D16309, 10.1029/2007JD009756, 2008.

[King et al.(2010)] King, S. M., Rosenoern, T., Shilling, J. E., Chen, Q., Wang, Z.,Biskos, G., McKinney, K. A., Poschl, U., and Martin, S. T.:Cloud droplet activation of mixed organic-sulfate particles produced by the photooxidation of isoprene, Atmos. Chem. Phys., 10, 3953–3964, doi:10.5194/acp-10-3953-2010, 2010.

[Kinne et al.(2006)] Kinne, S., Schulz, M., Textor, C., Guibert, S., Balkanski, Y., Bauer, S. E., Berntsen, T., Berglen, T. F., Boucher, O., Chin, M., Collins, W., Dentener, F., Diehl, T., Easter, R., Feichter, J., Fillmore, D., Ghan, S., Ginoux, P., Gong, S., Grini, A., Hendricks, J., Herzog, M., Horowitz, L., Isaksen, I., Iversen, T., Kirkevåg, A., Kloster, S., Koch, D., Kristjansson, J. E., Krol, M., Lauer, A., Lamarque, J. F., Lesins, G., Liu, X., Lohmann, U., Montanaro, V., Myhre, G., Penner, J., Pitari, G., Reddy, S., Seland, O., Stier, P., Takemura, T., and Tie, X.: An AeroCom initial assessment – optical properties in aerosol component modules of global models, Atmos. Chem. Phys., 6, 1815–1834, 10.5194/acp-6-1815-2006, 2006.

[Koehler(1936)] Köhler, H.:The nucleus in and the growth of hygroscopic droplets. Trans.Faraday Soc., 32, 1152–1161, 1936.

[Koehler et al.(2009)] Koehler, K. A., Kreidenweis, S. M., DeMott, P. J., Petters, M. D., Prenni, A. J., and Carrico, C. M.: Hygroscopicity and cloud droplet activation of mineral dust aerosol, Geophys. Res. Lett., 36, L08805, 10.1029/2009GL037348, 2009.

[Kondo et al.(2006)] Kondo, Y., Komazaki, Y., Miyazaki, Y., Moteki, N., Takegawa, N., Kodama, D., Deguchi, S., Nogami, M., Fukuda, M., Miyakawa, T., Morino, Y., Koike, M., Sakurai, H., and Ehara, K.: Temporal variations of elemental carbon in Tokyo, J. Geophys. Res., 111, D12205, doi:10.1029/2005JD006257, 2006.

[Koren et al. (2004)] Koren, I., Kaufman, Y.J., Remer, L.A., Martins, J.V.: Measurement of the effect of Amazon smoke on inhibition of cloud formation, Science, 303, 1342–1345, 2004.

[Koren et al.(2008)] Koren, I., Martins, J. V., Remer, L. A., and Afargan, H.: Smoke invigoration vs. inhibition of clouds over the Amazon, Science, 321, 946–949, 2008.

[Kreidenweis et al.(2009)] Kreidenweis, S. M., Petters, M. D., and Chuang, P. Y.: Cloud particle precursors, in: Clouds in the Perturbed Climate System: Their Relationship to Energy Balance, Atmospheric Dynamics, and Precipitation, Strüngmann Forum Report, edited by: Heintzenberg, J. and Charlson, R. J., The MIT Press, 13, Cambridge, Massachusetts, ISBN 978-0-262-01287-4, 291–317, 2009.

[Lance et al.(2004)] Lance, S., Nenes, A., and Rissman, T. A.: Chemical and dynamical effects on cloud droplet number: implications for estimates of the aerosol indirect effect, J. Geophys. Res., 109, D22208, 10.1029/2004JD004596, 2004.

[Lauer et al.(2007)] Lauer, A., Eyring, V., Hendricks, J., Jöckel, P., and Lohmann, U.: Global model simulations of the impact of ocean-going ships on aerosols, clouds, and the radiation budget, Atmos. Chem. Phys., 7, 5061–5079, 10.5194/acp-7-5061-2007, 2007.

[Levy et al.(2010)] Levy, R. C., Remer, L. A., Kleidman, R. G., Mattoo, S., Ichoku, C., Kahn, R., and Eck, T. F.: Global evaluation of the Collection 5 MODIS dark-target aerosol products over land, Atmos. Chem. Phys., 10, 10399–10420, 10.5194/acp-10-10399-2010, 2010.

[Loeb et al.(2009)] Loeb, N. G., Wielicki, B. A., Doelling, D. R., Smith, G. L., Keyes, D. F., Kato, S., Manalo-Smith, N., and Wong, N.: Toward optimal closure of the Earth's top-of-atmosphere radiation budget, J. Climate, 22, 748–766, 2009.

[Lohmann and Feichter(1997)] Lohmann, U. and Feichter, J.: Impact of sulfate aerosols on albedo and lifetime of clouds: a sensitivity study with the ECHAM4 GCM, J. Geophys. Res., 102, 13685–13700, 1997.

[Lohmann and Feichter(2005)] Lohmann, U. and Feichter, J.: Global indirect aerosol effects: a review, Atmos. Chem. Phys., 5, 715–737, 10.5194/acp-5-715-2005, 2005.

[Lohmann and Lesins(2003)] Lohmann, U. and Lesins, G.: Comparing continental and oceanic cloud susceptibilities to aerosols, Geophys. Res. Lett., 30, 1791, 10.1029/2003GL017828, 2003.

[Lohmann et al.(1999)] Lohmann, U., Feichter, J., Chuang, C. C., and Penner, J. E.: Prediction of the number of cloud droplets in the ECHAM GCM, J. Geophys. Res., 104, 9169–9198, 1999.

[Lohmann et al.(2007)] Lohmann, U., Stier, P., Hoose, C., Ferrachat, S., Kloster, S., Roeckner, E., and Zhang, J.: Cloud microphysics and aerosol indirect effects in the global climate model ECHAM5-HAM, Atmos. Chem. Phys., 7, 3425–3446, 10.5194/acp-7-3425-2007, 2007.

[Lohmann et al.(2010)] Lohmann, U., Rotstayn, L., Storelvmo, T., Jones, A., Menon, S., Quaas, J., Ekman, A. M. L., Koch, D., and Ruedy, R.: Total aerosol effect: radiative forcing or radiative flux perturbation?, Atmos. Chem. Phys., 10, 3235–3246, 10.5194/acp-10-3235-2010, 2010.

[Matsui et al. (2006)] Matsui, T., Masunaga, H., Kreidenweis, S. M., Pielke Sr., R. A., Tao, W.-K., Chin, M., and Kaufman, Y. J.: Satellite based assessment of marine low cloud variability associated with aerosol, atmospheric stability, and the diurnal cycle, J. Geophys. Res.,D17204, 2006.

[Mann et al.(2014)] Mann, G. W., Carslaw, K. S., Reddington, C. L., Pringle, K. J., Schulz, M., Asmi, A., Spracklen, D. V., Ridley, D. A., Woodhouse, M. T., Lee, L. A., Zhang, K., Ghan, S. J., Easter, R. C., Liu, X., Stier, P., Lee, Y. H., Adams, P. J., Tost, H., Lelieveld, J., Bauer, S. E., Tsigaridis, K., van Noije, T. P. C., Strunk, A., Vignati, E., Bellouin, N., Dalvi, M., Johnson, C. E., Bergman, T., Kokkola, H., von Salzen, K., Yu, F., Luo, G., Petzold, A., Heintzenberg, J., Clarke, A., Ogren, J. A., Gras, J., Baltensperger, U., Kaminski, U., Jennings, S. G., O'Dowd, C. D., Harrison, R. M., Beddows, D. C. S., Kulmala, M., Viisanen, Y., Ulevicius, V., Mihalopoulos, N., Zdimal, V., Fiebig, M., Hansson, H.-C., Swietlicki, E., and Henzing, J. S.: Intercomparison and evaluation of global aerosol microphysical properties among AeroCom models of a range of complexity, Atmos. Chem. Phys., 14, 4679–4713, 10.5194/acp-14-4679-2014, 2014.

[Mazzola et al.(2010)] Mazzola, M., Lanconelli, C., Lupi, A., Busetto, M., Vitale, V., and Tomasi, C.: Columnar aerosol optical properties in the Po Valley, Italy, from MFRSR data, J. Geophys. Res., 115, D17206, doi:10.1029/2009JD013310, 2010.

[McFiggans et al.(2006)] McFiggans, G., Artaxo, P., Baltensperger, U., Coe, H., Facchini, M. C., Feingold, G., Fuzzi, S., Gysel, M., Laaksonen, A., Lohmann, U., Mentel, T. F., Murphy, D. M., O'Dowd, C. D., Snider, J. R., and Weingartner, E.: The effect of physical and chemical aerosol properties on warm cloud droplet activation, Atmos. Chem. Phys., 6, 2593–2649, 10.5194/acp-6-2593-2006, 2006.

[Menon et al.(2002)] Menon, S., Del Genio, A. D., Koch, D., and Tselioudis, G.: GCM simulations of the aerosol indirect effect: sensitivity to cloud parameterization and aerosol burden, J. Atmos. Sci., 59, 692–713, 2002.

[Middlebrook et al.(1998)] Middlebrook, A. M., D. M. Murphy, and D. S. Thomson, Observations of organic material in individual marine particles at Cape Grim during the First Aerosol Characterization Experiment (ACE 1), J. Geophys. Res., 103, 16,475–16,483, 1998

[Mikhailov et al.(2009)] Mikhailov, E., Vlasenko, S., Martin, S. T., Koop, T., and Pöschl, U.: Amorphous and crystalline aerosol particles interacting with water vapor: conceptual framework and experimental evidence for restructuring, phase transitions and kinetic limitations, Atmos. Chem. Phys., 9, 9491–9522, 10.5194/acp-9-9491-2009, 2009.

[Ming et al.(2006)] Ming, Y., Ramaswamy, V., Donner, L. J., and Phillips, V. T. J.: A new parameterization of cloud droplet activation applicable to general circulation models, J. Atmos. Sci., 63, 1348–1356, 10.1175/JAS3686.1, 2006.

[Moore et al.(2012)] Moore, R. H., Cerully, K., Bahreini, R., Brock, C. A., Middlebrook, A. M., and Nenes, A.: Hygroscopicity and composition of California CCN during summer 2010, J. Geophys. Res., 117, D00V12, 10.1029/2011JD017352, 2012.

[Morgan et al.(2009)] Morgan, W. T., Allan, J. D., Bower, K. N., Capes, G., Crosier, J., Williams, P. I., and Coe, H.: Vertical distribution of sub-micron aerosol chemical composition from North-Western Europe and the North-East Atlantic, Atmos. Chem. Phys., 5389–5401, 2009.

[Nenes et al. (2001)] Nenes, A., Ghan, S., Abdul-Razzak, H., Chuang, P. and Seinfeld, J.: Kinetic limitations on cloud droplet formation and impact on cloud albedo, Tellus, Ser. B, 53, 133–149, 2001.

[Nenes et al. (2002)] Nenes, A., Charlson,R. J., Facchini, M. C., Kulmala, M., Laaksonen, A. and Seinfeld J. H.:Can chemical effects on cloud droplet number rival the first indirect effect?, Geophys. Res. Lett., 29(17), 1848, doi:10.1029/2002GL015295, 2002.

[Nenes and Seinfeld(2003)] Nenes, A. and Seinfeld, J. H.: Parameterization of cloud droplet formation in global climate models, J. Geophys. Res., 108, 4415, 10.1029/2002JD002911, 2003.

[Niedermeier et al.(2008)] Niedermeier, D., Wex, H., Voigtländer, J., Stratmann, F., Brüggemann, E., Kiselev, A., Henk, H., and Heintzenberg, J.: LACIS-measurements and parameterization of sea-salt particle hygroscopic growth and activation, Atmos. Chem. Phys., 8, 579–590, 10.5194/acp-8-579-2008, 2008.

[Novokov et al.(1997)] Novakov, T., Corrigan, C.E., Penner, J. E., Chuang, C.C., Rosario, O. and Bracero, O.L.M.: Organic aerosols in the Caribbean trade winds: A natural source?, Journal of Geophysical Research 102: doi: 10.1029/97JD01487. issn: 0148-0227, 1997.

[O'Dowd et al.(2004)] O'Dowd, C. D., Facchini M. C., Cavalli F., Ceburnis, D., Mircea, M., Decesari, S., Fuzzi, S., Yoon, Y. J., and Putaud, J. P.: Biogenically driven organic contribution to marine aerosol, Nature, 431, 67680, 2004.

[Patra et al.(2005)] Patra, P. K., Behera, S. K., Herman, J. R., Maksyutov, S., Akimoto, H., and Yamagata, Y.: The Indian summer monsoon rainfall: interplay of coupled dynamics, radiation and cloud microphysics, Atmos. Chem. Phys., 5, 2181–2188, 10.5194/acp-5-2181-2005, 2005.

[Peng and Lohmann(2003)] Peng, Y. and Lohmann, U.: Sensitivity study of the spectral dispersion of the cloud droplet size distribution on the indirect aerosol effect, Geophys. Res. Lett., 30, 1507, 10.1029/2003GL017192, 2003.

[Penner et al.(2003)] Penner, J. E., Zhang, S. Y., and Chuang, C. C.: Soot and smoke aerosol may not warm climate, J. Geophys. Res., 108, 4657, 10.1029/2003JD003409, 2003.

[Penner et al.(2004)] Penner, J. E., Dong, X., and Chen, Y.: Observational evidence of a change in radiative forcing due to the indirect aerosol effect, Nature, 427, 231–234, 2004.

[Penner et al.(2006)] Penner, J. E., Quaas, J., Storelvmo, T., Takemura, T., Boucher, O., Guo, H., Kirkevåg, A., Kristjánsson, J. E., and Seland, Ø.: Model intercomparison of indirect aerosol effects, Atmos. Chem. Phys., 6, 3391–3405, 10.5194/acp-6-3391-2006, 2006.

[Petters et al.(2012)] Peters, G. P., Davis, S. J., and Andrew, R.: A synthesis of carbon in international trade, Biogeosciences, 9, 3247–3276, doi:10.5194/bg-9-3247-2012, 2012.

[Petters and Kreidenweis(2007)] Petters, M. D. and Kreidenweis, S. M.: A single parameter representation of hygroscopic growth and cloud condensation nucleus activity, Atmos. Chem. Phys., 7, 1961–1971, 10.5194/acp-7-1961-2007, 2007.

[Pio et al.(2007)] Pio, C. A., Legrand, M., Oliveira, T., Afonso, J., Santos, C., Caseiro, A., Fialho, P., Barata, F., Puxbaum, H., Sanchez-Ochoa, A., Kasper-Giebl, A., Gelencser, A., Preunkert, S., and Schock, M.: Climatology of aerosol composition (organic versus inorganic) at nonurban sites on a west-east transect across Europe, J. Geophys. Res., 112, D23S02, doi:10.1029/2006JD008038, 2007.

[Pincus et al.(2008)] Pincus, R., Batstone, C. P., Hofmann, R. J. P., Taylor, K. E., and Gleckler, P. J.: Evaluating the present-day simulation of clouds, precipitation, and radiation in climate models, J. Geophys. Res., 113, D14209, 10.1029/2007JD009334, 2008.

[Pöschl et al.(2009)] Pöschl, U., Rose, D., and Andreae, M. O.: Climatologies of cloudrelated aerosols – Part 2: Particle hygroscopicity and cloud condensation nuclei activity, in: Clouds in the Perturbed Climate System, edited by: Heintzenberg, J. and Charlson, R. J., MIT Press, Cambridge, ISBN 978-0-262-012874, 58–72, 2009.

[Posselt and Lohmann(2008)] Posselt, R. and Lohmann, U.: Introduction of prognostic rain in ECHAM5: design and single column model simulations, Atmos. Chem. Phys., 8, 2949–2963, 10.5194/acp-8-2949-2008, 2008.

[Pozzer et al.(2010)] Pozzer, A., Pollmann, J., Taraborrelli, D., Jöckel, P., Helmig, D., Tans, P., Hueber, J., and Lelieveld, J.: Observed and simulated global distribution and budget of atmospheric $C_2 - -C_5alkanes, Atmos.Chem.Phys., 10, 4403 - -4422, 10.5194/acp - 10 - 4403 - 2010, 2010$.

[Pozzer et al.(2012)] Pozzer, A., de Meij, A., Pringle, K. J., Tost, H., Doering, U. M., van Aardenne, J., and Lelieveld, J.: Distributions and regional budgets of aerosols and their precursors simulated with the EMAC chemistry-climate model, Atmos. Chem. Phys., 12, 961–987, 10.5194/acp-12-961-2012, 2012.

[Pringle et al.(2010a)] Pringle, K. J., Tost, H., Message, S., Steil, B., Giannadaki, D., Nenes, A., Fountoukis, C., Stier, P., Vignati, E., and Lelieveld, J.: Description and evaluation of GMXe: a new aerosol submodel for global simulations (v1), Geosci. Model Dev., 3, 391–412, 10.5194/gmd-3-391-2010, 2010a.

[Pringle et al.(2010b)] Pringle, K. J., Tost, H., Pozzer, A., Pöschl, U., and Lelieveld, J.: Global distribution of the effective aerosol hygroscopicity parameter for CCN activation, Atmos. Chem. Phys., 10, 5241–5255, 10.5194/acp-10-5241-2010, 2010b.

[Pruppacher and Klett(2000)] Pruppacher, H. R. and Klett, J. D.: Microphysics of Clouds and Precipitation, Kluwer Acad. Publ., Dordrecht, 2000.

[Quaas et al.(2004)] Quaas, J., Boucher, O., and Breon, F.-M.: Aerosol indirect effects in POLDER satellite data and the Laboratoire de Meteorologie Dynamique-Zoom (LMDZ) general circulation model, J. Geophys. Res., 109, D08205, 10.1029/2003JD004317, 2004.

[Quaas et al.(2008)] Quaas, J., Boucher, O., Bellouin, N., and Kinne, S.: Satellite-based estimate of the direct and indirect aerosol climate forcing, J. Geophys. Res., 113, D05204, 10.1029/2007JD008962, 2008.

[Quaas et al.(2009)] Quaas, J., Ming, Y., Menon, S., Takemura, T., Wang, M., Penner, J. E., Gettelman, A., Lohmann, U., Bellouin, N., Boucher, O., Sayer, A. M., Thomas, G. E., McComiskey, A., Feingold, G., Hoose, C., Kristjánsson, J. E., Liu, X., Balkanski, Y., Donner, L. J., Ginoux, P. A., Stier, P., Grandey, B., Feichter, J., Sednev, I., Bauer, S. E., Koch, D., Grainger, R. G., Kirkevåg, A., Iversen, T., Seland, Ø., Easter, R., Ghan, S. J., Rasch, P. J., Morrison, H., Lamarque, J.-F., Iacono, M. J., Kinne, S., and Schulz, M.: Aerosol indirect effects – general circulation model intercomparison and evaluation with satellite data, Atmos. Chem. Phys., 9, 8697–8717, 10.5194/acp-9-8697-2009, 2009.

[Reeves et al.(2010)] Reeves, C. E., Formenti, P., Afif, C., Ancellet, G., Attie, J.-L., Bechara, J., Borbon, A., Cairo, F., Coe, H., Crumeyrolle, S., Fierli, F., Flamant, C., Gomes, L., Hamburger, T., Jambert, C., Law, K. S., Mari, C., Jones, R. L., Matsuki, A., Mead, M. I., Methven, J., Mills, G. P., Minikin, A., Murphy, J. G., Nielsen, J. K., Oram, D. E., Parker, D. J., Richter, A., Schlager, H., Schwarzenboeck, A., and Thouret, V.: Chemical and aerosol characterisation of the troposphere over West Africa during the monsoon period as part of AMMA, Atmos. Chem. Phys., 10, 7575–7601, doi:10.5194/acp-10-7575-2010, 2010.

[Reichler and Kim(2008)] Reichler, T. and Kim, J.: How well do coupled models simulate today's climate?, B. Am. Meteorol. Soc., 89, 303–311, 10.1175/BAMS-89-3-303, 2008

[Reichler et al. (2012)] Reichler, T., Kim, J., Manzini, E., and Kroeger, J.: A stratospheric connection to Atlantic climate variability, Nature Geos., 783–787, doi: 10.1038/ngeo1586, 2012.

[Reid et al.(1999)] Reid, J. S., Eck, T. F., Christopher, S. A., Hobbs, P. V., and Holben, B. N.: Use of the Ångström exponent to estimate the variability of optical and physical properties of aging smoke particles in Brazil, J. Geophys. Res., 104, 27473–27489, 1999.

[Reutter et al.(2009)] Reutter, P., Su, H., Trentmann, J., Simmel, M., Rose, D., Gunthe, S. S., Wernli, H., Andreae, M. O., and Pöschl, U.: Aerosol- and updraft-limited regimes of cloud droplet formation: influence of particle number, size and hygroscopicity on the activation of cloud condensation nuclei (CCN), Atmos. Chem. Phys., 9, 7067–7080, 10.5194/acp-9-7067-2009, 2009.

[Richardson et al.(2007)] Richardson, M. I., Toigo, A. D., and Newman, C. E.: PlanetWRF: A general purpose, local to global numerical model for planetary atmospheric and climate dynamics, J. Geophys. Res., 112, E09001, doi:10.1029/2006JE002825, 2007

[Roeckner et al.(2006)] Roeckner, E., Brokopf, R., Esch, M., Giogetta, M., Hagemann, S., Kornblueh, L., Manzini, E., Schleese, U., and Schulzweida, U.: Sensitivity of simulated climate to horizontal and vertical resolution in the ECHAM5 atmosphere model, J. Climate, 19, 3771–3791, 2006.

[Roger and Yau(1989)] Rogers, R. R. and Yau, M. K.:A Short Course in Cloud Physics, 3rd Ed. Pergamon Press. 293 pp, 1989.

[Rose et al.(2008)] Rose, D., Gunthe, S. S., Mikhailov, E., Frank, G. P., Dusek, U., Andreae, M. O., and Pöschl, U.: Calibration and measurement uncertainties of a continuous-flow cloud condensation nuclei counter (DMT-CCNC): CCN activation of ammonium sulfate and sodium chloride aerosol particles in theory and experiment, Atmos. Chem. Phys., 8, 1153–1179, 10.5194/acp-8-1153-2008, 2008.

[Rose et al.(2010)] Rose, D., Nowak, A., Achtert, P., Wiedensohler, A., Hu, M., Shao, M., Zhang, Y., Andreae, M. O., and Pöschl, U.: Cloud condensation nuclei in polluted air and biomass burning smoke near the mega-city Guangzhou, China – Part 1: Size-resolved measurements and implications for the modeling of aerosol particle hygroscopicity and CCN activity, Atmos. Chem. Phys., 10, 3365–3383, 10.5194/acp-10-3365-2010, 2010.

[Rose et al.(2011)] Rose, D., Gunthe, S. S., Su, H., Garland, R. M., Yang, H., Berghof, M., Cheng, Y. F., Wehner, B., Achtert, P., Nowak, A., Wiedensohler, A., Takegawa, N., Kondo, Y., Hu, M., Zhang, Y., Andreae, M. O., and Pöschl, U.: Cloud condensation nuclei in polluted air and biomass burning smoke near the mega-city Guangzhou, China – Part 2: Size-resolved aerosol chemical composition, diurnal cycles, and externally mixed weakly CCN-active soot particles, Atmos. Chem. Phys., 11, 2817–2836, 10.5194/acp-11-2817-2011, 2011.

[Rosenfeld(2000)] Rosenfeld, D.: Suppression of rain and snow by urban and industrial air pollution, Science, 287, 1793–1796, 2000.

[Rosenfeld(2006)] Rosenfeld, D., 2006. Aerosolloud interactions control of earth radiation and latent heat release budgets. Space Sci. Rev.125 (1–4),149–157. doi:10.1007/s11214-006-9053-6.

[Rotstayn et al.(2007)] Rotstayn, L. D., Cai, W., Dix, M. R., Farquhar, G. D., Feng, Y., Ginoux, P., Herzog, M., Ito, A., Penner, J. E., Roderick, M. L., and Wang, M.: Have Australian rainfall and cloudiness increased due to the remote effects of Asian anthropogenic aerosols?, J. Geophys. Res., 112, D09202, 10.1029/2006JD007712, 2007.

[Ruehl et al.(2009)] Ruehl, C. R., Chuang, P. Y., and Nenes, A.: Distinct CCN activation kinetics above the marine boundary layer along the California coast, Geophys. Res. Lett., 36, L15814, 10.1029/2009GL038839, 2009.

[Sabbach et al.(2006)] Sabbah, I., Saeed, T., Al Jassar, H. K., and Rao, K. S.: Remote sensing of desert dust in Kuwait, J. Sci. Eng., 33, 101–117, 2006.

[Sander et al.(2005)] Sander, R., Kerkweg, A., Jöckel, P., and Lelieveld, J.: Technical note: The new comprehensive atmospheric chemistry module MECCA, Atmos. Chem. Phys., 5, 445–450, 10.5194/acp-5-445-2005, 2005.

[Schwartz et al.(2002)] Schwartz, S. E., Harshvardhan, and Benkovitz, C. M.: Influence of anthropogenic aerosol on cloud optical depth and albedo shown by satellite measurements and chemical transport modeling, P. Natl. Acad. Sci. USA, 99, 1784–1789, 2002.

[Seinfeld and Pandis(1998)] Seinfeld, J. H. and Pandis, S. N.: Atmospheric Chemistry and Physics: From Air Pollution to Climate Change, Wiley, New York, 1998.

[Shinozuka et al.(2010)] Shinozuka, Y., Clarke, A. D., DeCarlo, P. F., Jimenez, J. L., Dunlea, E. J., Roberts, G. C., Tomlinson, J. M., Collins, D. R., Howell, S. G., Kapustin, V. N., McNaughton, C. S., and Zhou, J.: Aerosol optical properties relevant to regional remote sensing of CCN activity and links to their organic mass fraction: airborne observations over Central Mexico and the US West Coast during MILAGRO/INTEX-B, Atmos. Chem. Phys., 9, 6727–6742, 10.5194/acp-9-6727-2009, 2009.

[Shipway and Abel(2010)] Shipway, B. J. and Abel, S. J.: Analytical estimation of cloud droplet nucleation based on an underlying aerosol population, Atmos. Res., 96, 344–355, 10.1016/j.atmosres.2009.10.005, 2010

[Sinha et al.(2003)] Sinha, P., Hobbs, P. V., Yokelson, R. J., Blake, D. R., Gao, S., and Kirchstetter, T.W.: Distributions of trace gases and aerosols during the dry biomass burning season in southern Africa, J. Geophys. Res., 108(D17), 4536, 2003.

[Small et al.(2009)] Small, J. D., Chuang, P. Y., Feingold, G., and Jiang, H.: Can aerosol decrease cloud lifetime?, Geophys. Res. Lett., 36, L16806, 10.1029/2009GL038888, 2009.

[Snider and Petters(2008)] Snider, J. R. and Petters, M. D.: Optical particle counter measurement of marine aerosol hygroscopic growth, Atmos. Chem. Phys., 8, 1949–1962, 10.5194/acp-8-1949-2008, 2008.

[Snider et al.(2010)] Snider, J. R., Wex, H., Rose, D., Kristensson, A., Stratmann, F., Hennig, T., Henning, S., Kiselev, A., Bilde, M., Burkhart, M., Dusek, U., Frank, G. P., Kiendler-Scharr, A., Mentel, T. F., Petters, M. D., and Pöschl, U.: Intercomparison of CCN and hygroscopic fraction measurements from LExNo, J. Geophys. Res., 115, D11205, 10.1029/2009JD012618, 2010.

[Spracklen et al.(2008)] Spracklen, D. V., Carslaw, K. S., Kulmala, M., Kerminen, V. M., Sihto, S. L., Riipinen, I., Merikanto, J., Mann, G. W., Chipperfield, M. P., Wiedensohler, A., Birmili, W., and Lihavainen, H.: Contribution of particle formation to global cloud condensation nuclei concentrations, Geophys. Res. Lett., 35, L06808, 10.1029/2007GL033038, 2008.

[Stevens and Feingold(2009)] Stevens, B. and Feingold, G.: Untangling aerosol effects on clouds and precipitation in a buffered system, Nature, 461, 607–613, 2009.

[Stier et al.(2005)] Stier, P., Feichter, J., Kinne, S., Kloster, S., Vignati, E., Wilson, J., Ganzeveld, L., Tegen, I., Werner, M., Balkanski, Y., Schulz, M., Boucher, O., Minikin, A., and Petzold, A.: The aerosol-climate model ECHAM5-HAM, Atmos. Chem. Phys., 5, 1125–1156, 10.5194/acp-5-1125-2005, 2005.

[Storelvmo et al.(2008)] Storelvmo, T., Kristjánsson, J.-E., and Lohmann, U.: Aerosol influence on mixed-phase clouds in CAM-Oslo, J. Atmos. Sci., 65, 3214–3230, 2008.

[Su et al.(2010)] Su, H., Rose, D., Cheng, Y. F., Gunthe, S. S., Massling, A., Stock, M., Wiedensohler, A., Andreae, M. O., and Pöschl, U.: Hygroscopicity distribution concept for measurement data analysis and modeling of aerosol particle mixing state with regard to hygroscopic growth and CCN activation, Atmos. Chem. Phys., 10, 7489–7503, 10.5194/acp-10-7489-2010, 2010.

[Sundqvist et al.(1989)] Sundqvist, H., Berge, E., and Kristjánsson, J. E.: Condensation and cloud parameterization studies with a mesoscale numerical weather prediction model, Mon. Weather Rev., 117, 1641–1657,1989.

[Swap et al.(1996)] Swap, R., Garstang, M., Macko, S. A., Tyson, P. D., Maenhaut, W., Artaxo, P., Kallberg, P., and Talbot, R.: The ong-range transport of southern African aerosols to the tropical South Atlantic, J. Geophys. Res., 101, 23777–23791, 1996.

[Tanré et al.(1997)] Tanré, D., Kaufman, Y., Herman, M., and Mattoo, S.: Remote sensing of aerosol properties over oceans using the MODIS/EOS spectral radiances, J. Geophys. Res., 102, 16971–16988, 10.1029/96JD03437, 1997.

[Taylor(2001)] Taylor, K. E.: Summarizing multiple aspects of model performance in a single diagram, J. Geophys. Res., 106, 7183–7192, 2001.

[Taylor (2005)] Taylor, K. E.: Taylor Diagram Primer. http://www-pcmdi.llnl.gov/about/staff/Taylor/CV/Taylor$_d iagram_p rimer.pdf$, 2005.

[Textor et al. (2007)] Textor, C., Schulz, M., Guibert, S., Kinne, S., Balkanski, Y., Bauer, S., Berntsen, T., Berglen, T., Boucher, O., Chin, M., Dentener, F., Diehl, T., Feichter, J., Fillmore, D., Ginoux, P., Gong, S., Grini, A., Hendricks, J., Horowitz, L., Huang, P., Isaksen, I. S. A., Iversen, T., Kloster, S., Koch, D., Kirkevag, A., Kristjansson, J. E., Krol, M., Lauer, A., Lamarque, J. F., Liu, X., Montanaro, V., Myhre, G., Penner, J. E., Pitari, G., Reddy, M. S., Seland, ., Stier, P., Takemura, T., and Tie, X.: The effect of harmonized emissions on aerosol properties in global models an AeroCom experiment, Atmos. Chem. Phys., 7, 4489501, doi:10.5194/acp-7-4489-2007, 2007.

[Tompkins (2002)] Tompkins, A. M.: A prognostic parameterization for the subgrid scale variability of water vapor and clouds in large-scale models and its use to diagnose cloud cover, J. Atmos. Sci., 59, 1917–1942, 2002.

[Tompkins (2005)] Tompkins, A. M.: The parameterization of cloud cover, ECMWF Moist Processes Lecture Note Series, available at: http://old.ecmwf.int/newsevents/training/lecture$_n otes/pdf_f iles/PARAM/Cloudcover.pdf$ ($lastaccess$: 26$August$2014), 2005.

[Tost et al.(2006)] Tost, H., Jöckel, P., Kerkweg, A., Sander, R., and Lelieveld, J. : Technical note: A new comprehensive SCAVenging submodel for global atmospheric chemistry modelling, Atmos. Chem. Phys., 6, 565–574, 10.5194/acp-6-565-2006, 2006.

[Tost et al.(2007a)] Tost, H., Jöckel, P., Kerkweg, A., Pozzer, A., Sander, R., and Lelieveld, J.: Global cloud and precipitation chemistry and wet deposition: tropospheric model simulations with ECHAM5/MESSy1, Atmos. Chem. Phys., 7, 2733–2757, 10.5194/acp-7-2733-2007, 2007a.

[Tost et al.(2007b)] Tost, H., Jöckel, P., and Lelieveld, J.: Lightning and convection parameterisations – uncertainties in global modelling, Atmos. Chem. Phys., 7, 4553–4568, 10.5194/acp-7-4553-2007, 2007b.

[Tost et al.(2010)] Tost, H., Lawrence, M. G., Brühl, C., Jöckel, P.: The GABRIEL Team, and The SCOUT-O3-DARWIN/ACTIVE Team: Uncertainties in atmospheric chemistry modelling due to convection parameterisations and subsequent scavenging, Atmos. Chem. Phys., 10, 1931–1951, 10.5194/acp-10-1931-2010, 2010.

[Twomy (2008)] Twomey, S. A.: The influence of pollution on the shortwave albedo of clouds, J. Atmos. Sci., 34, 1149–1152, 1977.

[Tyson(1986)] Tyson, P. D.: Climatic Change and Variability in Southern Africa, Oxford Univ. Press, 220–221, 1986.

[Wang et al.(2008)] Wang, J., Lee, Y.-N., Daum, P. H., Jayne, J., and Alexander, M. L.: Effects of aerosol organics on cloud condensation nucleus (CCN) concentration and first indirect aerosol effect, Atmos. Chem. Phys., 8, 6325–6339, 10.5194/acp-8-6325-2008, 2008.

[Wang and Penner(2009)] Wang, M. and Penner, J. E.: Aerosol indirect forcing in a global model with particle nucleation, Atmos. Chem. Phys., 9, 239–260, 10.5194/acp-9-239-2009, 2009.

[Weber et al.(2011)] Weber, T., Quaas, J., and Räisänen, P.: Evaluation of the statistical cloud scheme in the ECHAM5 model using satellite data, Q. J. Roy. Meteor. Soc., 137, 2079–2091, 2011.

[Wex et al. (2008)] Wex, H., Stratmann, F., Topping, D., and McFiggans, G.: The Kelvin versus the Raoult term in the Köhler equation, J. Atmos. Sci., 65, 4004–4016, 2008.

[Wex et al.(2009)] Wex, H., Petters, M. D., Carrico, C. M., Hallbauer, E., Massling, A., McMeeking, G. R., Poulain, L., Wu, Z., Kreidenweis, S. M., and Stratmann, F.: Towards closing the gap between hygroscopic growth and activation for secondary organic aerosol: Part 1–Evidence from measurements, Atmos. Chem. Phys., 9, 3987–3997, 2009.

]WC1976 Whitby KT, Cantrell BK. Proceedings of the International Conference on Environmental Sensing and Assessment (ICESA), Institute of Electrical and Electronic Engineers (IEEE) 1976. Atmospheric aerosols: characteristics and measurement. IEEE 75-CH 1004-1, ICESA paper 29-1, Washington, DC: IEEE. p. 6

[Wielicki et al.(1996)] Wielicki, B. A., Barkstrom, B. R., Harrison, E. F., Lee III, R. B., Smith, G. L., and Cooper, J. E.: Clouds and the Earth's Radiant Energy System (CERES): an earth observing system experiment, B. Am. Meteorol. Soc., 77, 853–868, 1996.

[Yoon et al.(2014)] Yoon, J., Burrows, J. P., Vountas, M., von Hoyningen-Huene, W., Chang, D. Y., Richter, A., and Hilboll, A.: Changes in atmospheric aerosol loading retrieved from space-based measurements during the past decade, Atmos. Chem. Phys., 14, 6881–6902, 10.5194/acp-14-6881-2014, 2014.

[Yuan et al. 2008] Yuan, T., Li, Z., Chang, F. L., Vant-Hull, B., and Rosenfeld, D.: Increase of cloud droplet size with aerosol optical depth: An observation and modeling study, J. Geophys. Res., 113, D04201, 2008.

Eidesstattliche Erklärung

Hiermit erklre ich eidesstattlich, die vorliegende Dissertation selbständig und nur mit den angegebenen Hilfsmitteln angefertigt sowie noch keinen Promotionsversuch unternommen zu haben.

Mainz, den _____

_____

Unterschrift